Cellular and molecular determinants of synapse remodeling

By

Andrea A Cuentas-Condori

Dissertation

submitted to the Faculty of the

Graduate School of Vanderbilt University

in partial fulfillment of the requirements

for the degree of

DOCTOR OF PHILOSOPHY

In

Cell and Developmental Biology

June 30th, 2021

Nashville, Tennessee

Approved:

David M. Miller, Ph. D., Advisor

Kathleen Gould, Ph. D., Committee Chair

Andrea Page-McCaw, Ph. D.

Kevin Ess, M.D., Ph. D.

Bruce Carter, Ph. D.

Ege Kavalali, Ph. D.

DEDICATION

A la memoria de mis padres, María Luisa y Hernán.

Y a mi familia, donde el amor solo se multiplica.

ACKNOWLEDGEMENTS

I want to start by thanking my parents, María Luisa Condori Flores and Hernán Adolfo Cuentas Anci, who always believed in me, who inspired me to follow my curiosity, to be true to my values, and whose passion continues to fuel each one of my dreams. They are the reason I got here.

But getting to Vanderbilt was only the very first step; my Ph.D. years would not have been as bearable without the help and support of my mentor, David M. Miller. I still remember our first meeting after I decided to join his lab. I asked him to push me as I could work well under pressure and I wanted to be productive. He, with his warm gaze, smiled at me and told me that everything was going to be fine. I remember that I was scared because he gave me the impression that he would not push me. However, how grateful I am that he guided me with patience and without unnecessary pressure. Obtaining this Ph.D. was a challenging quest by itself and David's mentoring just smoothed the process. He was exactly the mentor I needed. In these 6 years that we have worked together, David has not only taught me about science but also about priorities outside the lab. Priorities with myself, my health, my family and my life that go beyond the experiments I do or the papers I publish. David also taught me how to write. He is a great, meticulous writer and his detail-oriented editing style has taught me so much about academic English. Now I find myself comfortably writing my ideas in an organized fashion, synthesizing information, paraphrasing and highlighting why my science is important, in a language that I didn't grow up talking! It took some time, but I think it paid off. So, thank you so much David, for these good six years, for using your voice and position of power to advocate for my loved ones and me; for being willing to write so many letters of recommendations for every opportunity I found; for trusting that I could do it and for creating a space for my voice whenever I needed it. Thanks.

Also, thanks for creating such a collegial and healthy atmosphere in lab. All of my lab mates have always been very supportive and generous. They have been there in some of the best and toughest days in my life. Each member, they have all made me a better scientist, colleague and friend. Thanks, Sierra, Lakshmi, Siwei, Tyne, Seth, Tyler, Becky, Leah, John, Becca, Barbara, Jamie and Casey. I'll cherish all our many conversations, the ups and downs in the daily lab routine, our trips, hunting every mite, cleaning every bottle (or not). I am lucky to have learn from each one of you.

I also want to thank all the students and lab members I got the chance to mentor. Micah Foster, Kelly Wilson, Briza Vasquez, Sophie Rowlett, Nathan Hopkins, Alice Siqi Chen, Mia Brakebill, John Tipps, José Carlos Zepeda, Leah Flautt and Casey Gailey. They have all made me feel super proud. All of their questions have made me a better scientist and with each one of them I learned something about our project and about myself. They have shaped how I approach one-on-one teaching and for that experience I will always be thankful.

My training at Vanderbilt also benefitted from the whole community and the mentors I was able to find also outside the lab. First, Andrea Page-McCaw, who I met one year before entering the IGP class. She gave me the opportunity to intern in her laboratory and that experience just changed my life. I cannot stress enough how important she has been in my career inside and outside Vanderbilt. Especially suggesting professional moves that I did not know were possible. She suggested that I apply to postdoctoral fellowships before finishing the PhD and that, again, has changed the beginning of my next step only for good. Thank you, Andrea! Also, Kathy Gould, who I met at the end of my internship at Vanderbilt. She filled me with confidence into applying to Vanderbilt the following cycle and, since then, I have been impressed with her capacity to communicate the ins and outs of an academic career. She is one of my go-to persons regarding professional advice and career decisions, she has so much information, and she is always willing to share. Thank you, Kathy! I also want to specially thank Vivian Gama. I met her at a dinner organized by the Vanderbilt International Scholars Program (VIPS). VISP recruited me to

Vanderbilt and gave me an important support network during the first years of moving to the US. Since I met Vivian, many of the things she talked about resonated so much with me. I was just impressed by how much of what I was going through; she had already lived. I am lucky she is in my life and that she is willing to share with me all her experience in adopting a new culture, navigating the academic path as a Latina, creating networks and space for diverse voices. All of that while succeeding in her science and dedicated to training her students. My relationship with Vivian has shown me how important it is to know a Professor with your similar background and gain insight from their experience. She is an invaluable mentor to me, and I wish every student at Vanderbilt has the opportunity to find a mentor that shares their background and identity. It improves your sense of belonging, which has direct repercussions on building your persona and critical being.

I want to extend my gratitude also to other members in the Vanderbilt community, Bruce Carter, Kevin Ess and Ege Kavalali as members of my committee, and Teru Nakagawa, Dylan Burnette, Todd Graham, Lauren Jackson, Roger Colbran, Matt Tyska, Irina Kaverina, Ian Macara, just to name a few. They have given me great insights into my science and academic development. They were always willing to exchange ideas over an email, meeting together or chatting at the corridor or during retreats. I am very grateful for the collegial spirit established at Vanderbilt, which only teaches us trainees how to carry that healthy spirit everywhere we go. Also, thanks to Kristi Hargrove, Susan Walker and Lorie Franklin. They have saved me so many times! And have always encouraged me to keep going.

I also want to thank all the resources available at Vanderbilt that gave me the best training possible. The many resources available at the CISR, not only regarding equipment but most importantly the expertise from Jenny, Kari, Bryan, Bob, Stefanie and Nathan. Their vast experience with live-imaging has only improved my science and made it possible to test some very challenging predictions of my scientific models. The great scientific community that was built around the Microtubules and Motors club. They only pushed me to get out of my comfort zone

and learn, learn and learn. Their on-point advice has only made my science better and has broaden my knowledge very much. Also, the CV Clinic run by the BRET office. Their skilled advice has only made every cover letter and statement much better. To the point that my success rate went up since I started using the CV clinic, I truly recommend it to every student at Vanderbilt! In addition to working on my writing with David, I also took advantage of the English Language Center which is dedicated to students who use English as their second language. They introduced me to academic writing and to the many vowel sounds available in the English language - which I only discovered then, after speaking this language for more than ten years. It was mind blowing. The many resources, references and tips I got from them were super important for my development as a confident writer and presenter. Finally, I want to thank the University Counseling Center, through them I got access to a marvelous therapist who helped me navigate my grief and taught me to be kinder to myself. It definitely takes a village to become a successful and balanced graduate student, and Vanderbilt has one of the most resourceful villages. I am thankful for the resources available and encourage every student to be aware of them and to use them, they can only improve your training!

I also want to continue thanking my family. My siblings, the best gift my parents gave me. Each one of them, Luis, Paola, Claudia and Hernán have been my driving force and motivation during these past 7 years. The tenderness, complicity and understanding of each one of them. Despite being not only thousands of miles away, but in very different realities since the pandemic began, we have always been close. Luis, with his resilience and affection, has taught me to listen and to express what I think and feel. Pao, with her big heart and ability to listen, has taught me to have integrity, to keep sharing and to overcome my fears. Clau, with her powers of the soul and mind, has taught me to trust and enjoy the mirror of therapy. Hernán, with his honesty and courage to look inside, feel and understand, has taught me that there is always room to continue discovering myself. All of my siblings have helped me build a better version of myself, which has been vital to carry forward this PhD program.

I also want to thank each member of my extended family. My aunts, uncles, nieces, nephews and cousins, whose support and love are a large part of the reason I can be here learning. Every single one of them. My grandma, Mami Celia, who inspires me to always build the best family possible and whose generosity overflows everywhere she goes. Mami Celia has taught me that one can connect with members of the community and call them your family. She embodies the message that love only multiplies. Every member in our family is so caring and loving because Mami Celia taught us how. She is our strongest bond. I also want to thank my aunts Gloria and Berta, who were always close by with their love and delicious meals. They never let me feel alone. They have my love, my admiration and will be my inspiration forever.

Life has also given me more siblings along the way, amazing humans with whom I did not grow up but with whom I do not want to stop growing. Lore, who always amazes me with her practical solutions and transparency. Kitty, who inspires me with her honesty and her ability to communicate and synthesize information. Diego, the brother my age that I never had and who inspires me to be a passionate learner. Aichurok, whose kind heart and amazing sense of humor always teaches me to take it easy. I love them very much and I hope they are in my life forever.

I also want to give special thanks to Oscar who taught me that homes can also multiply. Day by day Oscar showed me that I can feel at home, being so many miles away from the only one I knew. His noble heart and curious mind will always inspire me, and the many memories we built will always be a happy place where to return.

To my fellow Peruvians, Jorge, Luz, Kenyi, Angelo, Caye, Ela, Ana Paula, Pieri, Daniel and Gabriela, who helped me build a little piece of Peru in Nashville. The sense of community they gave me has been invaluable and I will always miss our parties, full of dancing, delicious Peruvian food and laughter. To the other Latinos who are part of Vandy Latins, we had so much fun! Great dances, karaoke, barbecues and cookouts. All much needed to balance the uncertainties of doing science.

My friends from IGP, Masha, Nilay, Ben, Tess, Kalen, Kristin, they all invited me to get out of my comfort zone and introduced me to the beauty of their cultures and their ancestors. I am lucky they are in my life and that I know more of the world around me because of them.

Finally, to the beautiful cats who complement my life, Pola and Alma. Alma for teaching me how wonderful it is to have a cat and Pola for confirming it. Pola made me enjoy the gray winters in Nashville because she loves to cuddle in the cold mornings. She is the extra love I did not know I needed in my life.

ACKNOWLEDGEMENT OF FUNDING

This work was supported by the National Institute of Neurological Disorders and Stroke R01NS081259, R01NS106951 to DMM and a predoctoral fellowship from the American Heart Association 18PRE33960581 to ACC.

TABLE OF CONTENTS

LIST OF FIGURES

LIST OF TABLES

CHAPTER I

Section “The GABAergic motor circuit in *C. elegans* as a model system for synapse remodeling” has been published in the Journal of Neurogenetics, 2020.

Cuentas-Condori, A., & Miller, D. M. (2020). Synaptic remodeling, lessons from C . elegans. *Journal of Neurogenetics*, *34*(3–4), 307–322. https://doi.org/10.1080/01677063.2020.1802725

INTRODUCTION

Multicellular organisms adapt to the environment by sensing it and reacting to it. Sensory systems open the door to exploring our surroundings, and those inputs are processed through neuronal networks that are in place to transform a stimulus into a behavioral effect. Thus, efficient neuronal connections are the foundation for an organism’s survival.

For this reason, the nervous system has been widely studied across species to understand how it works with hopes of maintaining its function in pristine conditions. To date, we understand that the nervous system is highly plastic. During early development, new neuronal connections arise in order to establish synapses between partner neurons or tissues. In a second phase, synapses are refined by the regulated pruning of excessive connections through a competition-based strategy (Huttenlocher, 1979). For example, in the neuromuscular junction, single muscle fibers are initially innervated by more than one motor neuron. Motor neurons compete to maintain their connection, and the connection from the more active neuron is preserved while the weak one is pruned away (Misgeld et al., 2002; Sanes & Lichtman, 2009).

Recent work has shown, however, that synapse elimination implicates more steps than just the retraction or elimination of an extended axon (Piochon, Kano, & Hansel, 2016). For example: (1) bouton clustering precedes the retraction of Retinal Ganglion Cell (RGC) axons in the visual cortex (Hong et al., 2014); (2) neurotransmission might be eliminated by silencing synaptic boutons while maintaining an intact axon (Linkenhoker, Ohe, & Knudsen, 2005; Mcbride & Debello, 2015; Mcbride, Rodriguez-Contreras, Trinh, Bailey, & Debello, 2008); (3) boutons might be eliminated from stable axonal processes during development (Morgan, Soto, Wong, & Kerschensteiner, 2011) or in mature circuits (De Paola et al., 2006; Marik, Yamahachi, Mcmanus, Szabo, & Gilbert, 2010). In all these examples, presynaptic terminals are remodeled intracellularly and although this phenomenon has been widely reported, we do not clearly understand how presynaptic elimination functions at the cellular level. Is the presynaptic apparatus just collapsing? Is it an ordered process? Are components from the active zone eliminated in conjunction with synaptic vesicle material?

Prompted by all these open questions, I have exploited the developmentally regulated remodeling process that takes place in the motor circuit of *Caenorhabditis elegans*. In this paradigm, Dorsal D motor neurons are born embryonically and innervate ventral muscles. These ventral synapses are then removed and new ones appear on the other end of the DD neuron to innervate dorsal muscles (White, Albertson, & Anness, 1978). Using this developmental event of presynaptic remodeling in a genetically tractable and transparent organism, we have uncovered new aspects of synapse elimination and how it can be coupled to the assembly of new boutons.

Chapter II explores the hypothesis that a presynaptic ENaC channel subunit, UNC-8, upregulates Ca^{++} levels in remodeling presynapses; thus, synapses with increased UNC-8 levels can mimic a context of high synaptic activity. Chapter III describes an actin-dependent endocytic mechanism that works downstream of UNC-8 activation to recycle presynaptic material from old to new boutons, setting the precedent that synapse elimination and formation in en-passant

boutons might be coupled. This observation suggests that reported events of increased bouton turnover in other systems might also involve recycling mechanisms to dismantle and form new synapses with an effective strategy.

Chapter III also reports the differential regulation of the remodeling effectors Syndapin and Toca1 on the recycling of synaptic vesicle and active zone proteins. Chapter IV further explores this differential control and establishes that UNC-8 is important to remove synaptic-vesicle associated material but not the active zone proteins Munc13 or Elks. Together, these observations suggest that synaptic disassembly is likely orchestrated by distinct cellular routes that ensure the specificity and fidelity of synaptic destruction and reassembly.

Chapter V presents the systematic characterization of functional dendritic spines in the *C. elegans* motor circuit. Our approach demonstrates that *C. elegans* spines resemble those of mammalian neurons and offers a new in vivo paradigm for the exploration of spine biology. We believe this work is important because studies in *C. elegans* can accelerate our understanding of postsynaptic neurodevelopment.

Finally, Chapter VI explores remaining open questions and future avenues for these projects. Overall, this body of work is intended to broaden our understanding on the cellular and molecular determinants of synapse remodeling.

Activity-dependent refinement of neuronal circuits

Chemical synapses mediate neuronal communication

Neuronal communication is mediated through specialized cellular junctions termed chemical synapses. At one end of this junction, presynaptic neurons accumulate neurotransmitter-filled synaptic vesicles and organize a specialized scaffolding region, named the active zone, where synaptic vesicles fuse upon Ca^{++} entry. Synaptic vesicle exocytosis liberates

neurotransmitters into the synaptic cleft, where they diffuse and reach their receptor at the receiving end of the junction at the postsynaptic cell (Figure 1.1) (Murthy & De Camilli, 2003; T. C. Südhof, 2012).

The molecular components that organize presynaptic terminals are conserved across species. For example, there are six conserved proteins that form the core of active zones (Figure 1.1): RIM/UNC-10 - Rab3 Interacting Molecule (Gracheva, Hadwiger, Nonet, & Richmond, 2008; Yun Wang, Okamoto, Schmitz, Hofmann, & Sudhof, 1997), RIM-BP/RMPB-1 - RIM-Binding Protein (Kushibiki, Suzuki, Jin, & Taru, 2019; Yun Wang, Sugita, & Südhof, 2000), liprin-alpha/SYD-2 (Kittelmann, Hegermann, et al., 2013; Mel Zhen & Jin, 1999), ELKS/ELKS-1 (Deken, 2005; Held, Liu, & Kaeser, 2016), Piccolo/Bassoon/CLA-1 (Tom Dieck et al., 1998; X. Wang et al., 1999; Xuan et al., 2017) and Munc13/UNC-13 (Augustin, Rosenmund, Su, & Brose, 1999; Brose, Hofmann, Hata, & Sudhof, 1995; Richmond, Davis, & Jorgensen, 1999). In addition, synaptic vesicle proteins that mediate vesicle fusion are also conserved and include: The Ca^{++}-sensor Synaptotagmin/SNT-1 (T. C. Südhof, 2013), the Rab3 GTPase (Mollard et al., 1992; Nonet et al., 1997) and SNARE proteins like Synaptobrevin/SNB-1 (Nonet, Saifee, Zhao, Rand, & Wei, 1998; Schoch et al., 2002), which localize to the synaptic vesicle membrane. Both functional components, active zones and synaptic vesicles, are necessary for regulated neurotransmission, which is the foundation of neuronal communication.

Importantly, the organization of invertebrate synapses resembles mammalian central synapses (Ackermann, Waites, & Garner, 2015). In contrast to the enlarged active zones at sensory and peripheral synapses, both *C. elegans* neurons and mammalian central synapses possess less complex active zones, revealed by dense projections (Kaeser et al., 2011; White, Southgate, Thomson, & Brenner, 1986) and fibers that interconnect synaptic vesicles (Siksou et al., 2007; Stigloher et al., 2011). Additionally, the plasma membrane adjacent to the active zone, named the perisynaptic region is the main region of synaptic membrane endocytosis (Shupliakov

et al., 2002; Watanabe et al., 2013), which is necessary to replenish the pool of synaptic vesicles in order to maintain sustained neurotransmission.

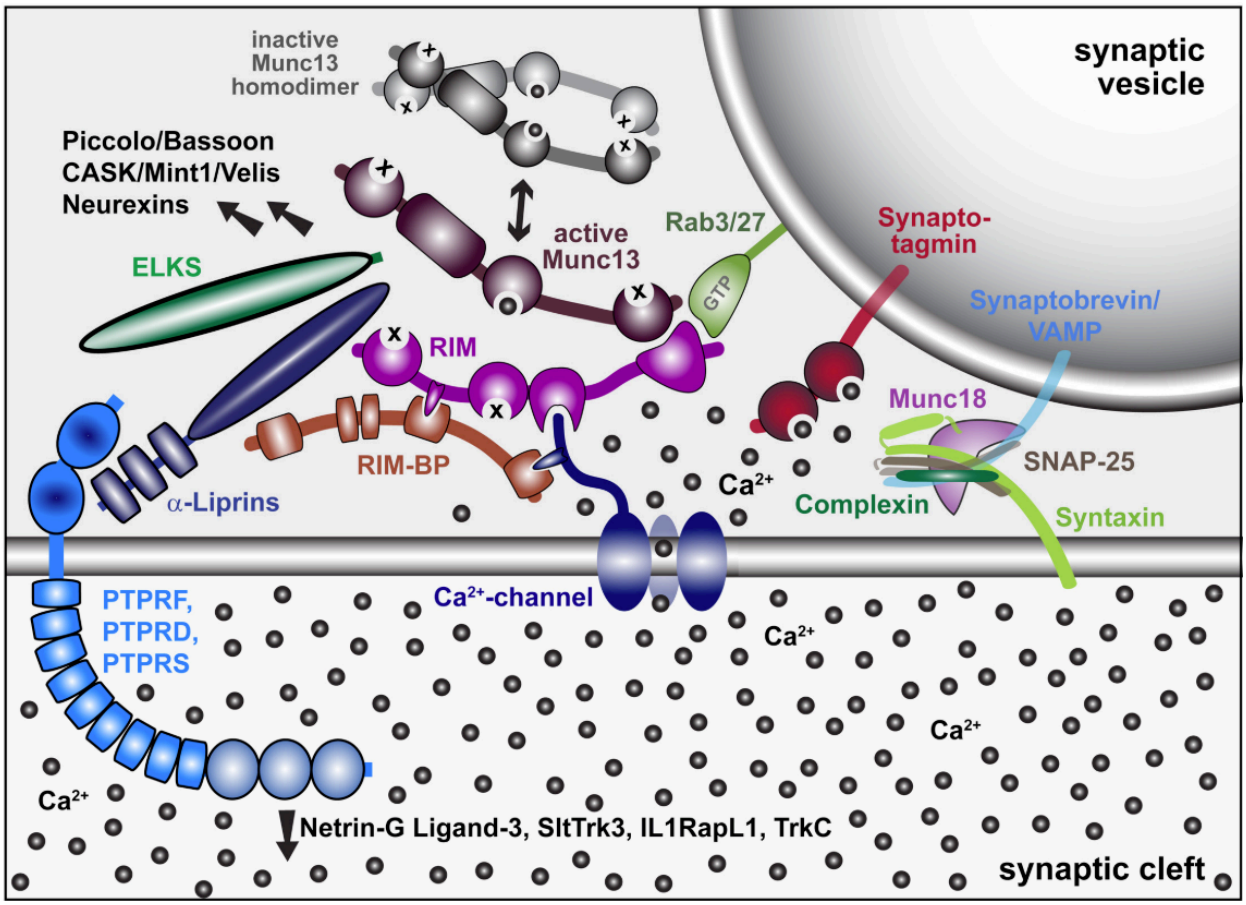

Figure 1. 1. The presynaptic active zone

Schematic depicting conserved proteins that arrange the presynaptic active zone and synaptic vesicle associated proteins. See text for description. Diagram taken from (T. C. Südhof, 2012).

Sustained neurotransmission in highly active neurons

At least four reported cellular strategies function in neurons to recycle synaptic vesicles for sustained neurotransmission (Chanaday, Cousin, Milosevic, Watanabe, & Morgan, 2019). In highly active neurons, the predominant mechanism is Activity-Dependent Bulk Endocytosis (ADBE), a fast clathrin-independent strategy that invaginates bulk endosomes that later give rise to synaptic vesicles (Emma L. Clayton & Cousin, 2009). Originally reported using ex vivo preparations of the neuromuscular junction of frogs, in two different studies, Heuser, Miller and Reese applied strong stimulation paradigms in the presence of K^+ channel blockers and high extracellular Ca^{++} concentration. After stimulation, time-course electron microscopy and freeze-fracture studies revealed large cisternae and deep invaginations at the periphery of the active zone just a few seconds after stimulation (Heuser & Reese, 1973; Miller & Heuser, 1984). This bulk endocytic mechanism was accompanied by clathrin-coated synaptic vesicles either originating from the recently formed cisternae or at the plasma membrane. As seen from their original diagram (Figure 1.2), Miller & Heuser had observed the endocytosis of large membrane invaginations that they hypothesized could later give rise to reformed synaptic vesicles (Miller & Heuser, 1984).

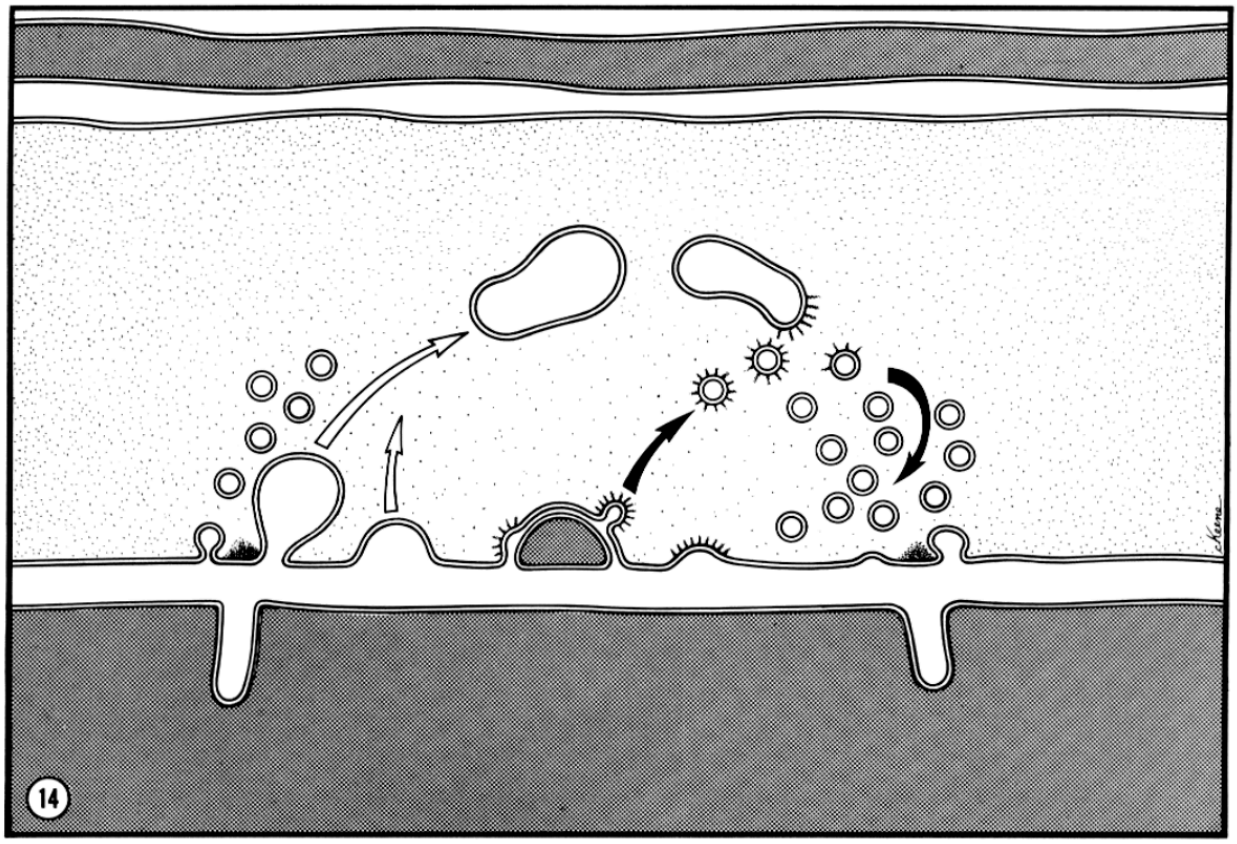

Figure 1. 2. Synaptic recycling at highly active neurons

This diagram summarizes the interpretation of Heuser and Miller's observations at the neuromuscular junction of frogs after triggering robust exocytosis. The presynaptic neuron (clear) shows two types of membrane invagination. Small invaginations similar in size to synaptic vesicles (black arrows) and a large and deep invagination that presumably gives rise to synaptic endosomes (clear arrows). From these endosomal structures, clathrin coats (black spikes) regenerate new synaptic vesicles for local replenishment.
Diagram taken from (Miller & Heuser, 1984).

More recent technology allowed the description of ADBE also in intact tissue of mammalian synapses. At the Calyx of Held of living animals, high-frequency sensory stimulation of intact animals revealed the formation of large synaptic cisternae during sustained neurotransmission using Horse Radish Peroxidase (HRP) (Körber, Horstmann, Sätzler, & Kuner, 2012) and later capacitance measurements (W. Wu & Wu, 2007). HRP is a non-permeable enzyme that can catalyze diaminobenzidine oxidation, which results in electron-dense patterns through electron microscopy and, thus, can label endocytosed compartments at active neurons (Zucker, Kullmann, & Kaeser, 2014). The Calyx of Held supports high-frequency stimulation before and after establishment of hearing (Sonntag, Englitz, Kopp-Scheinpflug, & Rübsamen, 2009). Importantly, although bulk endosomes are maintained through development, the population of synaptic vesicles that originate from them seems to shift from a loose distribution to a more concentrated one around the active zone (Körber et al., 2012). This different distribution pattern suggests that the cellular route and positioning of recycled synaptic vesicles can change during refinement of neuronal circuits.

ADBE relies on the presynaptic activation of Calcineurin (CaN) (Figure 2.1). CaN is a calmodulin and Ca^{++}-dependent phosphatase with micromolar affinity for Ca^{++} and is thought to localize freely in the cytosol (Klee, Crouch, & Krinks, 1979). Activation of Calcineurin upon sustained membrane depolarization is predicted to start a series of dephosphorylation events on target dephosphin proteins (E. L. Clayton et al., 2009; Cousin, Robinson, & Robinson, 2001). One of the most important and documented molecular interactions for ADBE is the dephosphorylation of dynamin by CaN (E. L. Clayton et al., 2009). Dynamin is a conserved GTPase that separates membranes and can generate new vesicles or endosomes (Ferguson & Camilli, 2012). For ADBE, dephosphorylation of dynamin is important to interact with syndapin and allow the invagination of large amounts of membrane in order to generate the bulk endosome (E. L. Clayton et al., 2009). Syndapin is predicted to recruit N-WASP to stimulate branched-actin nucleation and remodel the

membrane during endocytosis (Kessels & Qualmann, 2002). Consistent with this idea, several studies have implicated the need for an intact actin network in the formation of bulk endosomes. Bulk endosomes have two actin-dependent phases for their formation: bulk endosome invagination and scission from the membrane (Nguyen et al., 2012). Capacitance measurements at the Calyx of Held have shown that actin is required for the initial invagination of bulk endosomes (X. Wu et al., 2016). Because Syndapin can recruit N-WASP, the activator of the branched-actin nucleator, Arp2/3, this step is believed to be aided by branched-actin polymerization. Consistent with this idea, the bulk endosomes proteome revealed enrichment of several Arp2/3 subunits (A. C. Kokotos, Peltier, Davenport, Trost, & Cousin, 2018). Additionally, branched-actin polymerization has been shown to participate in different types of endocytosis across species (See section The actin cytoskeleton modulates local and distal synaptic vesicle recycling). The scission of bulk endosomes from the plasma membrane has been shown to require an additional contractile actin-myosin II network (Gormal, Nguyen, Martin, Papadopulos, & Meunier, 2015).

To date, the most reliable strategy to monitor synaptic bulk endosomes in intact tissue is still through electron microscopy. Large, circular and clear membranous vacuoles within presynaptic boutons are recognized as putative bulk endosomes modulated by increased synaptic activity across species (Cheung, Jupp, & Cousin, 2010; Kittelmann, Liewald, Hegermann, Schultheis, & Brauner, 2013). The lipid-binding FM1-43 dye and the large (40kDa) fluorescent dextran, due to its size, can only be endocytosed through bulk endosomes (E. L. Clayton et al., 2009). These synthetic molecules, however, are limited to cultured cells and cannot identify bulk endosomes at specific synapses in intact tissue. Recently, VAMP4, a mammalian SNARE protein has been identified as a molecular marker for bulk endosomes at mammalian synapses as it is specifically enriched during induction of ADBE (Nicholson-Fish, Kokotos, Gillingwater, Smillie, & Cousin, 2015). This molecular identity has permitted the isolation and identification of the bulk endosome proteome (A. C. Kokotos et al., 2018). The nature of VAMP4

makes it an ideal genetically-encoded tool for monitoring bulk endosomes across mammalian synapses. The new challenge is to identify specific bulk endosome proteins in other species since VAMP4 is not conserved in invertebrates or plants (Zeng, Tran, Tan, & Hong, 2003) even though examples of ADBE have been shown at least in *C. elegans* (Kittelmann, Liewald, et al., 2013) and *D. melanogaster* (Yao, Liu, Lee, Wang, & Wu, 2017).

Interestingly, ADBE has been linked to replenishment of the reserve pool (Cheung et al., 2010). In an active neuron, there are at least 4 different pools of synaptic vesicles described: the Readily Releasable Pool (RPP), recycling pool, resting pool and reserve pool. The RPP fuses during synchronous release mediated by the opening of Voltage-Gated Ca^{++} Channels (VGCCs) (Kaeser & Regehr, 2017). During ADBE, however, asynchronous release predominates, and it has been suggested that membrane retrieval through ADBE recycle synaptic vesicles that replenish the reserve pool (Nicholson-Fish et al., 2015; Raingo et al., 2012). Consistent with this idea, the bulk endosomes marker, VAMP4, has been shown to primarily modulate asynchronous release (Raingo et al., 2012).

Activity-dependent elimination of synapses

Throughout the literature, several examples demonstrate how activity of synapses can modulate the stability of specific presynaptic boutons within a stable axonal process (See also Chapter III and IV). Here, I will highlight some important examples and open questions that exist in the field, while pointing out how my work in *C. elegans* might help fill in those gaps.

The development of the visual circuit has been key for our understanding on how synaptic activity modulates circuit refinement. Of particular importance, the recent observation that presynaptic boutons can disassemble before axons are pruned away. During refinement of the visual circuit, Retinal Ganglion Cells branched out to innervate the thalamus. This dispersed axonal array allows the broad distribution of presynaptic boutons through the established axon.

Interestingly, through development, presynaptic boutons seem to cluster together, suggesting that there was elimination of distant synapses and assembly of new ones at a closer distance (Hong et al., 2014). Thus, bouton clustering might imply coupling of synapse elimination and formation along the same axon. Importantly, this mechanism in RGCs is activity-dependent since visual sensory deprivation results in decreased clustering (Hong et al., 2014) (Figure 1.3).

In another example, in the dentate gyrus where neurogenesis is sustained throughout life, the integration of new neurons into the dentate gyrus involves the competition between old and new axons that become less active with time. New axons establish more active connections at the dentate gyrus and replace the initial connectivity pattern by triggering the retraction of old axons. Inhibition of neurogenesis prevents the elimination of old axons, thus demonstrating that synaptic competition is necessary to activate the elimination of suboptimal axons in intact nervous systems (Yasuda et al., 2011). This observation is intriguing because a similar effect occurs in the *C. elegans* nervous system, where neurogenesis ensues during larval development and refinement of the motor circuit. Dorsal D (DD) motor neurons receive input from Dorsal A- and B-type (DA and DB) motor neurons in the embryonic motor circuit. In the transition to the second larval stage, DA and DB neurons eliminate their input onto DD neurons as it establishes new connections with the recently born Ventral D (VD) neuron. Interestingly, disruption of the development of post-embryonic VD neurons results in the maintenance of DA and DB innervation to DD neurons (White et al., 1978). Thus, inhibited neurogenesis prevents the likely competition between the dendrites of DD and VD neurons for input from DA and DB neurons.

In another example, the Bone Morphogenetic Protein 4 (BMP4) has been shown to traffic to peri-synaptic regions in dense core vesicles for their activity-dependent release. BMP4 release appears to act cell-autonomously on BMP receptors at the synaptic membrane to active local elimination of the synaptic vesicle protein Synaptophysin. Interestingly, the active zone protein Bassoon does not seem to be fully eliminated in this BMP4-dependent elimination of synapses

since a large fraction remains on boutons that were subjected to BMP4-elimination (Higashi, Tanaka, Iida, & Okabe, 2018). Thus, this finding suggests that BMP4 might trigger local

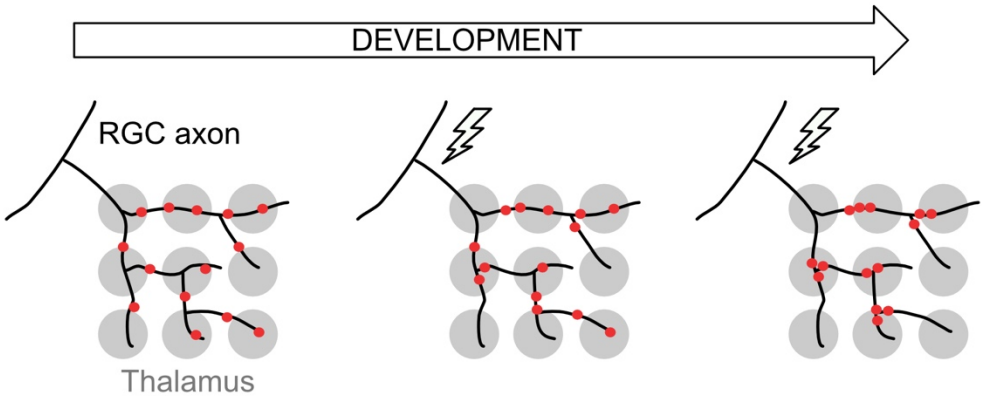

Figure 1. 3. Presynaptic remodeling within intact axons in vertebrate circuits

Initially, a Retinal Ganglion Cell (RGC) axon (black) innervates broadly multiple geniculate neurons in the thalamus (gray). Activity (lightning bolt) induces the relocation and clustering of RGC axons at proximal positions.

elimination of synaptic vesicle proteins but may display a minor role on the elimination of active zone proteins, suggesting the need of a parallel pathway that removes synaptic component that are not associated with synaptic vesicles in order to eliminate the full presynaptic bouton successfully. One main important question is regarding what are the cellular processes that mediate this effect. How is the presynaptic membrane remodeled in order to eliminate local synaptic vesicle replenishment and active zone scaffolding?

Interestingly, neurons subjected to BMP4-dependent synapse elimination do not just appear to reduce their number of synaptic boutons, but the overall turnover of boutons increases (formation and elimination) (Higashi et al., 2018). Thus, this observation suggests a possible increase in the overall neuronal plasticity when local elimination of boutons is triggered in stable axonal processes. This observation also highlights the possibility to suggest that the local elimination of boutons may be coupled with the consecutive appearance of new boutons on the axonal process. This possibility is intriguing since a similar effect has been observed during refinement of the *C. elegans* motor circuit where material from disassembling synapses can be incorporated into new boutons (Park et al., 2011) (See also Presynaptic remodeling depends on microtubule dynamics).

Strategies for presynaptic remodeling

Presynaptic boutons are highly dynamic

Besides presynaptic remodeling during development, several reports have shown that boutons can also be dynamic at basal conditions in the mammalian brain, with events of bouton formation and elimination (Holtmaat & Svoboda, 2009). Bouton dynamics have even been shown to increase with age (Grillo et al., 2013). Interestingly, although bouton dynamics increase, the total number of presynaptic boutons do not (Carrillo, Cheng, Ko, Jones, & Nishiyama, 2013),

suggesting a balance between the boutons that are assembled and disassembled. Upon neural perturbation, as sensory-input deprivation, the rate of dynamic boutons increases (Marik et al., 2010), whereas during memory formation, the rate of dynamic boutons decreases (Carrillo et al., 2013). Therefore, bouton dynamics play an active role in shaping neural circuits. Some have even proposed that dynamic boutons are responsible for allowing substantial morphological change after circuit damage (Yamahachi, Marik, Mcmanus, Denk, & Gilbert, 2009). For instance, photo-stimulation increases presynaptic bouton dynamics and successful motor recovery after stroke (Tennant, Taylor, White, & Brown, 2017), demonstrating that bouton plasticity may encode events to modulate circuit remodeling.

Synaptic material is shared between neighboring boutons

Studies in vitro and in vivo have revealed that presynaptic material can be exchanged between *en passant* boutons (Darcy, Staras, Collinson, & Goda, 2006; Herzog et al., 2011; Krueger, Kolar, & Fitzsimonds, 2003; Ratnayaka, Marra, Branco, & Staras, 2011; Staras et al., 2010). In 2003, Krueger et al. used the membrane-bound dye, FM1-43, to track the destination of recently endocytosed synaptic material. Time-lapse imaging of hippocampal neuronal cultures showed that FM1-43-labeled vesicles can traffic to neighboring presynaptic sites, evidencing that synaptic material can exchange between established synapses (Krueger et al., 2003). In an independent study, FM-dye fluorescence successfully recovers after photobleaching, likely due to the transfer of mobile synaptic vesicles from neighboring boutons (Darcy et al., 2006). Similarly, tracking the vesicular glutamate transporter, vGLUT, in cortical neurons showed that more than 35% of the signal is mobile between synapses both in neuronal cultures and in the cortex (Herzog et al., 2011). Overall, these findings demonstrate that synaptic vesicles can actively exchange between boutons along the same axon, in a mechanism that also takes place in native neuronal tissue.

Synaptic vesicles that are mobile between synapses can mediate neurotransmission. In an elegant experiment using correlative light and electron microscopy (CLEM), Darcy et al. demonstrated that distally recycled vesicles can be docked near the active zone of the new host synapse, indicating that exchanged vesicles are fusion competent. Significantly, release of this mobile pool of synaptic vesicles is triggered by synaptic activity (Darcy et al., 2006), demonstrating that they are subject to endogenous mechanisms of neurotransmission. Live-imaging additionally showed that FM1-43 vesicles can also move to extrasynaptic regions, between en passant boutons, where vesicles are fusion-competent even in the absence of evident postsynaptic partners (Krueger et al., 2003). Due to this observation, Krueger et al. introduced the concept of orphan synapses to describe the sites where recycled vesicles can fuse and potentially signal to neighboring tissues (Krueger et al., 2003). Later studies have shown that the release of mobile vesicles can be triggered upon electrical stimulation, showing that activity-dependent signaling can result in extrasynaptic release (Ratnayaka et al., 2011). Notably, CLEM studies on mobile synaptic vesicles have shown that in addition to clusters of synaptic vesicles across postsynaptic densities, there are individual “invasive” vesicles at the periphery, which have been speculated to be mobile vesicles between synapses (Darcy et al., 2006). Consistent with this observation, 3D reconstruction of *en passant* boutons from hippocampal slices has shown intersynaptic vesicles between varicosities (Shepherd & Harris, 1998). These populations of detached vesicles have been speculated to integrate the mobile pool of vesicles throughout an axon and is intriguing to see them consistently in mature synapses of the hippocampus. Overall, the evidence supports a model where the mobile pool of recycled vesicles plays an active role in neurotransmission, both at previously existent synapses and at extrasynaptic regions (orphan synapses). It is possible to speculate that extrasynaptic sites might mature into stable presynaptic boutons and boutons that “lose” vesicles might trigger events of synapse elimination. Overall, these events of synaptic plasticity along boutons might modulate changes in neuronal circuitry.

Based on this evidence and using modeling vesicle dynamics, recent groups have formulated the idea of a vesicle superpool. In this model, a population of synaptic vesicles is accessible to all boutons of a single axon upon neuronal stimulation (Staras et al., 2010). Thus, suggesting that recycling might not be limited to proximal boutons, but it may expand to a broader neighborhood. An important question would be to understand the relationship of such superpool in the context of neuronal specificity, especially in dual-transmitter axons where distinct pools of synaptic vesicles segregate to different boutons (S. Lee, Kim, & Zhou, 2010). One recently identified modulator of this superpool is vGLUT, which seems to restrain synaptic vesicle movement through molecular interactions of its intracellular proline-rich domain (PRD) and the SH3 domain of endophilin and intersectin. In this model, the PRD-SH3 intermolecular interactions strengthen vesicle clustering to prevent the exchange of local synaptic vesicles to neighboring boutons (Zhang et al., 2019).

The actin cytoskeleton modulates local and distal synaptic vesicle recycling

In the nervous system, the actin cytoskeleton is found in close proximity to the plasma membrane at active zones in the presynaptic region (Bloom et al., 2003), where it plays a key role in the synaptic vesicle cycle (Cingolani & Goda, 2008; Dillon & Goda, 2005; Doussau & Augustine, 2000). For example, several reports have confirmed that it is required during endocytosis to recycle presynaptic vesicle membrane (X. Wu et al., 2016). The first evidence for this relationship came from the giant reticulospinal synapse, where a rich F-actin cytomatrix appeared to polymerize after exhaustive stimulation (Shupliakov et al., 2002). This actin-containing cytomatrix was in contact with synaptic vesicles adjacent to the plasma membrane. Furthermore, disruption of the actin cytoskeleton resulted in the accumulation of membrane invaginations at synaptic releasing sites, suggesting that actin is required for synaptic vesicle excision during endocytosis (Shupliakov et al., 2002). In addition, at the neuromuscular junction, two different studies have

reported that the pool of vesicles is not restored after treatment with drugs that destabilize the actin cytoskeleton (Kuromi & Kidokoro, 1998; Richards, Rizzoli, & Betz, 2004). Overall, these studies point to a functional link between the actin cytoskeleton and endocytosis of local synaptic vesicles to recycle at the presynaptic bouton where they initially fused.

The branched actin nucleator, Arp2/3, plays conserved roles during endocytosis. It is composed of seven conserved subunits, which interact with the lattice of an existent F-actin filament to initiate polymerization of an actin branch (Mullins, Heuser, & Pollard, 1998; Rotty, Wu, & Bear, 2013; Schottler et al., 2001). Members from the WASP family and the WAVE complex are known activators of the Arp2/3 complex (Chen et al., 2010a; Eden, Rohatgi, Podtelejnikov, Mann, & Kirschner, 2002; Rohatgi et al., 1999; Takenawa & Suetsugu, 2007; Westphal, Soderling, Alto, Langeberg, & Scott, 2000). At the same time, they are activated by signaling molecules such as $PI_{(4,5)}P_2$, (Gallop, Walrant, Cantley, & Kirschner, 2013; Higgs & Pollard, 2000) Cdc42 or SH3-domain proteins, such as the F-BAR proteins TOCA-1 and Syndapin/SDPN-1 (Ho et al., 2004; Kessels & Qualmann, 2002; Rao et al., 2010). The role of the Arp2/3 complex in endocytosis was initially identified in budding yeast but subsequent studies pointed to evolutionary conservation of this functional link between the Arp2/3 complex and endocytosis from yeast to mammals (Girao, Geli, & Idrissi, 2008). Notably, only regulators of branched-actin polymerization (e.g. Arp2/3, WRC and WASP) and not linear actin were found enriched at presynaptic boutons in vivo using a proteomic approach (Dube et al., 2020). One molecular link between the actin cytoskeleton and endocytosis is mediated by proteins containing BAR, F-BAR or N-BAR domains that can directly interact with the plasma membrane and have been reported to regulate actin dynamics as well as endocytosis. (Bai & Grant, 2015; Fricke et al., 2009; Gleason, Nguyen, Hall, & Grant, 2016; F. B. Patel & Soto, 2013; Takano, Takano, Toyooka, & Suetsugu, 2008; Yamada et al., 2009). Interestingly, several proteins that contain BAR domains are enriched at synapses and promote synaptic vesicle endocytosis (Cousin et al., 2001; Murthy & De Camilli, 2003).

Recycled vesicles that traffic and are exchanged between boutons (See Section *Synaptic material is shared between neighboring boutons*) also seem to depend on actin dynamics. Application of jasplakinolide, a small molecule that promotes actin stabilization, reduces synaptic vesicle exchange between neighboring boutons (Darcy et al., 2006). Consistent with a role for actin in intersynaptic recycling, live imaging revealed that actin can be recruited to sites of mobile synaptic vesicles (Ratnayaka et al., 2011). More recently, thin actin filaments and myosin V were identified as the required molecular machinery to traffic synaptic vesicles between boutons (Chenouard, Xuan, & Tsien, 2020; Gramlich & Klyachko, 2017).

Notably, tracking the exchange of vesicles along a single process suggests that the overall signal redistributes through the axon and does not disappear (Herzog et al., 2011). This observation contrasts with the expectation that intersynaptic vesicle dynamics may lead to the elimination or addition of new synaptic material. In fact, this phenomenon suggests that there might be a balance between synaptic vesicles that leave and arrive between neighboring boutons, introducing the idea that synapse elimination and formation within stable axons might be a coupled process.

The GABAergic motor circuit in *C. elegans* as a model for synaptic remodeling

As a pioneer in the use of phage genetics to unravel the fundamental mechanisms of gene expression, Sydney Brenner possessed an insightful understanding of how mutant analysis could be exploited to tackle more complex questions in biology. With the overarching goal of understanding how genes build the brain, he chose *Caenorhabditis elegans* because its simple nervous system could be fully described and because its rapid, 3-day life cycle facilitates genetic analysis (Brenner, 1974). Its small size also mattered, not only for the practical advantage of culturing large numbers animals for mutant screens but also because Brenner understood that it

would be necessary to use electron microscopy (EM) to define the “wiring diagram” (Brenner, 1973). In an early step toward this goal, Brenner and colleagues published a description of serial section EM reconstruction of the adult ventral nerve cord (White, Southgate, Thomson, & Brenner, 1976). An accompanying analysis of the ventral cord cell lineage by John Sulston suggested that eight motor neuron classes were generated in two developmental periods (Sulston, 1976; Sulston & Horvitz, 1977), initially DA, DB and DD motor neurons in the embryo and then VA, VB, VC, VD and AS classes from a second wave of cell divisions late in the first larval stage. This finding was intriguing because it suggested that the motor circuit of newly hatched larvae with only three motor neuron types (DA, DB and DD) should differ from that of the adult with its full complement of eight motor neuron classes (DA, DB, DD, VA, VB, VC, VD, AS) (Figure 1.4A).

EM reconstruction of the early L1 larva yielded the unanticipated finding that the functional polarity of DD motor neurons is reversed in comparison to the adult. In the newly hatched L1, each of the six DD motor neurons innervates ventral muscles and also extends a circumferential commissure to the dorsal nerve cord to receive synaptic inputs from DA and DB motor neurons (Figure 1.4B). In the adult, this stereotypical DD morphology is retained but synaptic output is switched to dorsal muscles and input is provided by VA and VB motor neurons in the ventral nerve cord (Figure 1.4C). Reconstruction of an L2 larva revealed DD neurons with adult-like connectivity. Thus, DD synaptic remodeling was likely to occur during the L1 to L2 transition, when post-embryonic motor neurons are generated (Figure 1.4D). Importantly, the second member of the D class, ventral D (VD) motor neuron, develops post-embryonically and synapses onto ventral muscles while receiving input on the dorsal side (White et al., 1976). In other words, VD neurons adopt the synaptic arrangement of early L1 DD neurons (Figure 1.4B and 1.5A).

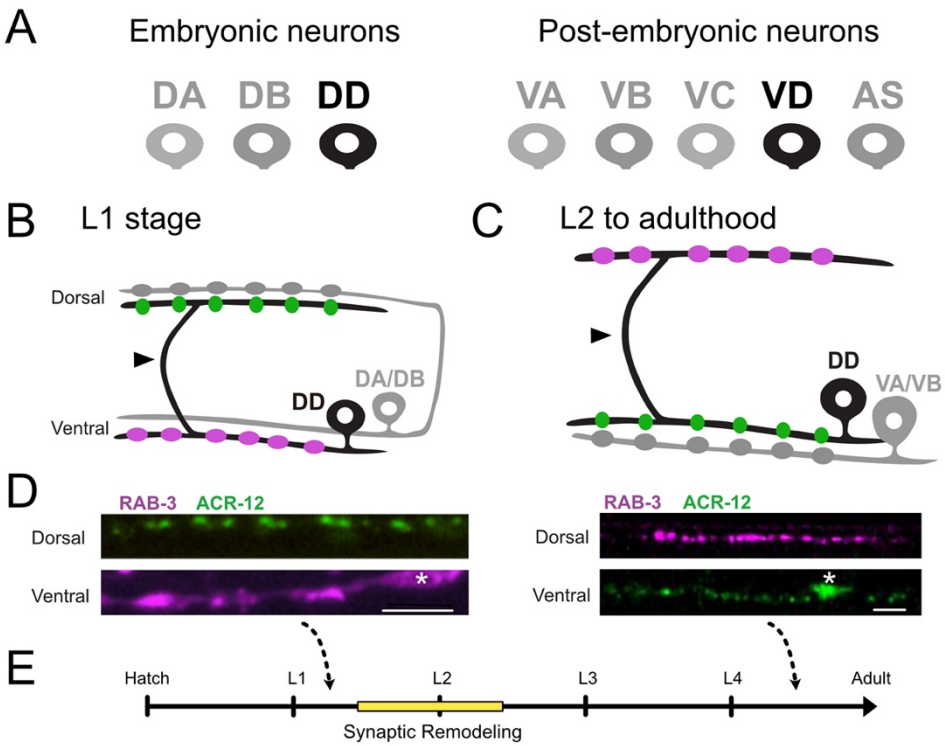

Figure 1. 4. Dorsal D (DD) motor neurons undergo synaptic remodeling during early development.

A. (Left) The newly hatched L1 larva contains three classes of ventral cord motor neurons: DA, DB, DD. (Right) Five additional postembryonic motor neuron classes (VA, VB, VC, VC, AS) are added to the ventral cord during the L1 to L2 larval transition.
B. During the first larval stage (L1), DD motor neurons (black) provide output to body muscles at ventral presynaptic boutons (purple) and receive input from cholinergic DA/DB neurons (gray) through ACR-12 nACh receptors at postsynaptic terminals (green) on the dorsal side. Arrowhead points to commissure.
C. (Top) DD motor neurons (black) remodel to place presynaptic boutons (purple) on the dorsal side, and relocate postsynaptic terminals (green) to the ventral side for cholinergic input from VA/VB motor neurons (gray). Arrowhead points to commissure. **D.** DD presynaptic boutons labeled with mCherry::RAB-3 and DD postsynaptic terminals marked with ACR-12::GFP before in early L1 (Left) and after (Right) remodeling at L4 stage. Asterisk labels cell bodies. Scale bar = 10 µm. Figures extracted from (He et al., 2015)
E. DD neurons remodel over a 4-6-hour period that spans the transition from the L1 to L2 larval stages (yellow).

To determine if the arrival of larval neurons was necessary for DD remodeling, White et al. reconstructed the dorsal and ventral nerve cords of a *lin-6* mutant that blocks post-embryonic cell division. This experiment showed that the relocation of DD presynaptic boutons to the dorsal cord is not impaired by the absence of postembryonic ventral cord motor neurons. However, input from DA and DB neurons, which is typically eliminated in the wild type, persists on the dorsal process of DD neurons in the *lin-6* mutant background (White et al., 1978). These results suggest that post-embryonic neurons are not required for presynaptic DD remodeling, but may be necessary for further refinement of this circuit, (i.e., elimination of DA and DB inputs).

Remarkably, 20 years elapsed before the publication of a subsequent study of DD remodeling, a breakthrough paper from Yishi Jin's lab reporting the first use of a novel GFP synaptic marker to monitor DD remodeling (Hallam & Jin, 1998). Hallam and Jim produced a transgenic line that used the *unc-25* promoter (Eastman, Horvitz, & Jin, 1999; Nonet et al., 1998) for selective labeling of GABAergic presynaptic terminals with SNB-1::GFP. Direct observation confirmed the earlier prediction from EM reconstruction (White et al., 1978) that DD presynaptic domains relocate from the ventral nerve cord to dorsal DD process during the L1 to L2 transition (Hallam & Jin, 1998) (Figure 1.4).

The additional key prediction, that the postsynaptic apparatus is also relocated during DD remodeling, was not confirmed by live-cell imaging until almost 40 years after the original EM reconstruction. As noted above, in the early L1, the dorsal arm of each DD neuron is postsynaptic to cholinergic DA and DB motor neurons (Figure 1.4B). After remodeling in the L2, DD inputs are switched to the ventral nerve cord where they are postsynaptic to cholinergic VA and VB motor neurons (Figure 1.4C) (White et al., 1978). With the determination that the nicotinic ACh (acetylcholine) receptor (nAChR) subunit, ACR-12, is required for cholinergic activation of ventral cord GABAergic neurons, it was possible to monitor the relocation of the DD postsynaptic domain in live animals (Cinar, Keles, & Jin, 2005; Petrash, Philbrook, Haburcak, Barbagallo, & Francis,

2013). ACR-12::GFP localizes as discrete puncta on the dendrites of both GABAergic motor neurons (DDs and VDs) in apposition to cholinergic presynaptic terminals (Cuentas-Condori et al., 2019; Petrash et al., 2013; Philbrook et al., 2018). In DD neurons, ACR-12::GFP puncta are initially positioned on the dorsal neurite at the L1 stage and then relocate to the ventral cord as remodeling ensues (He et al., 2015; Howell, White, & Hobert, 2015) (Figure 1.4B-C). Thus, as originally deduced from EM reconstruction, presynaptic and postsynaptic complexes are repositioned to opposite ends of the DD neuron and effectively switch locations during early larval development (Figure 1.4).

Synaptic remodeling of D-type motor neurons is transcriptionally-regulated

The stereotypical occurrence of DD remodeling during a specific developmental period (i.e., L1 stage larvae) points to regulation by a genetic program. This idea was substantiated by the finding that the heterochronic protein, LIN-14, controls the timing of DD remodeling. The presynaptic marker, SNB-1::GFP, is precociously relocated to the dorsal nerve cord in *lin-14* mutants, suggesting that LIN-14 normally prevents the premature activation of the presynaptic remodeling program (Hallam & Jin, 1998) (Figure 1.6A).

UNC-55/COUP-TF

Although LIN-14 was known to be nuclear-localized in 1998 and later confirmed to function as a transcription factor (Hristova, Birse, Hong, & Ambros, 2005), direct evidence of transcriptional control of the DD synaptic remodeling program first emerged from studies of the *unc-55* locus. As is the case for the majority of “uncoordinated” or “unc” loci, the original *unc-55* mutant alleles were isolated by Sydney Brenner (Brenner, 1974). *unc-55* mutants display a characteristic movement

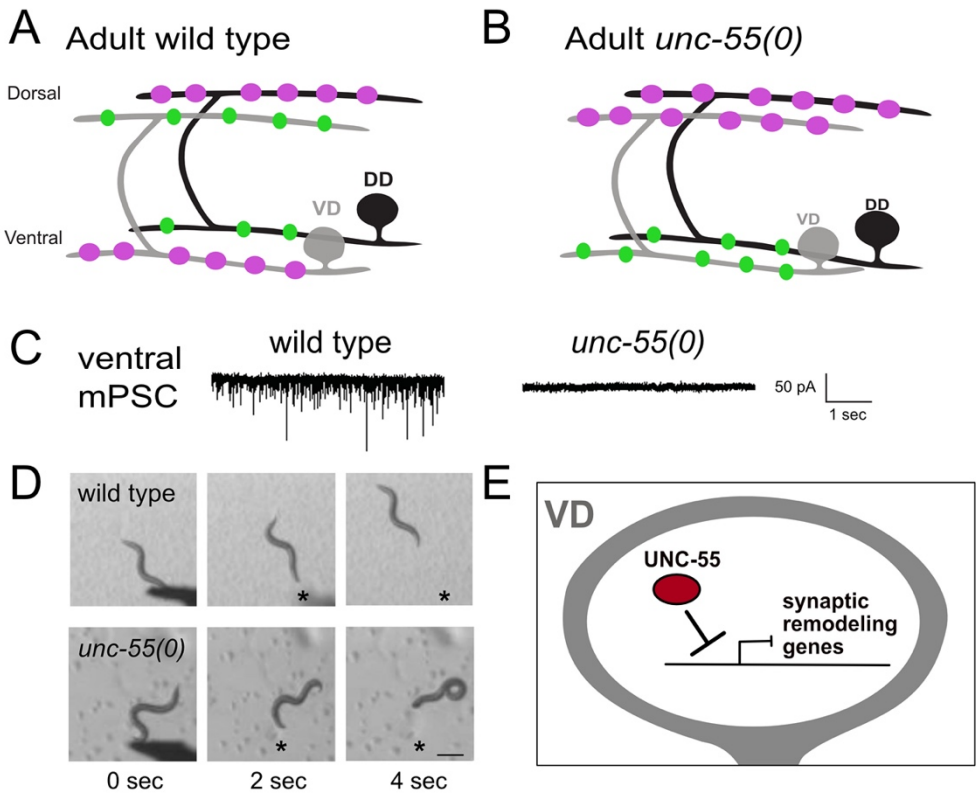

Figure 1. 5. Ventral D (VD) motor neurons ectopically remodel in *unc-55* mutants.

A. In adult wild-type worms, DD (black) presynaptic boutons (magenta) are located on the dorsal side and postsynaptic terminals (green) are positioned on the ventral side. VD (gray) presynaptic terminals are positioned on the ventral side (magenta) whereas postsynaptic terminals are located on the dorsal side.
B. In adult *unc-55(0)* mutants, both DD (black) and VD (gray) presynaptic boutons (magenta) are located on the dorsal side. Postsynaptic terminals (green) of both DD and VD neurons are positioned on the ventral side.
C. (Left) Wild-type worms show robust miniature Post Synaptic Currents (mPSCs) in ventral muscles whereas mPSCs are not detected in *unc-55* mutants (Right).
D. Head touch (asterisk) evokes backward movement in the wild type (top) but unc-55 mutants coil ventrally with head touch (asterisk) due to absence of inhibitory GABAergic input on the ventral side. Scale bar = 250 μm. Results extracted from (Petersen et al., 2011)
E. The UNC-55/COUP-TF transcription factor functions in VD motor neurons to antagonize expression of synaptic remodeling genes.

defect of strong ventral coiling during backward locomotion (Figure 1.5D). EM reconstruction by Leon Nawrocki, a postdoc with John White, revealed that VD class neurons adopt the DD pattern of dorsal synaptic output (Hardy, 1990) (Figure 1.5A-B), a conclusion confirmed by immunostaining results (Walthall & Plunkett, 1995). The absence of inhibitory GABA synapses on the ventral side (Figure 1.5B-C) (Miller-Fleming et al., 2016; Thompson-Peer, Bai, Hu, & Kaplan, 2012) results in excess ventral cholinergic excitation and the consequent coiling phenotype (Figure 1.5D).

Molecular cloning revealed that *unc-55* encodes a member of the conserved COUP-TF family of transcription factors that is selectively expressed in VD but not DD motor neurons (H. Zhou & Walthall, 1998). As a likely transcriptional repressor, UNC-55 was proposed to function in VD neurons to block ectopic activation of the DD synaptic remodeling program (Shan, Kim, Li, & Walthall, 2005) (Figure 1.5E). This idea is consistent with several lines of evidence: (1) In *unc-55* mutants, VD synapses are initially established with ventral muscles and then relocated to the dorsal nerve cord in a developmental sequence that mimics native DD remodeling (Petersen et al., 2011; Thompson-Peer et al., 2012); (2) Forced expression of UNC-55 in DD neurons antagonizes synaptic remodeling (Shan et al., 2005); (3) UNC-55 controls expression of downstream effectors of the DD remodeling program including transcription factors IRX-1/Iroquois (Petersen et al., 2011) and HBL-1/Hunchback (Thompson-Peer et al., 2012), the DEG/ENaC protein, UNC-8 (Miller-Fleming et al., 2016), and regulators of cAMP homeostasis (B. Yu et al., 2017).

IRX-1/Iroquois

The IRX-1/Iroquois transcription factor was initially identified by a gene expression profiling strategy that detected *unc-55*-regulated transcripts in VD neurons. A subsequent RNAi screen determined that IRX-1 is required for synaptic remodeling (Miller-Fleming et al., 2020;

Petersen et al., 2011). IRX-1 is a member of the conserved Iroquois family of homeodomain transcription factors that includes mammalian homologs that specify neuronal identity in the developing nervous system (Cavodeassi, Modolell, & Gómez-skarmeta, 2001; Houweling et al., 2001). In *C. elegans*, IRX-1/Iroquois is selectively expressed in DD motor neurons but is normally turned off by UNC-55 in the VD class (Figure 1.6). Ectopic expression of IRX-1/Iroquois in *unc-55* mutant VD neurons triggers the relocation of ventral VD presynaptic boutons to the dorsal nerve cord (Petersen et al., 2011) and also the reciprocal removal of dorsal postsynaptic nACh receptors for reassembly on the ventral side (He et al., 2015). In addition, forced expression of IRX-1/Iroquois in otherwise wild-type VD neurons is sufficient to induce the overall synaptic remodeling program (Petersen et al., 2011). Thus, IRX-1/Iroquois appears to orchestrate native DD synaptic remodeling by regulating expression of key downstream effectors that control both presynaptic and postsynaptic plasticity (see below) (Petersen et al., 2011). Although cell-specific RNAi of *irx-1* in DD neurons delays but does not block DD remodeling, the incomplete penetrance of this effect could be due to partial IRX-1 knockdown by RNAi.

HBL-1/Hunchback

An independent approach revealed that UNC-55 also negatively regulates expression of the HBL-1/Hunchback transcription factor in VD neurons (Figure 1.6). HBL-1 promotes the translocation of ventral presynaptic components to the dorsal side in *unc-55* mutant VDs and also drives synaptic remodeling in wild-type DD neurons. HBL-1 has not been tested, however, for a potential role in remodeling the DD postsynaptic apparatus (e.g., ACR-12, Figure 1.4). In addition, forced expression of HBL-1 in VD neurons is not sufficient to induce remodeling which suggests that HBL-1 could function downstream of IRX-1 (Thompson-Peer et al., 2012).

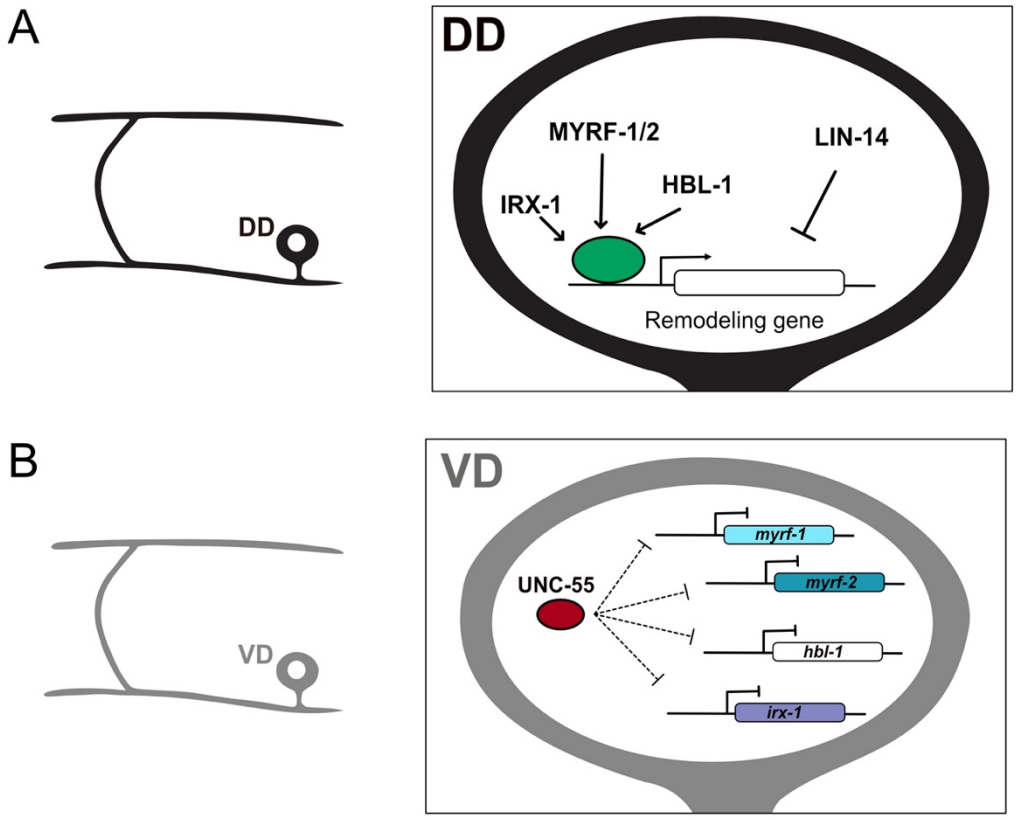

Figure 1. 6. Transcriptional regulation of synaptic remodeling in D-type GABAergic motor neurons.

A. (Left) Morphology of DD motor neuron. (Right) Transcription factors IRX-1/Iroquois MYRF-1/MYRF-2 and HBL-1/Hunchback promote expression of DD remodeling genes, whereas LIN-14 antagonizes remodeling genes.
B. (Left) Morphology of VD motor neuron. (Right) The transcription factor UNC-55/ COUP-TFII inhibits expression of IRX-1/Iroquois, HBL-1/Hunchback and MYRF-1/MYRF-2 in VD neurons to prevent ectopic synaptic remodeling.

MYRF1/2/ Myelin Regulatory Factor

A forward genetic screen revealed that members of Myelin Regulatory Factor (MYRF) family of transcription factors mediate the translocation of ventral DD presynaptic domains to the dorsal nerve cord (Figure 1.6) (J. Meng et al., 2017). MYRF transcription factors are highly conserved and notably regulate myelination in mammals (Bujalka et al., 2013). The *C. elegans* paralogs, MYRF-1 and MYRF-2, are expressed in DD neurons and function together in a heteromeric complex to regulate DD remodeling (J. Meng et al., 2017). Interestingly, MYRF transcription factors localize to the ER where an N-terminal fragment is released by proteolytic cleavage for translocation to the nucleus to function as a transcription factor (Bujalka et al., 2013; J. Meng et al., 2017). MYRF-1 and MYRF-2 display a similar cell biological mechanism but the signal that activates the pathway in DD neurons is not known. Remodeling is blocked in a genetic background that selectively eliminates MYRF-1 function in DD neurons which suggests that MYRF-1/2 function is essential for DD remodeling (J. Meng et al., 2017). It is still an open question whether MYRF-1/2 function is required for the removal of dorsal postsynaptic ACR-12 complexes in DD neurons and their reassembly on the ventral side. In the future it will be important to delineate the specific roles of MYRF-1/2 vs that of IRX-1/Iroquois in DD remodeling.

UNC-30/PITX

Finally, DD remodeling is also disrupted by mutations that disable the UNC-30/PITX transcription factor (Figure 1.6). In wild-type L1 larvae prior to remodeling, DD presynaptic (e.g. SNB-1) markers localize to the ventral side whereas postsynaptic (ACR-12) components are limited to the dorsal nerve cord (Hallam & Jin, 1998; He et al., 2015) (Figure 1.4). In *unc-30* mutants, however, DD presynaptic and postsynaptic markers are observed in both ventral and dorsal nerve cords of early L1 larvae (Howell et al., 2015). This effect of apparently precocious remodeling in *unc-30* mutants could arise in part from the dysregulation of LIN-14 and OIG-1,

both of which antagonize DD remodeling (Hallam & Jin, 1998; He et al., 2015; Howell et al., 2015). Alternatively, the abnormal synaptic organization of *unc-30* mutant DD neurons could result from the fundamental role of UNC-30 in GABA neuron differentiation (Eastman et al., 1999; Mcintire, Jorgensen, Kaplan, & Horvitz, 1993). In any case, the role of UNC-30 in DD remodeling is likely complex because UNC-30 is also necessary for IRX-1 expression which promotes remodeling (Petersen et al., 2011).

To summarize, some transcription factors promote synaptic remodeling (IRX-1/Iroquois HBL-1/Hunchback, MYRF-1/2/Myelin Regulatory Factor, UNC-30/PITX) (Meng et al. 2017; Petersen et al. 2011; Thompson-Peer et al. 2012), whereas others function to prevent it (UNC-55/COUP-TF, LIN-14) (Figure 1.6) (Hallam and Jin 1998; Walthall and Plunkett 1995). Understanding the relationship between these transcription factors and their targets (Petersen et al., 2011; B. Yu et al., 2017) will be key to determining how a genetic program orchestrates DD synaptic remodeling.

Cellular and molecular regulators of DD remodeling

Neuronal Activity promotes DD synaptic remodeling

Although several genetic programs regulate synaptic remodeling in D-type motor neurons (Fig 1.6), additional evidence suggests that neuronal activity is also required. For example, remodeling of the DD presynaptic domains is delayed by mutations that disable neurotransmitter release (e.g., *unc-13/Munc13* and *unc-18/Mun18*) and accelerated by mutations that increase neurotransmission (e.g., *tom-1/Tomosyn* and *slo-1/BK potassium channel*). DD expression of HBL-1/Hunchback, a transcription factor that promotes remodeling (Figure 1.6), is diminished in *unc-13* and *unc-18* mutants, which points to an activity-dependent mechanism for elevating HBL-1/Hunchback gene expression. A downstream role for HBL-1/Hunchback is also suggested by the finding that a *hbl-1* mutant blocks the acceleration of DD presynaptic remodeling by *tom-1*

and *slo-1* mutants (Thompson-Peer et al., 2012). Additionally, optogenetic activation of L1 larval DD neurons drives precocious presynaptic remodeling (Miller-Fleming et al., 2016). Although the activity-dependent mechanisms that promote HBL-1 expression are unknown, other downstream effectors of synaptic remodeling that depend on neuronal activity are beginning to emerge (Figure 4D). For example, the DEG/ENaC/UNC-8 channel which works downstream of the transcription factor Iroquois/IRX-1 and modulates Ca^{++} levels at synapses (See Chapter II).

cAMP levels regulate presynaptic remodeling in GABAergic neurons.

Genomic experiments (ChIP-Seq) to reveal targets of UNC-30/PITX and UNC-55/COUP-TF, transcription factors that regulate GABA neuron synaptic remodeling, detected key effectors of cAMP metabolism, notably PDE-4 (phosphodiesterase) and ACY-1 (adenylate cyclase). Genetic experiments that derive from these findings are consistent with the hypothesis that cAMP signaling promotes DD presynaptic remodeling (Figure 1.7). For example, VD motor neurons remodel ectopically in *unc-55* mutants (Figure 1.5) and this phenotype is correlated with reduced expression of PDE-4. This finding suggests that UNC-55 normally activates PDE-4 expression to limit cAMP levels and thus prevent VD remodeling (Figure 1.7B). Conversely, IRX-1/Iroquois, antagonizes PDE-4 expression, an effect consistent with the role of IRX-1/Iroquois in promoting DD remodeling (Figure 1.7A) (Petersen et al., 2011). Direct measurements with an *in vivo* FRET assay confirmed that cAMP levels are correlated with DD synaptic remodeling. The regulation of cAMP levels is apparently complex as other antagonists of the synaptic remodeling pathway, LIN-14 and OIG-1 (see below), also limit cAMP levels potentially by promoting PDE-4 expression (Figure 1.7). cAMP likely functions in combination with additional pathways because genetic mutants predicted to alter cAMP levels (*e.g., pde-4*) exert modest effects on synaptic remodeling (B. Yu et al., 2017). For example, the proposed role of UNC-8 in elevating intracellular Ca^{++} to promote presynaptic disassembly (Miller-Fleming et al., 2016) might also boost cAMP levels since

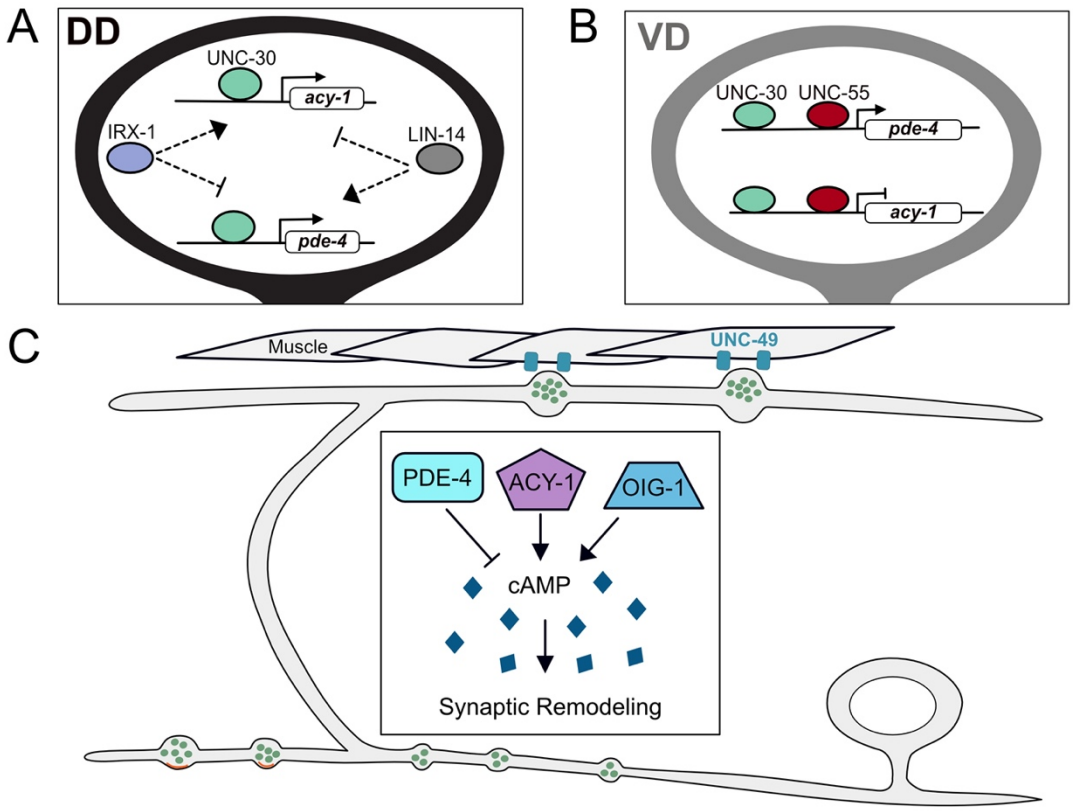

Figure 1. 7. cAMP promotes synaptic remodeling

A. Transcriptional control of biosynthetic (*acy-1*/adenylate cyclase) and metabolic (*pde-4*/phosphodiesterase) regulators of cAMP in DD neurons by IRX-1/Iroquois, UNC-30/PITX and LIN-14.
B. In VD neurons, UNC-30/PITX and UNC-55/COUP-TF promote expression of *pde-4/*phosphodiesterase and antagonize expression of *acy-1/*adenylate cyclase to prevent cAMP levels from exceeding a critical threshold that triggers presynaptic remodeling.
C. cAMP promotes the elimination of ventral presynaptic vesicles (green) and the localization of dorsal synaptic vesicles (green) adjacent to clusters of the postsynaptic UNC-49 GABAergic receptors (blue) in dorsal muscles in remodeling DD neurons. cAMP levels are reduced by PDE-4/phosphodiesterase and elevated by the ACY-1/adenylate cyclase and OIG-1/One-Ig-domain transmembrane protein.

adenylate cyclase activity is Ca^{++} dependent (Halls & Cooper, 2011; Koch et al., 2011). The downstream cell biological effects of cAMP are similarly uncharacterized but could potentially alter microtubule dynamics which is known to depend on cAMP signaling (Ghosh-Roy, Wu, Goncharov, Jin, & Chisholm, 2010) and to promote DD synaptic remodeling (see below) (Kurup, Yan, Goncharov, & Jin, 2015).

Presynaptic remodeling depends on microtubule dynamics

DD neurons adopt a "unipolar" morphology in which a single neurite maintains axonal and dendritic compartments in separate locations (Figure 1.4). Initially, in the early L1, the axonal neurotransmitter release machinery is restricted to a ventral region of the DD neurite proximal to the DD cell soma whereas the dendritic compartment is distally positioned in the dorsal segment of the DD neurite. With remodeling, these presynaptic (ventral) and postsynaptic (dorsal) domains exchange locations (Figure 1.4)(White et al., 1978). Interestingly, despite the switch in DD signaling polarity, microtubule (MT) orientation is not altered by remodeling. However, MTs dynamics is elevated during this period and is required for DD remodeling (Figure 1.8F) (Kurup et al., 2015).

Most MTs in DD neurons adopt the "plus-end out" orientation both before and after remodeling (Figure 1.8) (Kurup et al., 2015). "Plus-end" refers to the MT end to which more α and β tubulin dimers are added during MT growth and removed during MT shrinkage (Baas & Lin, 2010). The resultant "dynamic instability" of MTs is characteristically elevated during cell biological events (e.g., cell division) in which the MT cytoskeleton is actively reorganized (Gardner, Zanic, & Howard, 2013). Several lines of evidence indicate that DD remodeling depends on MT dynamics. First, genetic mutations that stabilize MTs block DD remodeling and this effect can be partially relieved by treatment with the MT depolymerizing drug, nocodazole. Second, factors that regulate MT catastrophe, the conserved kinase, DLK-1, and MT associated proteins, Kinesin-

3/KLP-7 and Spastin/SPAS-1, promote DD remodeling. Third, the MT stabilizing role of intermediate filaments that antagonizes remodeling (Figure 1.8D and 1.8F) (Kurup, Li, Goncharov, & Jin, 2018). A role for DLK-1 in synaptic remodeling is notable because DLK-1 also promotes axon regeneration in a cell biological mechanism that drives MT growth (Ghosh-Roy, Goncharov, Jin, & Chisholm, 2012). Additional unknown factors are likely required for activating MT dynamics in DD neurons, however, because a genetic ablation of DLK-1 activity results in only a slight delay synaptic remodeling (Kurup et al., 2015).

The plus-end motors, UNC-116/Kinesin1 and UNC-104/Kinesin3 function together to deliver presynaptic components to the dorsal neurite during remodeling (Figure 1.8A and 1.8C) (Park et al., 2011). Although MT dynamics is required for this kinesin-dependent function, the mechanistic basis for the effect is unknown (Kurup et al., 2015). Intriguingly, an optogenetic experiment suggests that at least some of the cargo delivered by UNC-104/Kinesin1 to the dorsal side may include recycled components of the presynaptic apparatus. The synaptic vesicle protein, RAB-3, was tagged with Dendra, a photoconvertible GFP, to confirm its translocation from disassembled ventral DD synapses to nascent dorsal synapses during remodeling (Figure 1.8B). In the future, it will be interesting to determine if additional presynaptic components are also recycled for reassembly at new DD synapses and to delineate the cell biological mechanism of potential endocytic events that are likely involved. The essential role for motor-dependent trafficking in DD remodeling is underscored by the finding that the cyclin-dependent kinase, CDK-5, functions upstream of UNC-104 and promotes remodeling. The molecular mechanism of CDK-5-dependent activation of UNC-104 is unknown (Park et al., 2011).

The cell death pathway promotes remodeling of D-type motor neurons

Presynaptic Synaptobrevin/SNB-1 puncta are transiently localized to the axially projecting neurites of RME neurons in a remodeling event that mimics the sequential assembly and removal

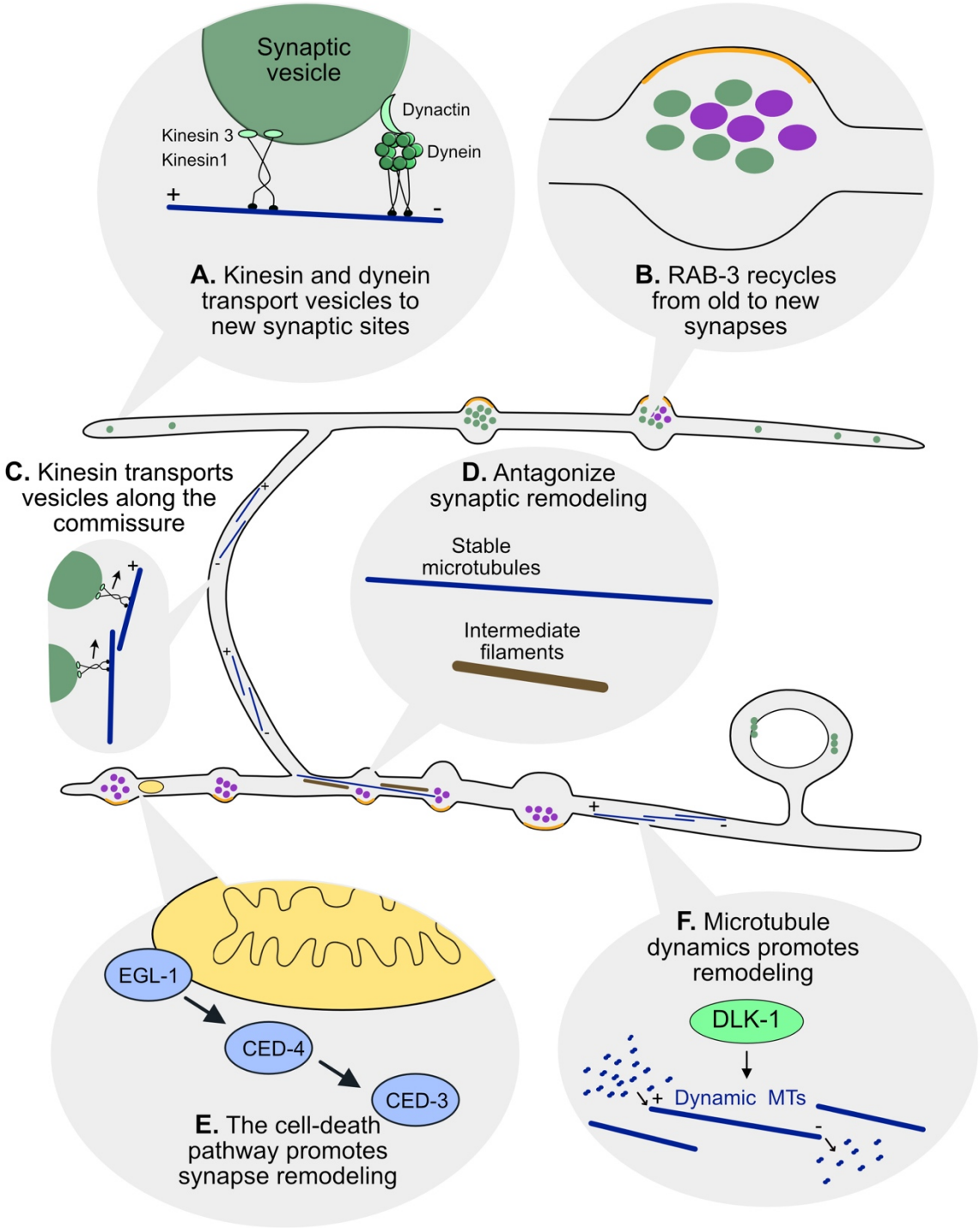

Figure 1. 8. Cellular regulators of synaptic remodeling

A. Anterograde transport of synaptic vesicles by motor proteins Kinesin1/UNC-116 and Kinesin3/UNC-104 on microtubules (blue) to the anterior distal tip of the dorsal DD neurite is opposed by the retrograde motor complex of Dynein/DHC-1 and Dynactin/DNC-4 that relocates synaptic vesicles to the posterior DD neurite (blue).
B. Experiments with photoconverted Dendra2::RAB-3 demonstrated that RAB-3 from old synaptic terminals (magenta) can be relocated to new dorsal synapses in remodeling DD neurons.

C. Kinesin1/UNC-116 transports synaptic vesicles along microtubules (blue) in the DD commissure.
D. Stable microtubules (blue), intermediate filaments (brown) and the kinase TTBK-3 antagonize synaptic remodeling in *tba-1(gf);dlk-1* double mutants (see text).
E. Cell-death pathway components, (EGL-1, CED-4, CED-3) associate with presynaptic mitochondria (yellow) to drive elimination of ventral synaptic terminals.
F. DLK-1 signaling promotes microtubule (blue) dynamics for synaptic remodeling.

of DD presynaptic domains (L. Meng et al., 2015). The RME remodeling phenotype was exploited in a genetic screen that revealed that members of the canonical cell-death pathway are required to remove transient RME presynaptic terminals. Interestingly, the apoptotic pathway is also involved in the removal of ventral presynaptic terminals during DD remodeling (Figure 1.8E). Additional genetic and imaging experiments suggested that apoptotic components are delivered to the presynaptic domain in association with mitochondria (L. Meng et al., 2015) where CED-3/Caspase-mediated activation of the actin severing protein, gelsolin, triggers presynaptic disassembly. Recent genetic results suggest that the apoptotic pathway may function in an activity-dependent mechanism of presynaptic disassembly that is triggered by transcriptionally-regulated expression of the UNC-8/DEG/ENaC sodium channel subunit (Miller-Fleming et al., 2016).

Regulation of postsynaptic remodeling in D-type motor neurons

Although both presynaptic and postsynaptic compartments are relocated in remodeling DD neurons (Figure 1.4), little is known of the postsynaptic mechanism in part because a reliable marker for the postsynaptic apparatus, ACR-12::GFP, was only recently identified (Petrash et al., 2013). ACR-12 encodes an α-subunit of a heteromeric nicotinic acetylcholine receptor (nAChR) in GABAergic motor neurons that also contains UNC-29, UNC-38, UNC-63 and LEV-1 AChR subunits (Philbrook et al., 2018). ACR-12::GFP localizes to the postsynaptic compartments of DD and VD neurons in close apposition to presynaptic input from ventral cord cholinergic motor neurons (Figure 1.4B-C) (Cuentas-Condori et al., 2019; Petrash et al., 2013; Philbrook et al., 2018). Initially, in early L1 larvae, ACR-12::GFP localizes to the dorsal DD neurite but then disappears as remodeling ensues and nascent ACR-12::GFP puncta emerge on the ventral side (Figure 1.4B-C) (He et al., 2015).

The Ig-domain protein, OIG-1, antagonizes DD synaptic remodeling

The translocation of dorsal ACR-12::GFP puncta to the ventral side is accelerated in *oig-1* mutants (He et al., 2015; Howell et al., 2015). The *oig-1* locus encodes a small protein of 137 amino acids with a single ImmunoGlobulin-(Ig) domain. OIG-1 is up-regulated by the UNC-30/PITX transcription factor in early L1 larval DD neurons (Howell et al., 2015) but is turned off in the late L1 by IRX-1/Iroquois as the DD remodeling program is activated (Figure 1.9A) (He et al., 2015). Thus, OIG-1 normally functions to antagonize DD remodeling and is repressed by the transcription factor IRX-1/Iroquois to prevent this effect. OIG-1 also appears to antagonize ectopic remodeling in VD neurons. OIG-1 is highly expressed in the VD neurons throughout development due to repression of IRX-1 by UNC-55/COUP-TF. In wild-type animals, ACR-12::GFP is exclusively localized to dorsal VD neurites but also appears on the ventral side in *oig-1* mutants (He et al., 2015). Remarkably, genetic analysis indicates that OIG-1 also antagonizes remodeling of the presynaptic apparatus in both DD and VD neurons. For example, DD presynaptic markers (e.g., SNB-1::GFP) are precociously translocated to the ventral side in *oig-1* mutants (He et al., 2015; Howell et al., 2015). Notably, OIG-1 is the only known downstream effector that regulates both presynaptic and postsynaptic remodeling.

The OIG-1 mechanism of action is unclear. Although OIG-1 contains a canonical signal peptide and is secreted when over-expressed in transgenic animals (He et al., 2015; Howell et al., 2015), secretion is not required for its synaptic remodeling function (He et al., 2015); when expressed at native levels, the endogenous OIG-1 protein is not secreted and shows an intracellular location (He, Cuentas-Condori, & Miller, 2019). An intracellular role is also consistent with the finding that OIG-1 expression in GABAergic neurons rescues the misplacement of ACR-12::GFP in *oig-1* mutants whereas forced expression of OIG-1 in nearby cholinergic ventral cord motor neurons does not complement the *oig-1* ectopic remodeling phenotype (He et al., 2015;

Howell et al., 2015). The reported role of OIG-1 in limiting cAMP levels for presynaptic remodeling is similarly unknown (B. Yu et al., 2017).

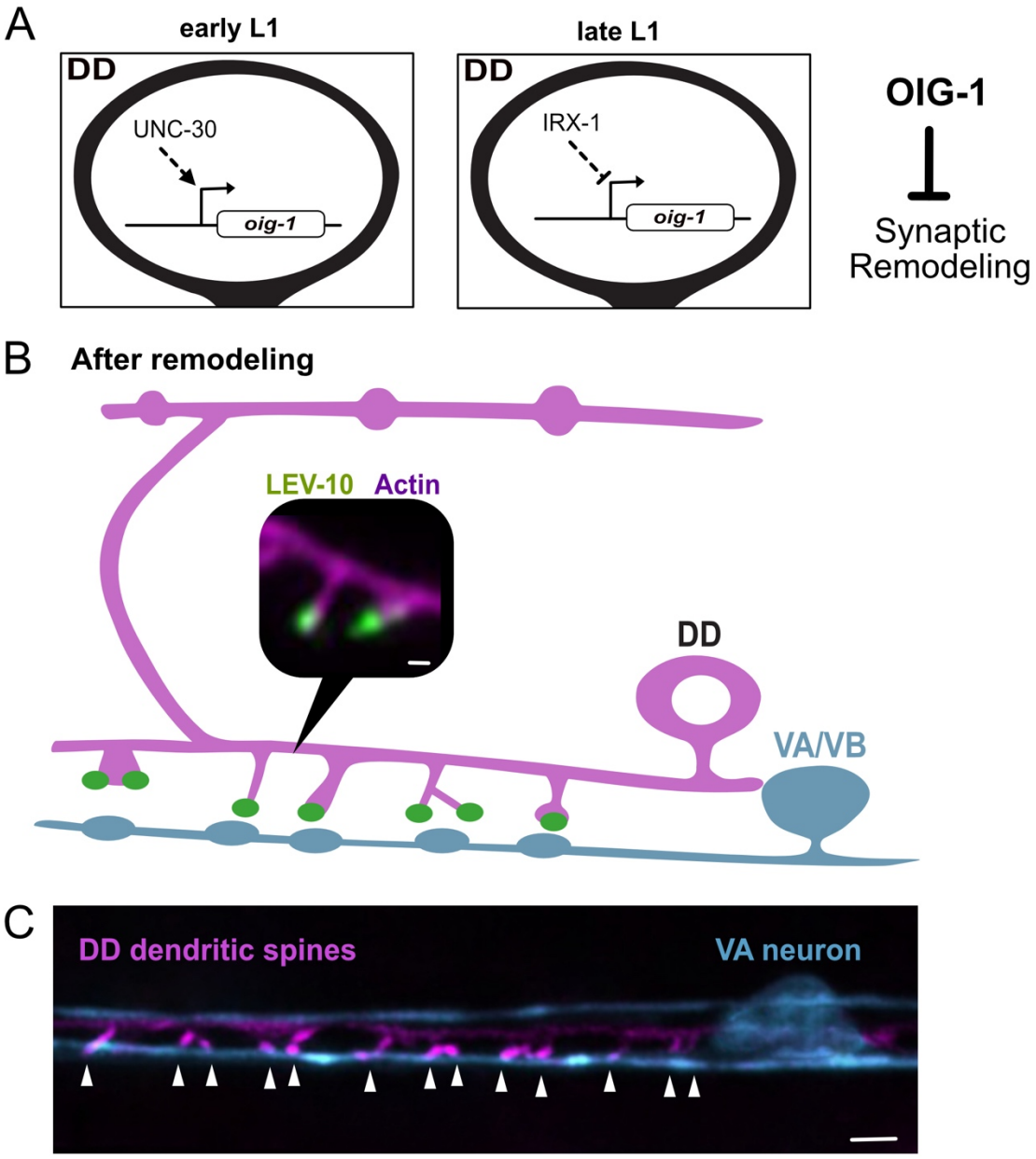

Figure 1. 9. Postsynaptic remodeling

A. The One-Ig-domain protein, OIG-1, is upregulated by the PITX/UNC-30 transcription factor in early L1 larval DD neurons but turned off by Iroquois/IRX-1 during the late L1 to prevent OIG-1 from antagonizing synaptic remodeling.
B. Graphical representation of dendritic spines protruding from the ventral postsynaptic neurite of a DD neuron and contacting presynaptic terminals of cholinergic VA/VB neurons. Inset shows a fluorescent image of the actin marker, LifeAct::mCherry (magenta), and the postsynaptic protein, LEV-10 (green) at the spine tip. Scale bar = 200 nm.

C. Fluorescent image shows DD dendritic spines (magenta) projecting toward a presynaptic VA neuron (blue). Arrowheads denote sites of contact between postsynaptic spines and the VA process. Scale bar = 1 μm. Figure extracted from (Cuentas-Condori et al., 2019)

Spine-like protrusion in the *C. elegans* motor circuit

In addition to the replacement of presynaptic components with the ACR-12 postsynaptic receptor, the remodeling mechanism transforms the initially oblong DD axonal compartments into dendritic spines that protrude from the ventral DD neurite (Figure 1.9B-C) (Cuentas-Condori et al., 2019; Philbrook et al., 2018). The possibility that DD neurons might display dendritic spines was first noted by John White and colleagues in EM reconstructions of the ventral cord (White et al., 1978, 1976, 1986). This idea is notable because dendritic spines are specialized postsynaptic structures that detect neurotransmitter release from presynaptic neurons. In mammalian neurons, spine morphogenesis is dynamic and responsive to stimuli correlated with learning and memory (Hering, Sheng, & Medical, 2001). In Chapter V, I will test key predictions that the protrusions in DD neurons share structural and functional characteristics with mammalian dendritic spines. Exploring these predictions is important because it could help us establish a new in-vivo paradigm for the study of postsynaptic spines in a genetically tractable and transparent model organism.

Endocytosis in the *C. elegans* NMJ

At *C. elegans* synapses, synaptic vesicles are regenerated through clathrin-independent and -dependent steps (Gan & Watanabe, 2018). First, clathrin-independent ultrafast endocytosis invaginates large amounts of presynaptic membrane that give rise to transient synaptic endosomes (Watanabe et al., 2013). Consecutively, clathrin and its adaptors function to generate synaptic vesicles from those endosomes. For example, loss of the clathrin adaptor AP2 leads to a 70% reduction of synaptic vesicles at NMJs and the accumulation of endosomal structures (Gu et al., 2013, 2008). Interestingly, loss of the clathrin-associated protein and dephosphin Eps15/EHS-1 results in decreased number of synaptic vesicles without apparent accumulation of

synaptic endosomes (Salcini et al., 2001). Thus, these findings argue that EHS-1 might be required for the initial formation of synaptic endosomes to recycle synaptic vesicles. Importantly, both steps that are required to recycle synaptic vesicle proteins seem to need active Dynamin/DYN-1 to separate the large endosomal vesicle from the plasma membrane (Watanabe et al., 2013) and then to excise single synaptic vesicles from the synaptic endosome (Clark, Shurland, Meyerowitz, Bargmann, & Van Der Bliek, 1997; Kittelmann, Liewald, et al., 2013).

Generation of large synaptic endosomes at the *C. elegans* NMJ can also be stimulated through increased synaptic activity. A single 20-millisecond activation of channelrhodopsin triggers fusion of docked synaptic vesicles (Watanabe et al., 2013), while prolonged photo-stimulation for 30 seconds leads to the exocytosis of most fusion-competent vesicles at a given cholinergic NMJ (Kittelmann, Liewald, et al., 2013). The first short-pulse paradigm gives rise to large vesicles with ~43 nm in diameter (Watanabe et al., 2013), larger than the stereotypical diameter of a single synaptic vesicle (30 nm). The second paradigm of continuous photo-stimulation leads to the formation of larger vesicular structures with an average diameter of ~100 nm (Kittelmann, Liewald, et al., 2013). In both paradigms, the large vesicular structures are circular and clear, resembling putative endosomal structures. These findings suggest that more synaptic activity leads to increase exocytosis, which can trigger the generation of larger endosomal structures at synaptic boutons. In both scenarios, the large vesicular structures disappear from the presynaptic terminal with time, probably because they regenerate the local pool of synaptic vesicles (Kittelmann, Liewald, et al., 2013; Watanabe et al., 2013). Besides increased synaptic stimulation, ablation of dynamin activity can also result in the generation of larger synaptic endosomes even in paradigms of mild stimulation (Watanabe et al., 2013), arguing that in situations of intense synaptic activity, molecular interactions could modulate dynamin to exacerbate plasma membrane invaginations and endocytose larger amounts of synaptic membrane. A similar neuronal adaptation takes place in mammalian synapses under intense

synaptic activity, where activation of Calcineurin triggers dephosphorylation of dynamin to form the dynamin-syndapin complex and promote invagination of bulk endosomes at synaptic sites (E. L. Clayton et al., 2009). Interestingly, similar to mammalian ADBE which requires the Calcineurin targets (dephosphins) for synaptic vesicle recycling (Emma L. Clayton & Cousin, 2009; Cousin et al., 2001), ablation of the conserved dephosphin Synaptojanin/UNC-26 impairs the generation of large endosomal structures after high stimulation at *C. elegans* NMJs (Kittelmann, Liewald, et al., 2013). These findings suggest that under contexts of high neuronal activity, *C. elegans* synapses could undergo a similar mechanism to ADBE.

CHAPTER II

The presynaptic DEG/ENaC cation channel subunit, UNC-8, maintains calcium levels in remodeling boutons

INTRODUCTION

The Epithelial Sodium Channels (ENaCs) are highly expressed in epithelial cells where they mediate cation flux, for example, in the distal nephron in the kidney (Hamm, Feng, & Hering-Smith, 2010). In the nervous system, ENaC channels are expressed in both neuronal and glial cells, and have been implicated in learning and memory formation (Hill & Ben-Shahar, 2018). For example, the mammalian ENaC channel ASIC1a is necessary for spatial learning and conditioning (Wemmie et al., 2002). The *C. elegans* ASIC-1 protein similarly promotes associative behavior in a learning paradigm (Voglis & Tavernarakis, 2008). These reports point to potentially conserved mechanisms for ENaC-mediated synaptic plasticity. Here, we investigate the role of the ENaC channel, UNC-8, in developmentally regulated synapse elimination in the nervous system of *C. elegans*. Our approach is important because synapse elimination is a crucial aspect of normal circuit refinement that may be misregulated in neurodevelopmental disorders (Hogenaar & van Bokhoven, 2021; Huttenlocher, 1979).

ENaC channels modulate presynaptic activity. Earlier work in vertebrate and invertebrate species have shown that ENaC channels can localize to presynaptic regions (Orr et al., 2017; Urbano et al., 2014; Voglis & Tavernarakis, 2008). At the neurophysiological level, ENaC channels have been shown to regulate evoked and spontaneous synaptic release, further

substantiating their presynaptic role (Cho & Askwith, 2008; Ievglevskyi et al., 2016; Urbano et al., 2014).

ENaC channels can be upregulated during circuit refinement to enhance neurotransmitter release from the presynaptic apparatus. For example, in the fly peripheral nervous system, members of the Pickpocket family of the ENaC channels, are transcriptionally upregulated to promote presynaptic function in a homeostatic mechanism (Orr et al., 2017; Younger, Mu, Tong, Pym, & Davis, 2013) and also during sexual maturation to modulate courtship behavior (Ng et al., 2019). In these examples, ENaC channels strengthen the presynaptic terminals through Ca^{++}-dependent mechanisms. A recent study from the Miller lab, however, found that the ENaC channel subunit, UNC-8, can be developmentally upregulated to promote the opposite effect: the elimination of synapses (Miller-Fleming et al., 2016; Petersen et al., 2011).

DD neurons undergo synaptic remodeling during the L1 to L2 larval stage transition (White et al., 1978) (Figure 2.2C). Using this developmentally regulated paradigm, previous work in the Miller Laboratory established that the DEG/ENaC cation channel subunit, UNC-8, triggers presynaptic disassembly of DD neurons in a mechanism that depends on intracellular Ca^{++} (Miller-Fleming et al., 2016). A reconstituted UNC-8 channel preferentially gates Na^{++} in Xenopus oocytes (Ying Wang, Matthewman, Han, Miller, & Bianchi, 2013) which suggests that the native UNC-8 DEG/ENaC channel could depolarize the GABA neurons in which it is expressed. In turn, this effect is predicted to enhance Ca^{++} import by presynaptic VGCCs, an idea supported by the additional findings that UNC-2/VGCC is required for UNC-8-dependent presynaptic disassembly (Miller-Fleming et al., 2016) (Figure 2.1). This model parallels an earlier finding in which a *Drosophila* Pickpocket/DEG/ENaC channel is synaptically localized in motor neurons where it elevates intracellular Ca^{++} to promote neurotransmitter release in the context of presynaptic homeostasis (Orr et al., 2017; Younger et al., 2013). The radically different outcome of synaptic destruction that arises from UNC-8 function in *C. elegans* depends on the serine/threonine

phosphatase CalcineurinA/TAX-6 and its regulatory subunit CalcineurinB/CNB-1. CaN is activated by intracellular Ca^{++} and genetic results suggest that it functions upstream of UNC-8 (Miller-Fleming et al., 2016). Thus, UNC-8/DEG/ENaC, UNC-2/VGCC and CaN/TAX-6 may constitute a positive feedback loop to amplify Ca^{++} influx (Figure 2.1).

Experiments in this chapter challenge key predictions of this model with the following questions: (1) Are UNC-8 levels upregulated during DD remodeling? (2) Is UNC-8 localized to presynaptic terminals? (3) Does UNC-8 upregulate presynaptic Ca^{++} in remodeling DD boutons? (4) Does CaN/TAX-6 localize to remodeling boutons? (5) Does CaN/TAX-6 also upregulate presynaptic Ca^{++}?

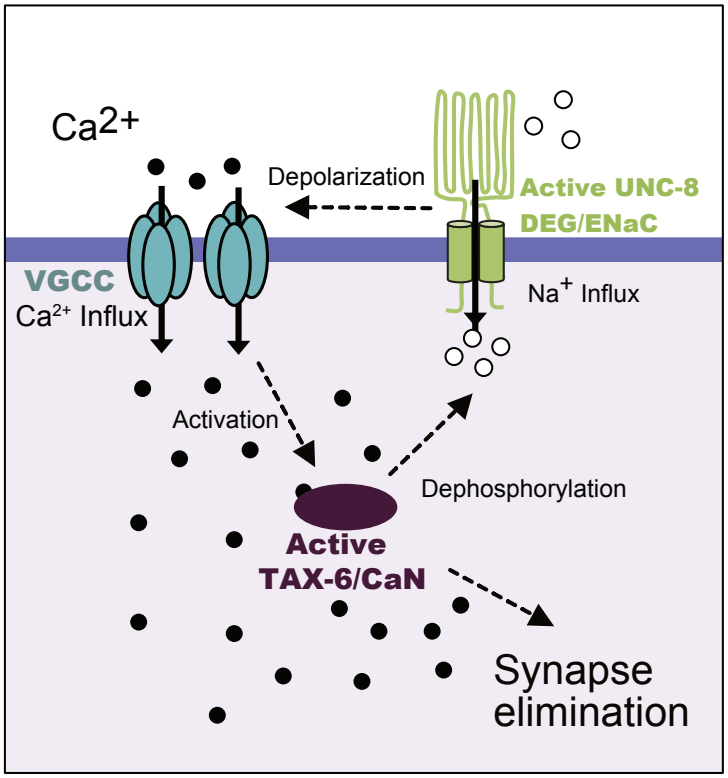

Figure 2. 1. Model of UNC-8-dependent synapse removal

Working model depicts a positive feedback loop involving DEG/ENaC/UNC-8 channel, a Voltage-Gated Ca++ Channel (VGCC) and Calcineurin (TAX-6/CaN) that upregulates presynaptic Ca^{++} (Miller-Fleming et al., 2016). This model predicts that UNC-8 and TAX-6 localize to presynaptic remodeling boutons to modulate Ca^{++} levels.

MATERIALS AND METHODS

Worm breeding and generation of new alleles

Worms were maintained at 20°- 23°C using standard techniques (Brenner, 1974). Strains were maintained on NGM plates seeded with *E. coli* (OP-50) unless otherwise stated. The wild type (WT) is N2 and only hermaphrodite worms were used for this study.

Generation of unc-8::gfp11x7(syb1624) and tax-6::gfp11x3(sy2783b) animals

Sunybiotech used CRISPR/Cas9 to add 7 copies of GFP11 to the *unc-8* locus or 3 copies of GFP11 to the *tax-6* locus animals at the C-terminus. To visualize the reconstituted GFP signal in DD neurons, complementary GFP1-10 was driven with the P*flp-13* promoter.

Molecular Biology

Plasmids were constructed using InFusion cloning. First, Snapgene software was used to design one pair of forward and reverse primers targeting the desired DNA vector backbone and another pair of primers targeting the desired DNA insert. (These primers contained ~15bp overlaps that are necessary for plasmid assembly. Additionally, every desired DNA insert requires its own specific primer pair.) The vector backbone was then PCR linearized and amplified by combining template DNA, which contained the desired backbone sequence, with the appropriate targeting primers and propriety “CloneAmp HiFi PCR Premix.” In a separate PCR reaction(s), the DNA insert(s) was likewise amplified and linearized, albeit using the primer pair targeting the desired insert and template DNA that contained the desired insert sequence. To check for amplification, all PCR products were run on a 1% agarose gel and were then gel purified using a “NucleoSpin Gel and PCR Clean-Up” kit. To assemble the desired plasmid, the purified vector

backbone DNA and insert DNA were combined and incubated in solution with “5x In-Fusion HD Enzyme Premix.” Following incubation, the reaction mixture containing the putatively assembled plasmid DNA was used to transform Stellar Competent Cells, which were subsequently plated and grown overnight on LB-Amp plates. All plasmids were verified with Sanger sequencing.

Worm staging or synchronization

Staging was achieved by picking 30-40 L4 larvae onto a fresh plate in the afternoon and leaving at 23C overnight. The next morning, once the animals had become gravid adults, 20-30 worms were picked from original plate onto a fresh plate. The worms were left undisturbed on the lab bench for exactly 1 hour to lay eggs. The worms were then removed from the plate and only eggs remained. The egg plate was then returned to 23C to allow the eggs (embryos) to hatch and larvae to develop until the timepoint at which the worms were imaged.

To identify progeny at the early L4 larval stage of development, a tabletop microscope was used to select 20-30 larvae with a visible gonad but no embryos in the uterus. The selected worms were then mounted on a 5% agarose slide with 4.5uL time lapse anesthetic. Each worm was then examined individually under the A1R confocal microscope, where the shape of its vulva was visible. A classification system of L4 sub-stages defined by morphological characteristics of the vulva was used to identify early L4 *C. elegans* (Mok, Sternberg, & Inoue, 2015). Worms with vulva shapes that matched L4.0, L4.1, or L4.2 vulva images were categorized as early L4s.

Laser Scan Confocal Microscopy

Larval or young adult animals were immobilized on 2-10% agarose pads with 4 µL of 15mM/ levamisole as previously described (Smith et al., 2010). Z-stacks were collected on a Nikon confocal A1R using Apo Fluor 40X/1.3 and 60X/1.4 N.A. oil objectives.

Synapse density analysis

To analyze puncta density along the ventral cord, Maximum Intensity Projections were created from Z-stacks using NIS Elements. All images were subject to background correction using the Rolling Ball algorithm. Analysis explorer was used to create a mask based on fluorescent thresholding for the RAB-3::GFP signal. ROIs were defined on the ventral regions to count the objects anterior to DD2 and DD3 cell soma. To calculate puncta density, each object was considered a RAB-3 punctum and the total number was normalized to a 10 μm neurite using the following equation: (# of objects detected in ROI / length of ROI)*10. To quantify the density of ventral synapses at late developmental time-point (e.g., early L4 stage) a more sensitive mask (lower fluorescent threshold) was created to detect dimmer GFP::RAB-3 puncta.

To analyze puncta density along the dorsal DD nerve cord, regions of interest (ROIs) were drawn using the polygonal ROI tool in NIS Elements. ROI lengths were measured using the Distance Measurement: Polyline tool in NIS Elements and were recorded in μm. The Automated Measurement Results tab in NIS Elements was used to record the number of objects (puncta) in a given ROI, and puncta density within the ROI was then calculated as described above. To designate a fluorescent signal as a punctum, a mask was generated in NIS Elements that labeled as puncta all fluorescent features in an image that met size, shape and intensity criteria set by the experimenter. Once generated, the same masking criteria were used for all treatment and control images included in a given experiment.

To quantify the density in the dorsal nerve cord, ROIs were drawn within the same general anatomical region of a worm (DD1-DD3) for all images in a given experiment. Because curvature of the dorsal cord in the XY plane could artificially increase or decrease the puncta density in the region (depending on whether the curvature was concave or convex), all dorsal chord regions had to meet straightness criteria to be included in analysis. To this end, the Angle measurement tool in NIS elements was used to approximate the extent of dorsal cord curvature by measuring

the angle of intersection between two lines drawn tangent to the regions of the dorsal cord immediately anterior and posterior to the apex of the curve in question. Regions with an intersection measurement of less than 160° (where 180° represents a perfectly straight region and 90° represents a region curved at a right angle) were excluded from analysis. ROIs were then drawn along the longest possible region of the dorsal cord that adhered to these straightness criteria. If the regions anterior and posterior to a curve met straightness criteria, then two ROIs were drawn for that image. Off target fluorescent features (autofluorescence) and commissures were excluded from ROIs.

Counting UNC-8::GFP11$_{x7}$ puncta

Worms were synchronized (see above) to track endogenous UNC-8 puncta before and throughout the remodeling window: early L1 (T_{16}), late L1 (T_{24}) and L2 stage (T_{30}). Z-stacks were collected using a laser scanning confocal microscope A1R. Worms were immobilized using a combination of 3µL of 100mM muscimol (TOCRIS biosciences #0289) and 7µL 0.05um polybeads (2.5% solids w/v, Polysciences, Inc. #15913-10) on a 10% agarose pad. Maximum Intensity projections were created for each image using NIS Elements. The experimenter was blinded to developmental time point to manually score each GFP puncta. UNC-8 density was calculated normalizing the number of puncta to a 10 µm neurite.

Presynaptic TAX-6 enrichment

Worms were synchronized (see above) to track endogenous TAX-6::GFP11$_{x3}$ fluorescence along the ventral and dorsal cords before, L1 (T_{16}), and after remodeling, L4 stage. Z-stack images were acquired using a laser scanning confocal microscope A1R. Maximum intensity projections were created using FIJI and a 3-pixel wide line scan was drawn on the ventral and dorsal cord of each animal to determine average fluorescence. The relative dorsal (D) and

ventral fluorescence (V) was normalized to the total fluorescence (D+V) for each DD neuron (DD1-DD4).

To detect endogenous TAX-6::GFP and mRuby::CLA-1s, Z-stacks were acquired using Nyquist Acquisition and small step size (0.2 µm) on a Nikon A1R confocal microscope. Z-stacks were subjected to 3D-deconvolution in NIS Elements and single plane images were used for line scans.

GCaMP6s imaging in remodeling DD axons

To detect GCaMP6s fluctuations at remodeling boutons (DD2-DD4), NC3569 animals were synchronized (T_{26}) on an OP-50-seeded plate with freshly added ATR or carrier (EtOH, no ATR). Image acquisition was performed on a Nikon TiE microscope equipped with a Yokogawa CSU-X1 spinning disk head, Andor DU-897 EMCCD camera, high-speed MCL piezo and 100X/1.49 Apo TIRF oil objective lens. Synchronized NC3569 worms at T_{26} (See synchronization method above) were immobilized using a combination of 3µL of 100mM muscimol (TOCRIS biosciences #0289) and 7µL 0.05um polybeads (2.5% solids w/v, Polysciences, Inc. #15913-10) on a 10% agarose pad.

To identify baseline GCaMP fluctuations, images 4-10fps (frames per second) were collected with 488 nm excitation on a single plane using a Perfect Focus System for 1 minute. The ventral processes of DD2-DD4 were imaged for this experiment. To detect evoked GCaMP changes, triggered acquisition was used to excite GCaMP with 488 nm and activate Chrimson with 561nm laser. Single plane movies were collected at 3.8 fps for 1 minute using emission filters 525nm (+/- 25nm) and 646 (+/- 66nm). The sample was illuminated with a 561nm laser at 5 sec intervals (e.g., every 20^{th} frame) to activate Chrimson expressed in cholinergic DA motor neurons of late L1 animals (T_{26}) (*Punc-4:*::ceChrimson::SL2::3xNLS::GFP) while maintaining constant illumination with a 488 nm laser to detect GCamP6s signals. This acquisition paradigm was

applied for 10 cycles (1 minute). Only neurites that were stable (not moving or sinking) at least for 2 cycles of acquisition were selected for further processing. For quantifying GCaMP6s fluorescence, ROIs were drawn on oblong, bouton-like structures near the base of the commissure and on a nearby region to capture background fluorescence. The same ROIs (bouton and background) were used to detect spontaneous and evoked GCaMP changes in videos from the same DD neuron. Mean fluorescence intensity of each ROI for each frame was exported into Excel for further analysis. Background was subtracted from each frame and measurements were normalized to three time-points before Chrismon activation for the first acquisition cycle (F_0). At each time-point, F_0 was subtracted from the measured GCaMP fluorescence and then divided by F_0 to determine $\Delta F/F_0$. Then, fluorescent values before and after each event of Chrimson activation were matched for paired comparisons.

Statistical Analysis

First, we used the Shapiro-Wilk test to determine if a sample is normally distributed. For comparisons between 2 normally distributed groups, Student's T-test was used and $p<0.05$ was considered significant. ANOVA was used to compare between 3 or more normally distributed groups followed by Dunnett's multiple-comparison test. Standard Deviations between two samples were compared using an F-test and considered $p<0.05$ as significant. If the samples were not normally distributed, we used a Mann-Whitney test to compare two groups and a Kruskal Wallis test to compare three or more groups. The specific test and n used in each experiment appears in each figure legend.

Table 2. 1. List of plasmids

Strain	**Genotype**
pSH4	p*myo-2*::RFP
pSH21	p*str-1*::GFP
pSH87	*pflp-13*::GFP1-10
pACC12	p*flp-13*::LifeAct::mCherry

pACC83	p*flp-13*::GCaMP6s::SL2::mCherry
pACC98	p*flp-13*::2xNLS::FLP_D5
pACC123	p*flp-13*::mRuby::CLA-1s

Table 2. 2. List of strains used in this chapter

Strain	**Genotype**
NC3629	*rab-3 (ox785[GFP*-FLP-ON::RAB-3 + loxp UNC-119+ loxp]) II; *unc-119* III; wdEx1127 [p*flp-13*::flippase; p*myo-2*::RFP]
NC3683	*rab-3 (ox785)* II; *unc-8 (tm5052)* IV; wdEx1127 [p*flp-13*::flippase; p*myo-2*::RFP]
NC3613	*unc-8::GFP11x7 (syb1624)* IV
NC3625	*unc-8::GFP11x7 (syb1624)* IV; wdEx1095 [p*flp-13*::GFP1-10; p*flp-13*::LifeActmCherry; p*myo-2*::mCherry]
NC3648	*unc-104(e1265) II; unc-8::GFP11x7 (syb1624)* IV; wdEx1095 [p*flp-13*::GFP1-10; p*flp-13*::LifeActmCherry; p*myo-2*::mCherry]
NC3647	*unc-8::GFP11x7 (syb1624)* IV; ufIs136 [p*flp-13*::mCherry::RAB-3; body GFP marker]; wdEx1136 [P*flp-13*::GFP1-10; p*myo-2*::mCherry]
NC3569	*lin-15(n765)* X; wdIs117 [p*unc-4*::Chrimson::SL2::3xNLSGFP; lin-15+] II? ; wdEx1112 [p*flp-13*::GCaMP6s::SL2::mCherry; pmyo-2::RFP]
NC3722	*unc-8 (tm5052)* IV*; lin-15(n765)* X*;* wdIs117 [p*unc-4*::Chrimson::SL2::3xNLSGFP; lin-15+] ; wdEx1112 [p*flp13*::GCaMP6s::SL2::mCherry; pmyo-2::RFP]
PHX2783	*tax-6::gfp11x3 (syb2783) IV*
NC3715	*tax-6::gfp11x3 (syb2783)* IV; wdEx1163 [p*flp-13*::GFP1-10; p*myo-2*::RFP]
Not frozen	*tax-6::gfp11x3 (syb2783)* IV; wdExYYY [pflp-13::GFP1-10; Pflp-13::mRuby::CLA-1s; pmyo-2::RFP]
NC3761	*tax-6 (p675)* IV; wdIs117 [p*unc-4*::Chrimson::SL2::3xNLSGFP; lin-15+] ; wdEx1112 [p*flp13*::GCaMP6s::SL2::mCherry; pmyo-2::RFP]

RESULTS

Synaptic remodeling of the native DD remodeling program

To avoid potential artifacts arising from over-expression of transgenic arrays, we used a fluorescent labeling strategy to mark endogenous synaptic proteins to monitor progressive synaptic changes during DD remodeling. For this purpose, we used a conditional *C. elegans* knock-in in which GFP is fused to the N-terminus of the RAB-3 in a flippase-dependent manner (Figure 2.2A) (Schwartz & Jorgensen, 2016). To limit expression of GFP::RAB-3 to DD neurons,

we used the *flp-13* promoter to drive flippase expression (Figure 2.2A). RAB-3 associates with synaptic vesicles and thus is a reliable marker for presynaptic terminals in DD neurons (Nonet et al., 1997). Because DD remodeling occurs during the L1 to L2 transition (Hallam & Jin, 1998; White et al., 1978), we evaluated GFP::RAB-3 puncta at five successive time-points that span this developmental period (Figure 2.2B). With this approach, we confirmed that GFP::RAB-3 is selectively localized to the ventral DD neurite at early L1 stages (T_{17} - T_{22}) when DD exclusively innervates ventral muscles. During the late L1 stage (T_{24}), some DD neurons start assembling new presynaptic boutons in the dorsal neurite. This gradual assembly of boutons with dorsal muscles is coupled with the progressive elimination of GFP::RAB-3 puncta from ventral muscles (T_{27}). Towards the end of the DD remodeling period (T_{32}), most presynaptic boutons had been disassembled from the ventral side and relocated to dorsal muscles (Figure 2.1C-E) (White et al., 1978). This detailed temporal description defines developmental windows that correspond to stages before, during and after remodeling (Figure 2.2F).

UNC-8 is transported to remodeling axons in an UNC-104/KIF1A-dependent manner to localize to dismantling boutons

Previous studies in the Miller Lab offered support for a model in which the DEG/ENaC/UNC-8 channel is transcriptionally upregulated to stimulate synapse elimination during DD remodeling (Figure 2.1) (Miller-Fleming et al., 2016; Petersen et al., 2011). In this model, UNC-8 expression is predicted to increase during the remodeling window and to localize near presynaptic terminals. To test these predictions, we devised a strategy for monitoring the endogenous UNC-8 protein during DD remodeling. For this purpose we used NATF, a two-component system (GFP1-10 and GFP11) that takes advantage of the self-annealing property of complementary split-GFP peptides (He et al., 2019).

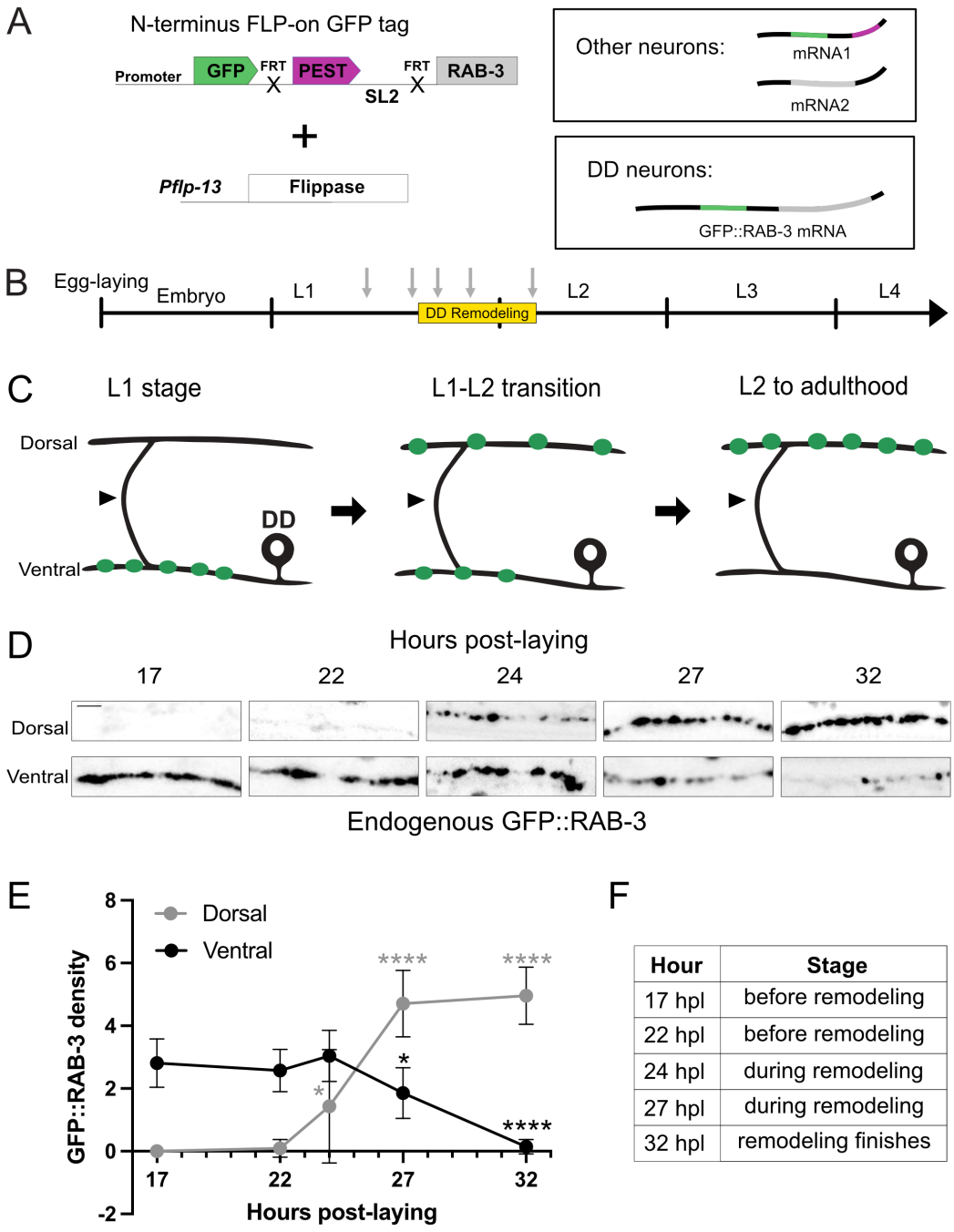

Figure 2. 2. Visualizing endogenous GFP::RAB-3 to monitor DD remodeling

A. Endogenous labeling of RAB-3 with GFP in DD neurons. *Pflp-13* drives flippase expression to attach GFP to the N-terminus of the endogenous RAB-3 protein in DD neurons (Schwartz & Jorgensen, 2016).
B. Timeline depicts developmental stages of *C. elegans*. Yellow box highlights the developmental window of DD remodeling, which starts late in the L1 stage and finishes after the L2 transition. Black arrowheads denote five timepoints, 17 to 32 hours post-laying (hpl), evaluated by live imaging.

C. Cartoons depict the localization of DD presynaptic boutons (green) before (left), during (center) and after (right) remodeling. Arrowheads point to the DD commissure.
D. Snapshots of endogenous GFP::RAB-3 in DD neurons at five timepoints encompassing the remodeling period (17-32 hpl). Scale bar = 2 μm.
E. GFP::RAB-3 density progressively decreases on the ventral cord (black): at 17 hpl (2.81 ± 0.8, n=21), 21 hpl (2.58 ± 0.7, n=51), 24 hpl (3.04 ± 0.8, n=22), 27 hpl (1.86 ± 0.8, n=22) and 32 hpl (0.14 ± 0.3, n=14). GFP::RAB-3 density progressively increases on the dorsal cord (gray): 17 hpl (0.0 ± 0, n=12), 22 hpl (0.09 ± 0.3, n=28), 24 hpl (1.44 ± 1.8, n=21), 27 hpl (4.71 ± 1.1, n=15) and 32 hpl (4.96 ± 0.9, n=14). Data are mean ± SD. Kruskal-Wallis test. * $p < 0.05$ and **** $p < 0.0001$.
F. Stages of remodeling based on temporal development.

We attached seven copies of GFP11 to the *unc-8* locus to amplify the net GFP signal and expressed the complementary GFP1-10 in DD neurons (Figure 2.3A). We used this strain to visualize expression of the endogenous UNC-8 protein at three different time-points: before remodeling (T_{16}), early remodeling (T_{24}) and late remodeling (T_{30}) (Figure 2.3B). We first observed dim UNC-8::GFP puncta that are sparsely detectable in the early L1 larvae before remodeling (T_{16}). As DD remodeling progressed, we observed robust elevation of UNC-8::GFP puncta density along the remodeling ventral process (Figure 2.3C-E). This finding is consistent with the proposed model in which UNC-8 is transcriptionally upregulated to elevate UNC-8 protein for DD remodeling.

To investigate how UNC-8 is transported in remodeling DD axons, we evaluated the developmental arrangement of UNC-8::GFP puncta in mutants for the presynaptic kinesin KIF1A/*unc-104*. In *unc-104* mutants, synaptic vesicles fail to populate the axon and accumulate in the cell soma (Hall & Hedgecock, 1991; Otsuka et al., 1991). Strikingly, most UNC-8::GFP puncta are sequestered in DD cell soma in KIF1A/*unc-104* mutants and fail to localize to remodeling axons (Figure 2.3D-F). This result demonstrates that the developmental arrangement of UNC-8 in remodeling DD axons requires KIF1A/*unc-104* activity.

Because KIF1A/UNC-104 transports synaptic vesicle components from the cell soma to the presynaptic apparatus, we reasoned that UNC-8 might also localize to DD presynaptic domains. To test this idea, we used a two-color imaging strategy to compare the localization of UNC-8::GFP vs RAB-3 labeled with mCherry. During remodeling (T_{24}), endogenous UNC-8::GFP puncta appeared in regions adjacent to mCherry::RAB-3 clusters in the remodeling axon (Figure 2.3G). Overall, results in this section demonstrate that UNC-8 is developmentally upregulated and localizes to remodeling DD boutons in an KIF1A/UNC-104-dependent manner.

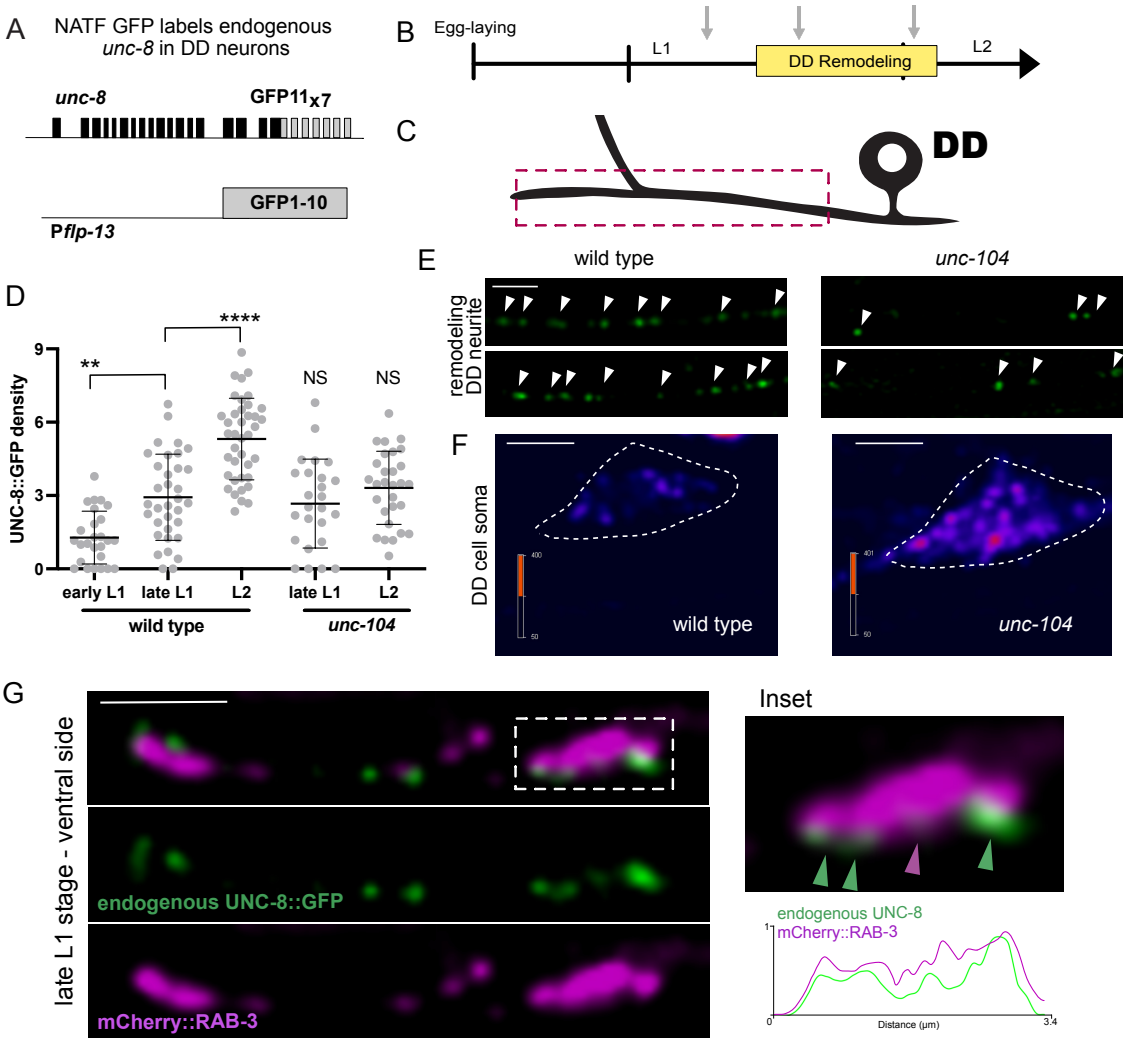

Figure 2. 3. UNC-8 localizes to remodeling DD presynaptic boutons

A. A split GFP strategy (NATF) (He et al., 2019) to tag endogenous UNC-8 in DD neurons. Seven copies of GFP11 ($GFP11_{x7}$) were inserted at the endogenous *unc-8* locus to produce a C-terminal UNC-8::$GFP11_{x7}$ fusion protein. An extrachromosomal array was used to drive the complementary GFP1-10 peptide in DD neurons under the *flp-13* promoter (P*flp-13*).
B. Endogenous UNC-8::GFP puncta were evaluated in DD neurons at developmental time points (arrows) spanning the remodeling period: early L1 (16hpl), late L1 (24 hpl) and L2 stages (32 hpl)
C. (Top) Schematic of DD neuron denoting region (dashed box) in which UNC-8::GFP puncta were imaged.
D. Quantification of UNC-8::GFP density (UNC-8 puncta/10µm) at each timepoint shows progressive upregulation in the wild type (left): early L1 (1.28 ± 1.1, n=26), late L1 (2.93 ± 1.8, n=34), L2 stages (5.31 ± 1.7, n=39) but not in an *unc-104*/Kif1A mutant (right): late L1 (2.66 ± 1.8, n=25) and L2 (3.31 ± 1.5, n=20). Data are mean ± SD. Kruskal-Wallis test. ** $p < 0.01$, **** $p < 0.0001$ and NS is Not Significant. All comparisons are relative to the 24hpl time-point in the wild type.
E. Representative images of UNC-8::GFP puncta at the L2 stage in the wild type (left) vs *unc-104*/Kif1A mutant (right). Scale bar = 2 µm.

F. Representative images showing the accumulation of UNC-8::GFP puncta in the DD cell soma of trafficking defective *unc-104*/Kif1A mutant. Color key denotes relative UNC-8::GFP signal intensity. Scale bar = 2 μm.
G. (Left) Dual-color imaging during the remodeling period (late L1, see Panel B) detects endogenous UNC-8::GFP puncta (green) neighboring ventral presynaptic DD boutons labeled with mCherry::RAB-3 region (magenta). (Right) Inset and line scan show close-up of UNC-8::GFP puncta (green) adjacent to presynaptic region (magenta). Scale bar = 2 μm.

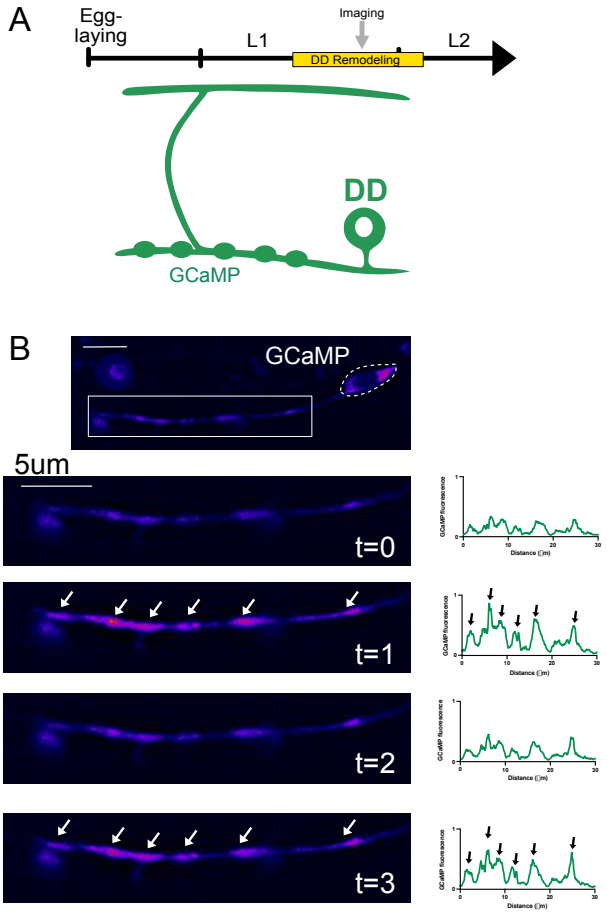

Figure 2. 4. Ca^{++} transients in presynaptic boutons during DD remodeling

A. Experimental set-up utilizes GCaMP (green) to monitor spontaneous Ca^{++} transients in DD neurons. Imaging was performed on synchronized L1 larvae during the remodeling window (T_{26}-T_{28}).
B. (Left) Snapshots of spontaneous GCaMP signal in remodeling DD over time (4 seconds) and (Right) corresponding line scans. Dashed circle demarks cell soma and arrows point to bouton-like structures. Scale bar = 5 μm.

UNC-8 maintains Ca^{++} levels in remodeling DD neurons

Previous work established that a reconstituted UNC-8 channel mediates Na+ influx in Xenopus oocytes (Ying Wang et al., 2013). The resultant depolarization of local membrane potential in DD presynaptic boutons is predicted to enhance VGCC/UNC-2 channels and the consequent elevation of intracellular Ca^{++} (Figure 2.1) (Miller-Fleming et al., 2016). To test this idea in vivo, we expressed the Ca^{++} sensor, GCaMP6s, in DD neurons to track spontaneous Ca^{++} changes at remodeling synapses (T_{26}) (Figure 2.4A). In wild-type animals, we detected striking Ca^{++} fluctuations confined to oblong bouton-like structures (Figure 2.4B), that likely correspond to DD presynaptic terminals (Kittelmann, Hegermann, et al., 2013). Live imaging revealed that at basal states, GCaMP fluorescence is downregulated in *unc-8* mutants (Figure 2.4B-C), suggesting that UNC-8 maintains Ca^{++} levels in remodeling DD neurons. This result parallels a previous finding in which the fluorescence of the calcium indicator OGB-1 was downregulated in presynaptic regions upon addition of the ENaC channel antagonist, Benzamil (Younger et al., 2013).

To determine if UNC-8 can also mediate evoked synaptic responses, we activated presynaptic DA motor neurons with the light-activated opsin, Chrimson (Schild & Glauser, 2015), and monitored Ca^{++} changes in DD neurons with GCaMP6s (Figure 2.5A). This experiment detected consistent upregulation of Ca^{++} at remodeling DD boutons with DA neuron activation in wild-type animals (Figure 2.5D-F). Importantly, this effect depends on ATR, a necessary channelrhodopsin cofactor (Figure 2.6A-B). In *unc-8* mutants, however, Ca^{++} levels in DD neurons were not elevated in response to DA activation either in the presence (Figure 2.5G-I) or absence of ATR. (Figure 2.6C-D). Thus, our results lend strong support to the proposal that the presynaptic UNC-8 channel mediates elevated Ca^{++} levels in remodeling boutons and substantiates a role for synaptic activity, through Ca^{++} signaling, in disassembly of DD presynaptic domains (Miller-Fleming et al., 2016).

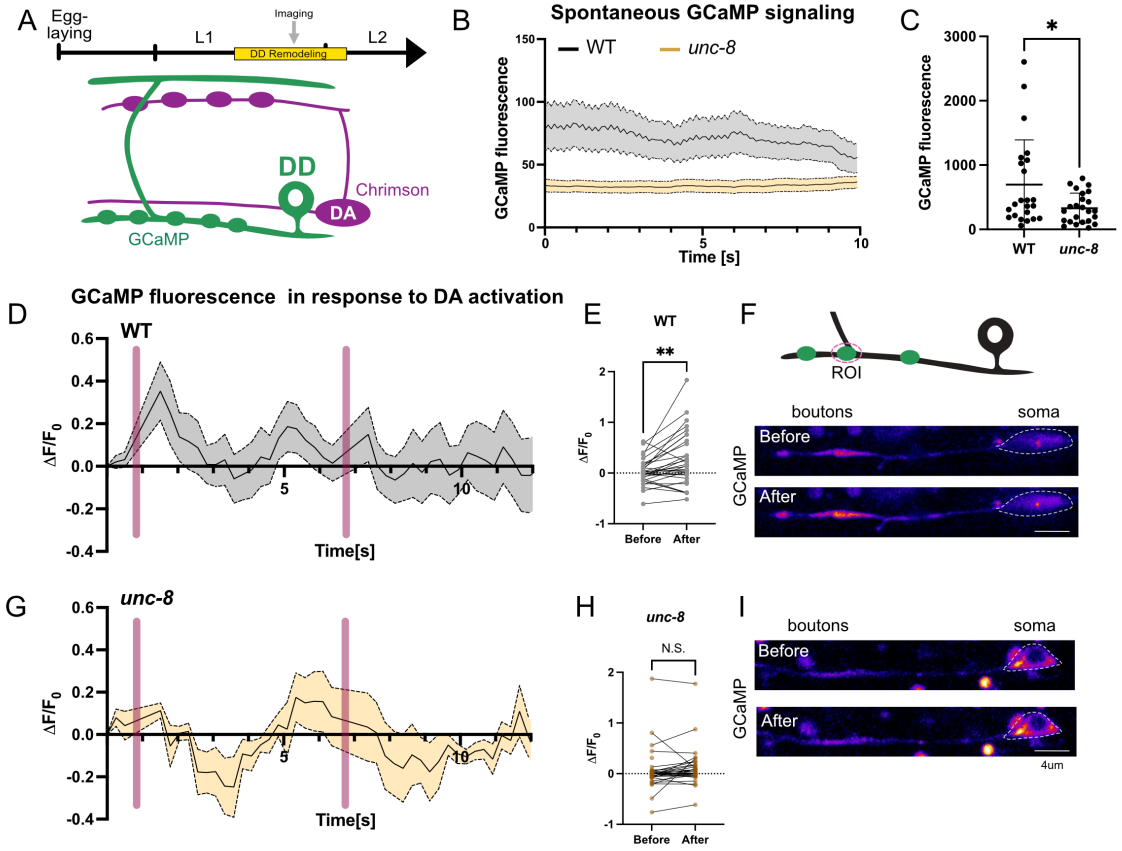

Figure 2. 5. UNC-8 is required for elevated Ca^{++} in remodeling boutons

A. Experimental set-up: (Top) Synchronized L1 larvae were imaged during the remodeling window (arrow). Ca^{++} transients (GCaMP) were detected in remodeling DD neurons. The red-light activated channelrhodopsin, Chrimson, was expressed in presynaptic DA neurons (magenta) for experiments that evoke Ca^{++} transients in DD neurons (Panels D-H).
B-C. Spontaneous Ca^{++} fluctuations were detected in wild-type (WT) and *unc-8* mutant animals. GCaMP fluorescence is elevated in WT (695.4 ± 145, n=23) vs *unc-8* (329.7 ± 47.69, n=24). Mann-Whitney test, * p = 0.0343.
D-F. (D) Chrimson activation in DA neurons with a pulse of 561nm light (magenta bars) evokes GCaMP transients in wild-type (WT) DD presynaptic boutons. **(E)** GCaMP signal (0.02 ± 0.3, n=32) increases (0.25 ± 0.5, n=32) after Chrimson activation. Non-parametric paired Wilcoxon test ** p = 0.002. **(F)** Snapshots of a remodeling bouton (ROI) shows that GCaMP levels are upregulated after Chrimson activation in the wild type.
G-I. (G) Chrimson activation of *unc-8* mutant DA neurons fails to evoke a GCaMP response in DD neurons. **(E)** GCaMP baseline (0.06 ± 0.4, n=32) does not increase after DA activation (0.07 ± 0.5, n=32). Non-parametric paired Wilcoxon test, p = 0.0803. **(F)** Snapshots of a remodeling bouton (ROI) show that GCaMP levels do not increase upon Chrimson activation in *unc-8* mutants.
All animals depicted were grown in the presence of ATR. Presynaptic boutons are positioned in the DD neurite anterior (left) of the cell soma (dashed circle). Scale bar = 4 µm.

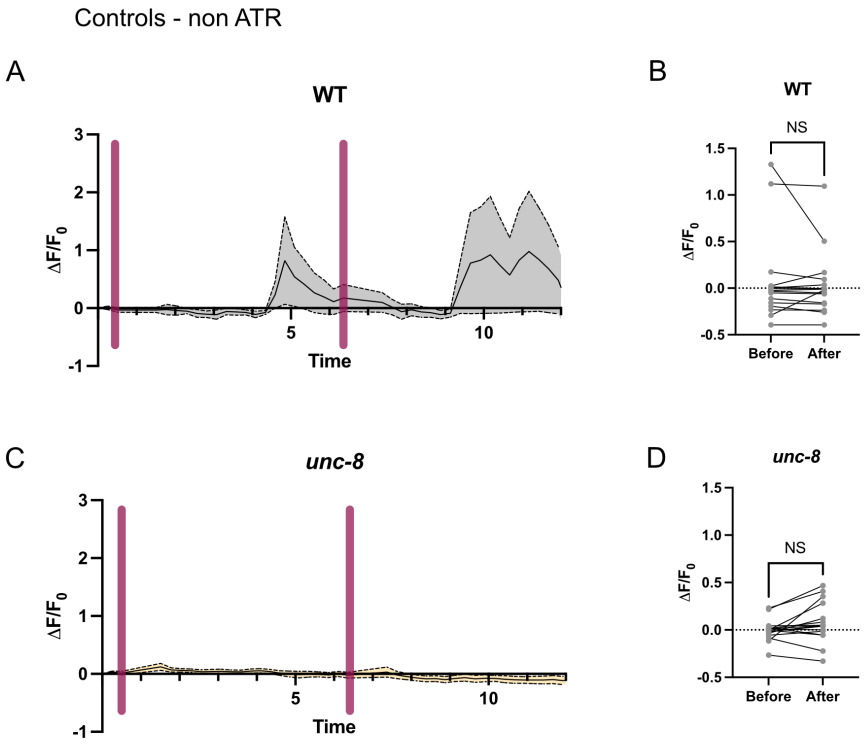

Figure 2. 6. Animals grown in the absence of ATR fail to upregulate Ca^{++}

In the absence of ATR, Chrimson activation (magenta bars) in DA neurons fails to elevate GCaMP fluorescence in either (**A-B**) wild type (baseline = 0.07 ± 0.5, n=16; after activation = 0.03 ± 0.4, n=16), p = 0.487 or (**C-D**) *unc-8* mutants (baseline = -0.002 ± 0.1, n=16, after activation = 0.07 ± 0.2, n=16), p = 0.0604. Paired t-test, N.S., Not Significant.

CaN/TAX-6 is enriched at DD neuron presynaptic terminals

Previous studies have shown that the conserved phosphatase Calcineurin/CaN functions with *unc-8* in a common genetic pathway to drive DD remodeling (Miller-Fleming et al., 2016). Because our results show that UNC-8 localizes to remodeling DD presynaptic boutons (Figure 2.3), we devised an experiment to determine if TAX-6, the catalytic subunit of CaN in *C. elegans*, is also presynaptically localized. To visualize endogenous TAX-6, we used the NATF strategy (He et al., 2019) to attach 3 copies of GFP to the *tax-6* locus and expressed the complementary GFP1-10 in DD neurons (Figure 2.7A). Imaging before the remodeling period (L1 stage) revealed that endogenous TAX-6 is enriched in the DD ventral neurite. In contrast, after remodeling, at the L4 stage, TAX-6::GFP is brightest on the dorsal side (Figure 2.7B-C). This localization pattern for TAX-6::GFP matches that of DD presynaptic domains during larval development (Figure 2.7D). Close inspection revealed both a diffuse TAX-6::GFP signal as well as locally enriched TAX-6::GFP puncta throughout the axon (Figure 2.7B). To test if TAX-6::GFP puncta are localized to presynaptic terminals, we labeled the Piccolo/Bassoon homologue and active zone protein, CLA-1, with mRuby (Xuan et al., 2017). Imaging revealed that TAX-6::GFP puncta are consistently enriched at CLA-1::mRuby-labeled active zones (Figure 2.7E-F). Thus, both presynaptic UNC-8 and TAX-6 are at the site of action where they can influence each other's function.

CaN/TAX-6 upregulates Ca^{++} in remodeling boutons

Because we found that UNC-8 maintains both intrinsic and evoked Ca^{++} responses in remodeling DD neurons (Figure 2.4), we predicted that TAX-6 might also play a role regulating intracellular Ca^{++}. To test this idea, we used GCaMP to monitor Ca^{++} levels in remodeling DD boutons in *tax-6* mutants. In contrast to *unc-8* mutants in which Ca^{++} transients in remodeling boutons are largely abrogated (Figure 2.5B-C), intrinsic Ca^{++} levels in *tax-6* mutants are similar to that of wild type (Figure 2.8A-B). To evaluate the role of TAX-6 in evoked synaptic function, we

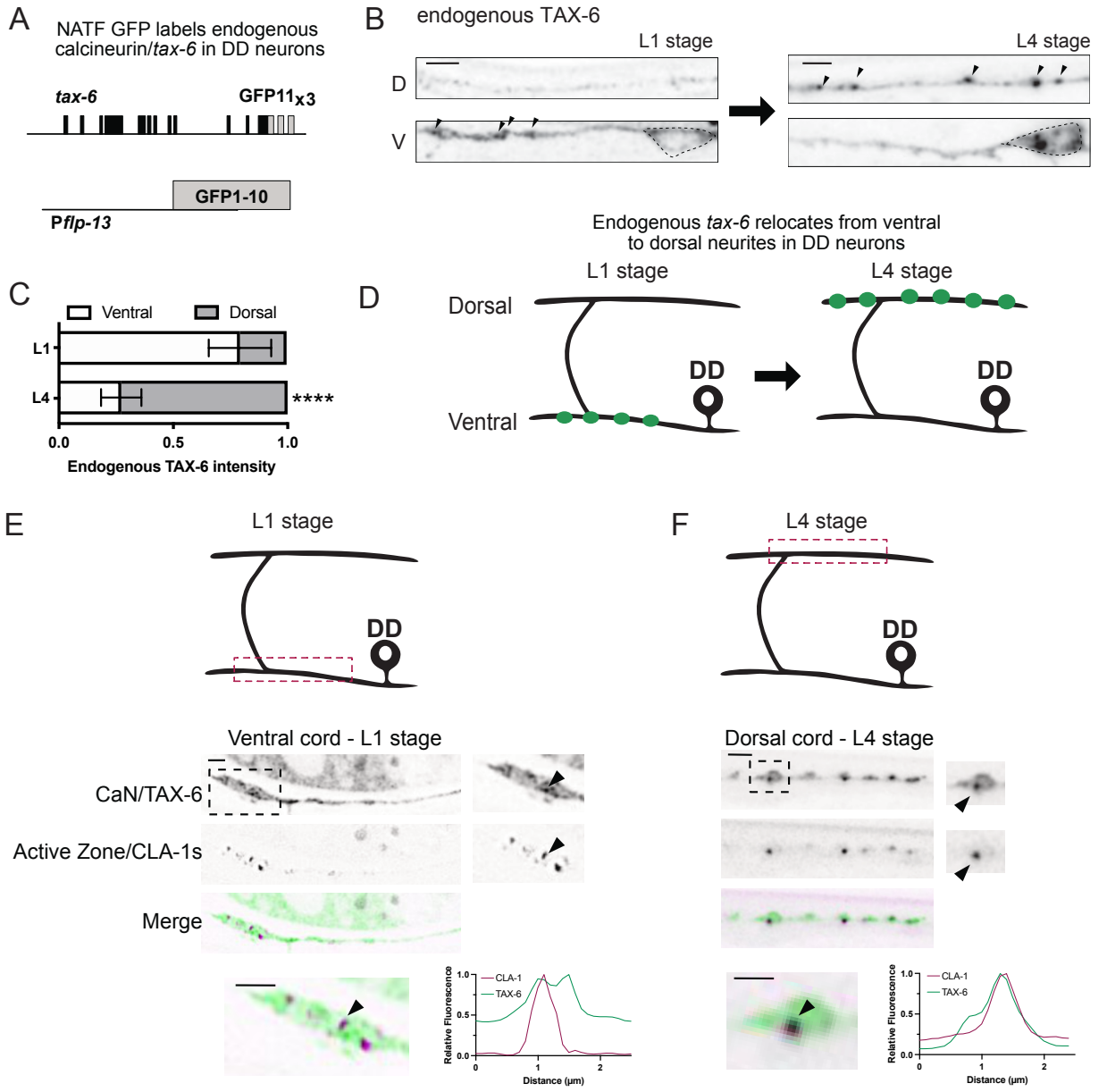

Figure 2. 7. Calcineurin is enriched at DD presynaptic boutons.

A. Split GFP (NATF) strategy for labeling endogenous CaN/TAX-6 in DD neurons. Three copies of GFP11 were inserted at the endogenous *tax-6* locus to produce a C-terminal TAX-6:: $GFP11_{x3}$ fusion protein. An extrachromosomal array was used to drive the complementary GFP1-10 peptide in DD neurons under the *flp-13* promoter (Pflp-13).
B. (Left) Before DD remodeling, at the L1 stage, endogenous TAX-6 is enriched (arrowheads) in the ventral (V) neurite but (right) relocates to the dorsal cord (D) after remodeling, at the L4 stage. Scale bar = 2 µm.
C-D. TAX-6 enrichment switches from the ventral to the dorsal cord during development. **(C)** Quantification of TAX-6::GFP detects initial enrichment in the ventral cord (V = 0.79 ± 0.1 vs D = 0.2 ± 0.1, n=29) in L1 larvae and later enrichment on the dorsal side at the L4 stage (V = 0.27 ± 0.1, n=21 vs D = 0.73 ± 0.1, n-21). One-Way ANOVA with Tukey's multiple comparisons test, ****

$p < 0.0001$ **(D)** Graphical representation of the relocation of TAX-6 from ventral (L1 stage) to dorsal (L4 stage) DD neurites.
E-F. CaN/TAX-6 is enriched at presynaptic active zones. Co-localization (arrowheads) of endogenous CaN/TAX-6::GFP (green) and active zone protein CLA-1s (magenta) **(E)** on the ventral side before remodeling (L1 stage) and **(F)** on the dorsal side (L4 stage) after remodeling. (bottom) Line scans of insets show co-localization of CaN/TAX-6 (green) and CLA-1s (magenta). Scale bar = 2 μm.

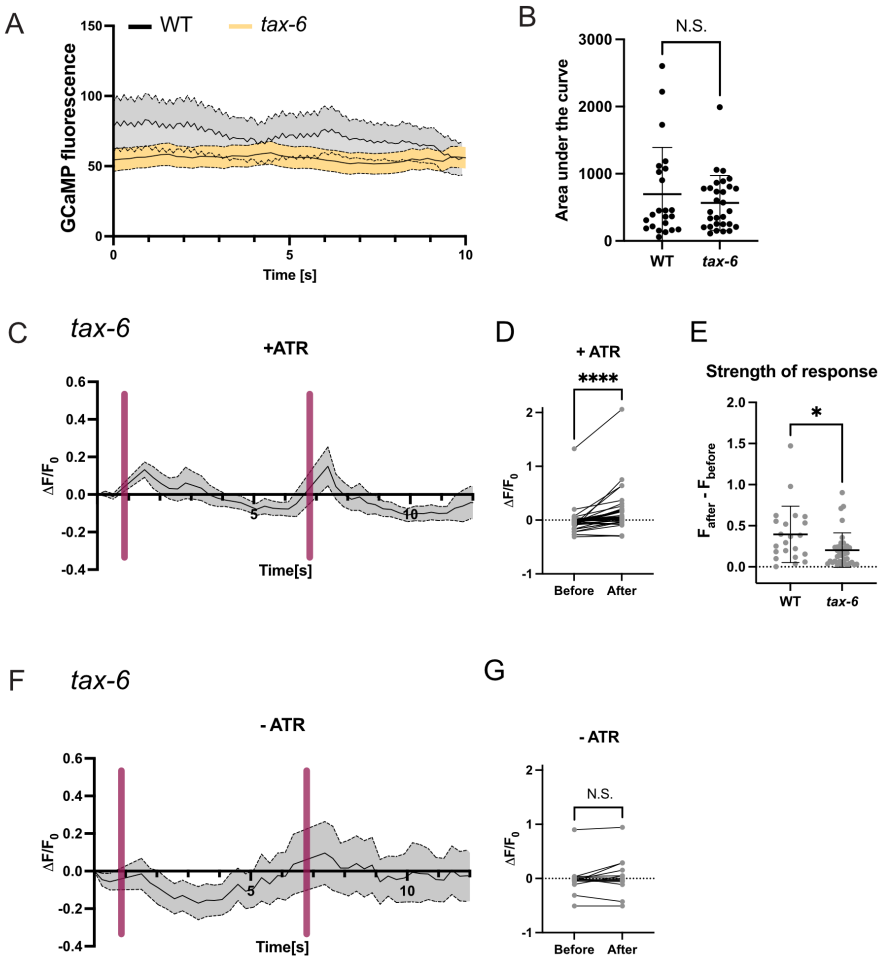

Figure 2. 8. Evoked Ca++ transients are reduced in *tax-6* mutants

A-B. The magnitudes (area under the curve) of spontaneous Ca^{++} fluctuations in wild type (WT) (695.4 ± 145, n=23) vs *tax-6* mutants (565.8 ± 408, n=29) are not significantly different. Mann-Whitney test, N.S., Not Significant, p = 0.7806. Data for WT also shown in Figure 2.5B.
C-D. In the presence of ATR (+ATR), Chrimson activation in DA neurons with a pulse of 561nm light (magenta bar) elevates DD GCaMP fluorescence (before activation = -0.02 ± 0.2, n=44, after activation = 0.14 ± 0.4, n=44). Delta F = (F_n) - (F_0), F_0 = T_{19}. Non-parametric Wilcoxon test, **** p < 0.0001.
E. Normalized GCaMP fluorescence difference before (F_{before}) and after (F_{after}) Chrimson activation in wild-type (WT) (0.04 ± 0.3, n=44) is higher than in *tax-6* mutants (0.04 ± 0.3, n=44). Mann-Whitney test, * is p = 0.0109.
F-G. (F) In the absence of ATR (-ATR), DA activation (magenta bar) does not elevate GCaMP fluorescence in *tax-6* mutant animals (magenta). **(G)** GCaMP baseline (-0.009 ± 0.3, n=14) does not increase after ceChrimson activation (0.04 ± 0.3, n=44). Non-parametric Wilcoxon test, N.S., Not Significant, p = 0.3054.

used Chrimson to activate presynaptic DA neurons and GCaMP in DD neurons to monitor Ca^{++} levels (Figure 2.5A). This experimental paradigm revealed that Ca^{++} levels are consistently elevated in *tax-6* mutants with activation of Chrimson (Figure 2.8C-D) and that this effect is dependent on ATR (Figure 2.8F-G). Interestingly, the strength of the evoked Ca^{++} response (F_{before}-F_{after}) in *tax-6* mutant animals is significantly reduced in comparison to wild type (Figure 2.8E). These findings are consistent with the idea that TAX-6 strengthens the Ca^{++} response, perhaps by tuning *unc-8* activity (Figure 1).

DISCUSSION

In this chapter, we have tested key predictions of a model for ENaC/UNC-8-dependent synapse elimination (Miller-Fleming et al., 2016) (Figure 1). First, we have shown that endogenous ENaC/UNC-8 is upregulated at the onset of DD synaptic remodeling and thus could function as a temporal trigger for synapse elimination (Figure 2.3D). Second, UNC-8 localizes to the DD presynaptic zone during remodeling and UNC-8 trafficking into the axon depends on KIF1A/UNC-104, the canonical kinesin motor for anterograde transport of presynaptic components (Figure 2.3D-F) (Hall & Hedgecock, 1991; Otsuka et al., 1991). Third, UNC-8 is required for elevated levels of presynaptic Ca^{++} in remodeling DD neurons as predicted by previous genetic evidence (Figure 2.5) (Miller-Fleming, 2016). Fourth, the Ca^{++}-dependent phosphatase CaN/TAX-6 is constitutively enriched at presynaptic boutons of GABAergic neurons (Figure 2.7). Fifth, consistent with the proposed positive-feedback loop that upregulates Ca^{++} signaling in remodeling boutons (Figure 2.1), CaN/TAX-6 enhances Ca^{++} responses during the remodeling window (Figure 2.8). Together, these results provide strong support for the hypothesis that UNC-8 elevates intracellular calcium in a positive feedback loop involving CaN/TAX-6 that drives presynaptic disassembly in remodeling DD neurons.

Previous studies have shown that ENaC channels can localize to presynaptic terminals. These studies, however, relied on over-expression strategies (Orr et al., 2017; Voglis & Tavernarakis, 2008) or lacked cell specificity (Urbano et al., 2014) to determine the intracellular localization of ENaC channels in vivo and throughout development. Our work offers the first evidence of the subcellular localization at single-cell resolution of an ENaC channel at its native level of expression and throughout circuit development. Our findings unequivocally show that ENaC/UNC-8 localizes to remodeling presynaptic boutons. We also determined that the conserved kinesin motor, KIF1A/UNC-104, is required for presynaptic UNC-8 placement (Figure 2.3). Consistent with our findings, a previous study described that DD remodeling is blocked in *unc-104* mutants as ventral synapses were not eliminated even at the L3 stage (Park et al., 2011). Thus, it is possible that the blockage to eliminate ventral synapses could arise from failure to localize UNC-8 to remodeling axons. This idea implies that one of the main roles of UNC-104 during DD remodeling is to transport UNC-8 to disassembling synapses. Because UNC-8 traffics to remodeling axons during the onset of DD remodeling, temporal ablation of UNC-104 during the remodeling window is predicted to prevent elimination of ventral synapses. To test this idea, one could monitor synaptic proteins (e.g., RAB-3) and UNC-8 using the temperature-sensitive allele, *unc-104(ce782)* (Edwards, Yorks, Morrison, Hoover, & Miller, 2015). Ablating UNC-104 activity at elevated (restrictive) temperature during DD remodeling should prevent the localization of UNC-8 to remodeling boutons and their consecutive elimination.

Notably, KIF1A/UNC-104 is known to traffic synaptic vesicles to active synapses (Hall & Hedgecock, 1991; Otsuka et al., 1991). Overall, because the localization pattern of UNC-8 and presynaptic RAB-3 is not identical (Figure 2.3), it is possible that KIF1A transports UNC-8 in a subpopulation of synaptic vesicles. Similarly, ATG-9, the sole transmembrane protein critical for the initiation of autophagy (Noda et al., 2000) is transported to synapses in a KIF1A-dependent manner and was recently shown to decorate the membrane of a subset of synaptic vesicles

(Stavoe, Hill, Hall, & Colón-Ramos, 2016; Yang et al., 2020). Hence, experiments involving immuno-electron microscopy against UNC-8 would be key to identify if UNC-8 is inserted in the membrane of synaptic vesicles.

We propose that UNC-8 channel activity and CaN upregulate Ca^{++} levels during DD remodeling in a positive-feedback loop (Figure 2.1). Although Ca^{++} transients are observed in CaN/*tax-6* mutants, the evoked response is quantitatively reduced in comparison to wild type (Figure 2.8), suggesting that CaN/TAX-6 functions to enhance UNC-8-dependent elevation of presynaptic Ca^{++}. Although the biochemical mechanism of this effect is unknown, direct phosphorylation is known to regulate ASIC channel activity (Duan et al., 2012). Our finding that UNC-8 elevates presynaptic Ca^{++} is consistent with previous studies in Drosophila which demonstrated that presynaptic ENaC channels upregulate local Ca^{++} levels (Younger et al., 2013). In contrast to *tax-6* mutants, however, *unc-8* mutants completely fail to upregulate Ca^{++} levels after presynaptic activation. Thus, these results show that UNC-8 has a more active role maintaining synaptic Ca^{++} levels. The strong positive effect of UNC-8 on intracellular Ca^{++} could explain why its expression is developmentally-regulated and why forced expression of UNC-8 in VD neurons is sufficient to trigger the elimination of VD synapses (Miller-Fleming et al., 2016). Our findings may also reflect the complex molecular changes that are taking place during synapse elimination. VGCCs are responsible for modulating synaptic Ca^{++} increase (T. C. Südhof, 2012, 2013), however, VGCC/UNC-2 is eventually eliminated from ventral boutons during DD remodeling. Thus, to understand how the Na^{+} channel UNC-8 plays such a substantial role maintaining Ca^{++} levels, it is necessary to understand the temporal relationship between UNC-8 activity and UNC-2 elimination.

Finally, genetic control to promote Ca^{++} transients in remodeling synapses suggests that there may be a downstream Ca^{++}-dependent mechanism that commands a cellular program that makes presynaptic remodeling possible. The robust localization pattern of CaN at presynaptic

terminals is intriguing and points to a possible role for known downstream targets of CaN in synapse elimination (Chapter III) (Cousin et al., 2001).

ACKNOWLEDGEMENTS

We thank E. Jorgensen for the GFP FLP-ON RAB-3 CRISPR/Cas9 knock in strain used in Figure 2.2 and Peri Kurshan for sharing a mRuby::CLA-1s plasmid and sequence. Some mutant alleles used in this study were provided by the CGC, which is funded by the NIH Office of Research Infrastructure Programs (P40 OD010440). This work used instruments in the Vanderbilt Cell Imaging Shared Resource (supported by NIH grants CA68485, DK20593, DK58404, DK59637 and EY08126). This work was supported by NIH grants R01NS081259, R01NS106951 to DMM and predoctoral fellowship from AHA to ACC (18PRE33960581).

AUTHOR CONTRIBUTIONS

Leah Flautt collected and analyzed data for experiments using the endogenous GFP::RAB-3 line (Figure 2.2). Sierra Palumbos assisted with integration og the wdIs117 transgene which expresses Chrimson in DA neurons of L2 stage animals (Figure 2.5, 2.6 and 2.8) The remaining experiments were performed by Andrea Cuentas-Condori.

CHAPTER III

An actin-dependent endocytic mechanism recycles synaptic proteins from old to new presynaptic sites during circuit refinement

INTRODUCTION

Neuronal circuits are typically modified during development to produce mature functional networks. In the developing mammalian visual circuit, for example, retinal ganglion cells (RGCs) project to the thalamus to innervate geniculate neurons. Initially, presynaptic boutons are dispersed throughout each RGC axon to synapse with multiple geniculate targets. This florid pattern of connectivity is then refined in an activity-dependent mechanism that eliminates distal RGC boutons while clustering others at proximal locations (Hong et al., 2014). Importantly, RGC axonal projections remain intact as boutons are relocated and are not retracted until a later, separate pruning step (Hong & Chen, 2011). Similarly, inputs to RGCs from rod Bipolar Cells (BCs) in the retina are also eliminated from stable axonal-dendritic contacts during development (Morgan et al., 2011). Thus, presynaptic boutons are highly dynamic during development and can drive remodeling of neuronal circuits.

Interestingly, presynaptic boutons are also dynamic within established circuits and this inherent plasticity has been proposed to mediate recovery of injury (Berry & Nedivi, 2016; Holtmaat & Svoboda, 2009; Monday & Castillo, 2017). Live-imaging of mammalian circuits revealed that presynaptic varicosities display dynamicity at basal conditions (Carrillo et al., 2013; De Paola et al., 2006; Marik et al., 2010; Marik, Yamahachi, Meyer, & Gilbert, 2014). Interestingly, both the elimination and formation of presynaptic boutons across stable axons can be modulated

by synaptic activity. Learning paradigms decrease presynaptic structural dynamics (Carrillo et al., 2013) whereas circuit ablation promotes presynaptic remodeling (Marik et al., 2014). In fact, increasing presynaptic bouton remodeling in-vivo improves motor circuit recovery after stroke (Tennant et al., 2017). Thus, a better understanding of the mechanisms that govern presynaptic elimination and formation within stable neuronal processes could aid the overarching goal of manipulating presynaptic structural plasticity to ameliorate damaged circuits or in neurodegenerative disease.

The elimination and addition of synapses within stable neuronal processes occurs across species and therefore likely depends on conserved underlying mechanisms. Thus, we are investigating circuit remodeling in the model organism, *C. elegans*, in which we can exploit powerful genetic strategies and live imaging methods for this purpose. During early larval development, the DD class of embryonically-derived GABAergic motor neurons remodel to accommodate newly arrived postembryonic VD class GABAergic motor neurons for a functional adult motor circuit (Sulston, 1976; Sulston & Horvitz, 1977). In the newly hatched larva (L1), DD neurons innervate ventral muscles. During the transition from the L1 to L2 larval stages, the ventral synapses of DD neurons are eliminated, and new DD inputs are established with dorsal muscles (White et al., 1978) (Figure 1.4). DD remodeling results from intracellular changes as the elimination and assembly of presynaptic boutons take place without any evident axonal pruning or extension of DD neurites (Hallam & Jin, 1998). Importantly, DD presynaptic remodeling is influenced by synaptic activity (Han, Bellemer, & Koelle, 2015; Miller-Fleming et al., 2016; Thompson-Peer et al., 2012). Of particular interest, the presynaptic ENaC/UNC-8 channel elevates intracellular Ca^{++} in DD neurons during remodeling to promote synapse elimination (Chapter II). The role of UNC-8 in remodeling presynaptic terminals depends on the conserved phosphatase, Calcineurin/CaN, which also promotes DD synapse elimination (Miller-Fleming et al., 2016). Because CaN is known to function as a key regulator of Activity-Dependent Bulk

Endocytosis (ADBE) (Emma L. Clayton & Cousin, 2009), we have investigated the possibility that an ADBE-like mechanism is involved in DD synapse elimination.

ADBE is an endocytic mechanism that recycles synaptic vesicles in highly active neurons (Emma L. Clayton & Cousin, 2009; Emma L Clayton, Evans, & Cousin, 2007). This mechanism depends on active presynaptic CaN, which triggers assembly of the dynamin-syndapin complex to enhance actin polymerization and drive the formation of bulk endosomes (Anggono et al., 2006; E. L. Clayton et al., 2009; Emma L. Clayton & Cousin, 2009; Cousin et al., 2001). Actin polymerization is required for the initiation and maturation of bulk endosomes during ADBE (Nguyen et al., 2012). The initial formation of bulk endosomes requires actin (X. Wu et al., 2016) and has been proposed to depend on branched actin polymerization triggered by the recruitment of N-WASP by Syndapin to the remodeling membrane (Kessels & Qualmann, 2002, 2004). N-WASP is a well-known activator of the branched-actin nucleator Arp2/3 (Rohatgi et al., 1999). Consistent with this finding, a recent proteomic study confirmed enrichment of Syndapin and several Arp2/3 subunits in bulk endosomes derived from highly active neurons (A. C. Kokotos et al., 2018). Other studies in neurosecretory cells, determined that the maturation of bulk endosomes, depends on the coordinated formation of an acto-myosin II ring to separate the invaginating bulk endosomes from the membrane (Gormal et al., 2015). Thus, at least two actin networks may participate in the formation and scission of bulk endosomes. In neurons, synaptic vesicles are then generated from endosomes in a clathrin-dependent mechanism (Watanabe et al., 2014) to replenish the local synaptic vesicle pool.

In this chapter, we challenge the idea that an ADBE-like mechanism functions downstream of UNC-8 to eliminate presynaptic sites from the ventral neurites of remodeling DD neurons. Our study confirms that canonical components of the ADBE mechanism including calcineurin, dynamin, syndapin and Arp2/3 are required for UNC-8-dependent removal of DD presynaptic components. We also show that the F-BAR protein, TOCA-1, functions in parallel to syndapin and

UNC-8 for synapse elimination and that both pathways promote actin polymerization during DD remodeling. Importantly, our results provide a possible explanation for the dramatically different outcomes of ADBE, which effectively maintains synaptic function, versus our proposed bulk endocytic mechanism, which effectively dismantles the synapse. As noted above, in ADBE, bulk endosomes give rise to synaptic vesicles that replenish the local pool. Our studies of remodeling DD neurons have revealed that ventrally located presynaptic components are also recycled, but in this case to distal synapses in the dorsal DD neurite. Further, we have shown that this mechanism depends on both the UNC-8/SDPN-1 and TOCA-1 pathways and on RAB-11, a canonical GTPase effector for recycling endosomes. Our findings are important because they suggest that a conserved endocytic mechanism could be widely utilized to couple synapse elimination with synapse formation during circuit refinement.

MATERIALS AND METHODS

C. elegans breeding and generation of new alleles

Worms were maintained at 20°- 23°C using standard techniques (Brenner, 1974). Strains were maintained on NGM plates seeded with *E. coli* (OP-50) unless otherwise stated. The wild type (WT) is N2 and only hermaphrodite worms were used for this study.

Generation of rab-3(syb2844) [Dendra-2 FLP-ON]) II

Sunybiotech used CRISPR/Cas9 to add a FLP-ON cassette at the N-terminus end of the *rab-3* locus (Schwartz & Jorgensen, 2016), which contains the photoconvertible protein Dendra-2. To visualize the endogenous RAB-3 tagged with Dendra-2, we expressed flippase in DD neurons using the *flp-13* promoter (P*flp-13*). Animals were outcrossed three times before they were used for experiments.

Generation of integrated wdIs124 [pflp-13::GFP::CLA-1s] transgene

pACC122 (P*flp-13*::GFP::CLA-1s) was generated from plasmid PK065 (P*mig-13*::GFP::CLA-1s) which was provided by Peri Kurshan (Xuan et al., 2017). pACC122 was injected with *lin-15+* plasmid (pSH10) into *lin-15(n765)* mutants. X-ray irradiation was used to produce double-stranded DNA breaks and worms were screened under the fluorescent microscope to detect successful integrated lines (no multivulva), generating transgene *wdIs124*. Animals were outcrossed three times before they were used for experiments.

Worm staging or synchronization

Staging was achieved by picking 30-40 L4 larvae onto a fresh plate in the afternoon and leaving at 23C overnight. The next morning, 20-30 gravid adults were transferred to a fresh plate, allowed to lay eggs for 1 hr and then removed. Embryos were maintained at 23C for hatching and larval growth until the timepoint at which the worms were imaged.

For imaging L4 stage larvae, a dissecting microscope was used to select 20-30 L4who's gonad was visible but small and had no eggs. The selected worms were then mounted on a 5% agarose slide with 4.5uL 0.1% tricaine/tetramisole anesthetic. Each worm was then examined individually under the A1R confocal microscope, where the shape of its vulva was visible. The Mok et al. (2015) classification system of L4 sub-stages defined by morphological characteristics of the vulva was used to identify early L4 *C. elegans*. We categorized animals with vulva shapes that matched L4.0, L4.1, or L4.2 vulva as early L4s.

Molecular Biology

Most plasmids (Table 3.1) were built using InFusion cloning. First, Snapgene software was used to design one pair of forward and reverse primers targeting the desired DNA vector

backbone and another pair of primers targeting the desired DNA insert. (These primers contained ~15bp overlaps that are necessary for plasmid assembly. Additionally, every desired DNA insert requires its own specific primer pair.) The vector backbone was then PCR linearized and amplified by combining template DNA, which contained the desired backbone sequence, with the appropriate targeting primers and proprietary "CloneAmp HiFi PCR Premix." In a separate PCR reaction(s), the DNA insert(s) was similarly amplified and linearized, using the primer pair targeting the desired insert and template DNA that contained the desired insert sequence. To check for amplification, all PCR products were run on a 1% agarose gel and were then gel purified using a "NucleoSpin Gel and PCR Clean-Up" kit. To assemble the desired plasmid, the purified vector backbone DNA and insert DNA were combined and incubated in solution with propriety "5x In-Fusion HD Enzyme Premix." Following incubation, the reaction mixture containing the putatively assembled plasmid DNA was used to transform Stellar Competent Cells, which were subsequently plated and grown overnight on LB-Amp plates. All plasmids were verified with Sanger sequencing.

Plasmid pACC161 (P*flp-13*::dyn-1AAA::SL2::3xNLSTagRFP) was built using Q5 site-directed mutagenesis kit. The pACC156 (P*flp-13*::dyn-1::SL2::3xNLSTagRFP) plasmid was used as a template to change three residues in the phospho-box for a triple-alanine mutant.

Cell-specific RNAi

Using In-Fusion cloning, for each cell-specific RNAi (csRNAi) experiment, we created two plasmids that express complementary strands of mRNA. Downstream of the sense or antisense transcript, each plasmid contains a transplicing sequence (SL2) followed by a fluorescent protein (cytosolic of nuclear-localized GFP and mCherry) to confirm expression of each plasmid. For example, for csRNAi knockdown of *arx-5*, *dyn-1*, *rab-11* and *rab-5* in DD neurons, we drove expression of each plasmid with either the *flp-13* or *ttr-39* promoters (See Table 3.1) which drive

expression to either DD or DD + VD neurons GABA motor neurons, respectively. In this arrangement, expression of both the sense and anti-sense plasmids is limited to DD neurons, thus resulting in a DD-specific knockdown of each targeted gene. csRNAi templates for each target gene were generated by PCR from genomic DNA with primers that excluded the ATG start codon as follows: 1210 bp of *p21/arx-5*, 1686 bp or *dyn-1*, 1174 bp of *rab-11.1* and 1275 of *rab-5*.

In this experimental design, csRNAi-treated DD neurons are marked by expression of both fluorescent markers (mCherry + GFP) whereas control DD neurons are unlabeled. To determine if remodeling of SNB-1::GFP was perturbed upon knockdown, ImageJ software was used to generate maximum intensity projections. All fluorescence intensity plots were created by drawing a linescan through the ventral and dorsal nerve cords of each worm and averaging the fluorescence intensity values across the anterior region of the DD neurons scored. Intensity of SNB-1::GFP was normalized to the total dorsal and ventral fluorescence.

To determine if remodeling of CLA-1::GFP was disturbed upon cell-specific knockdown, we used Analysis explorer function in NIS Elements to define a mask that filters CLA-1::GFP puncta based on fluorescence, size and circularity. The number of puncta on the ventral or dorsal process of DD1-DD3 was then normalized to a 10 µm neurite.

Feeding RNAi

Clones from the RNAi feeding library (Source BioScience) were used in this study (Lisa Timmons & Andrew Fire, 1998). RNAi plates were produced as previously described (Earls, Hacker, Watson, & Miller, 2010; Petersen et al., 2011). First, 15 mL culture tubes containing 2 ml LB broth with 10 µl (10mg/mL) ampicillin were inoculated with individual bacterial colonies and grown in a 37C shaker for 12-16 hr. Control RNAi cultures were inoculated with bacterial colonies containing the cloning vector but no insert (“empty vector” control) for each feeding RNAi

experiment. 250 µL of overnight culture was added to a mixture of 12.5 ml LB broth + 62.5 µl ampicillin in a 50 mL conical tube. The new culture was then returned to the 37C shaker until reaching log phase (OD > 0.8). The culture was then induced by adding 12.5 mL of LB broth, 62.5 µL ampicillin, and 100 µL 1M IPTG. After 3.5-4 hours incubating in 37C shaker, the culture was spun down using a tabletop centrifuge for 6 min at 3900 rpm to pellet the bacteria. The supernatant was discarded, and the pellet was resuspended in 1mL M9 mixed with 8µL IPTG. The bacterial mixture was dispensed onto 4 60 mm NGM plates (250 µl each), and the plates were left to dry overnight in the horizontal laminar hood and then stored at 4C until for up to a week.

To set-up each RNAi experiment, placed 3-5 L4 larvae (NC1852) were placed on each RNAi plate and maintained at 20°C. Four days later, F1 progeny was imaged as L4 animals. To count the number of puncta, see section below “Counting puncta number”.

Counting presynaptic markers as puncta

To screen candidate genes for a role in GABAergic synapse remodeling, we scored SNB-1::GFP puncta from the *juIs1* [p*unc-25*::SNB-1::GFP; *lin-15*] transgene (Hallam & Jin, 1998) in *unc-55; eri-1* mutants sensitive to feeding RNAi as previously described (Petersen et al., 2011). We compared animals treated with each candidate gene RNA feeding strain vs the blank RNAi (empty vector). Briefly, animals were anesthetized with 0.1% tricaine/tetramisole, mounted on a 2% agarose pad, and imaged with an inverted microscope (Zeiss Axiovert) using Micro Manager software and a 63X oil objective. Ventral puncta between VD3 to VD11 were counted following the mid-L4 stage for both RNAi control and RNAi-treated animals. Data were pooled at least from 2 separate experiments and the examiner was blinded to the treatment. One-Way ANOVA was performed with post hoc correction to compare each RNAi treatment against the control. Similarly, the scorer was blinded to genotype to test if Synaptojanin/*unc-26* promotes synapse remodeling

of SYD-2::GFP puncta from *hpIs3[punc-25::SYD-2::GFP; lin-15*] transgene (Yeh, 2005) in wild-type, *unc-55* and *unc-55; unc-26* double mutants.

Synapse density analysis

To analyze puncta density for presynaptic endogenous GFP::RAB-3 along the ventral cord, images were collected in an A1R laser scanning confocal. Maximum Intensity Projections were created from Z-stacks using NIS Elements. All images were subject to background correction using the Rolling Ball algorithm. Analysis explorer was used to create a mask based on fluorescent thresholding for the RAB-3::GFP signal (I don't understand this step?). ROIs were defined in ventral regions anterior to DD2 and DD3 cell soma. To calculate puncta density, each object was considered a RAB-3 punctum and the total number was normalized to a 10 µm neurite using the following equation: (# of objects detected in ROI / length of ROI in microns)*10. To quantify the density of ventral synapses at late developmental time-point (e.g., early L4 stage) a more sensitive mask (lower fluorescent threshold) was created to detect dim RAB-3 puncta (Is this justified?).

To analyze puncta density along the dorsal DD nerve cord, regions of interest (ROIs) were drawn using the polygonal ROI tool in NIS Elements. ROI lengths were measured using the Distance Measurement: Polyline tool in NIS Elements and were recorded in µm. The Automated Measurement Results tab in NIS Elements was used to record the number of objects (puncta) present in a given ROI, and puncta density within the ROI was then calculated using equation from above. To designate a fluorescent signal as a puncta, a mask was generated in NIS Elements that labeled as puncta all fluorescent features in an image that met size, shape, and intensity criteria set by the experimenter. Once generated, the same masking criteria were used for all treatment and control images included in a given experiment.

To quantify puncta GFP::RAB-3 density in the dorsal nerve cord, ROIs were drawn within the same general anatomical region of a worm (DD1-DD3) for all images in a given experiment. Because curvature of the dorsal cord in the XY plane could artificially increase or decrease the puncta density in the region (depending on whether the curvature was concave or convex), all dorsal cord regions had to meet straightness criteria to be included in analysis. To this end, the Angle measurement tool in NIS elements was used to approximate the extent of dorsal cord curvature by measuring the angle of intersection between two lines drawn tangent to the regions of the dorsal cord immediately anterior and posterior to the apex of the curve in question. Regions with an intersection measurement of less than 160° (where 180° represents a perfectly straight region and 90° represents a region curved at a right angle) were excluded from analysis. ROIs were then drawn along the longest possible region of the dorsal cord that adhered to these straightness criteria. If the regions anterior and posterior to a curve met straightness criteria, then two ROIs were drawn for that image. Off target fluorescent features (autofluorescence) and commissures were excluded from ROIs.

dyn-1(OE) analysis

Synchronized animals (T_{28}) (28 hours after egg laying) expressed either wild-type (WT) or phospho-resistant versions of *dyn-1* in DD neurons (P*flp-13*) in tandem with a nuclear-localized TagRFP protein to recognize cells expressing the array. Z-stacks were collected in an A1R laser scanning confocal spanning the whole depth (~ 3 microns) of the ventral nerve cord. Z-stacks were used to generate MaxIPs in NIS Elements and Analysis Explorer, to define a binary mask based on fluorescence and size to recognize cell soma that expressed nuclear TagRFP. DD1-DD3 neurons were categorized as Control (no red) or *dyn-1*(OE) (red nucleus) based on nuclear expression of TagRFP. An additional mask was defined in the GFP channel for ventral SNB-1::GFP puncta based on fluorescence and circularity. Each recognized punctum on the anterior

process of all DD1-DD3 neurons was counted. Then, puncta counts for each DD dendrite was normalized to the length of the counted region to calculate SNB-1::GFP density as puncta/10 µm.

VCA-1(OE) analysis

Synchronized animals (T_{26}) (26 hours after egg laying) expressed the VCA domain of the Wave Regulatory Complex in tandem with cytosolic mCherry that marks GABAergic cells (P*ttr-39*) expressing the array. Z-stacks spanning the depth of both nerve cords were collected in a Nikon A1R laser scanning confocal microscope. Z-stacks were used to generate MaxIPs in FIJI and the segmented line tool (3-pixel wide) was used to draw ROIs on top of the ventral and dorsal nerve cords. mCherry-positive DD cells carry a VCA(OE) transgenic array. All fluorescence intensity plots were created by drawing a segmented line through the ventral and dorsal nerve cords of each worm and averaging the fluorescence intensity values across the anterior region of the DD neurons scored. Intensity of SNB-1::GFP was normalized to the total dorsal and ventral fluorescence.

UNC-8(OE) analysis in RNAi-treated and *toca-1* mutant animals

FIJI was used to quantify presynaptic markers in VD neurons for effects of UNC-8(OE) (over-expression). Z-stacks were collected for the full length of the ventral nerve cord (VD3 – VD11). mCherry-positive VD cells carry an UNC-8 cDNA transgenic array (Miller-Fleming et al., 2016). Because UNC-8(OE) transgenic arrays are mosaic with expression limited to a random subset of VD neurons in each animal, data were collected from VD neurons (VD3-VD11) carrying the UNC-8 cDNA (mCherry-positive) vs an adjacent control VD neuron that does not carry the array. Neighboring mCherry-positive [e.g., UNC-8(OE)] and mCherry-negative [control] VD neurons were compared to quantify differences in the fluorescence signal for SNB-1::GFP due to UNC-8 over-expression when either *tax-6, sdpn-1*, *toca-1*, *arx-5*, or *rab-11* was downregulated.

For results involving unc-8(OE) experiments, intensity values were obtained from line scans anterior to the VD cell bodies of interest. Background fluorescence was obtained from a line scan of an adjacent region inside the animal and subtracted from the VD line scans.

Microscopy

Laser Scanning Confocal Microscopy

Larval or young adult animals were immobilized on 2-10% agarose pads with 15mM levamisole, 0.05% tricaine as previously described (Smith et al., 2010). Z-stacks were acquired with a Nikon confocal A1R using Apo Fluor 40X/1.3 and 60X/1.4 N.A. oil objectives.

In-vivo actin dynamics at remodeling synapses

For measurements of actin dynamics at synaptic regions in DD neurons (Figures 3.10 and 3.11), endogenous GFP::RAB-3 was used to mark synaptic vesicle clusters and LifeAct::mCherry (Riedl et al., 2008) to visualize actin dynamics. Live-imaging was performed in a Nikon TiE microscope equipped with a Yokogawa CSU-X1 spinning disk head, Andor DU-897 EMCCD camera or Photometrics Prime 95B sCMOS camera, high-speed piezo stage motor, a perfect focus system and a 100X/1.49 Apo TIRF oil objective lens. Synchronized animals at T_{16}-T_{18} (early L1) or T_{26}-T_{28} (late L1) were mounted on 10% agarose pads and immobilized using a combination of 3µL of 100 mM muscimol (TOCRIS biosciences #0289) and 7µL 0.05um polybeads (2.5% solids w/v, Polysciences, Inc. #15913-10). Single-plane snapshots were collected every 1 second using triggered acquisition. Movies were submitted to 2D-deconvolution on NIS-Elements using the Automatic algorithm and aligned with the NIS Elements alignment tool when necessary. To analyze GFP::RAB-3 dynamics, videos were shortened to 60-150 seconds, before any perceivable photobleaching, then local contrast was used in the 488 nm channel and to binarize the GFP signal using manual thresholding. The resultant binarized video was then submitted for

particle tracking to determine transient GFP::RAB-3 movement. The total number of transient events was normalized to events per minute per 10 µm neurite. Kymographs to visualize GFP::RAB-3 and actin dynamics (LifeAct::mCherry) were performed in NIS Elements. At sites of GFP::RAB-3 puncta, ROIs were defined in the 561nm channel to track LifeAct::mCherry transients (e.g, actin transients) in presynaptic regions. LifeAct::mCherry fluorescence changes throughout time were plotted and normalized with the first fluorescence value starting at zero. GFP::RAB-3 density (puncta/10 micron) for each genotype was determined from the first frame of each video, submitted for 2D deconvolution on NIS elements and then the line scan function was used in the 488nm channel to determine fluorescent peaks (RAB-3::GFP boutons). Any peak over 300AU fluorescent units was considered a GFP::RAB-3 punctum.

In-vivo dynamics of endogenous GFP::RAB-3 and TagRFP::RAB-11 during remodeling

We built a strain to follow endogenous GFP::RAB-3 and TagRFP::RAB-11 dynamics (Figure 3.14) during the remodeling window (T_{27} – T_{30}). Animals were placed on 10% agarose pads and immobilized using a combination of 3µL of 100mM muscimol (TOCRIS biosciences #0289) and 7µL 0.05um polybeads (2.5% solids w/v, Polysciences, Inc. #15913-10). Single plane movies were captured at 0.5fps (frames per second) on a Nikon TiE microscope with a Yokogawa CSU-X1 spinning disk head, Photometrics Prime 95B sCMOS camera, a high-speed MCL Piezo stage, a Perfect Focus system and a 100X/1.49 Apo TIRF oil objective lens. Movies were 2D-deconvolved using the automatic algorithm in NIS Elements and kymographs were created in FIJI with the Multi Kymograph tool. Kymographs were then exported and submitted to Kymobutler (Jakobs, Dimitracopoulos, & Franze, 2019) for identification of particle movement (https://www.wolframcloud.com/objects/deepmirror/Projects/KymoButler/KymoButlerForm).

Tracking of endogenous Dendra-2::RAB-3 during remodeling

This experiment consists of four steps: (1) worm synchronization, (2) photoconversion and collection of baseline data before remodeling, (3) worm recovery, and (4) analysis of photoconverted signal after remodeling. Larvae expressing endogenous Dendra-2::RAB-3 in DD neurons, were synchronized by allowing young adults to lay eggs for 1 hr (see above) and grown at 23 C until T_{18}. At T_{18}, L1 animals were photoconverted using a Mini Scanner equipped with a 405 nm, 100mW photo stimulation laser. Briefly, single worm was mounted on a 10% agarose pad with 2µL of anesthetic [from mixture of 3µL of 100mM muscimol (TOCRIS biosciences #0289) and 7µL 0.05um polybeads (2.5% solids w/v, Polysciences, Inc. #15913-10)]. Wax-paraplast 50/50 v/v combination was applied to each corner of the coverslip to secure it. Using NIS elements, we defined a targeted ROI limited to ventral Dendra-2::RAB-3 synaptic puncta visualized in the 488 nm channel. Dendra-2::RAB-3 was photoconverted at 30µs dwell time with 0.5% power of the 405 nm laser. We collected a Z-stack using 488nm and 561nm lasers before and after Dendra-2 photoconversion. In most cases, we photoconverted Dendra-2::RAB-3 puncta in the anterior ventral neurites of either DD2, DD3 or DD4.

To recover worms, we added 90µL of M9 to the space between the coverslip and the agarose pa and cut the sealant from each corner using a razor blade. The coverslip and agarose pad were rinsed with the addition of M9 buffer and allowed to drip on top of an NGM 60mm plate. Typically, two rounds of 90µL M9 was used to rinse the coverslip and five rounds for the agarose pad. After a few minutes, when the NGM plates had dried, each plate was placed in a 23C incubator. Each treated animal was maintained on a separate plate to match imaging data obtained before and after remodeling for each animal. Twenty hours after photoconversion (T_{38}), we mounted each worm on a 10% agarose pad using 3uL of the anesthetic mixture (see above) and collected a Z-stack using 488nm and 561nm lasers to track the Dendra-2::RAB-3 signal.

For analysis, we first used NIS Elements to 3D-deconvolve all Z-stacks and paired the images for each individual worm before (T_{18}) and after remodeling (T_{38}). After deconvolution, we

imported all images to FIJI and created maximum intensity projections. We drew a 3-pixel wide line scan on top of the Dendra-2::RAB-3 signal and exported the traces from each fluorescent channel (488 and 561nm) and time-point to Prism. We also collected traces from neighboring regions to define the background fluorescence. We used Prism to determine the area under the curve for line scans on the ROI (Dendra2::RAB-3 puncta) as well as neighboring regions (background). We subtracted the background area and plotted the relative photoconverted signal on the dorsal and ventral side at T_{38}, considering the signal at T_{18} as the baseline.

Statistical Analysis

First, we used the Shapiro-Wilk test to determine if a sample is normally distributed. For comparisons between 2 normally distributed groups, Student's T-test was used and $p<0.05$ was considered significant. ANOVA was used to compare 3 or more normally distributed groups followed by Dunnett's or Tukey's multiple-comparison test. If the samples were not normally distributed, we used a Mann-Whitney test to compare two groups and a Kruskal Wallis test to compare three or more groups. The specific test and N used in each experiment appears in each figure legend.

Table 3. 1. List of plasmids

pACC22	p*flp-13*::TOCA-1a::mCherry
pACC42	p*ttr-39*::VCA::SL2::mCherry
pACC50	p*flp-13*::*arx-5* sense::SL2::mCherry
pACC51	p*flp-13*:: *arx-5* antisense::SL2::3xNLS::GFP
pACC57	p*flp-13*::sdpn-1b::mCherry
pACC98	p*flp-13*::2xNLS::FLP_D5
pACC106	p*flp-13*::dyn-1F::SL2:mCherry
pACC107	p*flp-13*::dyn1R::SL2::3xNLS::GFP
pACC122	p*flp-13*::GFP::CLA-1s
pACC141	p*flp-13*:: 2xNLS::FLP_D5::SL2::LifeAct::mCherry
pACC150	p*flp-13*::RAB-11.1F::SL2::3xNLSGFP
pACC151	p*ttr-39*::RAB-11R::SL2::mCherry
pACC156	p*flp-13*::dyn-1::SL2::2xNLS::TagRFP
pACC157	p*flp-13*::TagRFP::RAB-11.1cDNA

pACC158	p*ttr-39*::RAB-11.1csRNAi_R::SL2::2xNLSTagRFP
pACC161	p*flp-13*::dyn-1-AAA::SL2::2xNLSTagRFP

Table 3. 2. List of strains used in this chapter

CZ2060	juIs137 [p*flp-13*::SNB-1::GFP] X
Not frozen	juIs137 X; wdEx1157 [p*flp13*::dyn-1F::SL2::mCherry; p*flp-13*::dyn1R::SL2::3xNLS::GFP; p*myo-2*::RFP]
NC3740	juIs137 X; wdEx1169 [p*flp-13*::dyn-1::SL2::2xNLS::TagRFP; p*str-1*::GFP]
NC3801	juIs137 X; wdEx1181 [p*flp-13*::dyn-1AAA::SL2::nuclearTagRFP]
NC1852	*unc-55(e1170)* I; juIs1 [p*unc-25*::SNB-1::GFP; lin-15+] *eri-1 (mg366)* IV
ZM54	hpIs3 [p*unc-25*::SYD-2::GFP; lin-15+] X
NC1849	*unc-55(e1170)* I; hpIs3 X
NC3535	*unc-55(e1170)* I; *unc-26 (s1719)* IV; hpIs3 X
NC3629	*rab-3 (ox785[GFP*-FLP-ON::RAB-3 + loxp UNC-119+ loxp]) II; *unc-119* III; wdEx1127 [p*flp-13*::flippase; p*myo-2*::RFP]
NC3683	*rab-3 (ox785)* II; *unc-8 (tm5052)* IV; wdEx1127 [p*flp-13*::flippase; p*myo-2*::RFP]
NC3742	*sdpn-1 (ok1667) X; rab-3 (ox785)* II; wdEx1127 [p*flp-13::flippase;* p*myo-2*::RFP*]*
NC3840	*unc-8 (tm5052) IV; sdpn-1 (ok1667) X; rab-3 (ox785) II;* wdEx1127 [p*flp-13*::flippase; p*myo-2*::RFP]
NC3371	*eri-1(mg366)* juIs1 *[punc-25*::SNB::GFP*; lin-15+]* IV ; Ex[p*ttr-39*::UNC-8, punc-25::mCherry::RAB-3; pmyo-2::RFP]
NC3364	*sdpn-1(ok1667) juIs137 [pflp13::SNB1::GFP] X; Ex[pflp13::SDPN-1a::mCherry; pstr-1::GFP]*
NC3316	*toca-1(tm2056) X;* wdEx1017[p*flp13*::TOCA1a:mCherry]
NC3571	wdEx1114[p*flp-13*::TOCA-1::mCherry; p*flp-13*::TAX-6::GFP]
NC3591	*toca-1(tm2056)* juIs137 [p*flp-13*::SNB-1::GFP] X; wdEx1115 [p*flp13*::TOCA-1::mCherry]
NC3750	*toca-1(tm2056) X; rab-3 (ox785) II; wdEx1127 [Pflp-13::flippase; pmyo-2::RFP]*
NC3751	*unc-8(tm5052) IV; toca-1(tm2056) X; rab-3 (ox785) II;* wdEx1127 [P*flp-13*::flippase; pmyo-2::RFP]
NC3609	*toca-1(tm2056)* X; wdEx1124 [p*flp-13*::TOCA-1::mCherry; p*flp-13*::LifeAct::GFP; pmyo-2::RFP]
NC3603	wdEx1122 [p*flp-13*::ARX-5::GFP; p*flp-13*::mCherry::RAB-3; p*myo-2*::RFP]
NC3529	juIs137 [p*flp-13*::SNB-1::GFP] X; wdEx1114 [p*flp-13*::ARX-5F::SL2::mCherry; p*flp-13*::ARX-5R::SL2::3NLSxGFP; p*myo-2*::RFP]
NC3372	juIs137 X; wdEx1043 [p*ttr-39*::VCA::SL2::mCherry, p*myo-2*::RFP]
NC3638	*rab-3 (ox785) II*; wdEx1131 [p*flp-13*::flipasse::SL2::LifeAct::mCherry; p*myo-2*::RFP]
NC3651	*toca-1(tm2056)* X; *rab-3 (ox785)* II; wdEx1131 [p*flp-13*::flipasse::SL2:: LifeAct::mCherry; p*myo-2*::RFP]
To freeze	*unc-8 (tm50526)* IV; *rab-3 (ox785)* II; wdEx1131 [p*flp-13*::flipasse::SL2:: LifeAct::mCherry; p*myo-2*::RFP]
NC3698	juIs137 [p*flp-13*::SNB-1::GFP] X; wdEx1158 [p*flp-13*::RAB1.11 sense::SL2::mCherry; p*ttr-39*::RAB11.1 antisense::SL2::3xNLSGFP; p*myo-2*::RFP]

NC3743	*rab-3 (ox785) II; unc-119 (ed3);* wdEx [P*flp-13*::flippase; P*flp-13*::TagRFP::RAB-11.1]
PHX2894	*rab-3 (syb2844* [Dendra-2 FLP-ON]*)* II
NC3758	*rab-3 (syb2844)* II; wdEx1127 [p*flp-13*::flippase; p*myo-2*::RFP]; wdEx1170 [p*flp-13*::rab-11.1 sense::SL2::nuclearGFP; p*ttr-39*::rab-11.1 antisense::nuclearRFP]
NC3719	*rab-3 (syb2844)* II; wdEx1127 [p*flp-13*::flippase; p*myo-2*::RFP]
NC3797	*rab-3 (syb2844)* II; *unc-8(tm5056) IV;* wdEx1127 [p*flp-13*::flippase; p*myo-2*::RFP]
NC3762	*rab-3 (syb2844)* II; *toca-1(tm2056) X;* wdEx1127 [p*flp-13*::flippase; p*myo-2*::RFP]
NC3617	*lin-15(0) X*; wdIs124 [p*flp-13*::CLA-1s::GFP; lin-15(+)] II?;
NC3623	*toca-1(tm2056) X*; wdIs124[p*flp-13*::CLA-1s::GFP; lin-15(+)]
NC3706	*sdpn-1(ok1667)* X; wdIs124[p*flp-13*::CLA-1s::GFP; lin-15(+)]
NC3694	*lin-15(0) X* ; wdIs124 [p*flp-13*::CLA-1s::GFP; *lin-15(*+) II?; wdEx1157 [p*flp-13*::dyn-1F::SL2::mCherry; p*flp-13*::dyn1R::SL2::3xNLS::GFP; p*myo-2*::RFP]
NC3645	wdIs124 [p*flp-13*::CLA-1s::GFP; *lin-15*(+)] ;wdEx1114 [p*flp-13*::ARX-5F::SL2::mCherry; p*flp-13*::ARX-5R::SL2::3NLSxGFP; p*myo-2*::RFP]
NC3721	wdIs124 [p*flp-13*::CLA-1s::GFP; *lin-15*(+)] II?; wdEx1158 [p*flp-13*::RAB11.1 sense::SL2::mCherry; p*ttr-39*::RAB11.1 antisense::SL2::3xNLSGFP; pmyo-2::RFP]

RESULTS

Calcineurin functions downstream of UNC-8 to trigger presynaptic disassembly

In results described in Chapter II, we showed that CaN/TAX-6 enhances the strength of evoked Ca^{++} transients in remodeling DD neurons (Figure 2.8). We have also shown that CaN/TAX-6 localizes to the DD neuron presynaptic termini throughout the remodeling period (Figure 2.7). Together, these findings are consistent with the idea that CaN/TAX-6 functions in a positive feedback loop with ENaC/UNC-8 and VGCC/UNC-2 to elevate intracellular Ca^{++} for disassembly of the DD presynaptic apparatus (Miller-Fleming et al., 2016) (Figure 3.1C). This model also predicts that a loss-of-function mutation in *CaN/tax-6* should abrogate ENaC/UNC-8-dependent presynaptic disassembly. In the wild type, Ventral D (VD) GABAergic neurons do not express ENaC/UNC-8 and do not undergo synaptic remodeling. Forced expression of ENaC/UNC-8 in VD neurons, however, is sufficient to drive the removal of the

Synaptobrevin/SNB-1::GFP from VD synapses (Figure 3.1A) (Miller-Fleming et al, 2016). We exploited this experimental paradigm to confirm that genetic ablation of CaN/*tax-6* prevents UNC-8-dependent elimination of VD synapses when treated with Blank-RNAi (Figure 3.1B). In addition to amplifying Ca^{++} import, potentially by enhancing UNC-8 channel activity, CaN/TAX-6 could also regulate additional downstream effectors for presynaptic disassembly (Figure 3.1C).

One of the known roles for CaN is to trigger Activity-Dependent Bulk Endocytosis (ADBE) during periods of high synaptic activity (Figure 3.1D). In this mechanism, intense activity elevates synaptic calcium which turns on CaN to function as a Ca^{++}-dependent phosphatase for dephosphorylation of a well characterized group of synaptic proteins known as dephosphins (Emma L. Clayton & Cousin, 2009; Cousin et al., 2001). For example, CaN dephosphorylates residues in a conserved phospho-box near the C terminus of the GTPase, Dynamin. The dephosphorylation of dynamin promotes the formation of the dynamin-syndapin complex (Anggono et al., 2006). Through its SH3 domain, Syndapin recruits components for the polymerization of branched-actin, which drives membrane invagination to form presynaptic bulk endosomes (Kessels & Qualmann, 2002). The canonical role of ADBE is to recycle large amounts of membrane for the local replenishment of synaptic vesicles for neurotransmission. Throughout this chapter we are going to test key predictions of this model to determine if a mechanism similar to ADBE also drives the elimination of presynaptic domains in remodeling DD synapses.

Dephosphins are required for presynaptic GABAergic remodeling

During ADBE, CaN targets dephosphins to drive bulk endocytosis of the presynaptic membrane (Emma L Clayton et al., 2007). If an ADBE-like mechanism is activated by CaN/TAX-6 in remodeling GABAergic neurons, then dephosphins should be necessary for synapse elimination. To test this prediction, we used RNAi to ask if conserved dephosphins (e.g.,

Amphiphysin/*amph-1*, Epsin/*epn-1*, Eps15/*ehs-1*, Synaptojanin/*unc-26i* and AP180/*unc-11*) are required for synapse elimination. For this experiment, we took advantage of the forced elimination

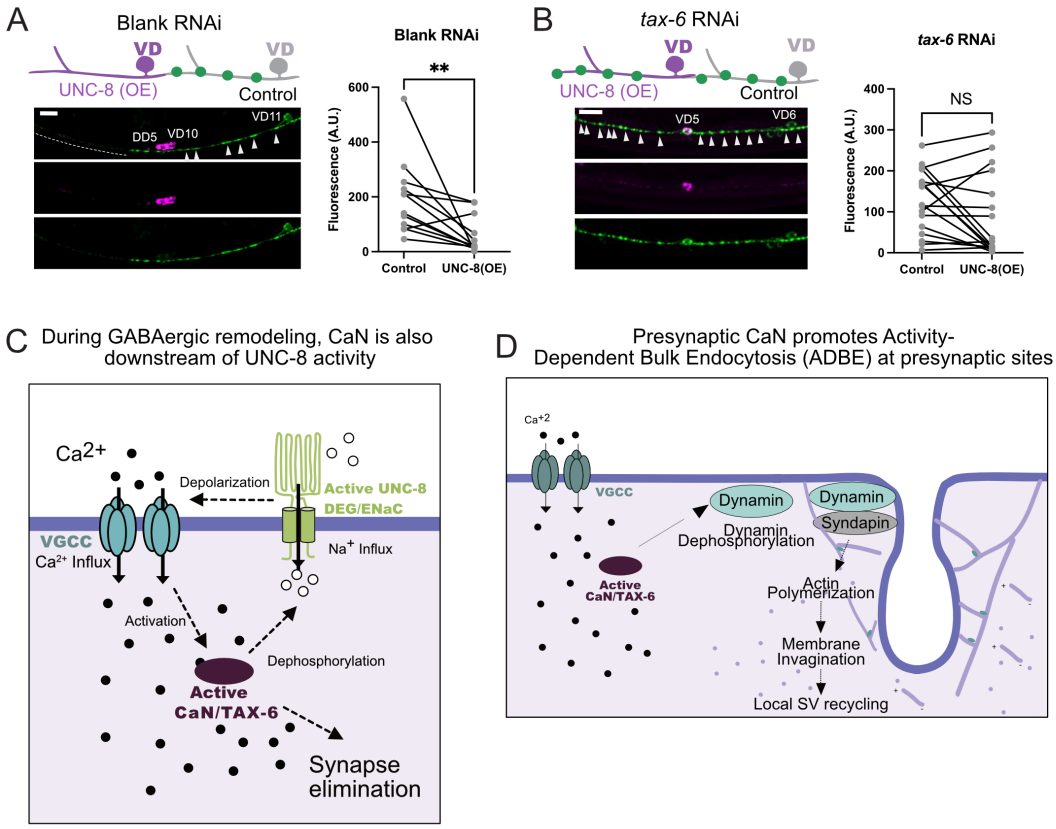

Figure 3. 1. CaN/TAX-6 functions downstream of UNC-8 to promote synaptic disassembly.

A. (Left) (L4 animals) Blank RNAi-treated VD neuron (VD11, gray) with prominent SNB-1::GFP puncta (arrowheads) vs anterior region of UNC-8 (OE) VD neuron (V10, magenta) with fewer SNB-1::GFP puncta (dashed line). (Right) Paired analysis of neighboring cells in animals treated with Blank RNAi: Control VDs (196 ± 139 A.U, n=12) and UNC-8 (OE) VD neurons (56.7 ± 67 A.U., n=12). Wilcoxon matched-pairs signed rank test, ** p = 0.0024. (B) (left) *tax-6* RNAi-treated UNC-8(OE) VD neuron (VD5, magenta) vs adjacent control VD neuron (VD6, gray) both with prominent SNB-1::GFP puncta (arrowheads). (Right) Paired analysis of neighboring VD neurons treated with *tax-6* RNAi: Control VDs (126 ± 76 A.U., n=17) and UNC-8 (OE) VD neurons (86 ± 99 A.U., n=17). Wilcoxon matched-pairs signed rank test, p = 0.16. NS is Not Significant. Scale bars = 10 µm.
C. Model depicting a positive-feedback loop involving presynaptic VGCC (Voltage Gated Calcium Channel, CaN/TAX-6 and ENaC/UNC-8 that elevates presynaptic Ca^{++} in remodeling boutons.
D. For Activity-Dependent Bulk Endocytosis (ADBE), intense synaptic activity elevates intracellular Ca^{++} to activate CaN/TAX-6. Dephosphorylation of dynamin by CaN promotes the formation of the dynamin-syndapin complex which localizes to the membrane to drive branched actin polymerization for bulk endosome formation and synaptic vesicles (SV) recycling (Emma L. Clayton & Cousin, 2009).

of VD synapses that occurs in *unc-55* mutants. Normally the UNC-55 COUP-TF transcription factor functions in VD neurons to block the canonical remodeling program. As a consequence, in wild-type adults, VD synapses are located in the ventral cord and DD GABAergic synapses are positioned on the dorsal side (Figure 3.2A). In *unc-55* mutants, however, VD neurons are forced to remodel, thus resulting in the elimination of all GABAergic synapses from ventral muscles (Figure 3.2B) (H. Zhou & Walthall, 1998). If a gene is necessary for disassembly of GABA synapses, a mutation that disrupts it should suppress the UNC-55 phenotype by impeding the elimination of ventral synapses (Figure 3.2C) (Petersen et al., 2011). In this case, we used RNAi or genetic mutants to knock down dephosphins in *unc-55* mutants and assessed the number of GABAergic synapses in the ventral nerve cord labeled with either Synaptobrevin/SNB-1::GFP or the active zone protein liprin-alpha/SYD-2::GFP. This candidate-based screen determined that Amphiphysin/*amph-1*, Epsin/*epn-1* and Eps15/*ehs-1* normally promote GABAergic presynaptic elimination. A genetic mutant of the dephosphin, Synaptojanin/*unc-26*, also suppressed the Unc-55 remodeling phenotype. Notably, the dephosphin AP180/*unc-11* and the clathrin-related proteins, the clathrin light chain/*clic-1* and the clathrin adaptor AP2/*dpy-23*, are dispensable for the removal of remodeling GABAergic synapses (Figure 3.2D). Thus, our findings support the hypothesis that conserved CaN targets, (e.g, dephosphins) are required for a clathrin-independent endocytic mechanism that dismantles the presynaptic apparatus of remodeling GABAergic neurons.

Phospho-resistant dynamin functions in DD neurons to promote presynaptic disassembly.

The GTPase, dynamin, is a known target of CaN and functions as a key effector of both ADBE and the canonical clathrin-dependent mechanism for recycling synaptic vesicle membrane at active synapses (Chanaday et al., 2019). To circumvent

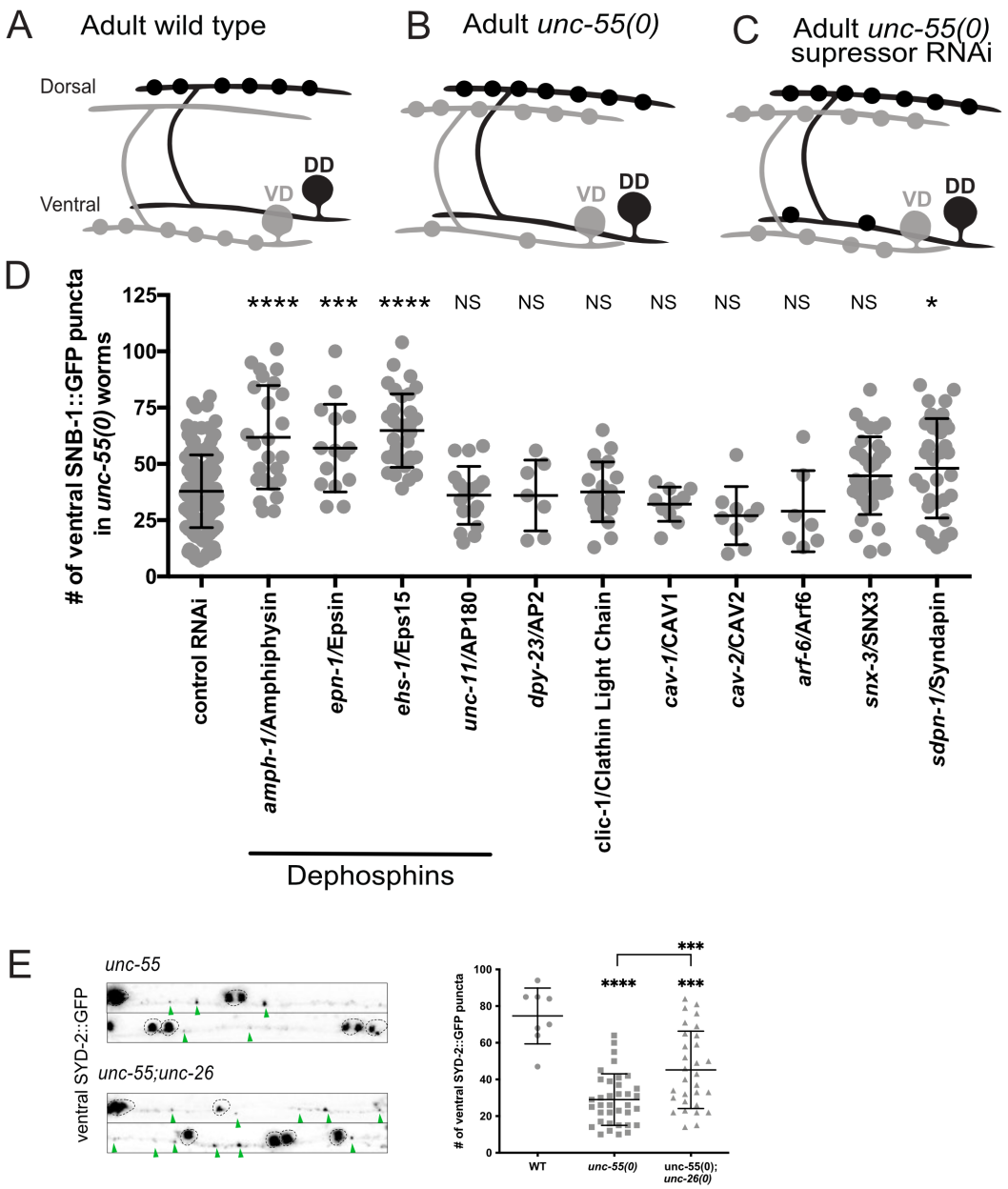

Figure 3. 2. Dephosphins are required for GABAergic neuron synaptic remodeling

A-C. Presynaptic boutons for DD (black) and VD (gray) neurons in adult animals. (**A**) In wild-type animals, DD boutons localize to the dorsal nerve cord and VD boutons are positioned on the ventral side. (**B**) In *unc-55* mutant animals, VD neurons ectopically remodel, eliminating ventral synapses and locating boutons on the dorsal side. (**C**) RNAi knockdown of genes required for the Unc-55 phenotype (i.e., "Suppressor genes"), results in the retention of ventral GABAergic synapses.

D. Number of ventral presynaptic boutons (SNB-1::GFP) in *unc-55* mutant animals treated with control RNAi (37.9 ± 16.2, n=153) or RNAi knockdown of dephosphins: *amph-1* (61.8 ± 22.9, n=25), *epn-1* (57.0± 19.5, n=15) and *ehs-1* (64.8 ± 16.3, n=33). Knockdown of regulators of clathrin-mediated endocytosis: *unc-11* (36.1 ± 12.9, n=18), *dpy-23* (36.0 ± 15.7, n=7), *clic-1* (37.6 ± 13.2, n=20). Knockdown of caveolins: *cav-1* (32.1 ± 7.6, n=10) and *cav-2* (27.0 ± 12.9, n=9).

Knockdown of *arf-6* (29.0 ± 18.1, n=7), retromer component *snx-3* (44.8 ± 17.3, n=34) and *sdpn-1* (48.1 ± 22.1, n=35). One-Way ANOVA with Dunnett's multiple comparison test. **** <0.0001, *** <0.001, * <0.05,NS is Not Significant.

E. Additional ventral SYD-2::GFP puncta are retained in adult *unc-55* mutants animals (29 ± 14.1, n=36) when *unc-26* is mutated (45.2 ± 21.1, n=30). Wild-type animals (74.6 ± 15.2, n=8) have more ventral SYD-2::GFP puncta than *unc-55; unc-26.* One-Way ANOVA with Dunnett's multiple comparison test. **** <0.0001 and *** <0.001.

the lethal phenotype of dynamin/*dyn-1* knockdown in *C. elegans*, we devised a cell specific RNAi (csRNAi) strategy for selective knockdown of *dyn-1* in DD neurons (Figure 3.3A). Removal of ventral SNB-1::GFP was impaired in *dyn-1(csRNAi)* treated DD neurons thus suggesting that dynamin normally functions in DD neurons to promote presynaptic disassembly (Figure 3.3B). Because CaN-dependent activation of dynamin involves the dephosphorylation of residues in a conserved "phospho-box" domain, we searched the phospho-proteome of *C. elegans* to identify residues on DYN-1 that are phosphorylated in vivo (Zielinska, Gnad, Jedrusik-bode, Wis, & Mann, 2009). This work showed that DYN-1 can be phosphorylated at three amino acid residues (S53, Y55, S59) in a proline-rich C-terminal domain (Figure 3.3C). To test if the dephosphorylation state of DYN-1 modulates its role in DD remodeling, we forced expression of a phospho-resistant mutant (S53A, Y55A and S59A) (dyn-1AAA::SL2::2xNLS::TagRFP) in DD neurons, which our model predicts should accelerate the rate of presynaptic disassembly (Figure 3.3D). This experiment showed that ectopic expression of the DYN-1AAA results in precocious removal of presynaptic SNB-1::GFP from remodeling DD neurons. In contrast, over-expression of wild-type DYN-1 (dyn-1::SL2::2xNLS::TagRFP) or DYN-1(OE) does not enhance the elimination of SNB-1::GFP from DD synapses (Figure 3.3G). These results confirm that dynamin can act cell-autonomously in DD neurons and that its dephosphorylation accelerates removal of DD synapses. Thus, our findings are consistent with the idea that CaN dephosphorylates dynamin and additional dephosphins to drive presynaptic disassembly in remodeling DD neurons. In addition, because ADBE depends on CaN-dependent activation of dynamin, our results substantiate the hypothesis that a bulk endocytic mechanism drives DD synaptic remodeling. Importantly, genes that are involved in other clathrin-independent endocytic mechanisms, e.g., caveolin or Arf6, are dispensable for synapse elimination of GABA neurons (Figure 3.2D). In sum, our evidence points to an endocytic mechanism that depends on regulators that also control ADBE but that results in

the strikingly different outcome of effectively dismantling the presynaptic domain rather than sustaining a local recycling mechanism for continued neurotransmission.

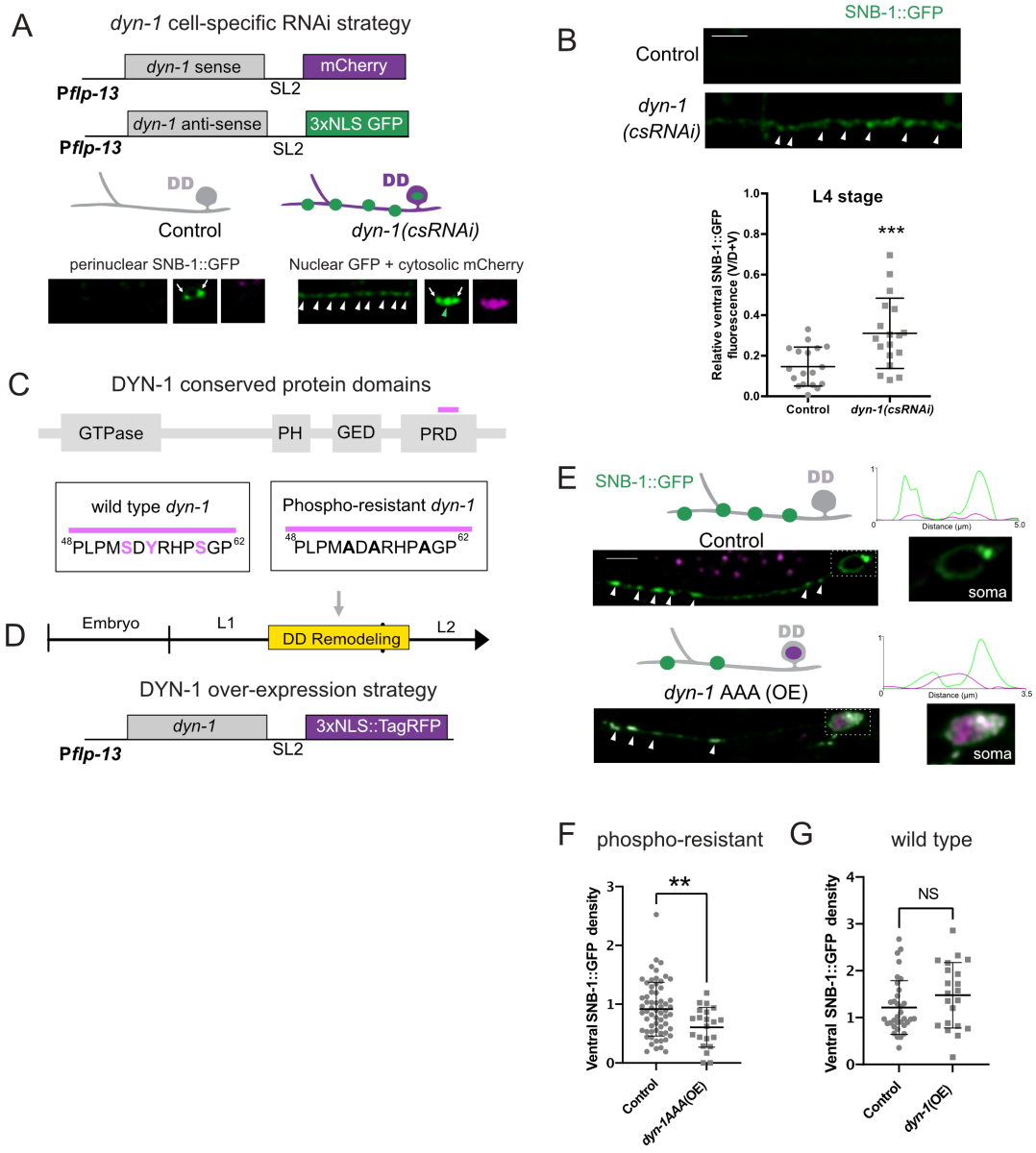

Figure 3. 3. Cell autonomous dynamin activity is required for presynaptic disassembly in remodeling DD neurons.

A. (Top) Transgenic strategy for cell-specific knockdown of *dyn-1(csRNAi)*. (Below) Control show perinuclear SNB-1::GFP (arrows). Knockdown cells are labeled with cytosolic mCherry, nuclear GFP (green arrowhead), perinuclear SNB-1::GFP (arrows) and retain SNB-1::GFP puncta (white arrowheads) in the ventral nerve cord
B. (Top) Representative images of ventral nerve cords of control vs *dyn-1(csRNAi)* treated DD neurons. White arrowheads denote residual SNB-1::GFP puncta (L4 stage). (Below) Fraction of SNB-1::GFP fluorescence in ventral DD neurites (V/V+D = Ventral/Ventral + Dorsal) showing that

dyn-1(csRNA) treatred DD neurons retain a greater fraction of ventral SNB-1::GFP fluorescence (0.31 ± 0.2, n=18) than controls (0.15 ± 0.1, n=18). Unpaired t-test, *** is p = 0.0006.
C. Schematic of conserved DYN-1 protein domains. Pink bar denotes location of putative dynamin phospho-box sequence (Zielinska et al., 2009) with phosphorylatable residues (S53, Y55, S59) in wild type and converted to Alanine (A) in phospho-resistant *dyn-1* mutant phospho-box sequence.
D. Synchronized larvae were imaged during the remodeling window (arrow) to assess ventral SNB-1::GFP. DD neurons that overexpress dynamin are labeled with nuclear-localized TagRFP (magenta).
E-G. (E) SNB-1::GFP puncta (green) in DD neurons for control (top) and (bottom) over-expression of phospho-resistant DYN-1 mutant protein [*dyn-1*AAA(OE)]. Insets (right) show tagRFP-labeled cell soma (magenta) of dyn-1AAA(OE) DD neurons. White arrowheads label SNB-1::GFP puncta. (F) (F) Over-expression of phospho-resistant DYN-1 [*dyn-1AAA(OE)*] accelerates SNB-1::GFP removal (0.61 ± 0.3, n=21) vs control DD neurons (0.92 ± 0.5, n=62). (G) Overexpression of wild type dynamin [dyn-1(OE)} (1.47 ± 0.7, n=21) does not result in fewer SNB-1::GFP puncta vs control DD neurons (1.21 ± 0.6, n=34). Density = SNB-1 puncta/10 micron.

Syndapin functions in a common pathway with UNC-8 to remove synaptic vesicle components in remodeling DD neurons.

Syndapin/SDPN-1 is an F-BAR protein that interacts with the plasma membrane through its F-BAR domain and also recruits downstream effectors through its SH3 domain (Figure 3.4A). During ADBE, Syndapin and Dynamin form a complex on the plasma membrane to promote the polymerization of branched-actin networks during endocytosis (E. L. Clayton et al., 2009; Kessels & Qualmann, 2004). Consistent with the idea that Syndapin also functions with Dynamin to drive synaptic remodeling, we observed that RNAi knockdown of *sdpn-1* in *unc-55* mutants impairs the removal of SNB-1::GFP from ventral GABAergic synaptic terminals (Figure 3.2D). Similarly, the elimination of endogenous GFP::RAB-3 from ventral neurites of DD neurons is disrupted in *sdpn-1* mutants (Figure 3.4B). Notably, removal of GFP::RAB-3 from remodeling DD synapses is impaired in *unc-8* mutants (Figure 3.4B) as predicted by our hypothesis that *unc-8* triggers a downstream bulk endocytic mechanism to dismantle the presynaptic domain. (Figure 3.1C-D). To challenge the idea that SDPN-1 functions in a common pathway with UNC-8, we created an *unc-8; sdpn-1* double mutant. This experiment confirmed that the ectopic retention of GFP::RAB-3 puncta in DD neurons of *unc-8; sdpn-1* double mutants is not significantly different from that of either the *unc-8* or *sdpn-1* single mutants (Figure 3.4B). Together, these findings argue that UNC-8 and SDPN-1 act in a common genetic pathway to remove synaptic vesicles in remodeling DD neurons.

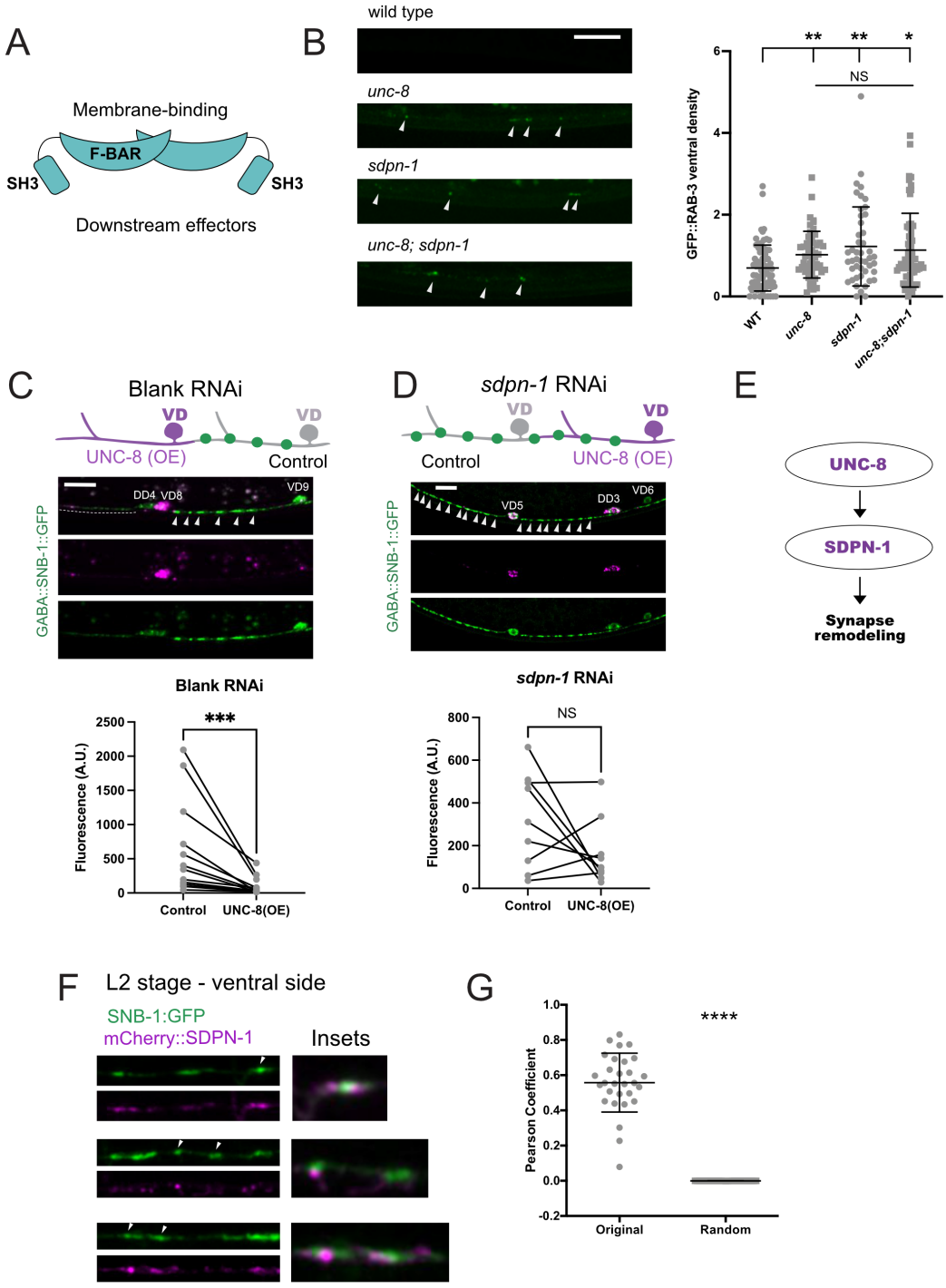

Figure 3. 4. The F-Bar protein, syndapin functions downstream of UNC-8

A. Protein domains common to F-BAR proteins like Syndapin/SDPN-1 and TOCA-1.
B. SDPN-1 and UNC-8 function in a common genetic pathway. (Left) Residual endogenous GFP::RAB-3 puncta (arrowheads) in ventral DD neurites in wild type, *unc-8*, *sdpn-1* and *unc-8; sdpn-1* double mutants in early L4 larvae. (Right) Ventral GFP::RAB-3 density (puncta/10 micron) is not significantly different among *unc-8* (1.02 ± 0.5, n=51), *toca-1* (1.22 ± 0.9, n=46) and *unc-8;*

toca-1 double mutants (1.13 ± 0.9, n=62) mutants but is elevated in comparison to wild type (0.69 ± 0.6, n=73).

C-D. (Top) Control VD neurons (gray) with anteriorly placed SNB-1::GFP puncta (white arrowheads) vs UNC-8 (OE) VD cells (magenta) in which SNB-1::GFP puncta are reduced (dashed line). (D) Treatment with *sdpn-1* RNAi results in retention of SNB-1::GFP puncta in UNC-8(OE) VD neurons. (C) This effect is not observed with the blank RNAi condition. (Bottom) **(C)** Paired analysis of neighboring cells [control vs unc-8(OE)] in blank RNAi animals: Control VDs (608 ± 688 A.U., n=13) and UNC-8 (OE) VD neurons (94.9 ± 129 A.U., n=13). Wilcoxon matched-pairs signed rank test, *** p = 0.0002. **(D)** Paired analysis of neighboring cells [control vs *unc-8(OE*)] in *sdpn-1* RNAi animals: Control VDs (321 ± 266 A.U., n=9) and UNC-8 (OE) VD neurons (163 ± 156 A.U., n=9). Wilcoxon matched-pairs signed rank test, p = 0.25. NS is Not Significant. Scale bar = 10 µm.

E. Genetic model depicting UNC-8 upstream of SDPN-1 in common pathway to promote DD synapse elimination.

F-G. (F) Airyscan imaging detects SDPN-1::mCherry (magenta) localized with presynaptic clusters labeled with SNB-1::GFP (green) in remodeling L2 stage DD neurons. (G) 3D Z-stacks were subjected to JACoP analysis, Pearson Coefficient between SDPN-1::mCherry and SNB-1::GFP signal is 0.56 ± 0.2 for original images and 0 ± 0.0004 for a randomized array of pixels in 3D. Mann Whitney test, *** is $p < 0.0001$. N = 29 boutons.

Our model also predicts that SDPN-1 functions downstream of UNC-8 to drive presynaptic disassembly (Figure 3.1C-D). To test this idea, we asked if SDPN-1 is required for the ectopic removal of ventral GABAergic synapses arising from forced expression of UNC-8 in VD neurons. As noted above, in the wild type, VD neurons do not express UNC-8 and normally establish stable synapses with ventral muscles. UNC-8 over-expression or UNC-8(OE) in VD neurons treated with blank-RNAi, however, is sufficient to remove SNB-1::GFP from ventral VD presynaptic domains (Miller-Fleming et al., 2016) (Fig. 3.4C). This effect is abrogated, however, by RNAi knockdown of *sdpn-1* (Figure 3.4D). This result offers further support for the idea that SDPN-1 acts downstream of UNC-8 for synapse elimination. Consistent with a presynaptic role for SDPN-1 for DD synaptic disassembly, SDPN-1::mCherry is closely associated with the presynaptic marker SNB-1::GFP during the remodeling window (Figure 3,4F-G). In summary, Results in this section are consistent with a model in which UNC-8 drives synaptic disassembly in a pathway that involves the F-BAR protein syndapin/SDPN-1 and thus suggests that a bulk endocytic mechanism resembling ADBE is required for synapse elimination in remodeling DD neurons.

The presynaptic F-BAR protein TOCA-1 functions in parallel to UNC-8 to promote synapse elimination

Having established that syndapin/SDPN-1 drives DD synaptic remodeling, we utilized the *unc-55* remodeling paradigm in a RNAi screen to test other F-BAR proteins for potential roles in remodeling. This approach revealed that RNAi knock down of the F-BAR protein-encoding gene, *toca-1*, impaired the removal of SNB-1::GFP from ventral synapses in remodeling GABAergic

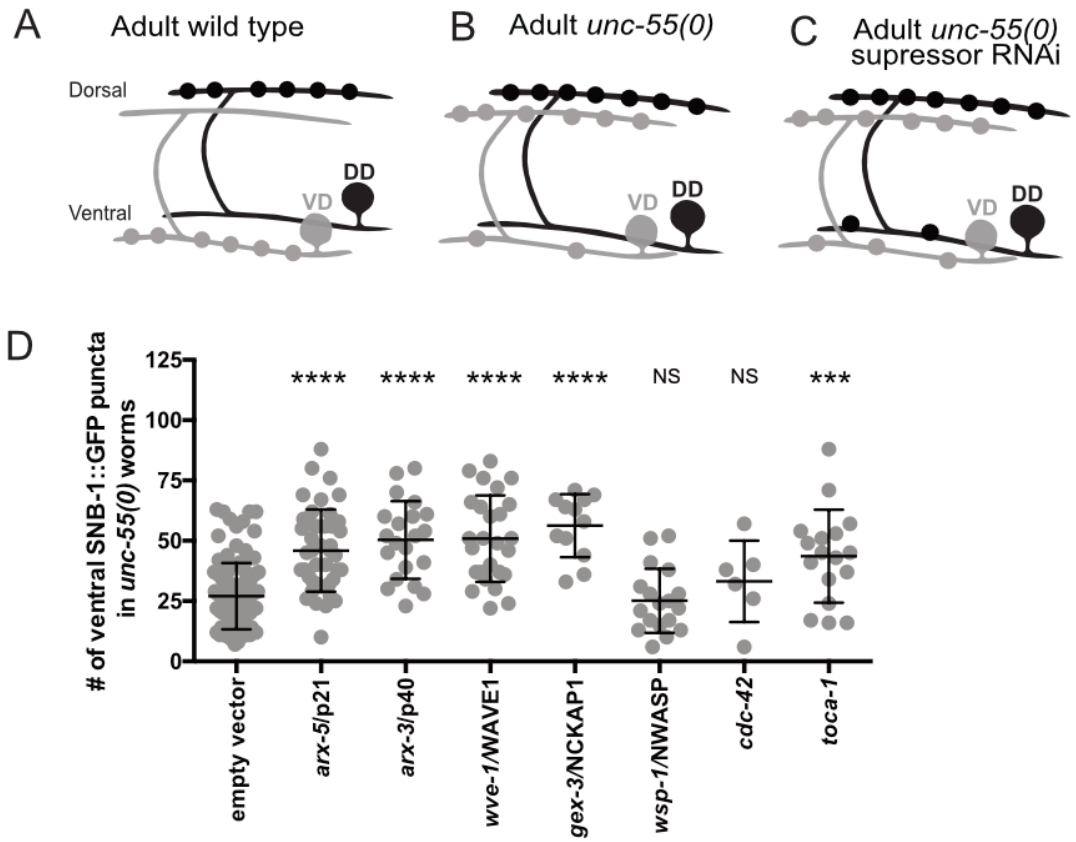

Figure 3. 5. Branched-actin promotes GABAergic neuron synaptic remodeling

A-C. Presynaptic boutons for DD (black) and VD (gray) neurons in adult animals. (**A**) In wild-type animals, DD boutons localize to the dorsal nerve cord and VD boutons are positioned on the ventral side. (**B**) In *unc-55* mutant animals, VD neurons ectopically remodel, eliminating ventral synapses and locating boutons on the dorsal side. (**C**) RNAi knockdown of genes required for the Unc-55 phenotype (i.e., "Suppressor genes"), results in the retention of ventral GABAergic synapses.

D. Number of ventral synapses in *unc-55* mutant animals subjected to control RNAi (27.0 ± 13.7, n=103) or RNAi knockdown of Arp2/3 subunits, *arx-5* (45.9 ± 16.9, n=43) and *arx-3* (50.3 ± 16.1, n=21). Knockdown of subunits of the Wave Regulatory Complex, *wve-1* (50.9 ± 17.9, n=26) and *gex-3* (56.3 ± 13.0, n=12). Knockdown of *WASP/wsp-1* (25.1 ± 13.3, n=18), GTPase *cdc-42* (33.2 ± 16.9, n=6) and F-BAR protein *toca-1* (43.6 ± 19.3, n=17). One-Way ANOVA with Dunnett's multiple comparison test. **** <0.0001, *** <0.001, NS is not significant.

neurons (Figure 3.5D). TOCA-1 is highly abundant in the nervous system of *C. elegans* (Figure 3.6A) and its mammalian homologue is largely expressed in the developing brain (Kakimoto, Katoh, & Negishi, 2006), where it has been shown to regulate neurite extension and endocytosis (Bu, Chou, Lim, Sudhaharan, & Ahmed, 2009; Fricke et al., 2009). Toca-1 was originally identified as a Transducer Of Cdc42 Activity, hence TOCA, for activating N-WASP and stimulating branched-actin polymerization (Ho et al., 2004). Thus, we found surprising that CDC-42 was dispensable for GABAergic synapse elimination (Figure 3.5D). To further understand the contribution of TOCA-1 during DD remodeling, we decided to explore the hypothesis that it promotes branched-actin polymerization at dismantling DD boutons.

A role for TOCA-1 in synapse elimination is consistent with our finding that TOCA-1::mCherry is enriched in DD axons throughout development (Figure 3.6B-C) and localizes to remodeling DD boutons with CaN/TAX-6::GFP (Figure 3.6D). In adult DD presynaptic terminals, TOCA-1::mCherry puncta flank synaptic boutons labeled with SNB-1::GFP (Figure 3.6E). Interestingly, centroid analysis revealed that TOCA-1::mCherry puncta are located ~300 nm of SNB-1::GFP labeled presynaptic region, which parallels the perisynaptic position of DYN-1 adjacent *C. elegans* active zones (Weimer et al., 2006). Notably, TOCA-1::mCherry also localizes to nascent dendritic spines as ventral DD neurites are transformed into postsynaptic dendrites during remodeling (Figure 3.6D''). Consistent with this observation, *toca-1* mutants have decreased numbers of dendritic spines (See Chapter V) (Cuentas-Condori et al., 2019). Thus, TOCA-1 might have pleiotropic roles in regulating membrane remodeling of both presynaptic and postsynaptic terminals in DD neurons.

To test if TOCA-1 is required for the native DD remodeling program, we monitored endogenous GFP::RAB-3 elimination from ventral DD synapses in *toca-1* mutants. Surprisingly, at the early L4 stage, the density of ventral GFP::RAB-3 puncta in *toca-1* mutants is not different

from the wild-type (WT) control although we also found that *toca-1* mutants have delayed GFP::RAB-3 removal at the L2 stage (See below, Figure 3.11). In contrast, *unc-8*; *toca-1* double

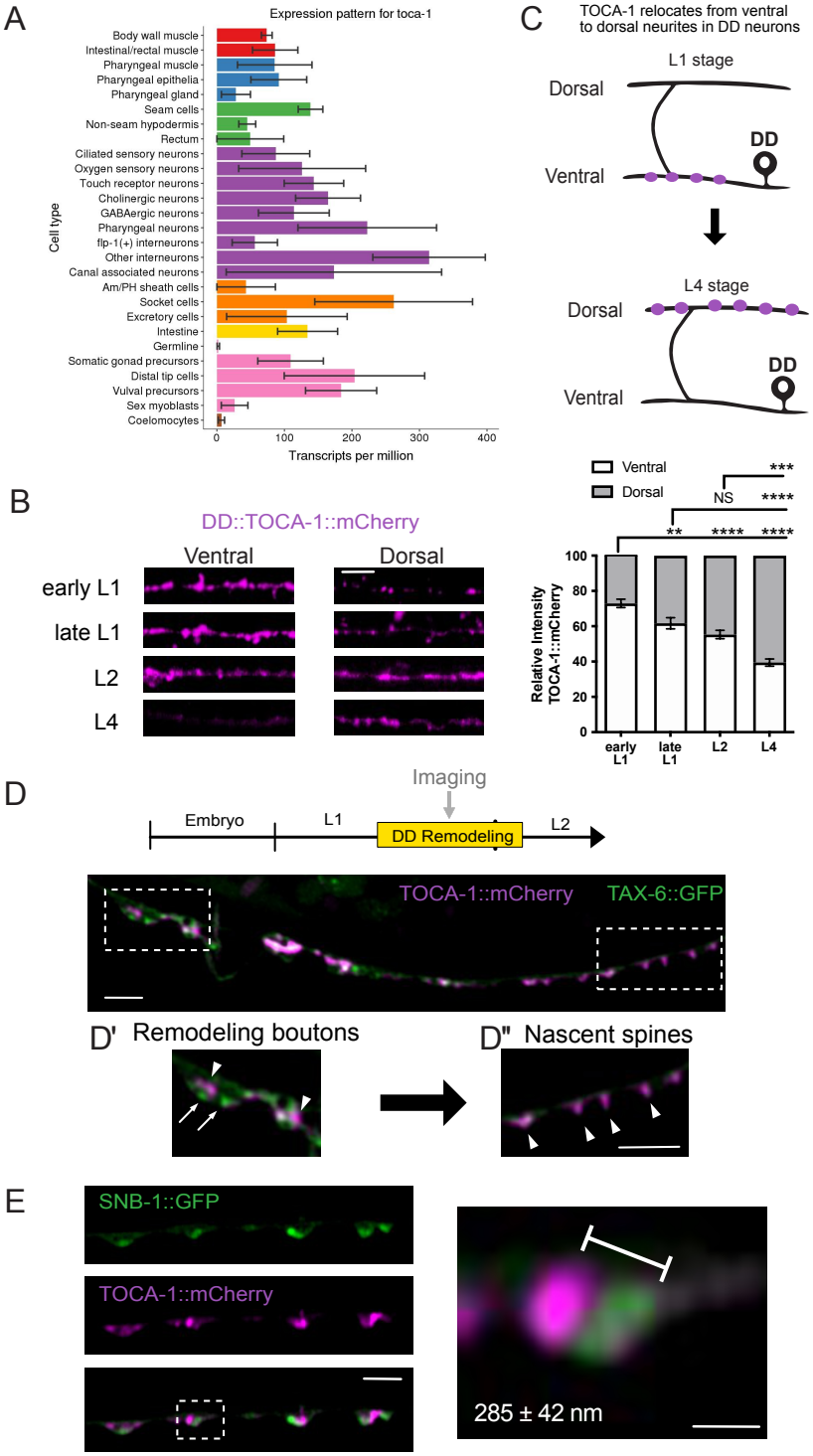

Figure 3. 6. TOCA-1 localizes to presynaptic boutons and remodels

A. Bar graph of *toca-1* expression across different tissues at the L2 stage. *toca-1* is highly expressed in neuronal tissues (purple bars). Data extracted from GExplorer: http://genome.sfu.ca/gexplore/

B-C. In DD neurons, TOCA-1::mCherry remodels during development. **(B)** (Left) Representative images of TOCA-1::mCherry puncta (magenta) across development on the ventral and dorsal nerve cords of wild type animals. which translocate from the ventral nerve cord (early L1 stage) to the dorsal nerve cord (L4 stage). (Right) Quantification of relative TOCA-1::mCherry fluorescence in early L1 (72.9 ± 11.9, n=25), late L1 (61.7 ± 13.9, n=19), L2 (55.3 ± 9.7, n=17) and L4 (39.4 ± 8.2, n=17) larvae. One-Way ANOVA with multiple comparison test, ** $p < 0.01$, *** $p < 0.001$ and **** $p < 0.0001$. Scale bar = 2 μm.

D. Airyscan imaging of DD neurons during remodeling (top) detects enrichment of TAX-6::GFP in remodeling boutons (D') and localization of TOCA-1::mCherry to remodeling boutons (D') and nascent dendritic spines (D''). Scale bar = 2 μm.

E. AiryScan imaging reveals that TOCA-1::mCherry (magenta) localizes to perisynaptic regions within 285 ± 42 nm of SNB-1::GFP (green), N = 209 boutons. Dashed box denotes region of inset to the right. L4 stage larvae. Scale bar = 2 μm.

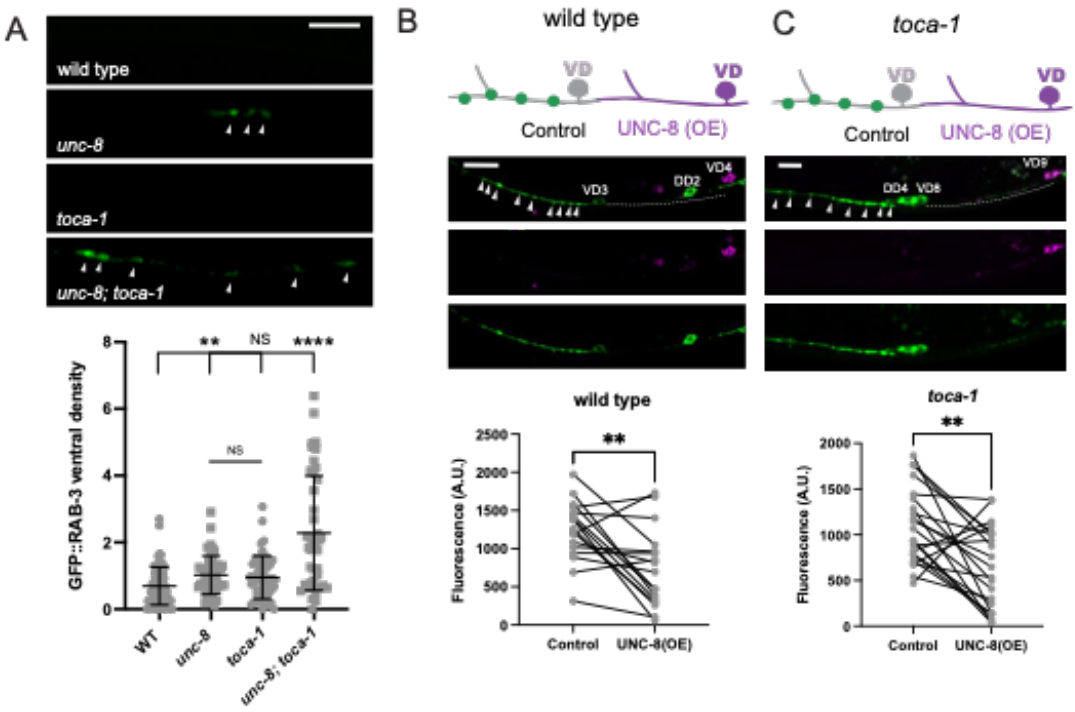

Figure 3. 7. TOCA-1 functions in parallel to UNC-8 to promote synaptic disassembly

A. (Top) Images depict endogenous GFP::RAB-3 puncta in DD neurons (white arrowheads) in the ventral nerve cord of wild type, single mutants of *unc-8* and *toca-1* and *unc-8; toca-1* double mutants. (Bottom) GFP::RAB-3 ventral density is higher in *unc-8; toca-1* double mutant animals (2.28 ± 1.7, n=45) than in *unc-8* (1.02 ± 0.5, n=51) and *toca-1* (0.95 ± 0.6, n=52) single mutants or wild-type animals (early L4 larvae) (0.69 ± 0.6, n=73). Kruskal-Wallis test with Dunn's multiple comparison. ** < 0.01 and *** < 0.0001. Scale bar = 5 µm.
B-C. (Top) Control VD neurons (gray) with anteriorly placed SNB-1::GFP puncta (arrowheads) and UNC-8 (OE) VD cells (magenta) with fewer SNB-1::GFP puncta (dashed line) for **(B)** wild type animals and **(C)** *toca-1* mutants. **(B)** (Bottom) Paired analysis of neighboring cells [Control vs unc-8(OE)] in wild-type animals: Control VDs (1240 ± 399 A.U., n=17) and UNC-8 (OE) VD neurons (736 ± 514 A.U., n=17). Paired t-test, ** < 0.01. **(C)** Paired analysis of neighboring cells [Control vs unc-8(OE)] in *toca-1* mutants: Control VDs (1092 ± 415 A.U. , n=22) and UNC-8 (OE) VD neurons (628 ± 451 A.U. , n=22). Paired t-test, ** < 0.01. Scale bar = 10 µm.

mutants show a robust level of residual GFP::RAB-3 puncta in ventral DD neurites that exceeds that of either *unc-8* or *toca-1* single mutants (Figure 3.7A). These findings suggest that TOCA-1 and UNC-8 function in parallel and partially redundant pathways to promote the elimination of DD synaptic terminals. For an independent test of this model, we exploited our earlier observation that over-expression of UNC-8 or UNC-8(OE) drives ectopic disassembly (i.e., removal of SNB-1::GFP) of ventral VD presynaptic domains (Figure 3.7B). A *toca-1* loss-of-function mutation does not impede UNC-8(OE)-dependent elimination of SNB-1::GFP, an observation consistent with the hypothesis that TOCA-1 functions in parallel but not downstream of UNC-8 (Figure 3.7B-C) In contrast, as noted above, syndapin/SDPN-1 is required for UNC-8(OE)-dependent synaptic elimination (Figure 3.4D). Together, these results suggest that UNC-8 activates the F-BAR protein syndapin/SDPN-1 to drive synaptic disassembly in a pathway the functions cooperatively with the synaptic remodeling function of the F-BAR protein, TOCA-1.

Branched actin polymerization acts cell-autonomously to drive DD remodeling

Because the F-BAR proteins syndapin/SDPN-1 and TOCA-1 promote branched actin polymerization through their SH3 domain (Giuliani et al., 2009; Kessels & Qualmann, 2002), we conducted a candidate screen of potential downstream effectors of synaptic remodeling. For this purpose, we utilized the *unc-55* paradigm (Figure 3.5A-C) to determine that RNAi knockdown of components of the Arp2/3 complex and the Wave Regulatory Complex (WRC) impairs the removal of SNB-1::GFP from ventral synapses in remodeling GABAergic neurons (Figure 3.5D) (Petersen et al., 2011). These findings suggest that the F-BAR proteins, SDPN-1 and TOCA-1, might drive synapse elimination by recruiting downstream effectors of actin polymerization, the WRC and Arp2/3 complex, to remodeling GABAergic synapses (Figure 3.9). Intriguingly, the additional Arp2/3 activator, N-WASP is dispensable for this process (Figure 3.5). For endocytosis, the F-BAR proteins interact with the WRC which in turn deploys its VCA domain to activate the

Arp2/3 complex (Chen et al., 2010b; Girao et al., 2008; Ismail, Padrick, Chen, Umetani, & Rosen, 2009; Mooren, Galletta, & Cooper, 2012) (Figure 3.8A). Close association of F-BAR domains with the plasma membrane mobilizes branched-actin activators to initiate membrane invagination during endocytosis (Kessels & Qualmann, 2004).

To track the Arp2/3 complex localization during remodeling, we GFP-labeled the conserved Arp2/3 component, p21/ARX-5, for dual-color imaging with the synaptic vesicle marker mCherry::RAB-3. Airyscan imaging during the remodeling window detected ARX-5::GFP puncta closely associated with RAB-3::mCherry at remodeling ventral DD presynaptic boutons (Figure 3.8B). To rigorously test the hypothesis that branched-actin polymerization is needed cell-autonomously for DD remodeling, we used cell specific RNAi (csRNAi) for DD-specific knockdown of *arx-5* (Figure 3.8C). Importantly, p21/ARX-5 is required for Arp2/3 function as depletion of the ARX-5 subunit decreases the rate of Arp2/3-dependent actin polymerization (Gottlieb, Ivanov, Adesnik, & Sabatini, 1993). We observed significant retention of SNB-1::GFP puncta at the presynaptic terminals of *arx-5(csRNAi)*-treated DD neurons in comparison to control cells, indicating the failure of SNB-1::GFP elimination in *arx-5*-depleted cells (Figure 3.8C).

Because the VCA domain of WRC is sufficient to activate the Arp2/3 complex (Machesky et al., 1999), we forced expression of the VCA domain in DD neurons to test the prediction that elevated VCA activity should accelerate DD remodeling. Consistently, in remodeling L1 larvae, DD neurons with forced VCA expression or VCA(OE) showed fewer SNB-1::GFP puncta than control DD neurons that did not express the VCA domain (Figure 3.8D). Overall, these results support the hypothesis that the WRC activates branched-actin polymerization in DD remodeling to promote disassembly of the presynaptic apparatus. Additional evidence suggests that this mechanism acts downstream of UNC-8 as knockdown of the WRC component, *wve-1*, impairs the removal of SNB-1::GFP from ventral synapses of VD neurons that over-express UNC-8

(Figure 3.8E-F). Thus, our results are consistent with the idea that UNC-8 drives synapse removal by activating branched actin polymerization via the F-BAR protein, Syndapin/SDPN-1 and WRC.

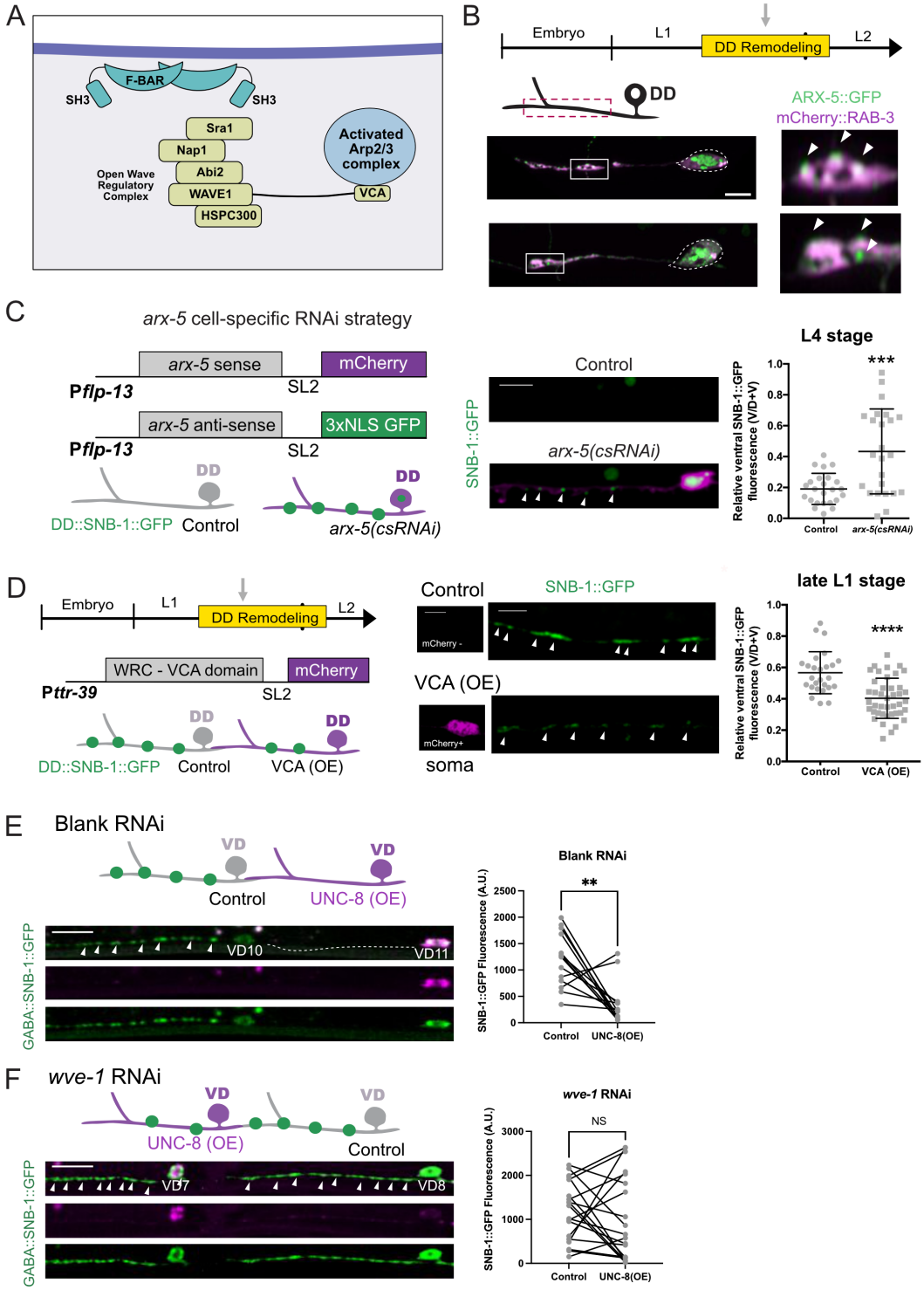

Figure 3. 8. Arp2/3 and the Wave Regulatory Complex (WRC) function downstream of UNC-8 to promote presynaptic disassembly.

A. F-BAR proteins associated with the plasma membrane recruit the Wave Regulatory Complex (WRC) to activate Arp2/3 for branched-actin polymerization. WRC components Sra1/GEX-2, Nap1/GEX-3, Abi2/ABI-1, WAVE1/WVE-1 and HSPC300/Y57G11C.1147 are conserved in C. elegans. The VCA domain (V: Verprolin homology domain, C: Central domain and A: Acidic domain) of WAVE1 directly interacts with Arp2/3 to promote its activation.
B. Airyscan imaging of remodeling DD neurons in the ventral nerve cord shows ARX-5::GFP (green) puncta (arrowheads) adjacent to synaptic vesicle clusters labeled with mCherry::RAB-3 (magenta) (insets). Dashed line denotes DD cell soma.
C. (Left) Cell specific RNAi of *arx-5* in DD neurons is achieved by expression of *arx-5* sense and antisense transcripts each co-expressed with cytosolic mCherry or nuclear-localized GFP, respectively. Non fluorescent DD neurons serve as controls (gray) whereas DDs with nuclear GFP and cytosolic mCherry labeling correspond to *arx-5(csRNAi)* knockdown cells. (Center) Representative images of ventral SNB-1::GFP puncta (arrowheads) in control and *arx-5(csRNAi)* DD cells in L4 stage larvae. (Right) Proportion of overall SNB-1::GFP fluorescence on the ventral side in control DDs (0.19 ± 0.1, n=24) and *arx-5(csRNAi)* (0.43 ± 0.3, n=24) cells of L4 stage larvae. Unpaired t-test, **** < 0.0001.
D. (Left) Experimental set-up: Pttr-39 drives over-expression of the WRC-VCA domain [VCA(OE)] and cytosolic mCherry (magenta) in DD neurons at the L1 stage. Remodeling is tracked with DD::SNB-1::GFP (green). (Middle) Representative images of ventral SNB-1::GFP puncta (arrowheads)in VCA(OE) DD neurons and control DD neurons. Scale bar = 5 µm. (Right) Proportion of overall SNB-1::GFP fluorescence on the ventral side of control DDs (0.56 ± 0.1, n=26) and VCA (OE) (0.40 ± 0.1, n=42) cells during remodeling at the late L1 stage. Unpaired t-test, **** < 0.0001.
E. (Left) Control VD neurons (gray) with anteriorly placed SNB-1::GFP puncta (arrowheads) and UNC-8 (OE) VD cells (magenta) with fewer SNB-1::GFP puncta (dashed line) for animals treated with blank RNAi. (Right) Paired analysis of SNB-1::GFP fluorescence in neighboring cells [Control vs UNC-8(OE)] in blank RNAi-treated animals: Control VDs (1197 ± 507 A.U., n=14) and UNC-8 (OE) VD neurons (342 ± 398 A.U., n=14). Scale bar = 10 µm.
F. (Left) Control VD neurons (gray) with anteriorly placed SNB-1::GFP puncta (arrowheads) and UNC-8 (OE) VD cells (magenta) that maintain SNB-1::GFP puncta in (arrowheads) animals treated with *wve-1* RNAi. (Right) Paired analysis of SNB-1::GFP fluorescence in neighboring cells [Control vs UNC-8(OE)] in *wve-1* RNAi-treated animals: Control VDs (1194 ± 669 A.U., n=19) and UNC-8 (OE) VD neurons (1048 ± 969 A.U., n=19). Scale bar = 10 µm.

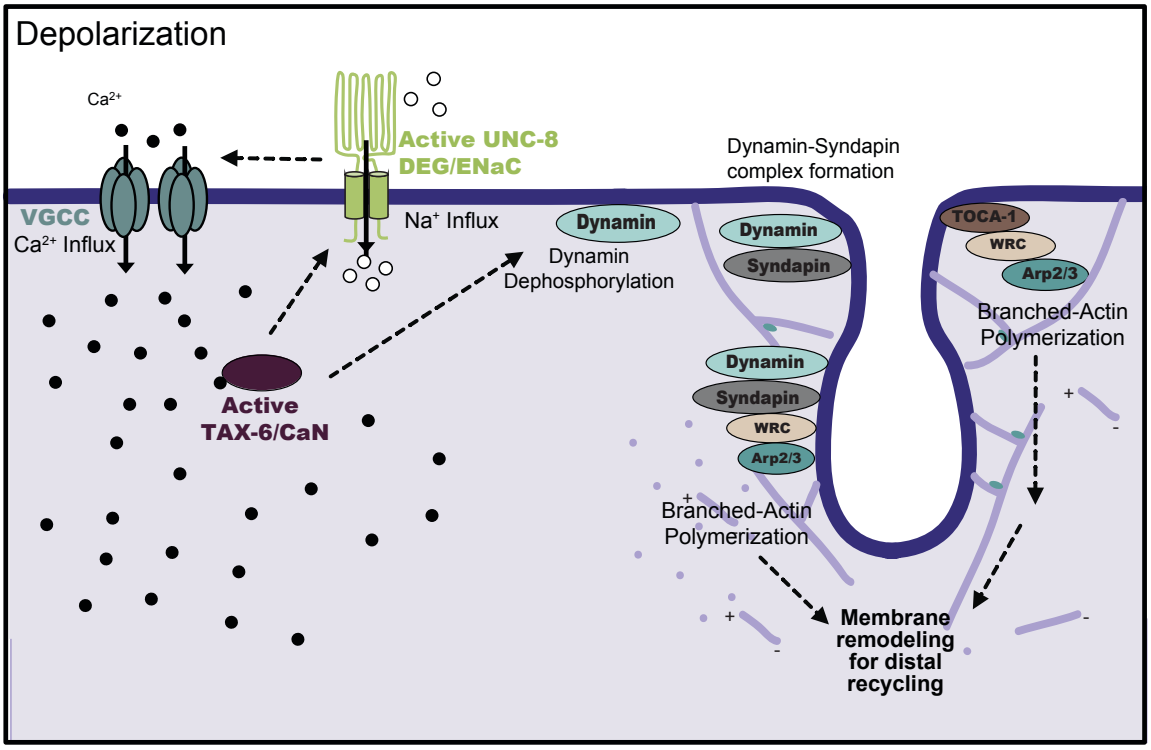

Figure 3. 9. TOCA-1 and UNC-8 function in parallel to promote actin polymerization and DD remodeling.

Actin polymerization and transient RAB-3 particles are elevated during DD synaptic remodeling

Our genetic studies show that branched-actin polymerizing genes promote elimination of DD synapses (Figure 3.8). These findings predict that actin polymerization is likely upregulated during DD remodeling. For an experimental test of this idea, we labeled the actin cytoskeleton with LifeAct::mCherry (Riedl et al., 2008) and synaptic vesicles with endogenous GFP::RAB-3 in DD neurons. Dual-color live cell imaging detected GFP::RAB-3 puncta surrounded by LifeAct::mCherry-labeled actin (Figure 3.10A-B). Actin dynamics at synapses was recorded by time-lapse imaging as changes in LifeAct::mCherry fluorescence in regions that corresponded to GFP::RAB-3 labeled synaptic clusters (Figure 3.10C-D) (See Methods). Kymograph analysis revealed a striking increase in both LifeAct::mCherry fluorescence intensity and dynamics during the remodeling window (Figure 3.10C', D', E-F). To quantify this effect, we calculated the standard deviation of all synaptic LifeAct::mCherry traces and determined that fluctuations in LifeAct::mCherry fluorescence are enhanced during the remodeling window in comparison to an earlier developmental period before remodeling (Figure 3.10A, G). Interestingly, live imaging detected instances of high actin dynamics in axonal regions with mobile GFP::RAB-3 particles (Figure 3.10D, arrows). These dynamic GFP::RAB-3 puncta are smaller than nearby and more stable GFP::RAB-3 clusters from which they appear to arise (Figure 3.10D, arrows). Dynamic and small GFP::RAB-3 puncta also appear short-lived as they can spontaneously disappear from the intersynaptic space (Figure 3.10D arrowhead). Quantification revealed that transient GFP::RAB-3 particles predominate during the remodeling window but are detected less often before DD remodeling ensues (Figure 3.10H). Importantly, we observed several instances in which the disappearance of a transient GFP::RAB-3 particle correlates with temporal elevation of LifeAct::mCherry (Figure 3.10D''). Notably, increased actin dynamics (Figure 3.10 G) and transient GFP::RAB-3 puncta (Figure 3.10H) are correlated with an overall reduction in the density

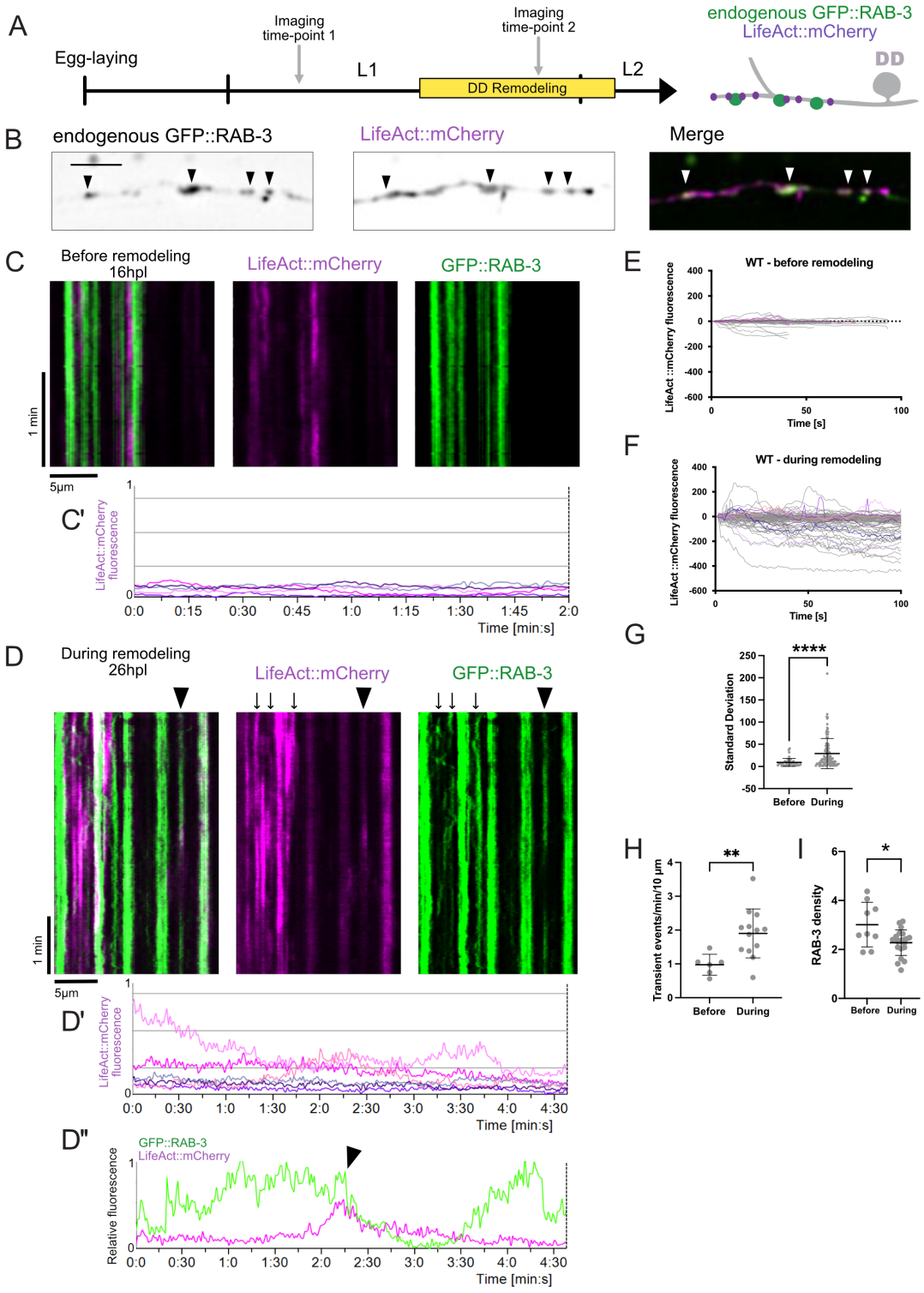

Figure 3. 10. Actin polymerization is upregulated during DD remodeling and correlates with synaptic vesicle (SV) dynamics

A. Ventral regions of DD neurons were imaged in L1 larvae before and during remodeling (gray arrows) to monitor actin dynamics with LifeAct::mCherry (magenta) and synaptic vesicles with endogenous GFP::RAB-3 (green).

B. Live-imaging reveals endogenous GFP::RAB-3 (green) associated with LifeAct::mCherry (magenta). Arrowheads point to locations of GFP::RAB-3 clusters. Scale Bar = 5 μm.
C-D. Elevated actin dynamics during DD remodeling. **(C)** Before remodeling (16 hpl), kymographs from live-imaging videos at 1fps (frame per second) show synaptic LifeAct::mCherry associated with stable GFP::RAB-3 puncta. C' Line scans from kymograph show stable LifeAct::mCherry fluorescence, n = 5 boutons. The Y-axis is normalized to the maximum value of LifeAct:mCherry fluorescence in line scans shown in D' below. **(D)** During remodeling, LifeAct::mCherry associates with both stable and transient GFP::RAB-3 puncta. Arrows and arrowhead (see below) point to locations of dynamic GFP::RAB-3 puncta. **(D')** Line scans from kymograph show dynamic LifeAct::mCherry fluorescence during remodeling, n = 6 boutons. The Y-axis is normalized to the maximum value of D' line scans. **(D'')** Line scans of LifeAct::mCherry and GFP::RAB-3 from kymograph trace (arrowhead) showing that GFP::RAB-3 is eliminated with transient elevation of LifeAct::mCherry signal.
E-F. Synaptic LifeAct::mCherry fluorescence is stable before remodeling (N = 6 videos) but fluctuates during DD remodeling (N = 14 videos).
G. The standard deviation of presynaptic LifeAct::mCherry signals before remodeling (9.04 ± 9.0, n=43 boutons from 6 videos) is significantly elevated during remodeling (29.1 ± 34.0, n=102 boutons from 14 videos). Values derived from absolute A.U values shown in E. and F.
H-I. (H) More transient GFP::RAB-3 events (See Methods) were detected during DD remodeling (1.86 ± 0.8, n = 13 videos) than before the remodeling period (0.93 ± 0.7, n = 6 videos). **(I)** Density of GFP::RAB-3 puncta (puncta/10 microns) is higher before remodeling (3.01 ± 0.9, n = 9 snapshots) than during the DD remodeling window (L2 larval stage) (2.28 ± 0.5, n = 21 snapshots).

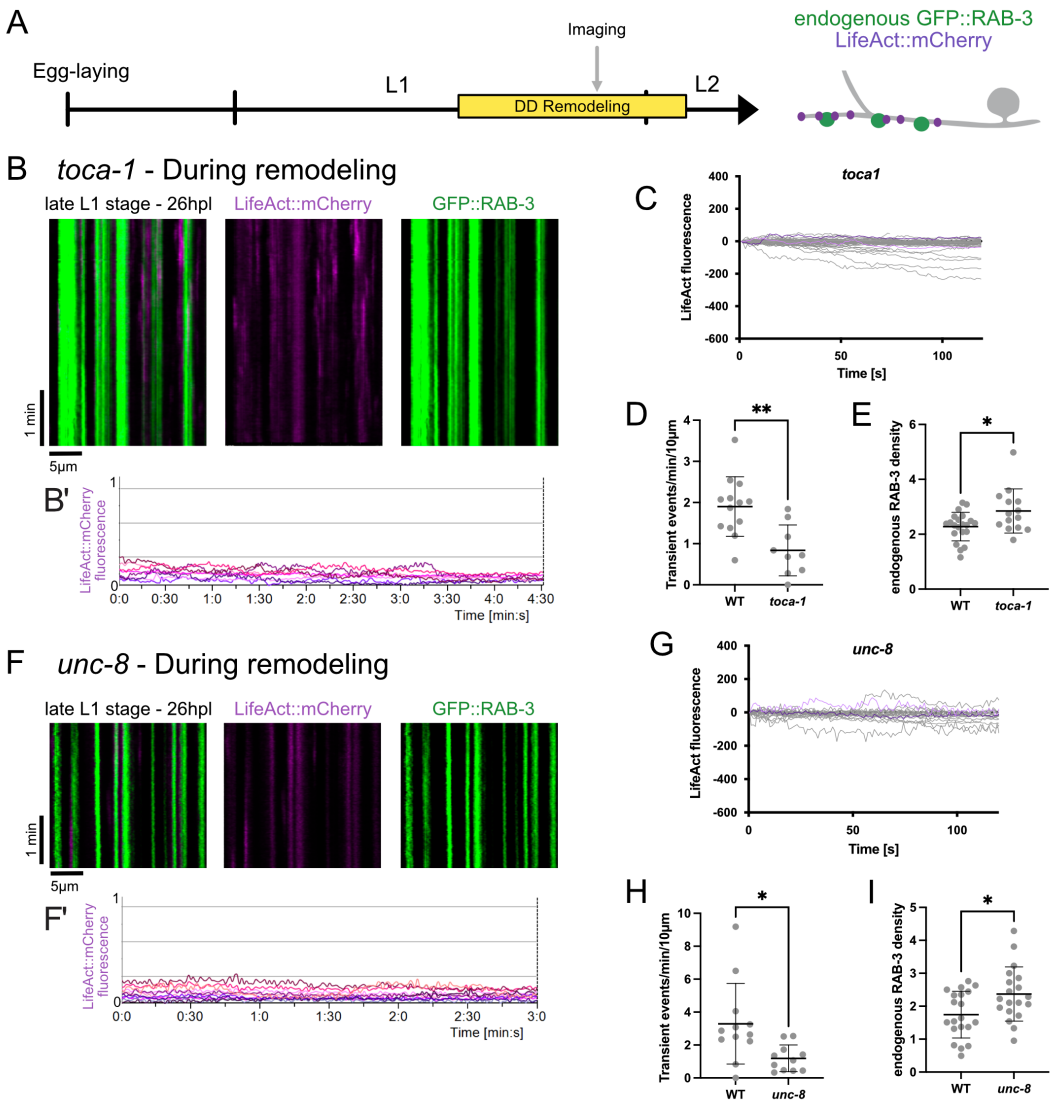

Figure 3. 11. Synaptic actin polymerization is downregulated in *toca-1* and *unc-8* mutants

A. (Left) Ventral regions of DD neurons were imaged in L1 larvae during remodeling (gray arrow) to monitor actin dynamics with LifeAct::mCherry (magenta) and synaptic vesicles with endogenous GFP::RAB-3 (green).

B-E. In *toca-1* mutants, **(B)** kymographs depict actin polymerization (LifeAct::mCherry) and stable GFP::RAB-3 puncta. **B'** Line scans from kymograph depict LifeAct::mCherry fluorescence at GFP::RAB-3 boutons (N = 8 boutons). Y-axis is normalized to values from Figure 3.10D'. **(C)** LifeAct::mCherry fluorescence at synaptic sites (GFP::RAB-3) of all videos analyzed (normalized to t_0 = 0?) (n = 13 videos). **(D)** Fewer transient GFP::RAB-3 events were detected in *toca-1* mutants (0.83 ± 0.6, n = 9 videos) compared to WT (1.86 ± 0.8, n = 13 videos). **(E)** *toca-1* mutants retain more GFP::RAB-3 puncta (2.85 ± 0.8, n = 14 snapshots) than wild type (2.28 ± 0.5, n = 21 snapshots) during the remodeling window (L2 larval stage). Data presented in panel D for WT also appears in Figure 3.10H

F-I. In *unc-8* mutants, **(F)** kymographs depict actin polymerization (LifeAct::mCherry) and stable GFP::RAB-3 puncta. **F'** Line scans from kymograph depict LifeAct::mCherry fluorescence at GFP::RAB-3 boutons (N = 11 boutons). Y-axis is normalized to values from Figure 3.10D'. **(G)**

LifeAct::mCherry fluorescence at synaptic sites (GFP::RAB-3) of all videos analyzed (normalized to $t_0 = 0$) (n = 11 videos). **(H)** Fewer transient GFP::RAB-3 events were detected in *unc-8* mutants (1.2 ± 0.8, n = 11 videos) compared to WT (3.2 ± 2.4, n = 12 videos). **(I)** *unc-8* mutants retain more GFP::RAB-3 puncta (2.37± 0.8, n = 19 snapshots) than wild type animals (1.74 ± 0.7, n = 20 snapshots) during the remodeling window (L2 larval stage).

of RAB-3::GFP puncta. Together, these results suggest that both actin dynamics and transient GFP::RAB-3 puncta are upregulated during DD remodeling when synapses are disassembled.

Actin polymerization and transient RAB-3 particles are downregulated in *toca-1* and *unc-8* mutants.

Because TOCA-1 is a known activator of the WRC (Giuliani et al., 2009), which promotes branched actin polymerization through the activation of the Arp2//3 complex, we next asked if actin polymerization is defective in *toca-1* mutants (Figure 3.11A). Our in vivo analysis detected a striking reduction in LifeAct::mCherry dynamics during the DD remodeling period in *toca-1* mutant L1 larvae in comparison to wild-type controls (Figure 3.11B-D). Mobile particles labeled with endogenous GFP::RAB-3 were also reduced in remodeling DD neurons relative to wild type in *toca-1* mutants (Figure 3.11D). We obtained similar results for *unc-8* mutants which showed less dynamic actin (Figure 3.11F-G) and fewer transient GFP::RAB-3 events than wild type in DD neurons during the remodeling period (Figure 3.11 H). Notably, these defects are correlated with increased density of residual ventral GFP::RAB-3 puncta in *toca-1* and *unc-8* mutants in during remodeling (Figure 3.11E and I). Together, these findings suggest that TOCA-1 and UNC-8 normally drive actin polymerization to accelerate removal of GFP::RAB-3 from remodeling DD synapses.

Actin polymerization also promotes dorsal assembly of DD neuron presynaptic domains

During DD remodeling, synapses are eliminated from ventral DD neurites as new DD synapses are assembled in the dorsal nerve cord (Figure 3.12A). As reported above, we determined that removal of the synaptic vesicle marker GFP::RAB-3 is impaired in ventral DD neurites in *toca-1; unc-8* double mutants (Figure 3.7). We also observed that dorsal

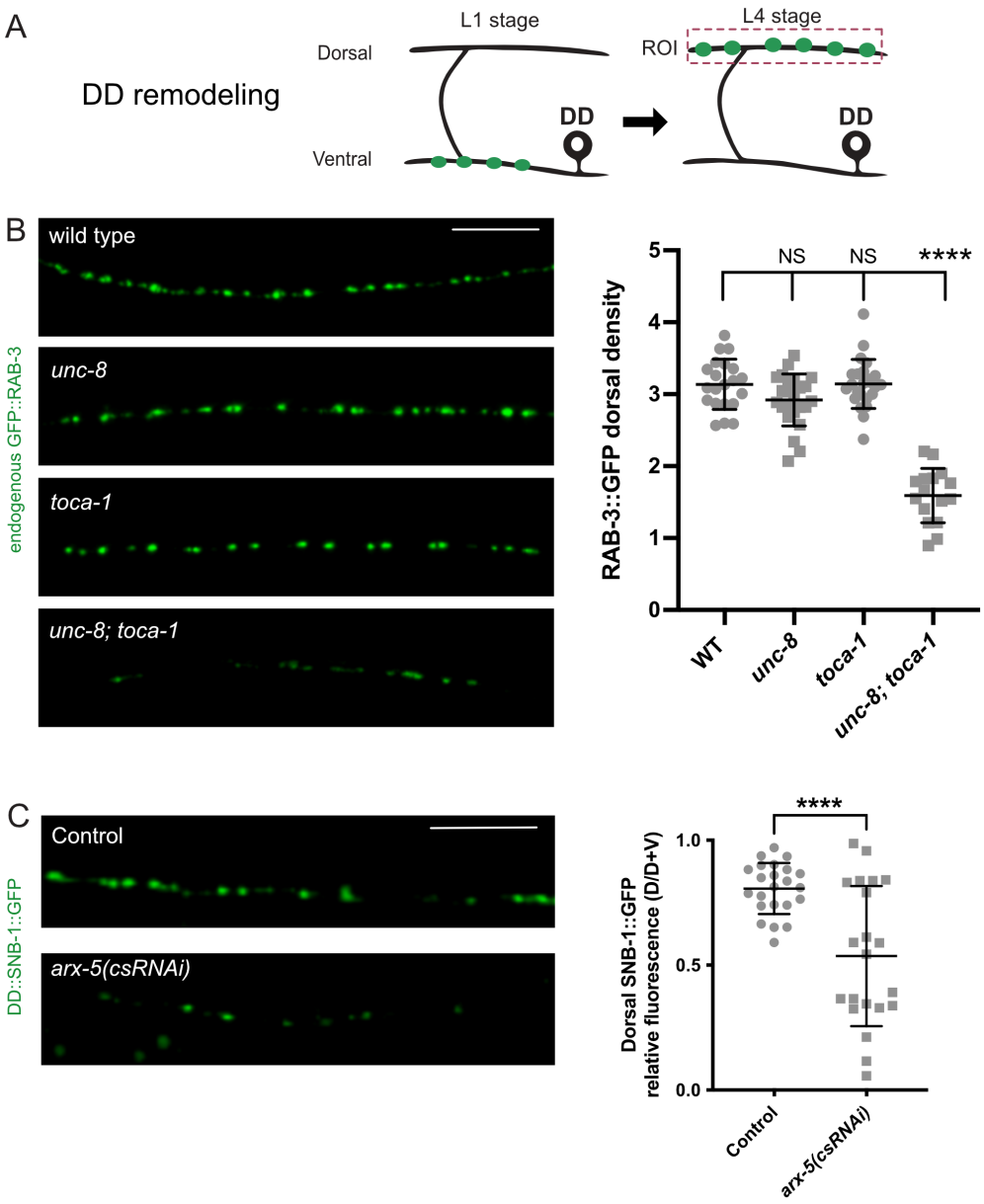

Figure 3. 12. Dorsal assembly requires branched-actin polymerization.

A. During DD remodeling, new synaptic sites (green) are established on the dorsal nerve cord (dashed box).
B. (Left) Representative images of the dorsal nerve cord labeled with endogenous GFP::RAB-3 of wild-type, *unc-8 and toca-1* single mutants, and *unc-8; toca-1* double mutants (early L4 larvae). (Right) GFP::RAB-3 density (puncta/10 micron) is substantially reduced in *unc-8; toca-1* double mutants (1.6 ± 0.4, n = 16) compared to wild-type (3.14 ± 0.4, n = 21), unc-8 (2.92 ± 0.4, n = 24) and toca-1 (3.14 ± 0.3, n = 24). One-Way ANOVA with Tukey's multiple comparison test. **** $p < 0.001$, NS is Not Significant.
C. (Left) Representative images of dorsal DD neurites labeled with SNB-1::GFP in control and *arx-5(csRNAi)*. (Right) The proportion of overall SNB-1::GFP fluorescence on the dorsal side (D/D+V) is reduced in *arx-5(csRNAi)* (0.54 ± 0.3, n = 21) vs Control (0.81 ± 0.1, n = 23).

GFP::RAB-3-labeled DD synapses are markedly reduced in *unc-8; toca-1* double mutants in L4 larvae which normally display robust dorsal GFP::RAB-3 puncta in the wild type at this developmental stage. Notably, dorsal GFP::RAB-3 puncta in *unc-8* and *toca-1* single mutants were not reduced (Figure 3.12A), again suggesting that the UNC-8 and TOCA-1 proteins function in parallel pathways.

The dorsal synaptic defect of *unc-8; toca-1* double mutants led us to hypothesize that the removal of old DD synapses from ventral regions might be coupled to the assembly of new DD presynaptic boutons in the dorsal cord. Because both *toca-1* and *unc-8* mutants display defective actin dynamics in DD neurons during the remodeling period (Figure 3.11), we reasoned that inactivation of the downstream Arp2/3 complex (Figures 3.8A & 3.9) might also result in a dorsal assembly defect. Accordingly, we used cell-specific RNAi (csRNAi) to target the conserved Arp2/3 component *p21/arx-5* and determined that dorsal assembly of SNB-1::GFP puncta is substantially reduced in *arx-5(csRNAi)*-treated DD neurons (Figure 3.12B). In a series of experiments described below, we test the hypothesis that UNC-8 and TOCA-1 drive an actin-dependent endocytic mechanism that dismantles ventral DD boutons to recycle presynaptic components to nascent DD synapses in the dorsal nerve cord.

Recycling endosomes function downstream of UNC-8 to mediate synapse elimination and dorsal assembly.

A mechanism for distal recycling of presynaptic components would likely require a transport system involving intracellular vesicles or endosomes. Rab11 is a small GTPase required for recycling endosome function (Ullrich, Reinsch, Urbé, Zerial, & Parton, 1996). We adopted two approaches to test the idea that RAB-11 proteins function to remodel DD presynaptic terminals. First, we used cell-specific RNAi to knockdown the GTPase Rab-11 in remodeling DD neurons. We observed that ventral SNB-1::GFP fluorescence was elevated in *rab-11(csRNAi)*-treated DD

neurons in concert with a reciprocal decrease in dorsal SNB-1::GFP signal in L4 larvae (Figure 3.13A-D). In contrast, control DD cells did not retain ventral SNB-1::GFP and successfully assembled SNB-1::GFP puncta in the dorsal cord by the L4 stage(Figure 3.13B-D). These findings support the notion that recycling endosomes are required for the removal of synaptic proteins from ventral terminals as well as for their assembly at dorsal synapses. To determine if RAB-11 functions downstream of UNC-8, we asked if UNC-8-dependent synapse removal in VD neurons requires RAB-11. In this experiment, global RNAi knockdown of *rab-11* was sufficient to prevent UNC-8(OE)-dependent elimination of VD synapses (Figure 3.13E-F), thus, suggesting that recycling endosomes could be required to transport disassembled ventral synapses to sites of nascent presynaptic assembly in dorsal DD neurites.

In a second experiment to test the idea that recycling endosomes are involved in DD synaptic remodeling, we designed a two-color labeling strategy to track the recycling endosome marker RAB-11::TagRFP and the synaptic vesicle-associated component, GFP::RAB-3, in remodeling DD neurons (Figure 3.14A). Live-imaging revealed that RAB-11::TagRFP is dynamic during the remodeling window and actively traffics along ventral and dorsal DD neurites in an anterograde and retrograde fashion (Figure 3.14B, purple arrowheads). Thus, suggesting that RAB-11 dynamics can transport synaptic material between both neurites. Further substantiating this idea, we find instances pf RAB-11::TagRFP particles entering the commissure that connects the ventral and dorsal neurites (data not shown). Other RAB-11::TagRFP particles are closely apposed with stable GFP::RAB-3 puncta (Figure 3.14B', magenta arrows) with striking examples of dynamic association and dissociation with the periphery of GFP::RAB-3 puncta (yellow arrowheads in Figure 3.14B-C). Intriguingly, in some cases, the association of dynamic RAB-11::TagRFP particles is correlated with the disappearance of otherwise stable GFP::RAB-3 puncta (Figure 3.14 C). Thus, suggesting that RAB-11 dynamics could influence the stability of

RAB-3::GFP puncta during the remodeling window. This idea is consistent with a model where RAB-11 endosomes might be promoting transient RAB-3 particles for distal recycling.

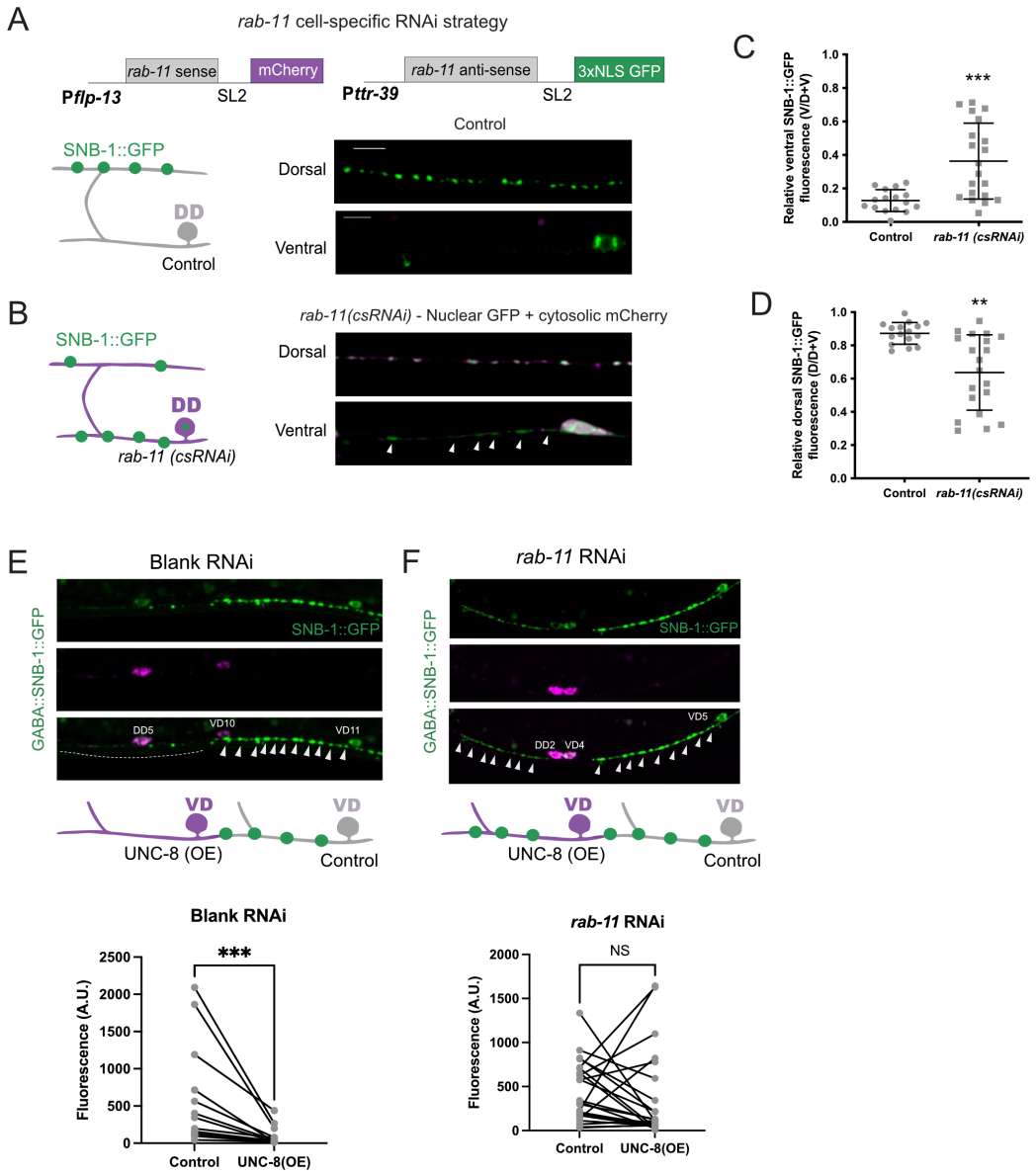

Figure 3. 13. The recycling endosome component, RAB-11, is required for UNC-8-dependent synapse elimination

A-D. Cell-specific RNAi (csRNAi) knockdown of RAB-11 in DD neurons is correlated with co-expression of cytosolic mCherry (magenta) and nuclear GFP (green) (dashed lines to denote cell soma, see. Representative images at the L4 larval stage **(A)** show enrichment of SNB-1::GFP in the dorsal nerve cord of control animals vs **(B)** reduced dorsal puncta and residual ventral SNB-1::GFP in *rab-11(csRNAi)* treated DD neurons. **(C)** Proportion of overall SNB-1::GFP fluorescence on the ventral side in control (0.13 ± 0.1, n = 16) vs *rab-11(csRNAi)*-treated (0.36 ± 0.2, n = 20) DD neurons. Mann-Whitney test, *** p = 0.0003 **(D)** Proportion of overall SNB-1::GFP

fluorescence on the dorsal side in control (0.87 ± 0.1, n = 16) vs *rab-11(csRNAi)*-treated (0.63 ± 0.2, n = 20) DD neurons, Unpaired t-test, ** p = 0.0058.

E. (Top) Control VD neurons (VD11, gray) with anteriorly placed SNB-1::GFP puncta (arrowheads) and UNC-8(OE) VD cells (VD10, magenta) with fewer SNB-1::GFP puncta in anterior region (dashed line) for animals exposed to blank RNAi. (Bottom) Paired analysis of ventral SNB-1::GFP fluorescence in neighboring cells, Control VDs (607 ± 688 A.U., n=13) vs UNC-8 (OE) VD neurons (94.8 ± 129 A.U., n=13). Wilcoxon matched-pairs signed rank test, *** p = 0.0002.

F. (Left) Anteriorly placed SNB-1::GFP puncta (arrowheads) in Control VD neurons (VD5, gray) and UNC-8 (OE) VD cells (magenta) treated with *rab-11* RNAi. (Right) Paired analysis of ventral SNB-1::GFP fluorescence in neighboring cells, Control VDs (439 ± 341 A.U., n=23) and UNC-8 (OE) VD neurons (360 ± 500 A.U., n=23). Wilcoxon matched-pairs signed rank test, p = 0.211. NS is Not Significant.

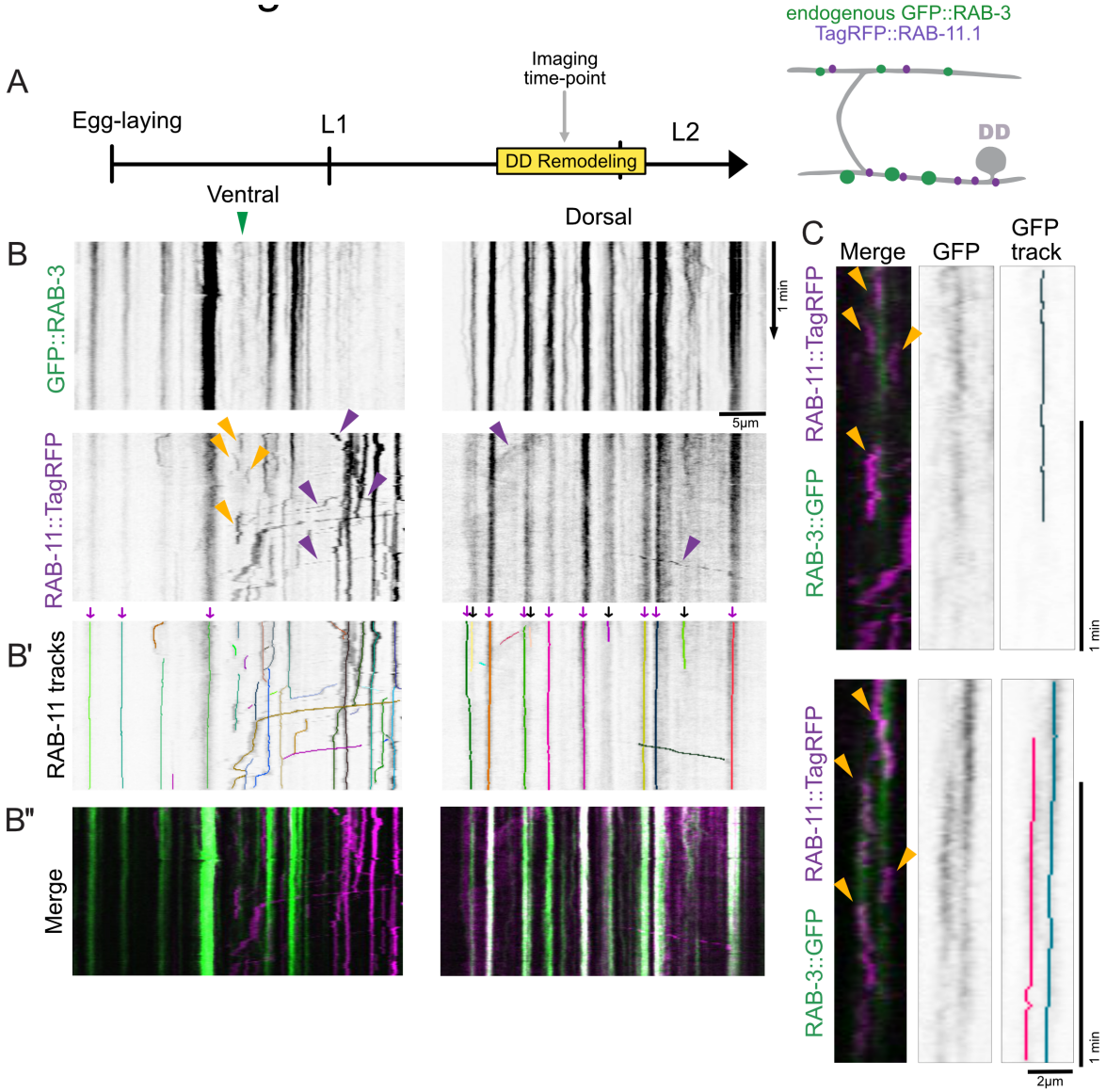

Figure 3. 14. RAB-11 endosome trafficking in remodeling DD neurites

A. Synaptic vesicles (endogenous GFP::RAB-3) and recycling endosomes (TagRFP::RAB-11.1) were imaged in ventral cord DD neurites during the remodeling window (arrow).
B. Kymographs from ventral (Left) and dorsal (Right) neurites of remodeling DD neurons. (Bottom) Dynamic TagRFP::RAB-11 particles interact with (Top) GFP::RAB-3 puncta. **B'** shows the identification of RAB-11 particles on both dorsal and ventral cords with Kymobutler (See methods). Kymographs reveal dynamic RAB-11 particles (purple arrowheads) and RAB-11 that associates with transient GFP::RAB-3 puncta (yellow arrowheads). **B''** shows the merged kyumogrpah for both TagRFP::RAB-11 (magenta) and GFP::RAB-3 (green) dynamics.
C. (Left) Representative kymographs showing dynamic association of RAB-11 (arrowheads) with transient GFP::RAB-3 puncta (green) in ventral DD neurites. (Middle) Kymographs of transient GFP::RAB-3 with (Right) Kymobutler tracks.

RAB-11 promotes recycling of ventral RAB-3 to nascent, dorsal synapses in remodeling DD neurons.

Having shown that *rab-11(csRNAi)* impairs DD remodeling and that RAB-11::TagRFP-labeled particles are actively trafficked in both dorsal and ventral DD neurites, we next performed an experiment to ask if distal recycling of ventral components to nascent dorsal synapses depends on RAB-11. First, we designed a flippase-dependent cassette at the N-terminus of the *rab-3* locus that encodes the photoconvertible fluorescent protein Dendra-2 (Figure 3.15A) and used a DD-specific promoter (*Pflp-13*) to drive expression of the resultant endogenous Dendra-2::RAB-3 in DD neurons. Exposure to UV light induces an irreversible green-to-red change in the Dendra-2 fluorescence emission spectrum (Figure 3.15B). We used this approach to expose Dendra-2::RAB-3 at ventral DD synapses (green) to UV light before the onset of remodeling (T_{18}-T_{20}) and to track photoconverted Dendra-2::RAB-3 (red) during (T_{28}) and after remodeling (T_{38}) (Figure 3.15C). Imaging during the remodeling window detected photoconverted Dendra-2::RAB-3 signal in both ventral and dorsal nerve cords. Later, by the L3 stage, photoconverted Dendra-2::RAB-3 had been efficiently removed from the ventral side with > 60% recovered at dorsal DD neurites. (Figure 3.15D-E). These findings confirm an earlier report that Dendra::RAB-3 over-expressed from a transgenic array is also recycled from ventral to dorsal synapses in remodeling DD neurons (Park et al., 2011).

To determine if RAB-11 is required for RAB-3 recycling, we used a *rab-11* cell-specific RNAi (csRNAi) strategy to knock down *rab-11* in DD neurons. In this experiment, the cell nuclei of *rab-11(csRNAi)*-treated DD neurons are marked with GFP and tagRFP whereas neighboring control DD neurons that display unlabeled nuclei should express native levels of *rab-11* (Figure 3.16B). Dendra-2::RAB-3 was photoconverted before remodeling (T_{18}) and tracked after remodeling, at the L3 stage (T_{38}) (Figure 3.16A). In control DD neurons, photoconverted Dendra2::RAB-3 protein was efficiently removed from the ventral side and ~70% recovered at

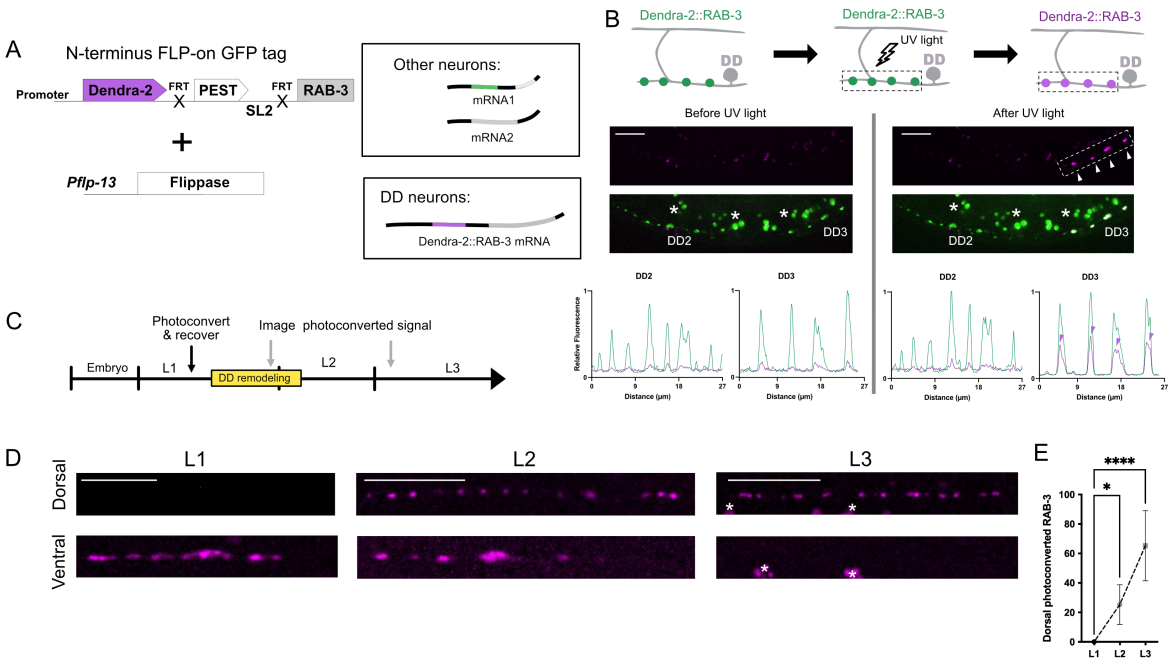

Figure 3. 15. RAB-3 recycles from old to new presynaptic boutons in remodeling DD neurons.

A. Endogenous labeling of RAB-3 with photoconvertible protein Dendra-2 in DD neurons. *pflp-13* drives flippase in DD neurons to fuse Dendra-2 to the N-terminus of the endogenous RAB-3 protein.
B. Treatment of ventral Dendra-2::RAB-3 puncta (green) in individual DD neurons (dashed box) with UV light produced photoconverted Dendra-2::RAB-3 puncta (magenta). Asterisks mark autofluorescent granules in the intestine.
C. Experimental set up: Dendra-2::RAB-3 was photoconverted and worms recovered (black arrow) for imaging either during remodeling (L2, T_{28}) or after remodeling (L3, T_{38}) (gray arrow)
D Representative images of photoconverted Dendra-2::RAB-3 puncta in dorsal and ventral nerve cords immediately after photoconversion (L1), during remodeling (L2) and after remodeling (L3) Asterisks denote autofluorescence.
(E) Progressive accumulation of photoconverted Dendra-2::RAB-3 on the dorsal side : L1 (0 ± 0, n = 17), at L2 (25.3 ± 13.5 %, n = 6) and at L3 (65.3 ± 23.7 %, n = 14). Kruskall-Wallis test with Dunn's multiple comparison test. * p = 0.019 and *** p < 0.0001. Scale bars = 10 µm.

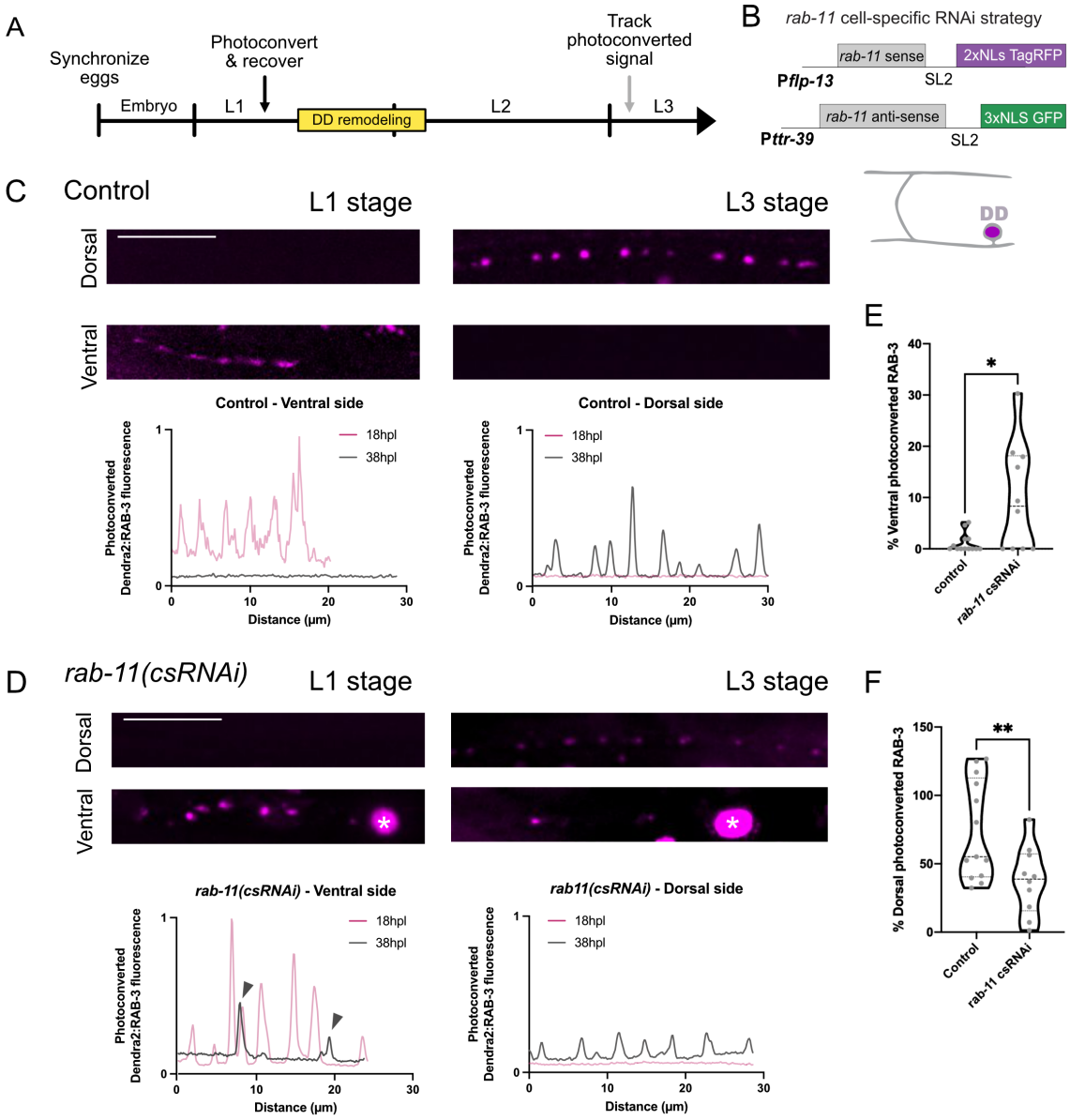

Figure 3. 16. RAB-11 is required for RAB-3 disassembly and recycling to new dorsal DD boutons.

A. (Left) Experimental set-up: Dendra-2::RAB-3 in individual DD neurons was photoconverted before remodeling (L1, T_{38}) and worms recovered (black arrow) for imaging after remodeling (L3 stage, T_{38}) (gray arrow). (Right) *rab-11(csRNAi)* cells express nuclear GFP and TagRFP.
C-D. (Top) Representative images of photoconverted Dendra-2::RAB-3 (magenta) in **(C)** control and **(D)** *rab-11(csRNAi)* DD neurons. Asterisks label nuclear TagRFP expressed in *rab-11(csRNAi)* DD cells. (Bottom) Line scans of photoconverted Dendra-2::RAB-3 before (T_{18}, pink) and after (T_{38}, gray) remodeling in ventral and dorsal DD neurites of **(C)** control and **(D)** *rab-11(csRNAi)* knockdown cells. Arrowheads denote ventral retention of photoconverted Dendra-2::RAB-3 signal at T_{38} (gray) in *rab-11(csRNAi)* neurons. Scale bar = 10 µm.
E-F. Percent of photoconverted Dendra-2::RAB-3 signal **(E)** that recycles to the dorsal cord **(F)** and remains on the ventral nerve cord at T_{38} or. *rab-11(csRNAi)* DD cells retain more photoconverted signal on the ventral side (9.96 ± 10.5 %, n=10) than controls (1.09 ± 1.8 %,

n=13). Mann Whitney test, * p = 0.0269. *rab-11(csRNAi)* DD cells recycle less photoconverted signal to the dorsal nerve cord (37.7 ± 24.8%, n=10) than controls (74.0 ± 36.2 %, n=13). Unpaired t-test, ** p = 0.0064.

nascent dorsal DD synapses (Figure 3.16C) as previously observed for the wild-type (Figure 3.15E). In contrast, *rab-11(csRNAi)*-treated DD neurons retained ventral photoconverted Dendra-2::RAB-3 signal and showed lower levels (~40%) of recycled RAB-3 at dorsal synapses (Figure 3.16D-F). Together, these findings establish that RAB-3 protein, initially associated with ventral DD synapses, is recycled to nascent dorsal synapses in remodeling DD neurons in a mechanism that depends on the canonical recycling endosome component, RAB-11.

TOCA-1 and UNC-8 promote RAB-3 recycling

As noted above, our results indicate that TOCA-1 and UNC-8 function in parallel pathways to drive DD neuron presynaptic remodeling (Figures 3.7 and 3.12). We therefore hypothesized that *unc-8* and *toca-1* mutants might impair recycling of synaptic proteins. To test this idea, we used our in vivo recycling strategy to track photoconverted Dendra-2::RAB-3 from ventral to dorsal synapses (Figure 3.16A). This experiment confirmed that *toca-1* and *unc-8* mutants show reduced levels of recycled (i.e., photoconverted) Dendra-2::RAB-3 at dorsal synapses (Figure 3.14A-C). Interestingly, dorsal accumulation of GFP::RAB-3 is not impaired in either *toca-1* or *unc-8* single mutants (Figure 3.12B). This disparity could mean that dorsal synapses are assembled from a combination of RAB-3 recycled from ventral synapses plus nascent RAB-3 that originates from the DD cell soma. In this model, *unc-8* and *toca-1* single mutants impair RAB-3 recycling but do not retard the incorporation of nascent RAB-3 at dorsal synapses. This possibility can be directly addressed by quantifying the proportion of photoconverted (red) vs nascent (green) Dendra-2::GFP at dorsal synapses in our photoconversion experiments (data not shown). In another surprise, removal of photoconverted Dendra-2::RAB-3 from ventral DD synapses at the L3 stage is not impaired in either *unc-8* or *toca-1* single mutants (Figure 3.17D-E). As noted above, residual ventral GFP::RAB-3 particles are elevated in comparison to wild type at the earlier L2 stage (i.e., during the remodeling window) in *unc-8* and *toca-1* mutants (Figure 3.11D, H). Perhaps, RAB-3 removal is delayed but not blocked in the *unc-8* and *toca-1* single mutants due to the partially

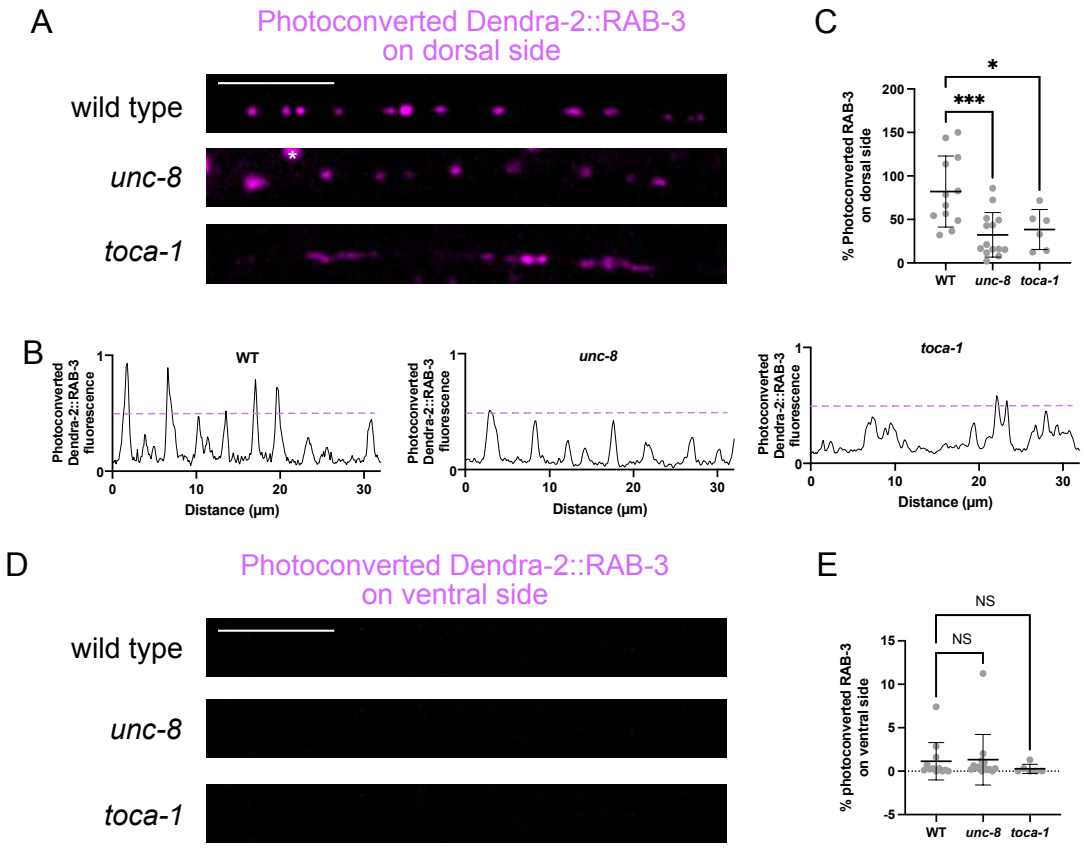

Figure 3. 17. UNC-8 and TOCA-1 promote recycling from ventral to dorsal DD boutons

A. Fluorescent images of photoconverted Dendra-2::RAB-3 in the dorsal nerve cord of (top) wild-type, (middle) *unc-8* and (bottom) *toca-1* animals after the remodeling period in L3. Asterisk denotes autofluorescence. Scale bar = 10 µm.
B. Normalized line scans across the dorsal cords of (left) wild-type (WT), (center) *unc-8* and (right) *toca-1* mutant animals. All Y-axes are normalized to the brightnes punctum in wild type. Dashed line shows threshold at 50% of the signal.
C. *unc-8* (32.3 ± 25.6%, n=14) and *toca-1* (38.4 ± 23.1%, n=6) mutants recycle less photoconverted Dendra-2::RAB-3 to the dorsal nerve cord than wild type (WT) (82.0 ± 40.8%, n=12). Ordinary One-Way ANOVA with Dunnett's multiple comparison test. * p = 0.02 and *** p = 0.0009.
D. Photoconverted Dendra-2::RAB-3 fluorescent signal is depleted in the ventral nerve cords of wild-type, *unc-8* and *toca-1* animals at the L3 stage. Scale bar = 10 µm.
E. Quantification confirms small fraction of photoconverted Dendra-2::RAB-3 signal retained on the ventral nerve cord at T_{38} in wild type (WT) (1.14 ± 2.1%, n=12), *unc-8* (1.32 ± 2.9%, n=14) and *toca-1* (0.27 ± 0.5%, n=6). Kruskal-Wallis with Dunn's multiple comparison test against WT, NS is Not Significant (WT vs *unc-8*, p = 0.96 and WT vs *toca-1*, p = 0.39).

redundant roles UNC-8 and TOCA-1 (Figures 3.7 and 3.12). This model predicts that removal of photoconverted ventral Dendra-2::RAB-3 should be severely impaired in *unc-8; toca-1* double mutants (see Figure 3.7A). In summary, TOCA-1 and UNC-8 promote the recycling of ventral RAB-3 for assembly at dorsal synapses but additional experiments are needed to delineate the underlying mechanism.

TOCA-1, but not SDPN-1, drives disassembly of the active zone protein, CLA-1, during DD remodeling.

In experiments described above, we used the synaptic vesicle markers, GFP::RAB-3 and synaptobrevin/SNB-1::GFP, to monitor synaptic remodeling. Our approach determined that the parallel-acting F-BAR proteins, TOCA-1 and syndapin/SDPN-1, which functions downstream of UNC-8, drive the relocation of synaptic vesicle proteins in remodeling DD neurons. Here we ask if TOCA-1 and syndapin/SDPN-1 are also required for disassembly of the active zone protein, CLA-1 from DD synapses. CLA-1, a distant ortholog of the active zone protein Piccolo/Bassoon, organizes the presynaptic density and clustering of synaptic vesicles (Xuan et al., 2017). For our studies we used a GFP-tagged version of the CLA-1s isoform or GFP::CLA-1s and expressed it specifically in DD neurons. GFP::CLA-1s initially distributes along the ventral cord at the L1 stage and then relocates to the dorsal cord at later developmental stages, thus indicating that CLA-1s is remodeled in developing DD neurons (Figure 3.18A). To determine if the SDPN-1 or TOCA-1 pathways regulate CLA-1s elimination from remodeling DD synapses, we quantified the density of GFP::CLA-1s puncta in the ventral cord at the L4 stage in *sdpn-1* and *toca-1* mutants (Figure 3.18B). In this experiment, ventral GFP::CLA-1s puncta are retained in *toca-1* mutant animals at the L4 stage in contrast to the wild type and *sdpn-1* mutants in which GFP::CLA-1s is largely absent. These results indicate that TOCA-1, but not SDPN-1, is required to eliminate the active zone protein CLA-1 in remodeling DD neurons.

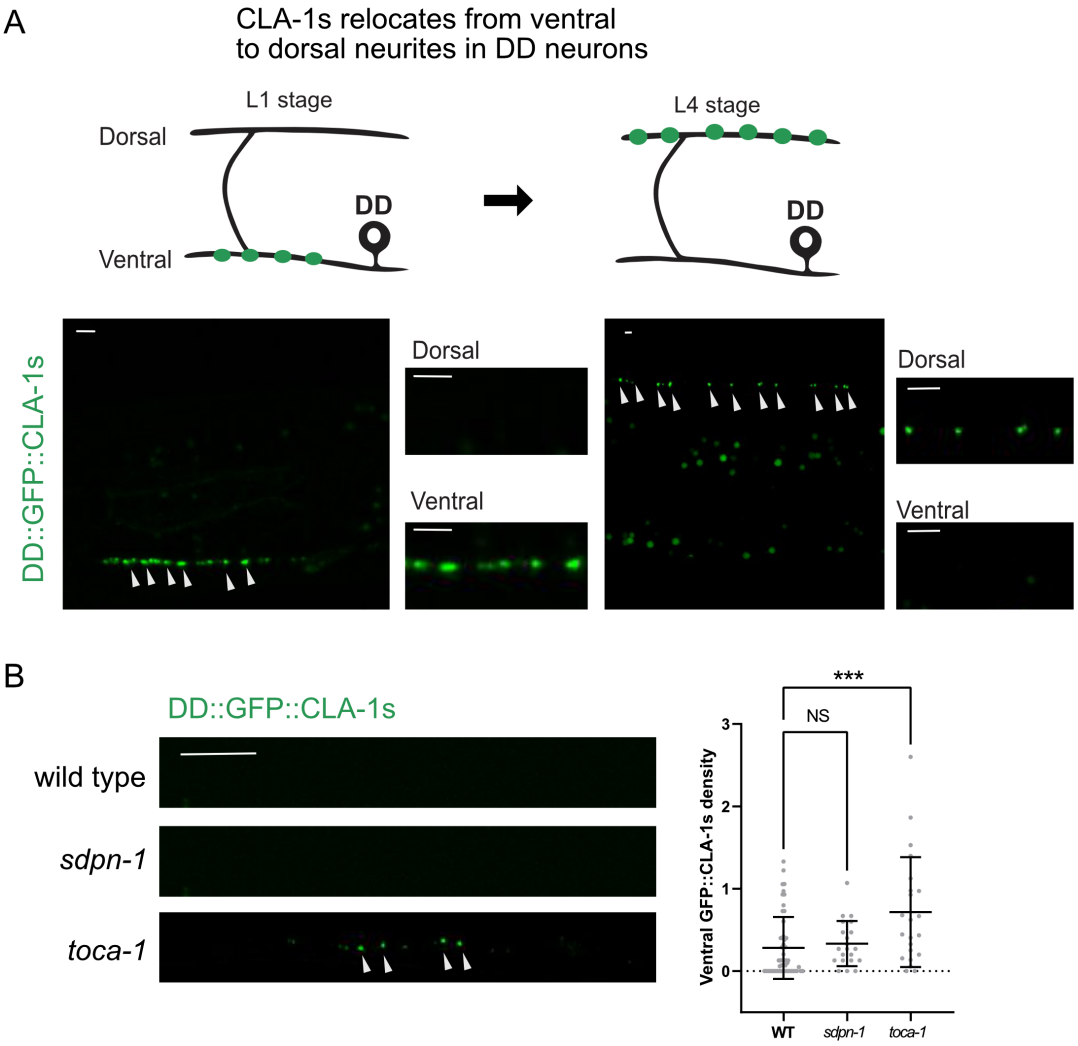

Figure 3. 18. Active zone protein, CLA-1, remodel in a TOCA-1-dependent fashion

A. Active zone protein GFP::CLA-1s remodels in DD neurons. (Left) At the L1 stage, CLA-1 puncta localize exclusively to the ventral side. (Right) At the L4 stage, CLA-1 puncta relocate to the dorsal side. (Top) Cartoon representation and (Bottom) representative images. Insets represent zoomed-in regions of the dorsal and ventral cords at the L1 and L4 stages. Scale bars = 2 µm.
B. Ventral GFP::CLA-1s puncta density of L4-stage animals is increased in *toca-1* mutants (0.72 ± 0.6%, n=22), in contrast to wild-type (0.28 ± 0.38, n=53) and *sdpn-1* mutants (0.33 ± 0.27, n=21). Kruskal-Wallis test with multiple comparisons. NS not significant p = 0.292 and *** p = 0.001.

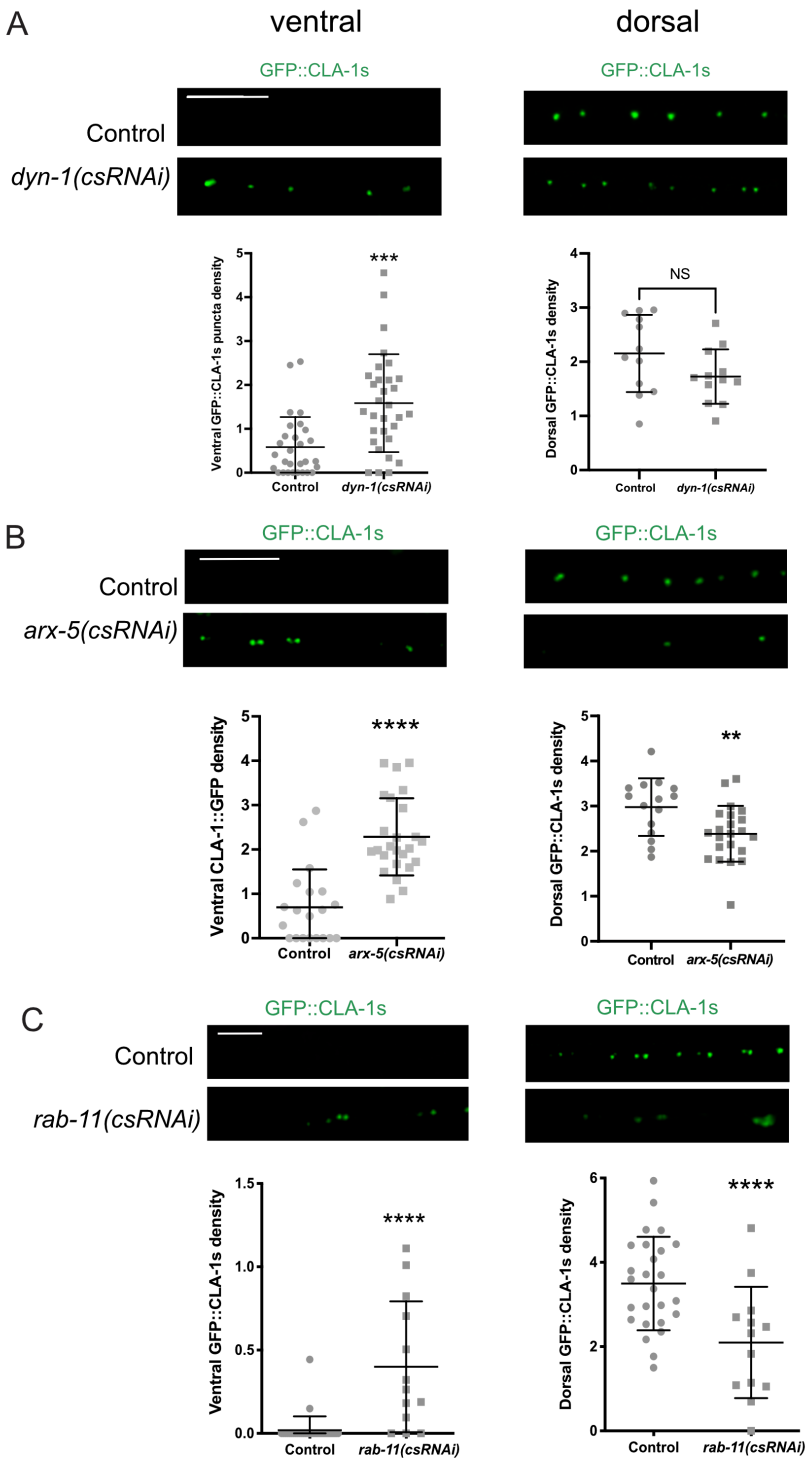

Figure 3. 19. Dynamin, the Arp2/3 complex and RAB-11 are required for remodeling of active zone protein CLA-1s in DD neurons.

A-C. GFP::CLA-1s puncta in the ventral (left) and dorsal (right) DD neurites of control and RNAi knockdown DD neurons. **(A)** *dyn-1(csRNAi)* cells retain more GFP::CLA-1s puncta on the ventral side (1.58 ± 1.1, n=31) than controls cells (0.58 ± 0.69, n=29). Mann-Whitney test, *** p = 0.0001, but are not different on the dorsal side: dy*n-1(csRNAi)* (1.73 ± 0.5, n=12); Control (2.15 ± 0.7,

n=12). Unpaired t-test, NS is Not Significant, p = 0.1048. **(B)** *arx-5(csRNAi)* cells retain more GFP::CLA-1s puncta on the ventral side (2.28 ± 0.9, n=25) than control cells (0.69 ± 0.85, n=20). Mann-Whitney test, **** p < 0.0001. *arx-5(csRNAi)* have less GFP::CLA-1s puncta on the dorsal side (2.39 ± 0.6, n=22) than control cells (2.98 ± 0.63, n=15). Unpaired t-test, ** p = 0.008. **(C)** *rab-11(csRNAi)* cells retain more GFP::CLA-1s puncta on the ventral side (0.4 ± 0.4, n=13) than control cells (0.02 ± 0.1, n=31). Mann-Whitney test, **** p < 0.0001. *rab-11(csRNAi)* have less GFP::CLA-1s puncta on the dorsal side (2.09 ± 1.3, n=13) than control cells (3.49 ± 1.1, n=26). Unpaired t-test, *** p = 0.0006. Density = GFP::CLA-1s puncta/ 10 microns.

To test additional components of the proposed endocytic pathway (Figure 3.9) for roles in GFP::CLA-1 remodeling, we used cell-specific RNAi to knockdown *dynamin/dyn-1*, *p21/arx-5* and *rab-11* in DD neurons. We found that both ARX-5 and RAB-11 are required for the elimination of GFP::CLA-1s at ventral synapses as well as its assembly at dorsal DD synapses (Figure 3.19B-C). Interestingly, the elimination of ventral GFP::CLA-1s is retarded in *dyn-1(csRNAi)*-treated DD neurons but assembly at dorsal synapses is not impaired in comparison to control DD neurons. (Figure 3.19A). Together, these results suggest that the active zone protein, CLA-1, is remodeled by an endocytic mechanism involving TOCA-1 whereas remodeling of synaptic vesicle components (e.g. RAB-3, SNB-1) depends on an endocytic pathway primarily involving UNC-8 and SDPN-1.

Bulk endosomes populate presynaptic boutons in remodeling DD neurons

During ADBE, actin polymerization at the membrane aids in the formation of bulk endosomes (Emma L. Clayton & Cousin, 2009). We have shown that UNC-8 elevates Ca^{++} at the synapse (Chapter II), mimicking high synaptic activity, and that key components of the ADBE mechanism function downstream of UNC-8 (Figure 3.1B, 3.4D and 3.8F). These findings led us to predict that bulk endosomes would populate remodeling DD synapses. Using serial section electron microscopy (EM), Ben Mulcahy, a postdoc in the laboratory of Mei Zhen (University of Toronto) generated a 3D-reconstruction of remodeling DD neurons. These data capture ultrastructural profiles of cellular changes at DD synapses as they are dismantled. Close inspection of remodeling synapses reveals large (80-100nm), clear, circular structures that resemble bulk endosomes (Figure 3.20A-B), thus, offering strong support for the role of bulk endocytosis in DD neuron synaptic remodeling.

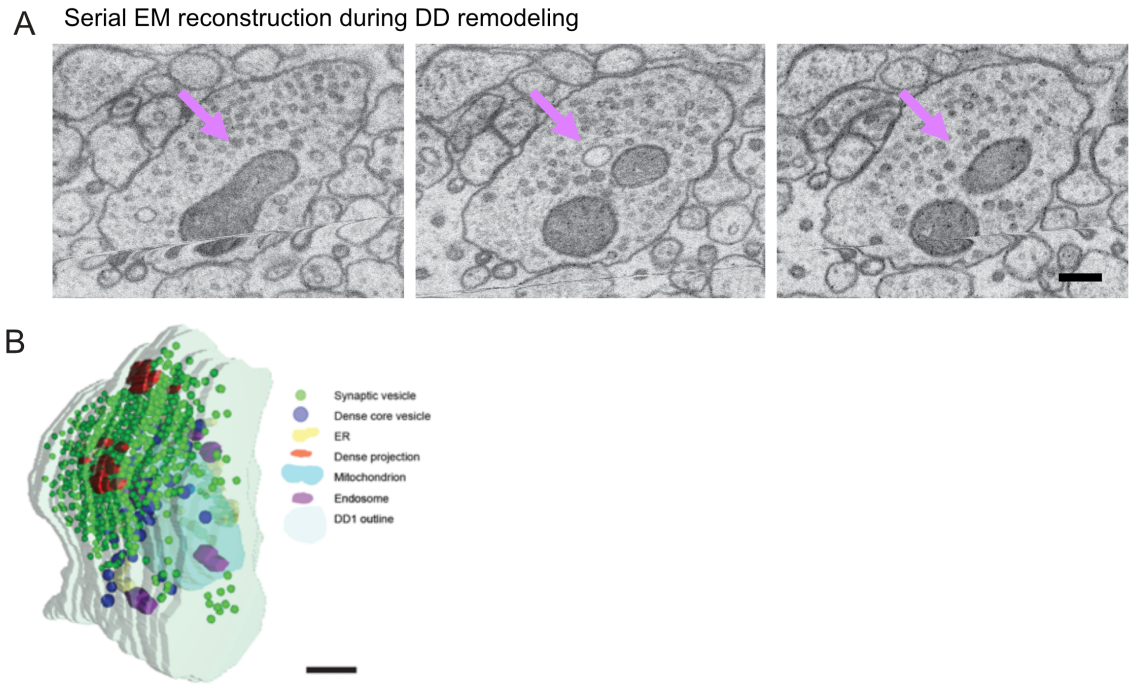

Figure 3. 20. Bulk endosomes populate remodeling boutons

A-B. Serial EM reconstruction reveals large, clear endosomes (pink arrow) and synaptic vesicles at remodeling synapses. (B) 3D EM reconstruction shows endosomes (purple) at the periphery of remodeling synaptic boutons, close to the active zone (red) and synaptic vesicles (green). Scale bars = 200 nm. Images from Ben Mulcahy and Mei Zhen, University of Toronto.

DISCUSSION

Here, we show that synaptic vesicle components are recycled from old to new synapses for developmental circuit refinement in a mechanism that requires actin-dependent endocytosis. Our results show that the ENaC channel, UNC-8, drives presynaptic disassembly in a pathway that involves dynamin and its downstream effector, the F-BAR protein, syndapin/SDPN-1 (Figure 3.4). Intriguingly, TOCA-1, an F-BAR protein with an established role in endocytic recycling, functions in parallel to UNC-8/SDPN-1(Figure 3.7). Both pathways promote actin polymerization during the onset of DD neuron remodeling (Figure 3.11), likely requiring the WAVE Regulatory Complex (WRC) and Arp2/3 (Figure 3.5 and 3.8), and drive the relocation of the synaptic vesicle component, RAB-3, from old to new DD synapses (Figure 3.17). Underscoring the likely role of endocytic recycling in this mechanism, RAB-11, a key component of recycling endosomes, is required for the translocation of RAB-3 to new synaptic locations (Figure 3.16).

A mechanism of bulk endocytosis drives DD neuron synaptic remodeling

The remodeling pathway that we have identified resembles that of Activity-Dependent Bulk Endocytosis or ADBE. During periods of high synaptic activity, ADBE mediates the recovery of presynaptic membrane for recycling into the synaptic vesicle pool (Emma L. Clayton & Cousin, 2009). During ADBE, elevated intracellular Ca^{++} activates the phosphatase, Calcineurin/CaN, which targets a group of conserved proteins (dephosphins) for dephosphorylation (Cousin et al., 2001; Guiney, Goldman, Elias, & Cyert, 2015). Dephosphorylation of the GTPase, Dynamin mediates the formation of a Dynamin-Syndapin complex to promote branched-actin polymerization, which in turn stimulates the formation of bulk endosomes (Figure 3.1D) (Emma L. Clayton & Cousin, 2009). In support of the hypothesis that an ADBE-like mechanism drives DD remodeling, we determined that CaN/TAX-6, which localizes to the presynaptic domains of DD

neurons, functions with UNC-8 to drive synaptic disassembly. CaN/TAX-6 functions in a positive feedback-loop with UNC-8 to maintain high Ca^{++} levels at remodeling synapses (Chapter II) (Miller-Fleming et al., 2016). We propose that CaN/TAX-6 is also required downstream of UNC-8 to promote bulk endocytosis (Figure 3.1 and 3.9). In line with this idea, we used genetic analysis to confirm that dephosphins, are required for the elimination of remodeling GABAergic synapses (Figure 3.2). Strikingly, a phospho-resistant dynamin mutant is sufficient to accelerate DD remodeling, as predicted from a model in which CaN-dependent dephosphorylation of dynamin drives endocytic removal of presynaptic domains (Figure 3.3). In addition, we showed that the F-BAR protein and known ADBE effector, Syndapin/SDPN-1, localizes to remodeling synapses, functions in a common pathway with UNC-8 and is required for UNC-8-dependent elimination of ventral synapses in remodeling GABAergic neurons (Figure 3.4). Overall, these findings are consistent with the hypothesis that an ADBE-like mechanism is active at remodeling DD synapses. In this case, the effective destruction of the DD presynaptic domain that results from the proposed bulk endocytic mechanism differs dramatically from the canonical role of ADBE of maintaining presynaptic function.

In addition to the similarities between ADBE and the proposed endocytic mechanism for DD synaptic remodeling, we have also identified several differences that could be related to the strikingly different outcomes of synaptic maintenance vs destruction. First, during ADBE, Syndapin is proposed to recruit N-WASP to activate the Arp2/3 complex (Alexandros C. Kokotos & Low, 2015). However, N-WASP/WSP-1 protein is dispensable for remodeling GABAergic synapses (Figure 3.5). In contrast, the Wave Regulatory Complex (WRC), which also activates Arp2/3 (Machesky et al., 1999), is necessary and functions downstream of UNC-8-dependent synapse elimination (Figures 3.5 and 3.8). The observation that WRC, but nor WSP-1, is required for DD synaptic recycling mechanism is also consistent with the finding that WRC drives endocytosis in the *C. elegans* intestine and coelomocytes (F. B. Patel & Soto, 2013) (Figure 3.8).

Second, we determined that an additional F-BAR protein, TOCA-1, also promotes DD remodeling. Toca1 is an F-BAR protein that can activate either N-WASP or the WRC (Fricke et al., 2009; Giuliani et al., 2009; Ho et al., 2004). In DD neurons, we found that TOCA-1 localizes to a perisynaptic region, which is also occupied by dynamin (Weimer et al., 2006), and that it functions in a parallel, partially redundant, pathway with UNC-8/SDPN-1 (Figures 3.6, 3.7, 3.9). The identification of these two parallel pathways promoting branched-actin polymerization highlights the importance of coordinated stimulation of actin polymerization during DD remodeling.

Actin polymerization promotes presynaptic refinement

Our in vivo live-imaging confirmed that actin polymerization increases during the onset of DD remodeling and that regions of high actin dynamics correlate with the separation of transient RAB-3 clusters from stable synapses (Figure 3.10). We also showed that actin polymerization is reduced in *toca-1* and *unc-8* mutants and correlates with fewer transient RAB-3 events and with delayed elimination of stable RAB-3 clusters (Figure 3.11). Decreased actin polymerization in *toca-1* mutant animals is consistent with the established role of TOCA-1 in promoting branched-actin polymerization (Fricke, Gohl, & Bogdan, 2010; Giuliani et al., 2009; Ho et al., 2004). And, the observed actin polymerization defect in *unc-8* mutants is consistent with our finding that the F-BAR protein, syndapin/SDPN-1, which can also recruit nucleators of branched-actin polymerization (Kessels & Qualmann, 2004) functions downstream of UNC-8 (Figure 3.4). Ablation of both UNC-8/SDPN-1 and TOCA-1 pathways simultaneously, by creating for example a *toca-1; unc-8* double mutant should confirm further reduction in actin dynamics and transient RAB-3::GFP. Our finding that at least two different pathways regulate actin polymerization during DD remodeling also highlights the need for free barbed ends in order to promote Arp2/3-dependent nucleation, similar to the regulation of the branched actin network at the leading edge of migrating cells (Falet et al., 2002; Pollard & Borisy, 2003). Consistent with this idea, a previous

report showed that the Ca^{++}-sensitive F-actin severing protein, Gelsolin, promotes DD synapse elimination (L. Meng et al., 2015). We propose that the role of Gelsolin during DD remodeling might not be the destruction of the synaptic actin cytoskeleton for synapse collapse as previously proposed (L. Meng et al., 2015), but rather for liberating barbed ends for restructuring the actin cytoskeleton to drive endocytosis. The additional observation that Gelsolin is Ca^{++}-sensitive (Kinosian et al., 1998), also suggests that synaptic Ca^{++} levels maintained by UNC-8 (Chapter II) might be important to trigger Gelsolin activation.

Our in vivo imaging of RAB-3 and actin dynamics revealed increased actin polymerization as well as mobile RAB-3 particles transiting between ventral DD presynaptic domains during the onset of DD synaptic remodeling (Figure 3.10). The appearance of transient presumptive synaptic vesicle clusters (i.e., mobile GFP::RAB-3 particles) in intersynaptic regions has been previously proposed to drive the sharing of synaptic vesicles across *en-passant* boutons at mammalian synapses (Darcy et al., 2006; Herzog et al., 2011; Staras et al., 2010). Consistent with our model of endocytosis-mediated distal synaptic vesicle recycling, it was previously demonstrated that the population of synaptic vesicles shared between neighboring boutons arose from recently endocytosed synaptic vesicle membrane (Darcy et al., 2006). Moreover, synaptic vesicle sharing between boutons is also actin-dependent in mammalian synapses (Chenouard et al., 2020; Darcy et al., 2006; Ratnayaka et al., 2011). Thus, here we propose that a mechanism commonly used for local recycling may have been repurposed, in this case, for recycling of synaptic vesicles to distal synapses for circuit refinement.

Synaptic proteins recycle form old to new boutons during circuit refinement

We used a photoconvertible Dendra-2 tag to confirm that native RAB-3 is recycled from ventral boutons for reassembly at nascent dorsal synapses in remodeling DD neurons (Figure 3.15) (Park et al., 2011). RAB-3 recycling was drastically curtailed by RNAi knockdown of the

recycling endosome component, RAB-11. Cell-specific RNAi (csRNAi) of *rab-11* in DD neurons, retarded the removal of RAB-3 from ventral synapses as well as impaired its addition to dorsal DD synapses (Figure 3.13 and 3.16). This combined effect on both synaptic disassembly and construction by *rab-11(csRNAi)*, was replicated in *unc-8; toca-1* double mutants (Figure 3.12). This result is consistent with the idea that the RAB-11-dependent recycling endosomes act downstream of both UNC-8/SDPN-1 and TOCA-1 pathways. Interestingly, *unc-8* and *toca-1* single mutants impair dorsal assembly of photoconverted RAB-3 but do not delay its removal from ventral DD synapses, perhaps due to overlapping functions. To test this idea, I propose to track the photoconverted signal of Dendra-2::RAB-3 in *toca-1; unc-8* double mutants. This experiment is predicted to phenocopy *rab-11(csRNAi)* (Figure 3.16) and would thus offer further support for a model in which both the UNC-8/SDPN-1 and TOCA-1 pathways feed endocytic material into RAB-11 recycling endosomes for dorsal assembly during DD remodeling.

Different cellular mechanisms remove distinct subsets of presynaptic terminals

Interestingly, although both F-BAR proteins SDPN-1 and TOCA-1 promote endocytic recycling in the epithelium of *C. elegans*, each protein mediates recycling of different cargoes (Bai & Grant, 2015; Gleason et al., 2016). Similarly, our results point to distinct roles for SDPN-1 and TOCA-1 in synaptic remodeling. For example, the *sdnp-1* mutant impairs the elimination of the synaptic vesicle protein RAB-3 (Figure 3.4) but not that of the active zone component CLA-1 (Figure 3.18). Conversely, TOCA-1 appears to have a minor role in the elimination of RAB-3, (Figure 3.7 and Figure 3.11) but is required for removal of CLA-1 from remodeling DD synapses (Figure 3.18). This observation is notable because it demonstrates that different F-BAR proteins may recognize independent motifs or adaptor proteins at the synaptic membrane to distinguish the specific cargoes that they will endocytose. Consistent with this idea, recent work has shown that endocytic recycling is not a passive process that captures any membrane protein but that it

can be highly selective; specific motifs determine which transmembrane proteins will be endocytosed and the recycling route it will follow (Cullen & Steinberg, 2018). Thus, we propose that SDPN-1, which is activated by UNC-8, triggers endocytosis and distal recycling of synaptic vesicle proteins, whereas TOCA-1 primarily drives the endocytosis of proteins that maintain and organize the active zone. For example, TOCA-1 could be acting on the endocytosis of the adhesion protein PTP-3 which acts as a pioneer transmembrane protein in the assembly of synapses, upstream of the arrival of active zone proteins SYD-1, SYD-2 or CLA-1 (Ackley, 2005; M. R. Patel, 2010). Ours is the first description, at the level of effectors, that synaptic remodeling activates complementary cellular routes to eliminate subsets of synaptic proteins. In the next chapter (Chapter IV), we describe the transcriptional regulation of independent pathways that remove exclusive subsets of presynaptic proteins during refinement of the *C. elegans* motor circuit.

ACKNOWLEDGEMENTS

We want to thank Barth Grant for providing the *toca-1 (tm2056)* mutant allele and TOCA-1 cDNA, Erik Jorgenson for providing RAB-3::GFP FLP-ON, Ev Yemini for Nuclear Localization Sequence. Stefanie Wieckert, Nathan Grega, Jenny Schafer and Kari Seedle for expert advice on AiryScan imaging, and time-lapse image acquisition and analysis.

AUTHOR CONTRIBUTIONS

EM images and 3D reconstruction were provided by Ben Mulcahy from the laboratory of Mei Zhen. Siqi Chen assisted in the integration and outcrossing of transgene wdIs124 [Pflp-13::GFP::CLA-1s]; the analysis of wdIs124 in wild type and *toca-1* mutant animals; and the establishment of the

Dendra-2::RAB-3 photoconversion assay. Additionally, Siqi also built plasmids, strains, collected images and analyzed data regarding *arx-5(csRNAi)* with SNB-1::GFP and CLA-1::GFP markers. John Tipps built plasmids, strains, performed imaging and analysis of *unc-8* and *toca-1* mutants with GFP::RAB-3 marker and of *sdpn-1* mutants with the CLA-1::GFP marker at the L4 stage. Leah Flautt built strains and collected images for *sdpn-1* single and *sdpn-1; unc-8* double mutants with the synaptic vesicle marker GFP::RAB-3, and performed *dyn-1*(OE) experiment. Casey Gailey set-up feeding RNAi experiment and collected images for *tax-6* RNAi treatment. José Carlos Zepeda built P*flp-13*::TagRFP::RAB-11 plasmid. The rest of experiments and analysis were performed by Andrea Cuentas-Condori.

Chapter IV

Transcriptional control of parallel-acting pathways that remove specific presynaptic proteins in remodeling neurons

This paper has been published under the same title in the Journal of Neuroscience, 2021.

Miller-Fleming, T. W*., Cuentas-Condori, A*., Palumbos, S., Manning, L., Richmond, J. R., & Miller, D. M. (2021). Transcriptional control of parallel-acting pathways that remove discrete presynaptic proteins in remodeling neurons. *The Journal of Neuroscience.* https://doi.org/10.1523/JNEUROSCI.0893-20.2021

* denotes co-first authorship.

SUMMARY

Synapses are actively dismantled to mediate circuit refinement, but the developmental pathways that regulate synaptic disassembly are largely unknown. We have previously shown that the epithelial sodium channel ENaC/UNC-8 triggers an activity-dependent mechanism that drives the removal of presynaptic proteins liprin-α/SYD-2, Synaptobrevin/SNB-1, RAB-3 and Endophilin/UNC-57 in remodeling GABAergic neurons in *C. elegans* (Miller-Fleming et al., 2016). Here, we report that the conserved transcription factor Iroquois/IRX-1 regulates UNC-8 expression as well as an additional pathway, independent of UNC-8, that functions in parallel to dismantle functional presynaptic terminals. We show that the additional IRX-1-regulated pathway is selectively required for the removal of the presynaptic proteins, Munc13/UNC-13 and ELKS, which normally mediate synaptic vesicle fusion and neurotransmitter release. These findings are

notable because they highlight the key role of transcriptional regulation in synapse elimination during development and reveal parallel-acting pathways that coordinate synaptic disassembly by removing specific active zone proteins. Thus, our finding suggests that synaptic disassembly is not accomplished by en masse destruction but depends on mechanisms that dismantle the presynaptic structure in an organized process.

INTRODUCTION

The nervous system is actively remodeled during development as new synapses are constructed and others are removed to refine functional circuits. Although synaptic assembly has been extensively investigated, synapse elimination is a less understood phenomenon despite its widespread occurrence (Goda & Davis, 2003; Sudhof, 2018). In some cases, synaptic remodeling is limited to a specific developmental stage in which activity drives circuit plasticity. These “critical periods” are indicative of the necessary role of genetic programs that define specific developmental windows for activity-induced remodeling. Thus, synaptic remodeling mechanisms are likely to depend on the combined effects of both transcriptionally-regulated and activity-dependent pathways (Hensch, 2004; Hong & Chen, 2011; Kano & Watanabe, 2019).

In *C. elegans*, synapses in the GABAergic motor circuit are relocated by a stereotypical remodeling program during early larval development (Cuentas-Condori & Miller, 2020). Dorsal D (DD) motor neurons are generated in the embryo and initially synapse with ventral body muscles (Figure 4.1A). During the first larval stage, presynaptic domains are removed from ventral DD processes and then reassembled in the dorsal nerve cord (Figure 4.1B) (Hallam & Jin, 1998; White et al., 1978). Postembryonic Ventral D (VD) neurons are born during this early larval period (Sulston, 1976) and synapse exclusively with ventral muscles (Figure 4.1B). In the resultant

mature circuit, GABAergic output alternates between dorsal (DD) and ventral (VD) muscles for sinusoidal movement (White et al., 1976, 1986).

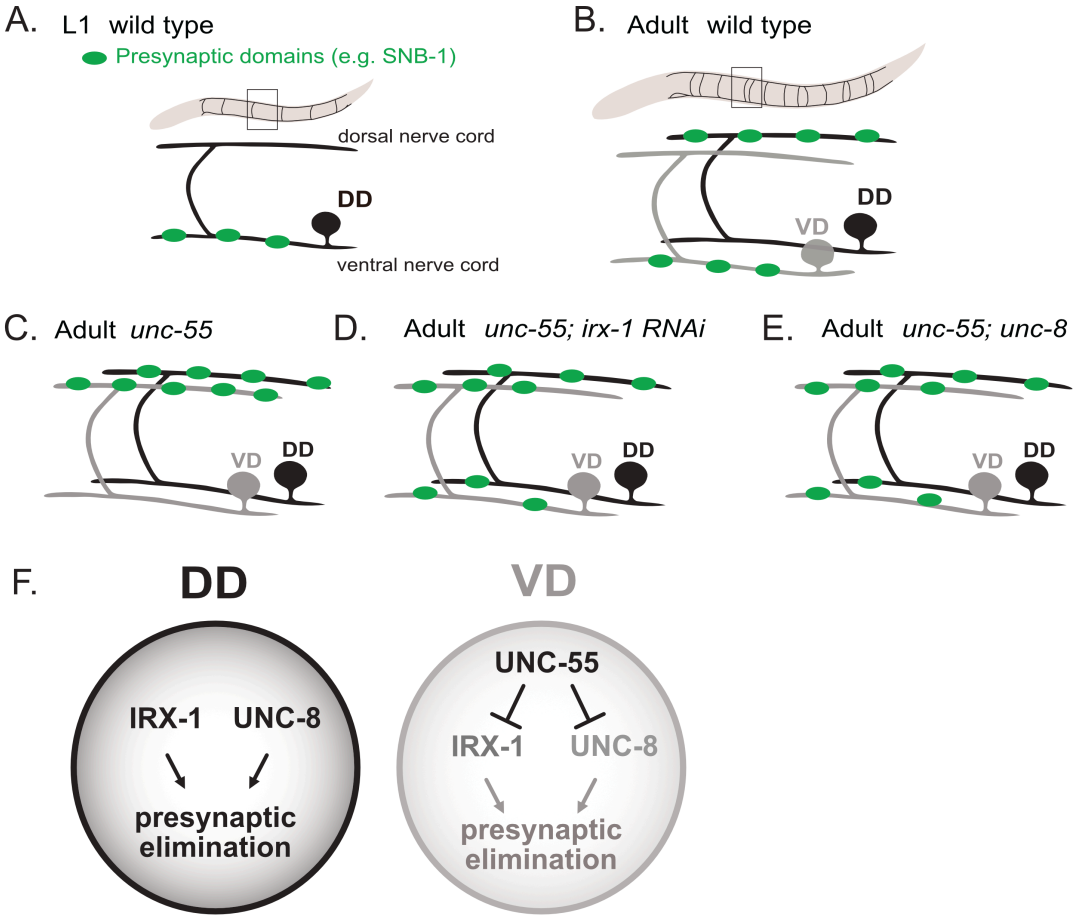

Figure 4. 1. A transcriptional program regulates GABAergic neuron synaptic remodeling

A. DD motor neurons innervate ventral muscles in early L1 stage larvae. GFP-tagged synaptobrevin (SNB-1::GFP) (green puncta) marks GABAergic presynaptic domains.
B. DD synapses are relocated to the dorsal nerve cord during early larval development as postembryonic VD class GABAergic motor neurons are generated to synapse with ventral muscles. These DD and VD connections are maintained in the adult motor circuit.
C. In *unc-55* mutants, both DD and VD presynaptic domains are relocated to the dorsal nerve cord.
D. RNAi knock down of the Iroquois family homeodomain transcription factor, IRX-1, antagonizes GABAergic neuron synaptic remodeling in *unc-55* mutants (Petersen et al., 2011).
E. Mutations that disable the DEG/ENaC cation channel, UNC-8, impair the removal of DD and VD GABAergic presynaptic domains in *unc-55* mutants (Miller-Fleming et al., 2016).
F. IRX-1 and UNC-8 are normally expressed in DD neurons to drive disassembly of the presynaptic apparatus. The COUP-TF transcription factor, UNC-55, blocks expression of IRX-1 and UNC-8 in VD neurons to prevent synapse elimination.

The COUP-TF transcription factor, UNC-55, is selectively expressed in VD neurons to prevent synaptic remodeling (Shan et al., 2005; H. Zhou & Walthall, 1998); in *unc-55* mutants, VD neurons initially synapse with ventral muscles but then mimic the native DD remodeling program by relocating presynaptic domains to the dorsal nerve cord (Figure 4.1C) (Petersen et al., 2011; Thompson-Peer et al., 2012). The idea that UNC-55 normally blocks expression of genes that drive synaptic remodeling is supported by the finding that forced expression of UNC-55 in DD neurons is sufficient to prevent the native remodeling program (Shan et al., 2005). In earlier work, we exploited the synaptic remodeling phenotype of *unc-55* mutants in cell-specific profiling experiments to identify UNC-55 targets. An RNAi screen detected a subset of *unc-55*-regulated genes that are required for synaptic remodeling. For example, the homeodomain transcription factor, Iroquois/IRX-1, is ectopically expressed in *unc-55* mutant VD neurons which consequently undergo aberrant synaptic remodeling. RNAi knockdown of Iroquois/IRX-1, however, prevented the removal of GABAergic presynaptic domains from the ventral nerve cord in *unc-55* mutants (Figure 4.1D) (Petersen et al., 2011). Similarly, the DEG/ENaC cation channel subunit gene, *unc-8*, is upregulated in *unc-55* mutants and an *unc-8* loss-of-function allele also antagonized VD synaptic remodeling (Figure 4.1E). Thus, these results argue that IRX-1 and UNC-8 are required for presynaptic elimination of remodeling GABAergic neurons. Additional experiments confirmed that both the Iroquois/IRX-1 and DEG/ENaC/UNC-8 normally promote the native DD remodeling program (Figure 4.1F) (Miller-Fleming et al., 2016; Petersen et al., 2011).

DEG/ENaC proteins function as cation channels and we have previously shown that UNC-8 gates sodium influx (Matthewman, Miller-Fleming, Miller, & Bianchi, 2016; Ying Wang et al., 2013). The resultant membrane depolarization arising from UNC-8 channel activity is predicted to open local voltage gated calcium channels (VGCC) which we have shown function with UNC-8 to promote presynaptic disassembly. Based on these findings we have proposed that UNC-8 promotes presynaptic disassembly in a pathway that depends on intracellular calcium and neural

activity (Miller-Fleming et al., 2016). Here we show that DEG/ENaC/UNC-8 is transcriptionally-regulated by Iroquois/IRX-1 to remove a core group of presynaptic components including liprin-α/SYD-2, Synaptobrevin/SNB-1, RAB-3 and Endophilin/UNC-57. Surprisingly, proteins involved in synaptic vesicle priming, UNC-13/Munc-13 and ELKS, are not disassembled by UNC-8 but are removed by a separate pathway regulated by IRX-1/Iroquois. Together, these findings show that remodeling of GABAergic synapses depends on the combined effects of neural activity (UNC-8) and developmentally-regulated transcription (IRX-1). Thus, our work shows that synaptic disassembly can be orchestrated by parallel-acting mechanisms that selectively target molecularly distinct components of the presynaptic apparatus for removal.

MATERIALS AND METHODS

Worm breeding

C. elegans strains were cultured at either 20° C or 23° C as previously described on standard nematode growth medium seeded with OP50 (Brenner, 1974). The mutant alleles and strains used in this study are outlined in Tables 4.1 and 4.2.

Microscopy

Confocal Microscopy

Larval or young adult animals were immobilized on 2% agarose pads with 15mM levamisole as previously described (Smith et al., 2010). Z-stack images (Figure 4.3A, 4.3D, 4.7A-F and 4.8A-F) were collected on a Leica TCS SP5 confocal microscope using a 63X oil objective (0.5 µm/step), spanning the focal depth of the ventral nerve cord GABA neurons and synapses. Leica Application Suite Advanced Fluorescence (LAS-AF) software was used to generate maximum intensity projections. Ventral nerve cord images were straightened using an ImageJ

plug-in. Z-stack images (Figure 4.4, 4.5I, 4.9 and 4.10) were acquired with Nikon confocal A1R using Apo Fluor 40X/1.3 and 60X/1.4 N.A. oil objective (0.3 µm/step).

Electron Microscopy

Young adult hermaphrodites of each strain were prepared for high-pressure freeze (HPF) fixation as described (Miller-Fleming et al., 2016; Rostaing, Weimer, Jorgensen, & Triller, 2004). 10–15 animals were loaded into a specimen chamber filled with *E. coli.* The specimens were frozen rapidly in a high-pressure freezer (Leica HPM100) at -180°C and high pressure. Freeze substitution was performed on frozen samples in a Reichert AFS machine (Leica, Oberkochen, Germany) with 0.1% tannic acid and 2% OsO_4 in anhydrous acetone. The temperature was kept at -90°C for 107 h, increased at 5°C/h to -20°C, and kept at -20°C for 14h. The temperature was then increased by 10°C/h to 20°C. Fixed specimens were embedded in Epon resin after infiltration in 50% Epon/acetone for 4h, 90% Epon/acetone for 18h, and 100% Epon for 5 hours. Embedded samples were incubated for 48h at 65°C. All specimens were prepared using the same fixation procedure and labeled with anonymous tags so that the examiner was blinded to genotype. Ultrathin (40 nm) serial sections were cut using an Ultracut 6 (Leica) and collected on formvar-covered, carbon-coated copper grids (EMS, FCF2010-Cu). Grids were counterstained in 2% aqueous uranyl acetate for 4 min, followed by Reynolds lead citrate for 2 min. Images were obtained on a Jeol JEM-1220 (Tokyo, Japan) transmission electron microscope operating at 80 kV. Micrographs were collected using a Gatan digital camera (Pleasanton, CA) at a magnification of 100k. Images were quantified using NIH ImageJ software. Dorsal and ventral cords were distinguished by size and morphology. GABAergic synapses were identified by previously established criteria, including position in the cord as well as the morphology of the synapse. GABAergic synapses are larger than their cholinergic motor neuron counterparts, and the active zones in these synapses form a direct, perpendicular angle with muscle arms. In contrast, the

presynaptic density in cholinergic synapses orient at an acute angle to the muscle, generally 30-45° and are often dyadic. Some images were collected at 30k to aid in identifying synaptic identity based on terminal position in the cord. Two colleagues with expertise in EM reconstruction of the *C. elegans* ventral nerve cord independently reviewed synapse images from each strain to verify identification. Each profile represents an image of a 40 nm section. A synapse was defined as a set of serial sections containing a presynaptic density with two flanking sections either side without presynaptic densities. Synaptic vesicles were identified as spherical, light gray structures with an average diameter of ~30 nm. Synaptic vesicles were considered docked if they were in direct contact with the membrane. Three to five animals were imaged for each genotype. Numbers of profiles for each genotype were (# analyzed / # imaged): wild type = 80/1330, *unc-55; unc-8* = 37/745, *unc-55;irx-1(csRNAi)* = 54/613 for ventral GABAergic synapse evaluation.

Image Analysis

Synapse density counts (Figures 4.3A-F, 4.7G and 4.8G) were collected by tracing segments of the ventral nerve cord using the segmented line tool in ImageJ (VD3 to VD11). Distance in micrometers and gray value plot traces were used to count the number of peaks (synapses) that occur over the specified distance. Synapses were defined as fluorescent peaks that reached a threshold of 25 arbitrary units of fluorescence intensity. Example in Figure 4.3.

NIS Elements 5.2 software was used to produce Figures 4.4, 4.8, 4.9 and 4.10. Synaptic density for each marker (SYD-2::GFP, RAB-3::mCherry, UNC-57::GFP, UNC-10::GFP, endogenous GFP::RAB-3 and endogenous GFP::ELKS-1) was calculated using the General Analysis tool. First, images were preprocessed to subtract background using Rolling Ball Correction. Then, the intensity threshold was defined for each marker and binary objects were filtered by size and circularity. Each object along the nerve cord was considered a synaptic punctum. Density was defined as the number of puncta per 10 µm of dendrite.

FIJI was used to quantify effects of UNC-8(OE) (over-expression) on presynaptic disassembly (Figures 4.7 and 4.8). Z-stacks were collected for the full length of the ventral nerve cord. In Figure 4.7H-K, mCherry-positive VD cells carry an UNC-8 cDNA transgenic array (Miller-Fleming et al., 2016). Neighboring mCherry-positive [e.g., UNC-8(OE)] and mCherry-negative [control] VD neurons were compared to quantify differences in the fluorescence signal for SNB-1::GFP and UNC-13L::GFP due to UNC-8 over-expression. In Figure 4.8J-K, GFP-positive VD neurons carry an UNC-8 cDNA transgenic array. Neighboring GFP-positive [e.g., UNC-8(OE)] and GFP-negative [control] VD neurons were compared to quantify differences in the fluorescence signal. Because unc-8 cDNA transgenic arrays are mosaic with expression limited to a random subset of VD neurons in each animal, data were collected from VD neurons (VD3-VD11) carrying the UNC-8 cDNA (mcherry-positive for Figure 4.7H-K or GFP-positive for Figure 4.8J-K) vs an adjacent control VD neuron that does not carry the array. For results shown in Figures 4.7H-K and 4.8J-K, intensity values were obtained from line scans anterior to the VD cell bodies of interest. Background fluorescence was obtained from a line scan of an adjacent region inside the animal and subtracted from the VD line scans.

Single molecule mRNA Fluorescence In Situ Hybridization (smFISH)

smFISH was performed with custom *unc-8* probes linked to Quasar® 670 (Biosearch Technologies). Synchronized larvae (from either late L1 or early L3 stage) were collected by washing plates with M9, fixed in 4% paraformaldehyde in 1X PBS for 45 min and permeabilized in 70% ethanol for 48 h. Hybridization followed the manufacturer's instructions (http://www.biosearchtech.com/stellarisprotocols) and was performed at 37°C for 16h in Stellaris RNA FISH hybridization buffer (Biosearch Technologies Cat# SMF-HB1-10) containing *unc-8* probe at 1:100. For *irx-1* cell specific RNAi (csRNAi) (Figure 4.2A), all DD motor neurons were marked with *Punc-47*::GFP (*oxIs12*) and specific DDs expressing the *irx-1(csRNAi)* constructs

(*pttr-39::irx-1* sense, *pttr-39::irx-1* antisense) were co-labeled with *Punc-25::*mCherry to distinguish them from DD neurons that did not express the *irx-1(csRNAi)* transgenic array. For *IRX-1(OE)* (IRX-1 over-expression) experiments (Figure 4.2C), GFP-tagged IRX-1 was expressed with the *ttr-39* promotor (*pttr-39::IRX-1::*GFP). In this setup, VDs and DDs were marked with *Punc-47::mCherry* (*wpIs39*) and individual DDs or VDs expressing IRX-1(OE) were detected by nuclear-localized IRX-1::GFP (Petersen et al., 2011). For UNC-8(OE) (over-expression) experiments (Figure 4.8H-I), UNC-8 was expressed in DD and VD neurons (*pttr39::*UNC-8) (Miller-Fleming et al., 2016) from a transgenic array also expressing p*unc-25*::GFP to label DD and VD neurons and compared to wild type DD and VD neurons in an *punc-25::*GFP marker strain (*juIs76*) (Huang, Cheng, Tessier-Lavigne, & Jin, 2002). In all cases, cell nuclei were stained with DAPI. Z-stacks were collected in a Nikon spinning disk confocal microscope with optical filters for DAPI, Quasar® 670 and GFP using an Apo TIRF 100X objective (NA=1.49) in 0.2 µm steps spanning the cell body and merged for quantification following 3D-deconvolution in NIS elements. smFISH puncta were defined in Nikon Elements as circular fluorescent spots (circularity filter) that exceeded the Quasar® 670 background signal (e.g., fluorescence threshold). To confirm localization within DD/VD cell soma, only puncta that co-localized with either GFP (Figure 4.2A, 8H) or mCherry (Figure 4.2C) labeled DD/VD cell bodies in both X-Y and Z axes were counted. At least 30 worms were scored for each group and the Mann-Whitney test used to determine significance (n >45 neurons). As a positive control, *unc-8* smFISH staining was noted in adjacent DA and DB ventral-cord neurons for all samples to confirm successful hybridization.

Electrophysiology

The *C. elegans* dissection and electrophysiological methods were as previously described (Miller-Fleming et al., 2016; Richmond & Jorgensen, 1999). Animals were immobilized along the dorsal axis with Histoacryl Blue glue, and a lateral cuticle incision was made with a hand-held

glass needle, exposing ventral medial body wall muscles. Muscle recordings were obtained in the whole-cell voltage-clamp mode using an EPC-10 patch-clamp amplifier and digitized at 1 kHz. The extracellular solution consisted of 150 mM NaCl, 5 mM KCl, 5 mM $CaCl_2$, 4 mM $MgCl_2$, 10 mM glucose, 5 mM sucrose, and 15 mM HEPES (pH 7.3, ~340 mOsm). The intracellular solution consisted of 120 mM KCl, 4 mM KOH, 4 mM $MgCl_2$, 5 mM (N-tris[Hydroxymethyl] methyl-2-aminoethane-sulfonic acid), 0.25 mM $CaCl_2$, 4 mM Na_2ATP, 36 mM sucrose, and 5 mM EGTA (pH 7.2, ~315 mOsm). GABAergic miniIPSCs and hyperosmotic responses were acquired at a holding potential of -60 mV by pressure-ejecting extracellular saline containing an additional 500 mOsm of sucrose. 10 mM d-tubocurare was added to both the extracellular solution and the pressure ejection pipette to block cholinergic hyperosmotic currents. Data were acquired using Pulse software (HEKA, Southboro, Massachusetts, United States) on a Dell computer. Subsequent analysis and graphing were performed using Pulsefit (HEKA), Mini analysis (Synaptosoft Inc., Decatur, Georgia, United States) and Igor Pro (Wavemetrics, Lake Oswego, Oregon, United States).

Molecular Biology

Generation of the punc-25::UNC-13L::GFP transgenic line

We used the In-Fusion cloning kit (Takara) to amplify the cDNA of the long isoform of UNC-13 (UNC-13L) from a plasmid provided by J. Kaplan (pTWM88). This fragment was ligated into a vector containing the *punc-25* GABA promoter and a C-terminal GFP tag. The resulting plasmid, pTWM90, was injected into *unc-13 (e51)* null mutants at 25 ng/µl with the co-injection marker *pmyo-2::mCherry* (2 ng/ µl). This transgenic array was integrated by x-ray irradiation and outcrossed for three generations to generate stable transgenic lines for analysis.

Generation of the pflp-13::flippase transgenic line

We used the In-Fusion cloning kit (Takara) to amplify the flippase sequence from a plasmid provided by the Jorgensen lab pMLS262 (Addgene # 73718). This fragment was ligated into a vector containing the *pflp-13* DD promoter. The resulting plasmid, pACC98, was injected at 25 ng/µl with the co-injection marker *pmyo-2::mCherry* (2 ng/ µl) generating the array *wdEx1127*. This array was later crossed with *rab-3(ox785), elks-1(wy1162)* and *elks-1(wy1162) unc-8(syb3726)* to activate GFP-tagging in DD neurons.

Generation of unc-8 (syb3726) in wy1162 animals

Sunybiotech used CRISPR/Cas9 to generate a deletion allele, *unc-8(syb3726),* in *wy1162* [*elks-1* FLP-ON GFP] animals. *unc-8(syb3726)* removes 6977 nucleotides from the R13A1.4b.1 *unc-8* transcript except for the first 8 base pairs and the last 44 nucleotides and thus is a likely null allele.

Feeding RNA Interference Experiments

Bacteria producing either double-stranded *irx-1* RNA or containing the RNAi empty vector were seeded on NGM plates and stored at 4°C for up to 1 week. Four L4 *unc-55, unc-55; eri-1,* or *unc-55; unc-8* animals were grown on each single RNAi plate at 23°C until progeny reached the L4 stage. Progeny were picked to fresh RNAi plates and the ventral synapses were quantified.

Movement Assays

Animals were first tapped on the tail to ensure that they were capable of forward locomotion, then tapped on the head to assess ability to execute backward locomotion. Animals were binned into the following categories: “unc” (uncoordinated: coil ventrally immediately upon tapping), “initiate backing” (initiate backwards movement but stop), and “wild-type” (sustain

backward locomotion with at least two body bends). In Figure 4.6, the “wild-type” and “initiate backing” categories were grouped into a single “initiate backing” category.

IRX-1 cell-specific RNAi

The *irx-1(csRNAi)* array (*wdEx959*) was outcrossed from NC2975 (He et al., 2015) and combined with synaptic markers displayed in Figure 4.5, 4.7, 4.9 and 4.10 using conventional genetic methods.

Experimental Design and Statistical Analysis

For samples that are not normally distributed, the Mann-Whitney test was used to compare two groups and determine significance. For comparisons between three or more groups, we used the Kruskal-Wallis test with multiple comparison. For samples that are normally distributed, Student’s T-test was used to compare two groups and One-Way ANOVA with Bonferroni correction for multiple comparisons among more than two groups. Figure legends specify the statistical test used in each case and the number of independent measurements (N) evaluated.

Table 4. 1. Mutant alleles and genotyping primers used in this study

Allele	Source	Genotyping Primer Sequences
unc-8(tm5052) IV	NBRP	TGGGGCCCTAATAATTTCGA
		AGTGACAGTATGAAGCCAGG
unc-55(e1170) I	CGC	TAAGGACTACACGGATCCTG
		CCCAAGAAAGAAAAGAGAGGT
eri-1(mg366) IV	CGC	CATGCAATTTCAATGCCTTTTA
		TGCATCATCCAATCCACTATGT
unc-13(e51) I	CGC	TAGGCCTCCAAACGGACATA
		TGTCCTTCTTCGTAGCCTTC
unc-8(syb3726) IV	Sunybiotech	CTCCTACACCCTCTTCTGCT
		CCGAGCAAATGTTTCAACCT

Table 4. 2. Strains used in this chapter

Strain	Genotype
NC2758	*wdEx959 [pttr-39::irx-1 cDNA; pttr-39::irx-1 reverse; pttr-39::mcherry; str-1::GFP]*
NC2325	*unc-119; wdEx753[pttr-39::IRX-1::GFP; unc-119+]*
KP5348	*nuIs279 [punc-25::UNC-57::GFP;punc-25::mCherry::RAB-3]*
NC2984	*unc-55(e1170)* I; *nuIs279*
NC3279	*unc-55 (e1170)* I; *nuIs279*; *eri-1(mg366)* IV
NC2873	*unc-55(e1170)* I; *unc-8(tm5052)* IV; *nuIs279*
ZM54	*hpIs3[punc-25::SYD-2::GFP; lin-15+]* X
NC1849	*unc-55(e1170)* I; *hpIs3* X
NC1910	*unc-55 (e1170)* I; *eri-1 (mg366)* IV; *hpIs3* X
NC2874	*unc-55(e1170)* I; *unc-8(tm5052)* IV; *hpIs3* X
NC2388	*unc-55(e1170)* I*; unc-8(tm5052) juIs1* IV
EG5052	*oxIs351[punc-47:ChR2::mCherry; lin-15+ LITMUS 38i]* X
NC2211	*unc-55(e1170)* I; *oxIs351* X
NC2807	*unc-55(e1170)* I; *unc-8(tm5052)* IV; *oxIs351* X
NC2212	*unc-55 (e1170)* I; *oxIs351* X; *wdEx686[irx-1 csRNAi]*
ZM1344	*hpIs61 [punc-25::UNC-10::GFP]* II
NC2872	*unc-55(e1170)* I; *hpIs61* II
NC2991	*unc-55(e1170)* I; *hpIs61* II; unc-8 (tm5052) IV
NC3337	*unc-55(e1170)* I; *hpIs61* II; *wdEx959* [*pttr-39*::irx-1 cDNA; *pttr-39*::irx-1 reverse; *pttr-39*::mcherry; *pstr-1*::GFP]
NC2324	*unc-8 (tm5052)* IV
CB1170	*unc-55 (e1170*) I
NC3326	*unc-55 (e1170)* I; *unc-8 (tm5052)* IV
NC3342	*unc-55(e1170*) I*; unc-8(tm5052)* IV*; wdEx959*
NC3330	*wdIs97 [punc-25::UNC-13L::GFP; pmyo-2::mCherry] ; unc-13(e51)* I
NC3216	*unc-55(e1170) unc-13(e51)* I; *wdIs97*
NC3341	*unc-55(e1170) unc-13(e51)* I; *unc-8 (tm5052)* IV; *wdIs97*
NC3339	*unc-55(e1170) unc-13(e51)* I; *wdIs97; wdEx959 [pttr-39::irx-1 cDNA; pttr-39::irx-1 reverse; pttr-39::mcherry; str-1::GFP]*
NC3511	*juIs1 [punc-25::SNB-1::GFP] IV; wdEx1104 [pttr39::UNC-8*cDNA*; punc-25::mCherry::RAB-3; pstr-1::GFP]*
NC3510	*unc-13(e51) I; wdIs105 [punc-25::UNC13L::GFP]; wdEx1102 [pttr39::UNC8cDNA; punc-25::mCherry::RAB-3; pstr-1::GFP]*
KP5085	*nuIs249 [punc-25-ELKS-1::tdTomato; myo-3::NLS::GFP]*
NC3334	*unc-55(e1170)* I*; nuIs249*
NC3333	*unc-55(e1170)* I*; unc-8(tm5052)* IV*; nuIs249*
NC3708	*nuIs249; wdEx1160 [pttr-39::UNC-8*cDNA*; punc-25::GFP; pmyo-2::RFP]*
CZ13799	*juIs76 [unc-25p::GFP + lin-15(+)] II*
NC3629	*rab-3 (ox785[GFP-FLPON::RAB-3 + loxp UNC-119+ loxp]) II; unc-19 III; wdEx1127 [pflp-13::flippase; pmyo-2::RFP]*
NC3683	*rab-3 (ox785) II; unc-8 (tm5052) IV; wdEx1127 [pflp-13::flippase; pmyo-2::RFP]*

NC3703	*rab-3 (ox785) II; wdEx1127 [pflp-13::flippase; pmyo-2::RFP]; wdEx959 [pttr-39::irx-1 cDNA; pttr-39::irx-1 reverse; pttr-39::mcherry; pstr-1::GFP]*
NC3704	*rab-3 (ox785) II; unc-8(tm5052) IV; wdEx1127 [pflp-13::flippase; pmyo-2::RFP]; wdEx959 [pttr-39::irx-1 cDNA; pttr-39::irx-1 reverse; pttr-39::mcherry; pstr-1::GFP]*
NC3696	*elks-1(wy1162, frt::PEST-degron::operon::frt = GFP::flp-on at N-terminus) IV; wdEx1127 [pflp-13::flipasse; pmyo-2::RFP]*
NC3702	*elks-1(wy1162) IV; wdEx1127 [pflp-13::flipasse;pmyo-2::RFP]; wdEx959[pttr-39::irx-1 cDNA; pttr-39::irx-1 reverse; pttr-39::mcherry; pstr-1::GFP]*
NC3803	*elks-1(wy1162) unc-8(syb3726) IV; wdEx1127 [pflp-13::flipasse; pmyo-2::RFP]*

RESULTS

The homeodomain transcription factor, Iroquois/IRX-1, drives DEG/ENaC/UNC-8 expression in remodeling GABAergic neurons

In previous work, we used gene expression profiling and an RNAi screen to identify protein-encoding genes that promote presynaptic disassembly in remodeling GABAergic neurons (Petersen et al., 2011). These studies determined that the homeobox transcription factor Iroquois/IRX-1 and the DEG/ENaC ion channel subunit UNC-8 promote removal of the presynaptic vesicular SNARE protein, synaptobrevin/SNB-1 (Figure 4.1D-E) (Miller-Fleming et al., 2016; Petersen et al., 2011). Because both IRX-1/Iroquois and DEG/ENaC/UNC-8 are expressed in remodeling DD neurons, we investigated the hypothesis that Iroquois/IRX-1 functions as a transcription factor to regulate DEG/ENaC/UNC-8 expression. First, we used single-molecule Fluorescent In-Situ Hybridization (smFISH) to confirm expression of *unc-8* transcripts in remodeling (control) DD neurons (Figure 4.2). We note that *unc-8* is highly expressed in adjacent DA and DB cholinergic neurons as previously reported (Miller-Fleming et al., 2016; Ying Wang et al., 2013). We then targeted *irx-1* in DD neurons with cell-specific RNAi (csRNAi) (See Methods) and detected significantly fewer *unc-8* transcripts in comparison to untreated (control) DD neurons (Figure 4.2A-B). These results are consistent with the idea that Iroquois/IRX-1 is required for DEG/ENaC/UNC-8 expression in DD neurons.

GFP reporters for *irx-1* and *unc-8* are not expressed in wild-type VD neurons which normally do not remodel. However, forced expression of Iroquois/IRX-1 in VD motor neurons is sufficient to trigger VD remodeling and drive the elimination of VD presynaptic terminals (Miller-Fleming et al., 2016; Petersen et al., 2011). Thus, we next asked if Iroquois/IRX-1 over-expression [*irx-1(OE)*] could also induce *unc-8* expression in VD neurons. smFISH quantification confirmed that *unc-8* transcripts are elevated in *irx-1(OE)* VD neurons in comparison to controls (Figure

4.2C-D). Together, these results demonstrate that the transcription factor, Iroquois/IRX-1, is both necessary and sufficient for ENaC/UNC-8 expression in remodeling GABA neurons (Figure 4.2E).

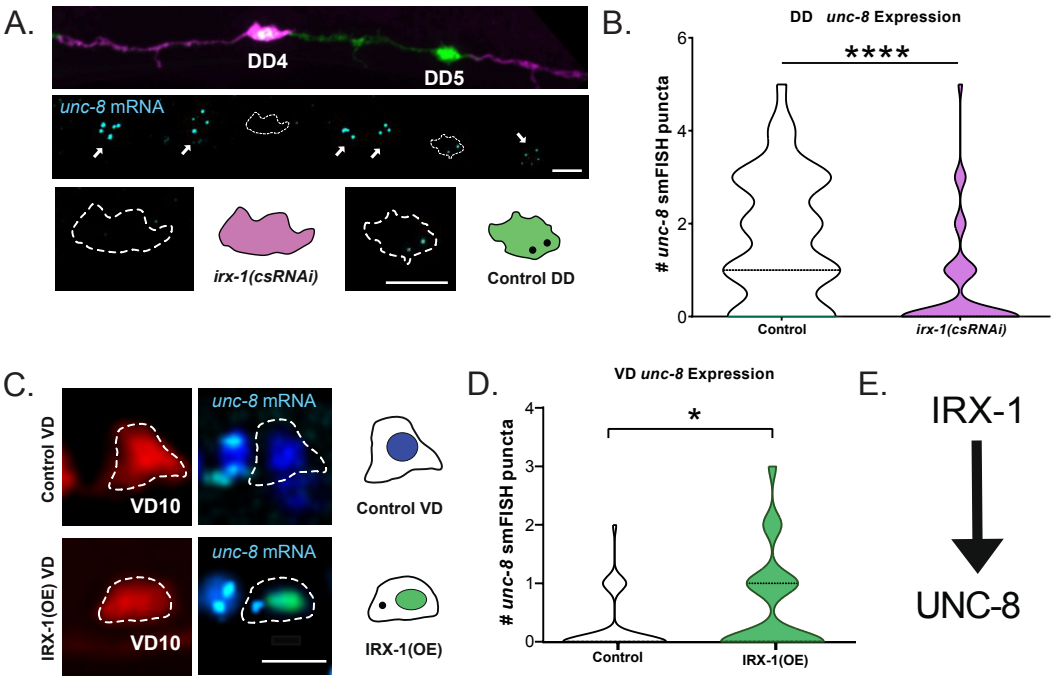

Figure 4. 2. IRX-1 drives expression of UNC-8/DEG/ENaC in GABAergic neurons.

A. *irx-1(csRNAi)* (cell-specific RNAi) blocks *unc-8* expression in DD neurons. (Top) Mosaic expression of *irx-1(csRNAi)* (magenta) in DD4 vs adjacent control DD5 neuron (green) in the L1 ventral nerve cord. (Middle) smFISH puncta for *unc-8* transcripts (cyan). Dashed lines demarcate DD cell soma and arrows denote *unc-8* smFISH puncta in adjacent cholinergic motor neurons. (Bottom) Dashed outlines and graphical representations depict *irx-1(csRNAi)*-marked DD4 neuron (magenta) and *unc-8* smFISH puncta in control DD5 neuron (green). Scale bar = 5μm.
B. Quantification of *unc-8* smFISH puncta in DD neurons. Violin plots for *unc-8* smFISH puncta in control (white) (n = 49) vs *irx-1(csRNAi*) (magenta) (n = 50) in L1 stage DD motor neurons. Dashed line represents median. Mann-Whitney test, P<0.0001
C. In the wild-type, VD neurons do not express *irx-1* or *unc-8* but forced expression of IRX-1 in VD neurons [*irx-1(OE)*] is sufficient to activate *unc-8* transcription. Representative images of VD neurons (VD10) in control (top) vs *irx-1(OE)* VD neurons (bottom). (Left) Dashed lines denote VD cell soma marked with mCherry. (Right) DAPI (dark blue) labels the nucleus. *unc-8* smFISH probe (cyan puncta). Note IRX-1::GFP (green) labels VD10 nucleus in *irx-1(OE)* (bottom right) . Scale bar = 5 μm.
D. Quantification of *unc-8* smFISH puncta in VD motor neurons. Violin plots for *unc-8* smFISH puncta in control`(white) (n = 40) and *irx-1(OE)* (green) (n = 50) in L3 stage VD neurons. Dashed line represents median. Mann-Whitney test, P = 0.0184.
E. Working model: IRX-1 promotes UNC-8 expression in GABAergic motor neurons.

Iroquois/IRX-1 drives a DEG/ENaC/UNC-8-dependent mechanism of presynaptic disassembly.

In addition to promoting the removal of Synaptobrevin/SNB-1::GFP from ventral presynaptic domains in remodeling GABAergic neurons (Figure 4.1), UNC-8 also drives the elimination of RAB-3/GTPase, liprin-α/SYD-2 and endophilin/UNC-57 (Miller-Fleming et al., 2016; Petersen et al., 2011). RAB-3/GTPase interacts with synaptic vesicles for exocytosis (Mollard et al., 1992; Nonet et al., 1997); liprin-α/SYD-2 is a scaffolding protein that defines the presynaptic dense projection area (Kittelmann, Hegermann, et al., 2013; Stigloher et al., 2011; Mel Zhen & Jin, 1999); and endophilin/UNC-57 mediates synaptic vesicle endocytosis and recycling (Schuske et al., 2003; S. Yu, Jánosi, Liewald, Wabnig, & Gottschalk, 2018).

If Iroquois/IRX-1 activates UNC-8 expression as predicted by our smFISH results (Figure 4.2), then Iroquois/IRX-1 should also promote removal of these additional presynaptic markers. To test this possibility, we exploited *unc-55* mutants in which the VD GABAergic presynaptic domains are eliminated due to ectopic activation of the native DD remodeling program (H. Zhou & Walthall, 1998) (Figure 4.1C). In this paradigm, removal of ventral GABAergic synapses in *unc-55* mutants is prevented by mutations that disable the pro-remodeling program (Petersen et al., 2011). For example, ventral mCherry::RAB-3 puncta are largely eliminated from GABAergic synapses in *unc-55* mutant animals but a significant fraction is retained in *unc-55; unc-8* double mutants (Figure 4.3A). This result indicates that UNC-8 function is required for the efficient removal of presynaptic RAB-3 in remodeling GABAergic neurons (Miller-Fleming et al., 2016). As an upstream activator of *unc-8* expression, Iroquois/IRX-1 is also predicted to remove mCherry::RAB-3 from ventral synapses of *unc-55* mutants. As expected, RNAi knockdown of *irx-1* prevents the elimination of ventral RAB-3::mCherry puncta in *unc-55* mutants (Figures 4.3A-C).

Additional experiments showed that ablation of either *unc-8* or *irx-1* also blocks the removal of SYD-2::GFP (Figure 4.3D-E) in the ventral nerve cord of *unc-55* mutants. Since Iroquois/IRX-1

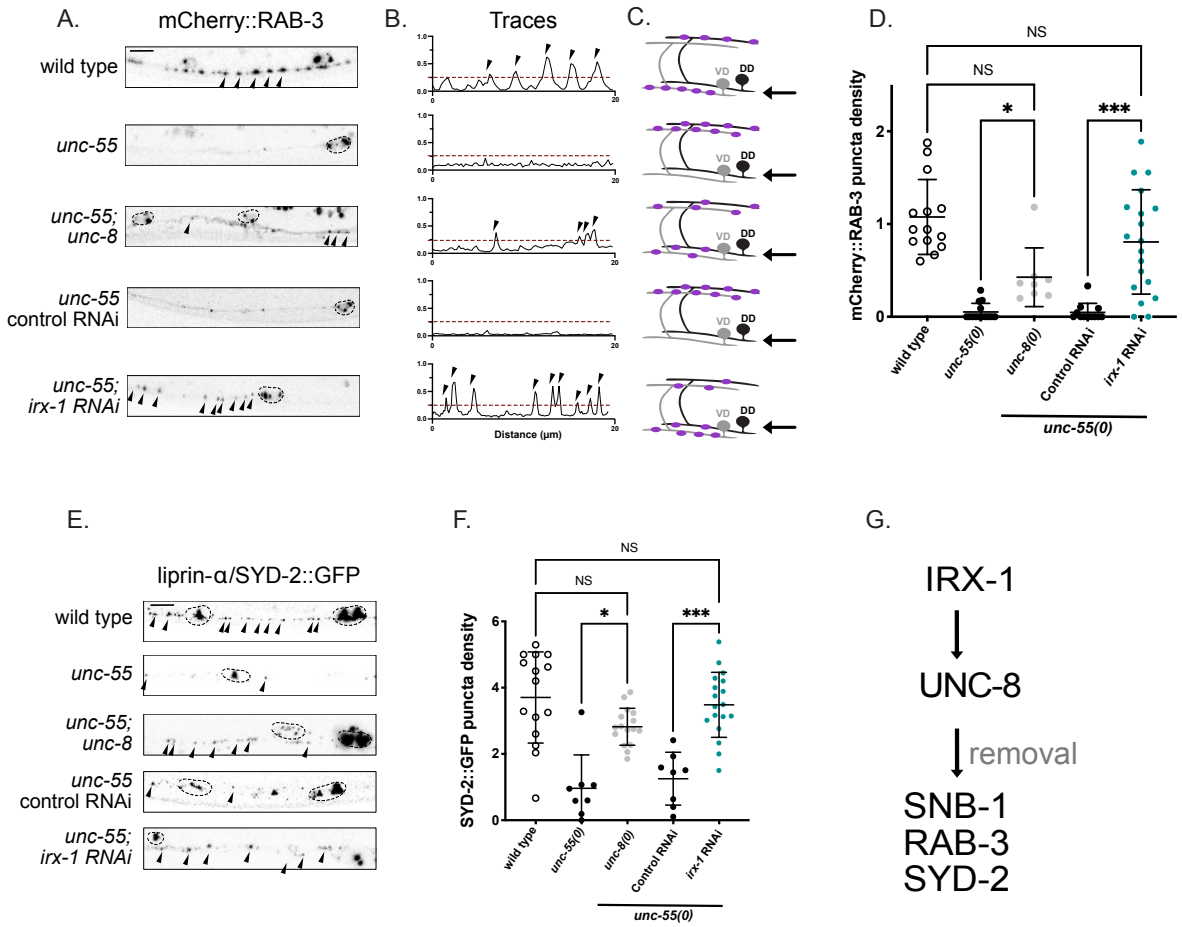

Figure 4. 3. IRX-1/Iroquois drives UNC-8 expression to dismantle the GABAergic presynaptic apparatus.

A. Representative images of RAB-3::mCherry-labeled GABA neuron synapses (arrowheads) in the ventral nerve cord of adult animals. Note that RAB-3::mCherry puncta are removed from the ventral nerve cord of *unc-55* mutants in which both DD and VD neurons remodel (See Figure 4.1C) but are partially retained in *unc-55; unc-8.* Similarly, residual RAB-3::mCherry puncta are detectable in *unc-55; irx-1* RNAi but not in unc-55 RNAi control animals.
B. Representative calculation of peak number (puncta). Line scans were drawn along the ventral nerve cord of each animal on the left. Peaks that passed a 25% threshold (dashed line) were counted (arrowheads).
C. Schematics of mCherry::RAB-3 puncta in each genotype. Arrow denotes ventral region depicted in panels A. and B.
D. RAB-3::mCherry puncta density quantified for each genotype: wild type (1.07 ± 0.4), *unc-55; unc-8* (0.43 ± 0.3 puncta/10 µm) and *unc-55; irx-1(RNAi)* (0.81 ± 0.6 puncta/10 µm) show more ventral RAB-3::mCherry-marked puncta than *unc-55* (0.05 ± 0.1 puncta/10 µm) and *unc-55* control RNAi (0.05 ± 0.1 puncta/10 µm). Data are Mean ± SD. * = p<0.05, *** = p<0.001. NS is not significant. Kruskal-Wallis test with multiple comparison because *unc-55, unc-55; unc-8 and unc-55* control RNAi samples are not normally distributed. N > 8 animals.
E. Representative images of liprin-□/SYD-2::GFP-labeled GABA neuron synapses (arrowheads) in the ventral nerve cord. Dashed lines demarcate DD and VD cell soma.

F. SYD-2::GFP puncta density (puncta/10 µm) quantified for each genotype: wild type (3.7 ± 1.4), *unc-55* (0.97 ± 1.0), *unc-55; unc-8* (2.82 ± 0.6), *unc-55* control RNAi (1.26 ± 0.8) and *unc-55; irx-1(RNAi)* (3.48 ± 0.9). Data are Mean ± SD. * = $p<0.05$, *** = $p<0.001$. NS is not significant. Kruskal-Wallis test with multiple comparison because *unc-55* data is not normally distributed. N > 8 animals. All images of L4 stage larva, anterior to left. Arrowheads denote GABA neuron presynaptic puncta. Scale bars =10 µm. VD3 - VD11 were scored on the ventral side for all genotypes.
G. Working model: The presynaptic components, Synaptobrevin/SNB-1, Rab3/RAB-3 and Liprin-alpha/SYD-2 are dismantled by IRX-1 and UNC-8.

induces UNC-8 expression (Figure 4.2), these results are consistent with the hypothesis that Iroquois/IRX-1 drives an UNC-8-dependent mechanism to remove presynaptic terminals in GABAergic neurons (Figure 4.3G).

Iroquois/IRX-1 drives a separate parallel-acting remodeling pathway that does not require UNC-8 for synaptic removal

Because *irx-1* encodes a transcription factor, we reasoned that Iroquois/IRX-1 might also regulate other targets in addition to the *unc-8* gene in the GABA neuron synaptic remodeling pathway. If Iroquois/IRX-1 regulates a downstream target that functions in tandem with UNC-8, then genetic ablation of *irx-1* should enhance the retention of ventral presynaptic markers in *unc-55; unc-8* double mutants. For this test, we used feeding RNAi for global knockdown of *irx-1* because the *irx-1* null allele is lethal (Petersen et al., 2011); the *unc-8(tm5052)* deletion allele used for these experiments is a likely null mutation (Miller-Fleming et al., 2016). We counted GFP puncta for the presynaptic proteins SNB-1::GFP, SYD-2::GFP and UNC-57::GFP in *unc-55; unc-8* double mutants vs *unc-55; unc-8* animals treated with *irx-1*-RNAi. This experiment revealed that RNAi knockdown of *irx-1* increases the number of ventral SNB-1::GFP, SYD-2::GFP and UNC-57::GFP puncta (Figure 4.4A-C) in *unc-55; unc-8* double mutant animals. Together, these results suggest that Iroquois/IRX-1 drives an additional genetic pathway, independent of UNC-8, that also eliminates presynaptic terminals in remodeling GABAergic neurons (Figure 4.4D). In the next series of experiments, we used a combination of ultrastructual analysis, electrophysiology and genetics to confirm that Iroquois/IRX-1 functions in tandem with *unc-8* to dismantle the presynaptic apparatus.

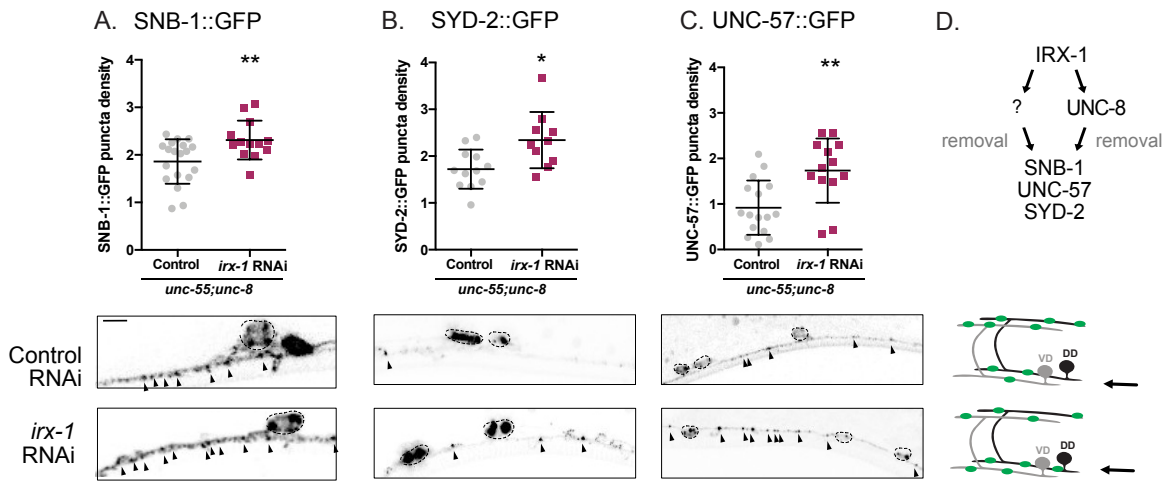

Figure 4. 4. IRX-1/Iroquois activates parallel-acting pathways that remove presynaptic components.

A. (Bottom) Representative images of *irx-1*-RNAi-treated *unc-55; unc-8* mutants show more ventral SNB-1::GFP (2.31 ± 0.4 puncta/10 µm) than *unc-55; unc-8* controls (1.86 ± 0.5 puncta/10 µm). Data are Mean ± SD. N >12. Unpaired T-test. **p = 0.0086.
B. *irx-1* RNAi-treated *unc-55; unc-8* mutants show more SYD-2::GFP (2.34 ± 0.6 puncta/10 µm) than *unc-55; unc-8* controls (1.72 ± 0.4, puncta/10 µm). Data are Mean ± SD. N > 9. Unpaired T-test. * p = 0.01.
C. *irx-1* RNAi-treated *unc-55; unc-8* mutants show more UNC-57::GFP (1.73 ± 0.7 puncta/10 µm) than *unc-55; unc-8* controls (0.92 ± 0.6 puncta/10 µm). Data are Mean ± SD. N > 12. Unpaired T-test. ** p = 0.0023.
D. Working Model: IRX-1 activates UNC-8 expression and an additional parallel-acting pathway (?) to remove Synaptobrevin/SNB-1, Endophilin/UNC-57 and Liprin-□/SYD-2 from remodeling GABAergic presynaptic terminals.

Iroquois/IRX-1 and DEG/ENaC/UNC-8 dismantle the presynaptic apparatus in remodeling GABAergic neurons

We previously used electron microscopy (EM) to establish that GABAergic presynaptic terminals are removed in *unc-55* mutants as predicted from experiments showing that presynaptic markers (e.g., mCherry::RAB-3, SYD-2::GFP) are eliminated (Walthall & Plunkett, 1995) (Figure 4.3). EM analysis also confirmed that ventral GABAergic presynaptic domains are retained in *unc-55; unc-8* adults, as expected since ectopic UNC-8 drives the elimination of ventral presynaptic markers in remodeling GABAergic neurons (Miller-Fleming et al., 2016). Since our assays with fluorescent presynaptic markers also showed that Iroquois/IRX-1 drives presynaptic disassembly (Figure 4.3), we used EM to ask if cell-specific RNAi (csRNAi) knockdown of *irx-1* would prevent the removal of ventral GABAergic synapses in an *unc-55* mutant. These experiments detected GABAergic presynaptic terminals in *unc-55; irx-1(csRNAi)* (Figure 4.4A), thus, confirming that IRX-1 is necessary for the removal of presynaptic domains in remodeling GABA neurons.

GABAergic synapses in *unc-55; unc-8* and *unc-55; irx-1(csRNAi)* animals are strikingly similar to wild-type GABAergic presynaptic domains (Figure 4.5A) with normal numbers of docked synaptic vesicles (Figure 4.5B-C). Previous work has shown that synaptic vesicle docking at the presynaptic active zone depends on the vesicular GTPase protein RAB-3 and the RAB-3-Interacting Molecule, RIM1/UNC-10 (Gracheva et al., 2008; Weimer et al., 2006). RAB-3 is largely absent from the ventral processes of GABAergic neurons in *unc-55* animals as a result of ectopic VD remodeling (Miller-Fleming et al., 2016; Thompson-Peer et al., 2012), but is at least partially restored in *unc-55; unc-8* and *unc-55; irx-1(csRNAi)* animals (Figure 4.3A) (Miller-Fleming et al., 2016). We additionally determined that fluorescently-labeled RIM1/UNC-10 localizes to ventral GABAergic synapses in *unc-55; unc-8* and *unc-55; irx-1(csRNAi)* animals (Figure 4.3G). Surprisingly, unlike other presynaptic markers, Rim1/UNC-10::GFP does not remodel in *unc-55* mutants and is retained on the ventral side (Figure 4.3G). Together, these results suggest that

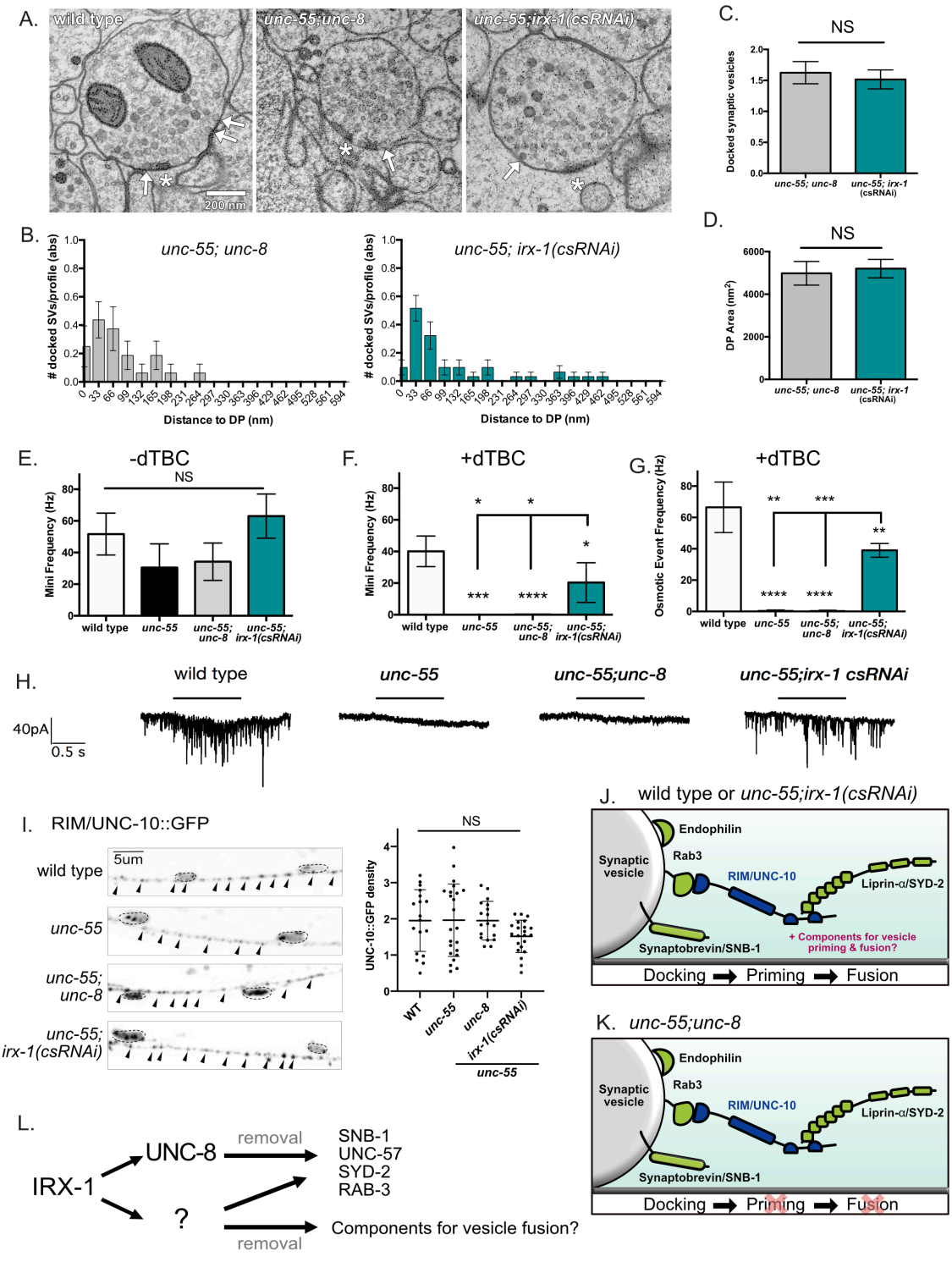

Figure 4. 5. The transcription factor IRX-1/Iroquois removes presynaptic components required for synaptic vesicle fusion and GABA release.

A. Representative electron micrographs of GABAergic motor neuron synaptic terminals with ventral muscles for wild type, *unc-55; unc-8,* and *unc-55*; *irx-1(csRNAi).* Asterisks denote presynaptic density. Arrows point to docked synaptic vesicles. Scale bar = 200 nm.
B. Distribution of docked synaptic vesicles per profile plotted in bins denoting distance from the dense projection (DP) of *unc-55; unc-8* (Left) and *unc-55; irx-1(csRNAi)* animals (Right). A Kruskal-Wallis test detected no significant difference between *unc-55; unc-8* vs *unc-55; irx-1(csRNAi)* in the distribution of docked vesicles either <100 nm (p = 0.52) or >100 nm (p = 0.13) from the dense projection.
C. Numbers of docked synaptic vesicles are similar between *unc-55; unc-8* (1.62 ± 0.18) and *unc-55; irx-1(csRNAi)* (1.52 ± 0.15) animals. Data are Mean ± SEM. Non-parametric Mann-Whitney test, p=0.2664. 16 synaptic profiles were evaluated for *unc-55; unc-8* double mutants and 31 synaptic profiles for *unc-55; irx-1(csRNAi).* NS = not significant.
D. Dense projection (DP) area is not significantly different between *unc-55; unc-8* (4981 ± 555.7 nm^2, n = 31 profiles) and *unc-55; irx-1(csRNAi)* (5201 ± 435.4 nm^2, n = 32 profiles) animals. Data are Mean ± SEM. Unpaired T-test, p= 0.378. NS = not significant.
E-F. Endogenous miniPSCs (both GABA and ACh minis are inward under these recording conditions) obtained from body wall muscles voltage-clamped at -60mV, before (E) and after (F) dTBC application, remaining minis in F represent GABA minis.
G. GABA release in response to hyperosmotic saline in the presence of dTBC were eliminated in *unc-55* (0 ± 0) and *unc-55; unc-8* animals (0 ±0.25). In contrast, *unc-55; irx-1(csRNAi)* (39.0± 2.5) partially restored hyperosmotic release, wild type (66.5 ± 8.1) . N ≥ 3, data are mean ± SEM, One-Way ANOVA Bonferroni correction, *** p = 0.001, ** p=0.01.
H. Representative traces showing that ventral mini-iPSCs are detected for wild-type and *unc-55; irx-1(csRNAi)* animals, but not for *unc-55* or *unc-55; unc-8* mutants. Horizontal lines denote hyperosmotic treatment which fails to evoke mini-iPSCs in either *unc-55* or *unc-55; unc-8* mutants.
I. (Left) Representative images of UNC-10::GFP-labeled GABA neuron synapses (arrowheads) in the ventral cord of wild-type, *unc-55, unc-55;unc-8* and *unc-55;irx-1(csRNAi)* animals. Dashed lines demarcate DD and VD cell soma. Scale bar = 10 µm. (Right) Ventral density (puncta/10 µm) of UNC-10::GFP is not different between wild-type (WT) (1.97 ± 0.9, n = 18), *unc-55* (2.05 ± 1.2, n = 23), *unc-55; unc-8* (1.95 ± 0.5, n = 18) and *unc-55; irx*-1 (csRNAi) (1.51 ± 0.4, n = 22) animals. Data is Mean ± SD. One-Way ANOVA, p= 0.149. NS is not significant across individual pairs between all genotypes.
J. In wild-type and *unc-55; irx-1(csRNAi)* animals, synaptic vesicles can dock, prime and fuse.
K. In *unc-55; unc-8* animals, synaptic vesicles can dock but do not fuse with the presynaptic membrane to release GABA.
L. Working Model: IRX-1 activates UNC-8 expression to remove structural components of the presynaptic apparatus. IRX-1 drives a parallel acting pathway (?) that also dismantles presynaptic proteins that are required for vesicle fusion and release.

dual localization of both RAB-3 and Rim1/UNC-10 in ventral GABAergic synapses of *unc-55; unc-8* and *unc-55; irx-1(csRNAi)* mutants could account for our EM observation of numerous docked vesicles (Figure 4.5B-C). In addition, the ventral synapses detected in *unc-55; unc-8* and *unc-55; irx-1*(*csRNAi)* animals show comparable dense projections (Figure 4.5D). This characteristic presynaptic structure has been previously shown to depend on SYD-2 (Kittelmann, Hegermann, et al., 2013; Stigloher et al., 2011; Mel Zhen & Jin, 1999) and its normal appearance in *unc-55; unc-8* and *unc-55; irx-1(csRNAi)* GABAergic synapses is consistent with the persistence of ventral SYD-2::GFP in these animals (Figure 4.3D-E). Taken together, our EM data are consistent with the independent findings that SNB-1, SYD-2, RAB-3 and UNC-57 puncta (Figures 4.3 and 4.4) (Miller-Fleming et al., 2016; Petersen et al., 2011) are retained in *unc-55; unc-8* and *unc-55; irx-1(csRNAi)* animals and thus support the hypothesis that functional UNC-8 and IRX-1 proteins are required for the removal of the ventral presynaptic apparatus in remodeling GABAergic motor neurons.

Iroquois/IRX-1 removes fusion-competent synaptic vesicles in remodeling GABAergic neurons

Because ventral GABAergic synapses with apparently normal ultrastructure are observed in *unc-55; unc-8* and *unc-55; irx-1(csRNAi)* (Figure 4.5A-D), we next performed experiments to determine if these synapses are functional. We first examined whether the docked synaptic vesicles in *unc-55; unc-8* animals are fusion-competent by recording iPSCs from ventral muscles. For these experiments, we used d-tubocurare (dTBC) to block cholinergic signaling. As previously reported, tonic release of ventral iPSCs was restored in *unc-55; irx-1(csRNAi)* animals, but iPSCs were not detected in *unc-55; unc-8* mutants despite the presence of organized clusters of fluorescent presynaptic proteins (Figure 4.3), electron dense active zones and docked vesicles in both strains (Figure 4.5A-D) (Miller-Fleming et al., 2016; Petersen et al., 2011). Previously, we determined that the postsynaptic $GABA_A$ receptor UNC-49 was also properly localized and

functional in *unc-55;unc-8* animals (Miller-Fleming et al., 2016), thus excluding the possibility that the absence of iPSCs in *unc-55; unc-8* animals is due to a postsynaptic defect. The lack of tonic release in *unc-55; unc-8* animals could be due to defective vesicle priming or downstream Ca^{2+}-sensing. To determine if the morphologically-docked synaptic vesicles in *unc-55; unc-8* animals are primed, we measured iPSCs in response to hypertonic sucrose perfusion which is sufficient to induce neurotransmitter release from the primed synaptic vesicle pool (Figure 4.5E-H). Hyperosmotic treatment of *unc-55; unc-8* animals failed to trigger ventral GABA release suggesting that these animals are defective in synaptic vesicle priming (Figure 4.5G-H). As expected, hyperosmotic stimulation triggered robust iPSCs in wild-type and in *unc-55; irx-1(csRNAi)* animals, whereas ventral muscles in *unc-55* mutants were unresponsive. To rule out the possibility of a general defect in synaptic vesicle fusion, we confirmed that preparations of *unc-55* and *unc-55; unc-8* mutants exhibited spontaneous cholinergic activity that could be abolished by dTBC (Figure 4.5E-F). Together with our EM results (Figure 4.5A-D) (Miller-Fleming et al., 2016), these data indicate that synaptic vesicles at ventral GABAergic synapses in *unc-55; unc-8* animals are capable of docking with the presynaptic membrane but are not fusion competent. We further conclude that synaptic vesicles at ventral GABAergic synapses in *unc-55; irx-1(csRNAi)* animals can dock and are also fusion competent since endogenous miniature IPSCs were detected and hyperosmotic treatment evoked robust IPSCs in *unc-55; irx-1(csRNAi)* adults (Figure 4.5F-H). Thus, our results are consistent with the idea that Iroquois/IRX-1 and UNC-8 eliminate a shared set of presynaptic proteins (e.g., RAB-3, Synaptobrevin/SNB-1) in the remodeling program but that Iroquois/IRX-1 selectively removes specific presynaptic components for vesicle priming and neurotransmitter release in a mechanism that does not require UNC-8.

A behavioral assay for functional GABAergic synapses in the motor circuit

As an additional test of our ultrastructural and electrophysiological results, we devised a behavioral assay to evaluate the functionality of GABAergic synapses in remodeling defective mutants (Figure 4.6). Ventral synapses for both DD and VD neurons are dismantled in *unc-55* mutants and reassembled in the dorsal nerve cord (Figure 4.1D). The resultant imbalance of excess inhibitory GABAergic output to dorsal muscles versus excess excitatory cholinergic input to ventral muscles results in a striking behavioral phenotype in which *unc-55* animals coil ventrally when tapped on the head instead of initiating coordinated backward locomotion (Shan et al., 2005; Walthall & Plunkett, 1995). We have shown that *irx-1(csRNAi)* restores fusion-competent GABAergic presynaptic densities to *unc-55* mutants (Figure 4.5G-H). If these restored synapses are functional, then the tapping assay should detect improved backward locomotion. Indeed, *unc-55; irx-1(csRNAi)* animals (Figure 4.6) show robust backward movement in comparison to *unc-55* mutants (Petersen et al., 2011). This result is congruent with our previous finding that GABAergic release is restored to ventral cord synapses of *unc-55* mutants by RNAi knockdown of *irx-1* (Figure 4.5G-H). In contrast, *unc-55; unc-8* mutant animals show severely defective backward locomotion that is not significantly different from that of *unc-55* mutants (Figure 4.6). This finding is in agreement with our observation that hyperosmotic treatment fails to evoke GABA release (Figure 4.5G-H) and reinforces the idea that ventral GABAergic synapses in *unc-55; unc-8* mutants are not functional. Genetic ablation of *unc-8* activity in *unc-55; irx-1(csRNAi)* does not further enhance backward locomotion (Figure 4.6) as predicted by our conclusion that residual ventral cord GABAergic synapses in *unc-55; unc-8* double mutants are dysfunctional (Figure 4.5F-G) and by our finding that Iroquois/IRX-1 regulates expression of the *unc-8* gene (Figure 4.2). To summarize, the results of the behavioral assay suggest that although ultrastructurally normal ventral GABAergic synapses are visible by EM in both *unc-55; unc-8* and in *unc-55; irx-1(csRNAi)* animals (Figure 4.5A), GABAergic release is selectively reactivated by knockdown of

irx-1, but not by genetic removal of *unc-8*. This striking difference suggests that Iroquois/IRX-1 must drive the removal of key determinants of presynaptic neurotransmitter release that are not targeted by UNC-8.

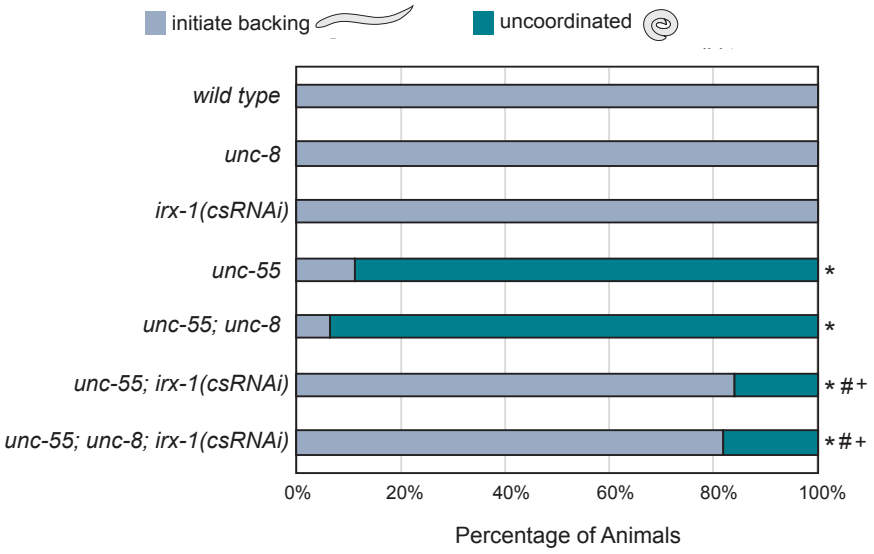

Figure 4. 6. A behavioral assay for functional GABAergic synapses in the motor circuit

Behavioral assays to detect backward locomotion. Young adult animals were tapped on the head and scored for wild-type (gray) versus uncoordinated (teal) backward movement. *unc-55* and *unc-55; unc-8* animals coil ventrally with head tap indicating that a loss-of-function *unc-8* mutation does not rescue backward locomotion in *unc-55* mutants (NS, not significant, Fisher's Exact Test, n ≥ 100 animals per genotype). Cell-specific RNAi (*csRNAi*) knock-down of *irx-1* restores backward locomotion to *unc-55* animals and this effect is not enhanced in *unc-55; unc-8; irx-1(csRNAi).* * denotes significantly different from wildtype with $p < 0.002$. # denotes significantly different from *unc-55* with $p < 0.002$. + denotes significantly different from *unc-55; unc-8* with $p < 0.002$.

Iroquois/IRX-1, but not DEG/ENaC/UNC-8, removes the synaptic vesicle priming protein UNC-13 in remodeling GABAergic neurons

The cytosolic protein Munc13/UNC-13 functions as a conserved component of the presynaptic apparatus to mediate synaptic vesicle fusion (Augustin et al., 1999; Brose et al., 1995; Kohn et al., 2000; Richmond et al., 1999; T. C. Südhof, 2012; Weimer et al., 2006). Mammalian neurons express four UNC-13-related proteins whereas only two distinct UNC-13 proteins, a long (UNC-13L) and a short (UNC-13S) version, are expressed in *C.elegans*. Because synaptic vesicles appear docked, but are incapable of fusion in *unc-55; unc-8* mutants (Figure 4.5A-D), we hypothesized that UNC-13 could be absent from ventral GABAergic synapses in these animals. To test this idea, we generated a strain expressing GFP-tagged UNC-13L protein in GABA neurons. We selected UNC-13L for this experiment because it co-localizes with UNC-10/RIM whereas the short isoform, UNC-13S, shows a diffuse distribution in GABAergic motor neurons (data not shown), as also reported for *C. elegans* cholinergic motor neurons (Hu, Tong, & Kaplan, 2013). As previously observed for other presynaptic proteins (Figure 4.3) (Hallam & Jin, 1998; Miller-Fleming et al., 2016; Petersen et al., 2011; Thompson-Peer et al., 2012), UNC-13L::GFP is restricted to the ventral nerve cord prior to DD remodeling in early L1 larvae, but is detectable post-remodeling in both the dorsal and ventral nerve cords in adults (Figure 4.7A-B). This finding indicates that UNC-13L::GFP remodels to DD presynaptic domains in the dorsal nerve cord and is also a component of ventral VD synapses in the adult. We quantified the number of UNC-13L::GFP puncta in the ventral nerve cord and determined that UNC-13L::GFP is largely removed in *unc-55* mutants (4.7D, G) thus demonstrating that UNC-13L::GFP is disassembled from the ventral presynaptic domains of DD neuron and also VD neurons that undergo remodeling in *unc-55* mutants. In contrast to other presynaptic markers (e.g. SNB-1::GFP) (Figure 4.3A-C), UNC-13L::GFP is also eliminated from ventral GABAergic synapses in *unc-55; unc-8* mutants (Figure 4.7E, G). Thus, wild-type UNC-8 activity is not required for the removal of UNC-13L from

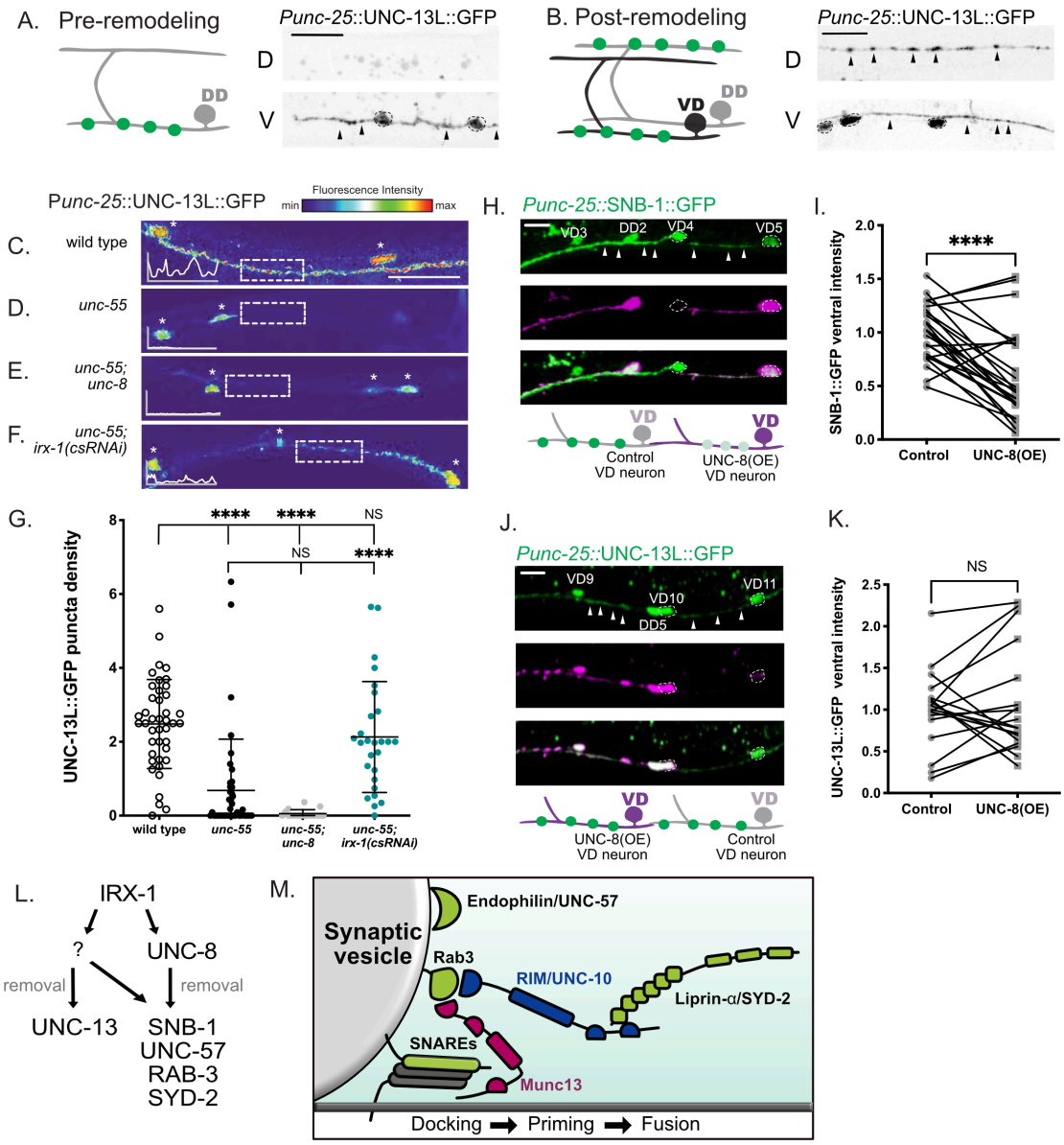

Figure 4. 7. IRX-1/Iroquois, but not UNC-8, drives removal of Munc13/UNC-13 from the presynaptic domains of remodeling GABAergic neurons.

A-B. (A) GFP-tagged UNC-13L (*Punc-25::*UNC-13L::GFP) is expressed in GABAergic neurons and localized to the ventral (V) nerve cord before DD remodeling in early L1 larvae. Scale bar = 5µm. **(B)** UNC-13L::GFP is visible in both the dorsal (D) and ventral (V) nerve cords after DD remodeling at the L4 stage. Arrowheads mark UNC-13L::GFP puncta and dashed circles denote GABA neuron cell soma. Scale bar = 10 µm.
C-F. Representative fluorescence intensity heat maps and line tracings of UNC-13L::GFP-labeled GABA neuron synapses in the ventral nerve cord of **(C)** wild type, **(D)** *unc-55*, **(E)** *unc-55; unc-8* and **(F)** *unc-55; irx-1(csRNAi)*. UNC-13L::GFP signal is depleted in **(D)** *unc-55* and **(E)** in *unc-55; unc-8*, but partially restored in **(F)** *unc-55; irx-1(csRNAi)* (boxes with dashed lines). Asterisks denote GABAergic neuron cell soma. Scale bar = 10 µm.

G. Quantification of UNC-13L::GFP (puncta/10 µm) at ventral GABAergic synapses (VD3 – VD11) for wild type (2.48 ± 1.2), *unc-55* (0.68 ± 1.4), *unc-55; unc-8* (0.05 ± 0.1) and *unc-55; irx-1(csRNAi)* (2.19 ± 1.5). Data are mean ± SD. N > 16. Kruskal-Wallis test with multiple comparison because *unc-55* and *unc-55;unc8* samples are not normally distributed. **** is $p < 0.0001$. NS = not significant.
H. (Top) Representative image of SNB-1::GFP in ventral nerve cord of mosaic animal with forced UNC-8 expression [UNC-8(OE)] in a subset of VD neurons (magenta, VD5, dashed outline) versus neighboring control cells (VD4, dashed outline). Arrowheads denote regions of SNB-1::GFP signal in control and UNC-8(OE) VD neurons. (Below) Schematic depicting brighter SNB-1::GFP signal (green) in control (gray) vs UNC-8(OE) VD neurons (magenta). Scale bar = 10 µm.
I. Forced expression of UNC-8 in VD neurons (1.00 ± 0.3) reduces SNB-1::GFP in GABAergic terminals [UNC-8(OE)] compared to neighboring control VD neurons that do not express UNC-8 (0.58 ± 0.4). N = 24 animals. Paired T-test. **** $p < 0.0001$.
J. (Top) Representative image of UNC-13L::GFP in ventral nerve cord of mosaic animals with forced UNC-8 expression [UNC-8(OE)] in a subset of VD neurons (magenta, VD10, dashed outline) versus neighboring control cells (VD11, dashed outline). Arrowheads point to examples of UNC-13L::GFP signal in control and UNC-8(OE) VD neurons. (Below) Schematic of UNC-13L signal (green) in control (gray) and UNC-8(OE) cells (magenta). Scale bar = 10 µm.
K. Forced expression of UNC-8 in VD neurons (1.00 ± 0.5) does not reduce UNC-13L::GFP in ventral VD neuron GABAergic terminals [UNC-8(OE)] compared to neighboring control VD neurons that do not express UNC-8 (1.08 ± 0.6). Data are mean ± SD. N = 18. NS = not significant. $p = 0.723$. Paired T-test. All images from L4 animals, anterior to left.
L. Working Model: IRX-1 promotes an *unc-8*-independent pathway involving unknown downstream components (?) that removes UNC-13L from remodeling GABAergic synapses.
M. IRX-1 knockdown blocks remodeling of GABAergic synapses which retain presynaptic structural components (green), RIM/UNC-10 (blue) and Munc13 (magenta) allowing docked vesicles to prime and fuse with the plasma membrane. Also depicted are the plasma-membrane SNAREs (gray) because these are required for functional synapses, which are removed by IRX-1 (Figure 4.5G).

remodeling GABAergic synapses. This finding suggests that although the ventral presynaptic active zone in *unc-55; unc-8* mutant GABAergic neurons appears normal by EM (Figure 4.5A-D) (Miller-Fleming et al., 2016), UNC-13L is not localized at these terminals thus likely accounting for their synaptic vesicle fusion defect (Figure 4.5E-I).

Since UNC-8 expression in VD neurons was shown to drive elimination of SNB-1::GFP (Miller-Fleming et al., 2016), we devised an additional experiment to test the idea that removal of UNC-13L is UNC-8-independent. We confirmed that forced expression of UNC-8 in VD neurons is sufficient to remove SNB-1::GFP from ventral GABAergic synapses (Figure 4.7H-I), but does not displace UNC-13L::GFP (Figure 4.7J-K). Together, these results show that UNC-8 function is neither necessary nor sufficient for UNC-13L removal from remodeling GABAergic synapses.
RNAi knock down of *irx-1* in *unc-55* mutants is sufficient to restore ventral GABAergic synaptic release (Figure 4.5E-G). Thus, we next asked if UNC-13L::GFP is retained in the ventral nerve cord of *unc-55; irx-1(csRNAi)* animals. Indeed, we found that ventral UNC-13L::GFP puncta are detectable in both wild-type and in *unc-55; irx-1(csRNAi)* animals (Figure 4.7F-G) thus indicating that Iroquois/IRX-1 is required for the removal of UNC-13L from remodeling GABAergic synapses (Figure 4.7L-M).

Iroquois/IRX-1, but not DEG/ENaC/UNC-8, removes the RIM-binding protein ELKS-1 in remodeling GABAergic neurons

Based on previous work demonstrating that the RIM-binding protein ELKS-1 recruits the mammalian protein bMunc-13-2 to active zones and that *Drosophila* ELKS homologue, Bruchpilot, recruits UNC-13L/Unc13A (Böhme et al., 2016; Kawabe et al., 2017), we next asked if ELKS-1 is also removed by IRX-1/Iroquois. We determined that expression of ELKS-1::tdTomato (Cherra & Jin, 2016) in wild-type adult GABA neurons results in bright fluorescent puncta characteristic of DD synapses in the dorsal nerve cord and VD synapses in the ventral

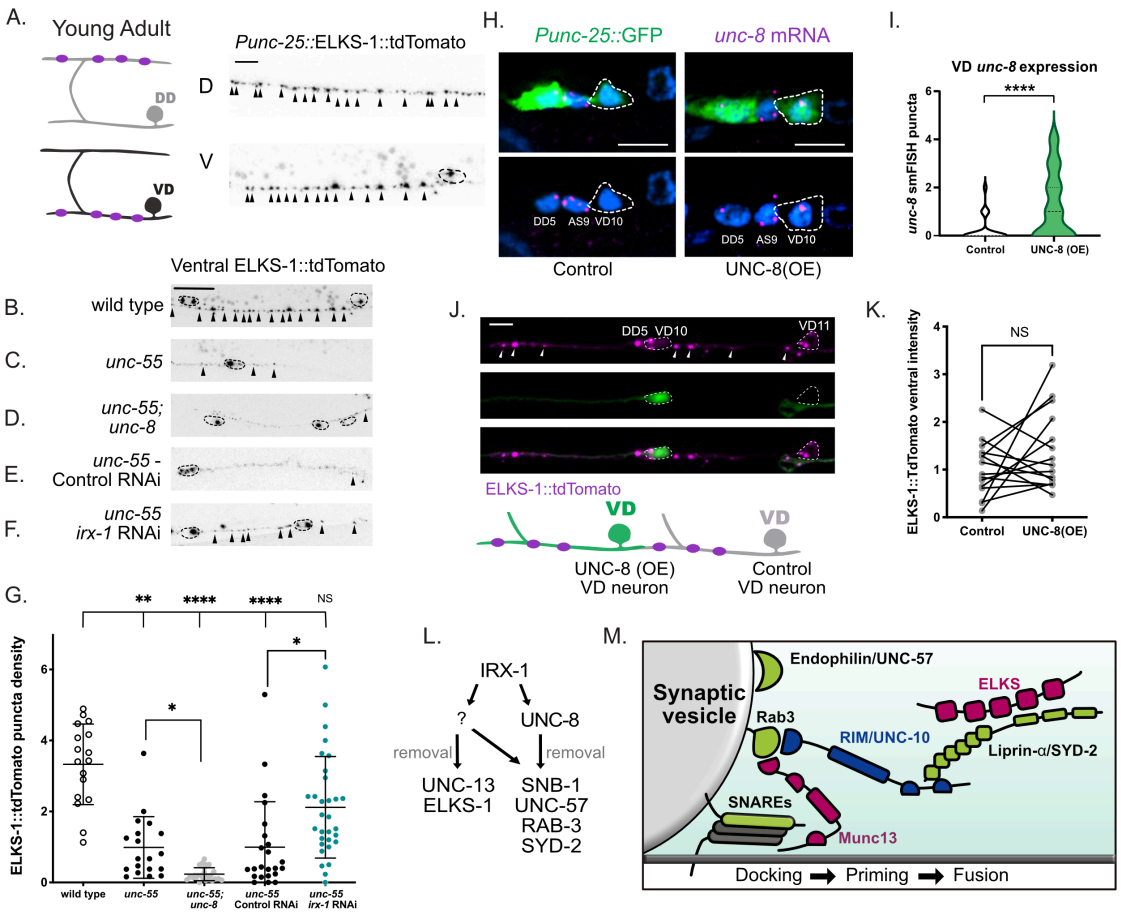

Figure 4. 8. IRX-1, but not UNC-8, drives removal of ELKS-1 from the presynaptic domains of remodeling GABAergic neurons.

A. ELKS-1::TdTomato puncta (magenta) are visible in both the dorsal (D) and ventral (V) nerve cords after DD remodeling at the L4 stage. Arrowheads point to ELKS-1::TdTomato puncta and dashed circles demark cell soma. Scale bar = 5 µm.
(B-F). Representative images of ELKS-1::TdTomato-labeled GABA neuron synapses in the ventral nerve cord of **(B)** wild type **(C)** *unc-55* **(D)** *unc-55; unc-8* **(E)** *unc-55* control RNAi **(F)** *unc-55; irx-1* RNAi. Arrowheads point to ELKS-1::TdTomato puncta and dashed circles demark cell soma. GABAergic ELKS-1::TdTomato ventral puncta are largely absent in **(C)** *unc-55* **(D)** *unc-55; unc-8* and **(E)** *unc-55*; control RNAi animals but are restored with **(F)** *irx-1* RNAi treatment of *unc-55* mutants. Scale bar = 10 µm. Images from L4 larvae, anterior to left.
G. Quantification of ventral GABAergic synapses (VD3 – VD11) labeled with ELKS-1::tdTomato, density (puncta/10 µm) in wild-type (3.33 ± 1.1), *unc-55* (0.99 ± 0.9), *unc-55; unc-8* (0.23 ± 0.2), *unc-55* control RNAi (0.99 ± 1.2) and *unc-55; irx-1* RNAi (2.12 ± 1.4) L4 stage larvae. Data are mean ± SD. Kruskal-Wallis test with multiple comparison because *unc-55, unc-55;unc8 and unc-55;* control RNAi samples are not normally distributed. N > 16 animals. * $p < 0.05$; ** $p<0.01$, **** $p < 0.0001$. NS = not significant.
H. Representative images of VD10 neuron in control (left) vs VD10 with forced UNC-8 expression [UNC-8(OE)] (right). Puncta are *unc-8* smFISH probe (magenta) and nuclei are labeled with DAPI (blue). Dashed outlines denote VD10 cell soma marked with P*unc-25*::GFP. Scale bar = 5 µm.

I. Violin plots for *unc-8* smFISH puncta in control (white) (n = 42 cells) vs UNC-8(OE) (green) (n = 45 cells) in L3 stage VD motor neurons confirm elevated *unc-8* transcripts in UNC-8(OE) VD neurons. Dashed line denotes median. Mann-Whitney test was used to determine significance because the control sample was not normally distributed, **** is p<0.0001.
J. (Top) Representative image of ELKS-1::TdTomato (magenta) in the ventral nerve cord of mosaic animals with forced UNC-8 expression [UNC-8(OE)] in a subset of VD neurons (dashed outline, green, VD10) versus neighboring control VD neurons (dashed outline, VD11). Arrowheads point to ELKS-1::TdTomato puncta in control and UNC-8(OE) VD neurons. Dashed circles demark VD cell soma. (Below) Schematic of ELKS-1 puncta (magenta) in control (gray) and UNC-8(OE) cells (green). Scale bar = 5 μm. Images from L4 animals, anterior to left.
K. Forced expression of UNC-8 in VD neurons [UNC-8(OE)] (1.00 ± 0.6) does not reduce ELKS-1::tdTomato levels in VD presynaptic terminals compared to neighboring control VD neurons that do not express UNC-8 (1.38 ± 0.8). Data are Mean ± SD. N = 15. NS = not significant. Paired T-test, p = 0.0923.
L. Working Model: IRX-1 drives expression of UNC-8 and also activates an additional pathway (?) that removes UNC-13 and ELKS-1 from remodeling GABAergic synapses.
M. Schematic of components that are selectively removed from remodeling GABAergic presynaptic domains by UNC-8 (green) or by IRX-1 (green + magenta). Plasma-membrane SNAREs (gray) are shown because these are required for functional synapses (Figure 4.5G).

nerve cord (Figure 4.8A). Ventral ELKS-1::tdTomato-labeled puncta are largely absent in *unc-55* mutants indicating that ELKS-1 is dismantled from the presynaptic domains of remodeling GABAergic motor neurons (Figure 4.8C,G). Ventral ELKS-1 puncta are also missing in *unc-55; unc-8* mutants (Figure 4.8D, G). Thus, UNC-8 function is not required to remove ELKS-1 from the presynaptic domain. Surprisingly, the ventral ELKS-1 signal is reduced in *unc-55; unc-8* animals relative to *unc-55.* However, the significance of this finding is unclear because we do not observe a similar negative effect of the *unc-8* mutation on ELKS-1 levels in remodeled DD neurons (Figure 4.10D).

In contrast to results obtained from *unc-55; unc-8* mutants (Figure 4.8D, G), a substantial number of ELKS-1 puncta are retained in the ventral nerve cord of *unc-55* animals treated with *irx-1* RNAi (Figure 4.8F-G). This finding suggests that IRX-1/Iroquois promotes the removal of ELKS-1 in remodeling GABAergic neurons but that UNC-8 is not required. For a direct test of this model, we used a transgenic strategy to over-express UNC-8 in VD neurons (Figure 4.8H-I). Although UNC-8(OE) in VD neurons drives the removal of ventral SNB-1::GFP (Figure 4.7H-I), we observed that UNC-8(OE) is not sufficient to eliminate ELKS-1 (Figure 4.8J-K). Thus, our results support the idea that Iroquois/IRX-1 removes ELKS-1 from ventral synapses of remodeling GABAergic motor neurons in a genetic pathway that is independent of UNC-8 (Figure 4.8L-M).

To summarize, our results show that IRX-1 drives the removal of multiple components of the presynaptic apparatus in remodeling GABAergic neurons including Synaptobrevin/SNB-1, RAB-3, liprin-α/SYD-2, Endophilin/UNC-57, UNC-13L and ELKS-1 (Figures 4.3, 4.4, 4.7 and 4.8). In contrast, DEG/ENaC/UNC-8 promotes the disassembly of Synaptobrevin/SNB-1, RAB-3, liprin-α/SYD-2 and Endophilin/UNC-57 (Figure 4.3) but is not required for the removal of Munc-13/UNC-13L and ELKS-1 (Figures 4.7-4.8).

Iroquois/IRX-1 and DEG/ENaC/UNC-8 drive the removal of RAB-3 from remodeling DD neuron GABAergic synapses

We have exploited the ectopic remodeling phenotype of *unc-55* mutant VD neurons to show that both IRX-1 and UNC-8 act to dismantle the presynaptic apparatus. In addition, our findings suggest that IRX-1 functions as a transcription factor to orchestrate the overall mechanism by activating expression of UNC-8 as well as another downstream pathway that functions in parallel to drive synapse removal. To determine if a similar mechanism also drives synapse elimination in the native DD remodeling program, we used an endogenous GFP::RAB-3 marker that is specifically expressed in DD neurons (Figure 4.9 A). As expected, in the wild type, endogenous RAB-3::GFP remodels from ventral to dorsal locations during early larval development; few ventral GFP::RAB-3 puncta are detectable by the L4 larval stage (Figure 4.9B). In contrast, *unc-8* mutants at the L4 stage show significant retention of GFP::RAB-3 signal (Figure 4.9C), likely resulting from failed synapse elimination (Miller-Fleming et al., 2016). Similarly, cell-specific RNAi of *irx-1* in DD neurons prevents the elimination of GFP::RAB-3 (Figure 4.9D-F), indicating that IRX-1 is also necessary for the efficient removal of presynaptic GFP::RAB-3 in DD neurons (Petersen et al., 2011). Notably, significantly more GFP::RAB-3 puncta are retained in *irx-1(csRNAi)*-treated DD neurons than in *unc-8* mutants (Figure 4.9F), a result consistent with the idea that IRX-1 drives expression of both *unc-8* and an additional pathway for synapse elimination. This model of parallel-acting pathways predicts that *irx-1(csRNAi)* should enhance the synaptic removal defect of *unc-8* mutants, which we also observe (Figure 4.9E-F). Finally, genetic ablation of *unc-8* does not enhance retention of residual GFP::RAB-3 by *irx-1(csRNAi)* (Figure 4.9F), a result consistent with the idea the IRX-1 is required for *unc-8* expression.

In sum, our results have confirmed that (1) IRX-1 and UNC-8 promote the elimination of RAB-3 from ventral terminals of DD neurons (Figure 4.9), (2) IRX-1 functions upstream of UNC-8 to remove RAB-3 (Figure 4.2) and (3) IRX-1 controls an additional pathway that disassembles

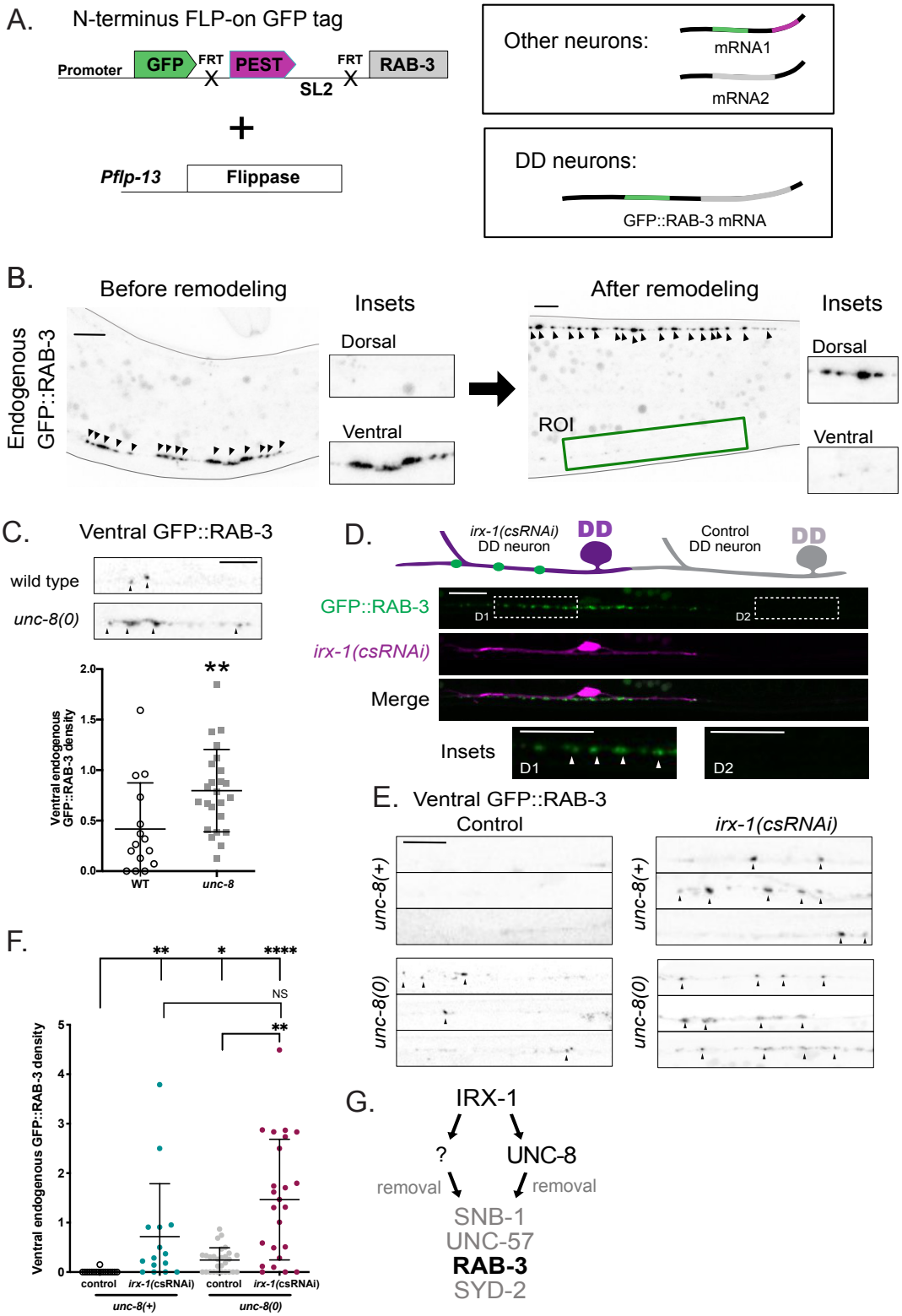

Figure 4. 9. IRX-1 activates parallel pathways that remove RAB-3 from the ventral terminals of remodeling DD neurons.

A. Endogenous labeling of RAB-3 with GFP in DD neurons. *Pflp-13* drives flippase expression to attach GFP to the N-terminus of the endogenous RAB-3 protein in DD neurons (Schwartz & Jorgensen, 2016).
B. Fluorescent images of endogenous GFP::RAB-3 in DD neurons in the ventral nerve cord before remodeling (left) and in the dorsal nerve cord after remodeling (right). Green box denotes Region of Interest (ROI) in L4 stage larva for counting DD-specific ventral GFP::RAB-3 puncta. Arrowheads point to GFP::RAB-3 puncta. Scale bar = 5 μm.
C. (Top) Representative images of ventral nerve cords of wild-type and *unc-8* mutant L4 stage larvae. Arrowheads denote ventral GFP::RAB-3 puncta. Scale bar = 5 μm. (Bottom) *unc-8* mutants (0.80 ± 0.4, n=24) retain more GFP::RAB-3 puncta than wild type (0.41 ± 0.5, n=15). Data are mean ± SD. Unpaired T-test. ** p = 0.0051. Ventral puncta in DD2 and DD3 were scored for this analysis.
D. (Top) Schematic of ventral GFP::RAB-3 puncta (green) retained at the L4 larval stage in *irx-1(csRNAi)* DD neurons (magenta) but not in neighboring DD neurons (control) that do not express *irx-1(csRNAi)* (gray). (Bottom) Representative image of *irx-1(csRNAi)*-expressing DD2 neuron (magenta) that retains ventral GFP::RAB-3 (green) and DD3 (control) in which GFP::RAB-3 puncta are removed from the ventral nerve cord. D1 inset shows GFP::RAB-3 puncta (arrowheads) that remain in the ventral nerve cord of DD neurons with *irx-1(csRNAi)* knockdown. Neighboring D2 inset shows control DD neuron that remodels and eliminates GFP::RAB-3 puncta. Scale bar = 10 μm.
E. Representative images of ventral regions of control and *irx-1(csRNAi)* DD neurons in *unc-8(+)* (Top) and *unc-8(0)* mutant (Bottom) L4 stage larvae. Arrowheads denote GFP::RAB-3 puncta. Scale bar = 5 μm. Note that *irx-1(csRNAi)* enhances retention of GFP-RAB-3 puncta in *unc-8* mutants.
F. *irx-1(csRNAi)* enhances retention of GFP::RAB-3 puncta in *unc-8* mutants**.** Density (puncta/10 μm) of GFP::RAB-3 puncta in the ventral nerve cords of control (0.01 ± 0.03, n=17) and *irx-1(csRNAi)* (0.72 ± 1.1, n=15) DD neurons in control (gray) (0.24 ± 0.3, n=28) and *irx-1(csRNAi)* (1.47 ± 1.2, n=24) in *unc-8(+)* (left) vs *unc-8(0)* mutant (right) backgrounds. Data are mean ± SD. Non-parametric Kruskal-Wallis test because control datasets are not normally distributed. * p<0.05; **p<0.01; ****p<0.0001 and NS = not significant.
G. Working model: In DD neurons, IRX-1 activates UNC-8 and a parallel pathway (?) to remove RAB-3 (bold) from the ventral terminals of remodeling DD neurons. Additional presynaptic components (SNB-1, UNC-57, SYD-2) are removed from ventral GABAergic boutons in *unc-55* mutants in which both DD and VD neurons remodel.

RAB-3 independently of UNC-8 (Figure 4.9E-F). Because these findings were also observed for ectopically remodeling VD neurons (Figure 4.3 and 4.4), we propose that the additional presynaptic components, Synaptobrevin/SNB-1, Endophilin/UNC-57 and liprin-α/SYD-2, are similarly regulated during DD synapse removal (Figure 4.9G).

Iroquois/IRX-1, but not DEG/ENaC/UNC-8, removes ELKS-1 from ventral synapses in DD neurons

Our results obtained from ectopic remodeling of VD neurons in *unc-55* mutants showed that IRX-1, but not UNC-8, promotes removal of a specific subset of active zone proteins, ELKS-1 and UNC-13 (Figure 4.7 and 4.8). To determine if ELKS-1 is similarly regulated in remodeling DD neurons, we used an endogenous GFP::ELKS-1 marker that is selectively expressed in DD neurons (Figure 4.10A). In the wild type, GFP::ELKS-1 is initially deposited at ventral DD synapses and then relocated to dorsal DD synapses as predicted for the DD remodeling program (Figure 4.10B). GFP::ELKS-1 is also removed from ventral DD synapses of *unc-8* mutants (Figure 4.10C-D), suggesting that UNC-8 is not required for ELKS-1 elimination. In contrast, we observed that *irx-1* knockdown by *irx-1(csRNAi)* antagonizes the elimination of GFP::ELKS-1 from ventral synapses of DD neurons (Figure 4.10E-F). Thus, our results demonstrate that IRX-1 but not UNC-8 drives ELKS-1 removal in DD neurons. Because Munc13/UNC-13 is also selectively removed by IRX-1 in ectopically remodeling VD neurons (Figure 4.7), we propose that Munc13/UNC-13 is similarly regulated in remodeling DD neurons (Figure 4.10G). Our findings are notable because they show that distinct genetic pathways can dismantle the presynaptic apparatus in remodeling GABAergic neurons by targeting specific active zone components.

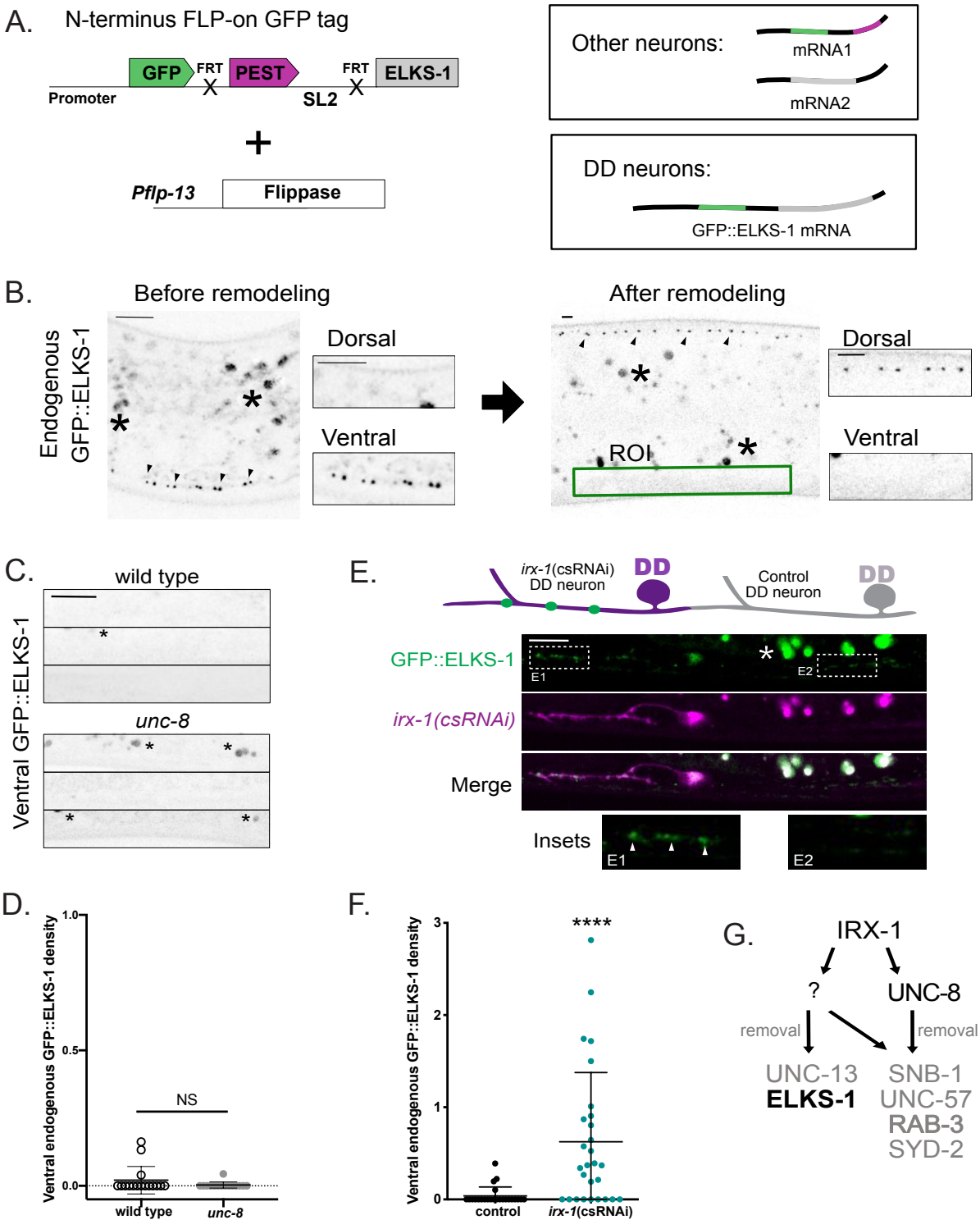

Figure 4. 10. IRX-1, but not UNC-8, drives removal of endogenous ELKS-1 from ventral terminals of remodeling DD neurons.

A. Endogenous labeling of ELKS-1 with GFP in DD neurons. *pflp-13* drives flippase in DD neurons to fuse GFP to the N-terminus of the endogenous ELKS-1 protein (Schwartz & Jorgensen, 2016).
B. Fluorescent images of endogenous GFP::ELKS-1 in DD neurons in the ventral nerve cord before remodeling (left) in L1 larvae vs the dorsal nerve cord after remodeling (right) at the L4 stage. Green box defines Region of Interest (ROI) for counting DD-specific ventral GFP::ELKS-1 puncta (arrowheads). Asterisks denote autofluorescence. Scale bar = 5 µm.
C-D. Representative images of ventral nerve cords of wild-type (0.020 ± 0.05, n=16) and *unc-8* mutant (0.003 ± 0.01, n=15) L4 stage larvae which eliminate GFP::ELKS-1. density = puncta/10 µm. Asterisks denote autofluorescence. Data are Mean ± SD. Mann-Whitney test, NS is Not Significant, p = 0.1913. Scale bar = 5 µm.
E. (Top) Schematic of ventral GFP::ELKS-1 puncta (green) retained at the L4 larval stage in *irx-1(csRNAi)* treated DD neurons (magenta) but not in neighboring DD neurons (control) that do not express *irx-1(csRNAi)* (gray). (Bottom) Representative image of DD1(*irx-1(csRNAi)* that retains ventral GFP::ELKS-1 puncta (green) and DD2 (control) that eliminates GFP::ELKS-1 puncta from the ventral nerve cord (green). E1 inset shows residual ventral GFP::ELKS-1 puncta that remain in the DD1 neuron with *irx-1(csRNAi)* knockdown. Neighboring E2 inset shows control DD2 neuron that remodels and eliminates ventral GFP::ELKS-1 puncta. Scale bar = 5 µm.
F. GFP::ELKS-1 puncta (0.63 ± 0.8, n=28) are elevated in *irx-1(csRNAi)* DD neurons at the L4 larval stage compared to control DD neurons that undergo remodeling (0.04 ± 0.1, n=24). density = puncta/10 µm . Data are mean ± SD. Mann-Whitney test, **** is p<0.0001.
G. Working model: IRX-1, but not UNC-8, removes ELKS-1 from the ventral terminals of remodeling DD neurons and UNC-13 in *unc-55* mutants in which both DD and VD neurons remodel (Figure 4.8).

DISCUSSION

Presynaptic disassembly in remodeling GABAergic neurons

Synaptic plasticity is a key dynamic feature of the nervous system as neurons actively assemble new synapses while also dismantling others (De Paola et al., 2006; Hong et al., 2014; Linkenhoker et al., 2005; Mcbride & Debello, 2015; Stettler, Yamahachi, Li, Denk, & Gilbert, 2006). In contrast to synaptic assembly about which much is known, the molecular mechanisms that drive synaptic elimination are relatively unexplored (T. Südhof, 2018; T. C. Südhof, 2017). In this study, we investigated a developmentally-regulated mechanism of presynaptic disassembly in *C. elegans* (Cuentas-Condori & Miller, 2020; Hallam & Jin, 1998; White et al., 1978). Our findings revealed parallel-acting pathways that selectively remove different components of the presynaptic active zone in remodeling GABAergic synapses (Figure 4.11). We have shown that the conserved transcription factor Iroquois/IRX-1 drives expression of the DEG/ENaC channel subunit UNC-8 (Figure 4.2) to remove the presynaptic proteins Synaptobrevin/SNB-, liprin-α/SYD-2, Endophilin/UNC-57 and RAB-3 (Figure 4.3 and 4.9) (Miller-Fleming et al., 2016). IRX-1 regulates a parallel-acting mechanism that also removes these presynaptic components (Figure 4.4) (Petersen et al., 2011). In addition, Iroquois/IRX-1 promotes the selective disassembly of ELKS-1 and Munc13/UNC-13 in a separate mechanism that does not require UNC-8 activity (Figures 4.7, 4.8 and 4.10). Together, our findings show that synaptic disassembly can be transcriptionally-regulated and involve molecularly distinct mechanisms that differentially eliminate selected subsets of presynaptic proteins.

Activity-dependent active zone remodeling

The active zone region of the presynaptic terminal mediates synaptic vesicle (SV) fusion for neurotransmitter release (T. C. Südhof, 2012). This active zone function is defined by a core

group of components including Voltage-gated Ca^{++} Channels (VGCCs), ELKS, Munc13/UNC-13, liprin-α/SYD-2, SYD-1, RIM/UNC-10, and Rim Binding Protein (RBP) (T. C. Südhof, 2012). Notably, the composition and size of the SV release machinery can be modulated by synaptic activity. For example, additional copies of specific active zone proteins (i.e. ELKS, RBP, VGCCs and Munc13) are incorporated into the presynaptic zones of *Drosophila* neuromuscular junctions (NMJs) in a homeostatic mechanism that elevates neurotransmitter release to compensate for reduced postsynaptic sensitivity (Böhme et al., 2019; Gratz et al., 2019). Elevated activity in *Drosophila* photoreceptors can also have the opposite effect of selectively removing a subset of these presynaptic proteins (liprin-α, RIM and RBP) while leaving others intact (VGCCs and SYD-1) to adapt the synapse to different sensory inputs (Sugei et al., 2015).

Our findings point to a related effect in remodeling GABAergic neurons in *C. elegans* in which neuronal activity promotes the elimination of selected presynaptic components. In previous work, we determined that the DEG/ENaC channel UNC-8 functions in an activity-dependent pathway that dismantles the presynaptic active zone. Genetic results, for example, show that UNC-8 acts in a common pathway with the VGCC, UNC-2 (Miller-Fleming et al., 2016). Thus, we propose here that UNC-8 drives the removal of a core group of presynaptic proteins including; Synaptobrevin/SNB-1, liprin- α/SYD-2, Endophilin/UNC-57 and RAB-3, which depends on GABA neuron activity and cytoplasmic calcium. In contrast, synaptic elimination of Munc13 and ELKS does not require UNC-8 and is selectively regulated in a separate pathway driven by the transcription factor Iroquois/IRX-1. Additionally, our studies show that IRX-1 drives disassembly of the same core group of presynaptic proteins (Synaptobrevin/SNB-1, liprin-α/SYD-2, Endophilin/UNC-57, RAB-3) (Figure 4.11). Although UNC-8 is a key downstream effector for this mechanism, our genetic evidence also indicates that Iroquois/IRX-1 must regulate at least one additional downstream gene to remove this core group of components from the active zone

(Figure 4.4 and 4.9). Future studies are needed to define the additional downstream IRX-1 effectors that drive presynaptic disassembly. These IRX-1 targets could emerge from previously

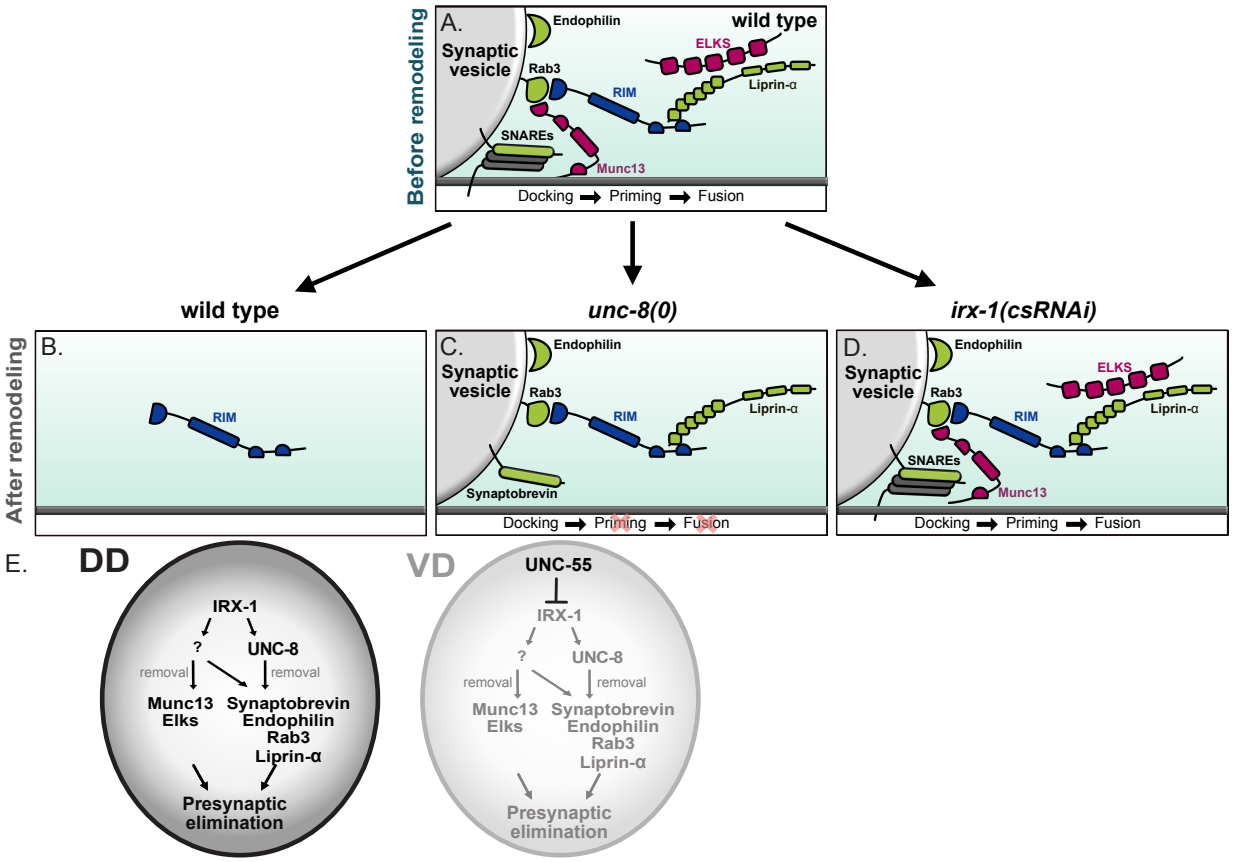

Figure 4. 11. Parallel-acting pathways dismantle the presynaptic apparatus in remodeling GABAergic neurons.

A. Top: Before remodeling, presynaptic proteins SNAREs, Rab3, RIM, endophilin, liprin-alpha, Munc13 and ELKS mediate synaptic vesicle fusion and neurotransmitter release on the ventral side of GABAergic neurons.
B. After remodeling, presynaptic markers except RIM are removed from the ventral nerve cord.
C. Synaptobrevin, Rab3, RIM, endophilin, and liprin-alpha are retained at ventral presynaptic regions of GABAergic neurons in *unc-8* mutants. Note that *unc-8* activity is not required for removal of ELKS and Munc13.
D. With RNAi knockdown of the Iroquois/IRX-1 transcription factor, Synaptobrevin, Rab3, RIM, endophilin, liprin-alpha, Munc13 and ELKS persist in the ventral nerve cord to mediate GABA release from functional terminals. Plasma-membrane SNAREs are depicted because these synapses are functional.
E. Transcriptional regulation of parallel-acting pathways that drive presynaptic disassembly. In DD neurons (left), the transcription factor IRX-1/Iroquois activates expression of at least two downstream targets: (1) The DEG/ENaC channel subunit, UNC-8, which promotes removal Synaptobrevin, Rab3, endophilin and liprin-alpha but not the active zone proteins Munc13 or

ELKS. (2) A second pathway (?), that promotes removal of Synaptobrevin, Rab3, endophilin and liprin-alpha as well as Munc13 and ELKS. In VD neurons (right), the COUP-TF transcription factor UNC-55 blocks expression of IRX-1 thereby preventing the elimination of ventral presynaptic terminals.

defined data sets of genes regulated by the UNC-55/COUP-TF transcription factor (Petersen et al., 2011; B. Yu et al., 2017) since UNC-55 controls IRX-1 expression in VD GABAergic neurons (Figure 4.11) (He et al., 2015; Petersen et al., 2011).

Presynaptic domains are remodeled within intact axons

We have described an example of activity-dependent circuit refinement in *C. elegans* in which presynaptic termini are eliminated in a mechanism that does not perturb axonal morphology (White et al., 1978). Presynaptic domains are also selectively dismantled from intact axons in activity-dependent mechanisms that sculpt the developing mammalian visual circuit. Initially, retinal ganglion cells (RGCs) extend exuberant axonal projections to the lateral geniculate nucleus. Later, RGC inputs to each geniculate neuron are reduced. During this period, axonal pruning for at least one class of RGCs (BD-RGCs) is preceded by the internal reorganization of presynaptic boutons which are eliminated in distal axonal regions and simultaneously assembled in proximal locations (Hong et al., 2014). Axons denuded of presynaptic domains are then retracted in a later phase of refinement (Hong & Chen, 2011). Inputs to RGCs from rod Bipolar Cells (BCs) in the retina are also eliminated from stable axonal-dendritic contacts during development (Morgan et al., 2011). Thus, the reorganization of presynaptic domains within intact RGC and BC axons is similar to the remodeling mechanism in *C. elegans* GABAergic neurons in which the presynaptic apparatus is dismantled without visible alterations in axonal morphology (Hallam & Jin, 1998; White et al., 1978). Presynaptic boutons are also actively assembled as well as removed within intact axonal processes in the adult brain (De Paola et al., 2006; Stettler et al., 2006). Notably, key components involved in presynaptic remodeling in *C. elegans* GABAergic neurons are highly conserved (Figure 4.11). Together, these findings suggest that the molecular

pathways that control presynaptic remodeling in *C. elegans* may also regulate circuit refinement and plasticity in mammals.

Remodeling and "silent" synapses

Our work has revealed a synaptic remodeling mechanism that disables neurotransmitter release while leaving synaptic vesicles and the presynaptic density intact. We showed, for example, that proteins with essential roles in synaptic vesicle priming, Munc13/UNC-13 and ELKS, can be selectively removed from the presynaptic apparatus in a genetic background that preserves the ultrastructural integrity of the active zone (Figure 4A), thus, effectively "silencing" an otherwise normal appearing synapse (Figure 5C). A potentially related phenomenon of synaptic silencing has been reported in the auditory circuit of the barn owl. Juvenile owls fitted with optical prisms learn to associate auditory cues with a new imposed visual location (Knudsen & Knudsen, 1989). Adaptation in this case involves innervation of a new midbrain region in the auditory localization circuit. Synaptic boutons are also maintained, however, in the nearby anatomical domain in which object association normally occurs (Mcbride et al., 2008) which could account for the restoration of normal responses to auditory cues in adult owls after the training prisms are removed (Mcbride & Debello, 2015). The retention of these inactive synaptic structures could correspond to more broadly observed "learning traces" that facilitate the ready reacquisition of quiescent behavioral responses (Knudsen, 2002). We thus suggest that the elucidation of mechanisms that disable synapses by removing specific functional components could reveal the molecular underpinning of presynaptic silencing mechanisms with key roles in learning and memory circuits.

ACKNOWLEDGEMENTS

We thank K. Shen for the GFP FLP-ON ELKS-1 CRISPR/Cas9 knock in strain used in Figure 4.10, E. Jorgensen for the GFP FLP-ON RAB-3 CRISPR/Cas9 knock in strain used in Figure 4.9, J. Kaplan, and J. Dittman for additional reagents and M. Kittelman and M. Zhen for advice on scoring GABA synapses by electron microscopy. Some strains used in this study were provided by the CGC, which is funded by the NIH Office of Research Infrastructure Programs (P40 OD010440). This work used instruments in the Electron Microscopy Core of the UIC Research Resources Center; the BioCryo facility of Northwestern University's NUANCE Center, which has received support from the Soft and Hybrid Nanotechnology Experimental (SHyNE) Resource (NSF ECCS-1542205); the MRSEC program (NSF DMR-1720139) at the Materials Research Center; the International Institute for Nanotechnology (IIN); and the State of Illinois, through the IIN; and CryoCluster equipment, which has received support from the MRI program (NSF DMR-1229693). Imaging experiments were performed in part in the Vanderbilt Cell Imaging Shared Resource (supported by NIH grants CA68485, DK20593, DK58404, DK59637 and EY08126). This work was supported by NIH grants R01NS081259, R01NS106951(DMM) and predoctoral fellowships from the NIH to TWFM (1F31NS084732), NSF to SP (DGE:1445197) and AHA to SP (19PRE34380582) and ACC (18PRE33960581).

AUTHOR CONTRIBUTIONS

Tyne Miller-Fleming created strains, collected and analyzed data for experiments using the UNC-55 paradigm (Figures 4.3, 4.6, 4.7A-G and 4.8A-G). Sierra Palumbos performed and analyzed single molecule FISH to detect *unc-8* transcripts in remodeling neurons (Figure 4.2). Electron microscopy collection and analysis was performed by Laura Manning (Figure 4.5). Janet Richmond recorded and analyzed electrophysiological traces from *C. elegans* muscles applying high-osmolarity puffs to trigger synaptic vesicle fusion events (Figure 4.5). The remaining

experiments were performed by Andrea Cuentas-Condori (Figure 4.4, Figure 4.7H-M, Figure 4.8H-M, Figure 4.9, Figure 4.10).

CHAPTER V

C. elegans neurons have functional dendritic spines

This paper has been published under the same title in eLife, 2019.

Cuentas-Condori, A., Mulcahy, B., He, S., Palumbos, S., Zhen, M., & Miller, D. M. (2019). *C. elegans* neurons have functional dendritic spines. *eLife*, *8*, 1–23.

https://doi.org/10.7554/elife.47918

SUMMARY

Dendritic spines are specialized postsynaptic structures that transduce presynaptic signals, are regulated by neural activity and correlated with learning and memory. Most studies of spine function have focused on the mammalian nervous system. However, spine-like protrusions have been reported in *C. elegans* (Philbrook et al., 2018), suggesting that the experimental advantages of smaller model organisms could be exploited to study the biology of dendritic spines. Here, we used super-resolution microscopy, electron microscopy, live-cell imaging and genetics to show that *C. elegans* motor neurons have functional dendritic spines that: (1) are structurally defined by a dynamic actin cytoskeleton; (2) appose presynaptic dense projections; (3) localize ER and ribosomes; (4) display calcium transients triggered by presynaptic activity and propagated by internal Ca^{++} stores; (5) respond to activity-dependent signals that regulate spine density. These studies provide a solid foundation for a new experimental paradigm that exploits the power of *C. elegans* genetics and live-cell imaging for fundamental studies of dendritic spine morphogenesis and function.

INTRODUCTION

The majority of excitatory synapses in the mammalian brain feature short, local protrusions from postsynaptic dendrites that respond to presynaptic neurotransmitter release (Rochefort & Konnerth, 2012). These dendritic “spines” were originally described by Ramon y Cajal (Yuste, 2015) and are now recognized as key functional components of neural circuits. For example, spine morphology and density are regulated by neural activity in plastic responses that are strongly correlated with learning and memory (Kozorovitskiy et al., 2005; May-Britt, Mari, Thore, & Per, 1998). Although spine-like protrusions have been reported for invertebrate neurons (Leiss et al., 2008; Petralia, Wang, Mattson, & Yao, 2016), few studies (Bushey, Tononi, & Cirelli, 2011; Scott, Reuter, & Luo, 2003) have rigorously determined if these structures share functional features with vertebrate spines.

The anatomy of the *C. elegans* nervous system was originally defined by reconstruction of electron micrographs (EM) of serial sections. This approach revealed that a small subset of neurons displays short, spine-like protrusions. These include five classes of motor neurons (RMD, RME, SMD, DD, VD) and an interneuron (RIP) (White et al., 1976, 1986). Light and electron microscopy detected similar dendritic protrusions extending from motor neurons in the nematode, *Ascaris* (Angstadt, Donmoyer, & Stretton, 1989; Stretton et al., 1978). More recently, reports using light microscopy to explore the spine-like protrusions on the DD class motor neurons have shown that a postsynaptic acetylcholine receptor is localized near the tips in direct apposition to presynaptic termini (Oliver, Alexander, & Francis, 2018; Philbrook et al., 2018). In this chapter, we have adopted a systematic approach to demonstrate that spine-like structures in GABAergic motor neurons (DD and VD) exhibit the salient hallmarks of dendritic spines.

MATERIALS AND METHODS

Worm Breeding

Worms were maintained at 20°- 25°C using standard techniques(Brenner, 1974). Strains were maintained on NGM plates seeded with *E. coli* (OP-50) unless otherwise stated. The wild type (WT) is N2 and only hermaphrodite worms were used for this study. Staging as L3, early L4 (eL4), L4 and young adult worms was defined following vulva development as previously reported (Schindler & Sherwood, 2013).

Molecular Biology

Gateway cloning was used to build pACC06 (*punc-25::*LifeAct::GFP). Briefly, plasmid pDONR221 (Plastino Lab) (Havrylenko, Noguera, Abou-ghali, Manzi, & Pollard, 2015) was used in the LR reaction with pMLH09 (*punc-25*::ccdB::GFP) to create pACC06. Additional plasmids were created using InFusion cloning (Takara). The InFusion cloning module (SnapGene) was used to design primers to create the desired plasmid. Briefly, vector and insert fragments were amplified using CloneAmp HiFi polymerase. PCR products were gel-purified and incubated with In-Fusion enzyme for ligations. Constructs were transformed into Stellar Competent cells and confirmed by sequencing (See full list of plasmids). Addgene provided sequences for GCamP6s (#68119), and ceChrimson (#66101) (Schild & Glauser, 2015). miniSOG sequence was a gift from the Jin lab (Qi, Garren, Shu, Tsien, & Jin, 2012). pSH40 was a gift from the Bargmann Lab (Pokala, Liu, Gordus, & Bargmann, 2014). mRuby sequence was a gift from the Kurshan Lab.

Microscopy

Electron Microscopy

Young adult animals were fixed using high pressure freezing followed by freeze substitution, as previously described (Mulcahy et al., 2018; Rostaing et al., 2004), with minor modification: they were held at -90°C in acetone with 0.1% tannic acid and 0.5% glutaraldehyde for 4 days, exchanged with 2% osmium tetroxide in acetone, raised to -20°C over 14h, held at -20°C for 14h, then raised to 4°C over 4h before washing. Additional *en bloc* staining was performed with uranyl acetate for 2h at room temperature, followed by lead acetate at 60°C for 2h. Samples were embedded in Epon, cured at 60°C for 24h, then cut into 50nm-thick serial sections. Sections were not poststained. Images were taken on an FEI Tecnai 20 transmission electron microscope with a Gatan Orius digital camera, at 1nm/pixel.

3D electron microscopy reconstruction

Images were aligned into a 3D volume and segmented using TrakEM2 (Cardona et al., 2012), a Fiji plugin (Schindelin et al., 2012). Neuron identity was assigned based on characteristic morphology, process placement, trajectory and connectivity (Mulcahy et al., 2018; White et al., 1986). The ventral and dorsal cord volumes contained the anterior-most 25 μm of DD1, and 27 μm of VD2, respectively. Volumetric reconstructions were exported to 3Ds Max for processing (3Ds Max, Autodesk)

AiryScan Microscopy

Worms were mounted on 10% agarose pads and immobilized with 15mM levamisole/0.05% tricaine dissolved in M9. A Zeiss LSM880 microscope equipped with an AiryScan detector and a 63X/1.40 Plan-Apochromat oil objective lens was used to acquire super resolution images of the DD neuron. Images were acquired as a Z-stack (0.19μm/step), spanning the total volume of the DD ventral process and submitted for AiryScan image processing using

ZEN software. Developmental stage was determined by scoring gonad and vulva development (Schindler & Sherwood, 2013).

FIJI (Schindelin et al., 2012) and NIS-Elements software were used for data quantification. Z-stacks were flattened in a 2D projection and line scans were manually drawn along protrusions and perpendicular to the proximal shaft (Figure 5.1D) to determine the Protrusion/Shaft ratio (Figure 5.1E). Spine density was calculated using the counting tool in NIS Elements and then normalized to number of spines per 10 μm of dendrite length.

Time-lapse imaging of actin dynamics

A Nikon microscope equipped with a Yokogawa CSU-X1 spinning disk head, Andor DU-897 EMCCD camera, high-speed piezo stage motor, 100X/1.49 Apo TIRF oil objective lens and a 1.5X magnification lens was used for live imaging. For measurements of LifeAct::GFP and cytosolic mCherry dynamics, young adults (NC3315 and XMN46) were mounted on 10% agarose pads and immobilized with 15mM levamisole/0.05% tricaine dissolved in M9. Z-stacks (0.5μm/step) were collected every 3 minutes. Movies were submitted to 3D-deconvolution on NIS-Elements using the Automatic algorithm and aligned with the NIS Elements alignment tool. For each movie, ROIs were defined along the dendritic shaft for each spine. Mean ROI Intensity was calculated for each time point and exported to Microsoft Excel. Background was determined from a neighboring region inside the worm and subtracted from the ROI in each timepoint. Mean intensity changes where normalized to the mean Intensity from the first timepoint of each movie. Intensity changes for LifeAct::GFP and mCherry were graphed using Prism6 software.

GCaMP6s dynamics in DD spines

GCaMP6s imaging was performed on a Nikon microscope equipped with a Yokogawa CSU-X1 spinning disk head, Andor DU-897 EMCCD camera, high-speed piezo, 100X/1.49 Apo

TIRF oil objective lens and a 1.5X magnification lens. NC3484 worms were immobilized using a combination of 3μL of 100mM muscimol (TOCRIS biosciences #0289) and 7μL 0.05um polybeads (2.5% solids w/v, Polysciences, Inc. #15913-10). Triggered acquisition was used to excite the GCaMP and mCherry signals with 488nm and 561nm lasers. Single plane movies were collected every second for at least 24 seconds. Movies were submitted for 2D-deconvolution on NIS-Elements using the Automatic algorithm. Movies collected with NIS-elements were aligned through time using the ND alignment tool. ROIs with the same area for each channel were defined in spines and on a neighboring region to determine background intensity for every time point. Mean ROI intensity was exported to Microsoft Excel for subtraction of mean fluorescence background intensity. Fluorescence at each timepoint was normalized to intensity at t=0 for GCaMP6s and mCherry signals. Local peaks of GCaMP6s fluorescence were identified between neighboring spines and the difference between the timepoints (deltaT) was calculated. Traces were graphed on Prism6.

To detect evoked calcium responses in DD neurons, NC3569 were grown for 1 generation on an OP-50-seeded plate with freshly added ATR or carrier (EtOH). L4 worms were glued (Super Glue, The Gorilla Glue Company) to a microscope slide in 2μL 0.05um polybeads (2.5% solids w/v, Polysciences, Inc. #15913-10) plus 3μL of M9 buffer and imaged under a coverslip. GCaMP6s imaging was performed on a Nikon microscope equipped with a Yokogawa CSU-X1 spinning disk head, Andor DU-897 EMCCD camera, high-speed piezo and 100X/1.49 Apo TIRF oil objective lens. Single plane images encompassing DD1 postsynaptic spines and adjacent VA and DA motor neurons were collected at 2 frames/second for 15 seconds. The sample was illuminated with a 561nm laser at 2.5 sec intervals (e.g., every 5th frame) for red light activation of Chrimson expressed in cholinergic DA and VA motor neurons (*Punc-4*::ceChrimson::SL2::3xNLS::GFP) while maintaining constant illumination with a 488nm laser to detect GCamP6s signals. For quantifying GCaMP6s fluorescence, videos were aligned and 2D-

deconvolved using NIS Elements software. ROIs were drawn on the spines and on a nearby region to capture background fluorescence. Mean fluorescence intensity of each ROI for each frame was exported into Excel for further analysis. Background was subtracted from each frame and measurements were normalized to t = 0. Mean fluorescence traces were plotted using Prism6. Standard deviations of each time point between conditions (EtOH vs ATR) or ceChrimson activation (before vs after) were compared using the F-test in Prism6.

Classification of spines

Spine shapes were determined from Z-projections of AiryScan images and by 3D-EM reconstruction. Mean and standard deviation (SD) were determined using Prism6. Spines were classified as thin/mushroom, filopodial, stubby or branched. Thin/mushroom spines displayed a constricted base (neck) and an expanded tip (head). Filopodial spines do not have a constricted base (no neck) but are protrusions of constant width. Stubby spines were recognized as protrusions with a wide base and tip. Branched spines were identified as protrusions with more than one visible tip.

Ribosomal protein labeling in DD spines

To label ribosomes in DD spines, we used DD-specific RIBOS(Noma, Goncharov, Ellisman, & Jin, 2017). To label DD spines, we injected *Pflp-13::*LifeAct::mCherry plasmid into CZ20132 and used AiryScan imaging to examine transgenic animals (See AiryScan microscopy section).

Temporal synaptic manipulation

Neuronal silencing

Gravid adults were allowed to lay eggs for 2 hours on an OP50-seeded plate at 20 C to produce a synchronized population of L1 larvae. The middle time-point of the egg-laying session was considered T_0. At T_{19} (time in hours), L1 larvae were transferred to control or histamine plates and maintained at 20°C until imaging on an LSM880 AiryScan microscope at the young adult stage. For control plates, 200µL of water was added to OP-50 seeded NGM plates. For histamine plates, 200µL of 0.5M Histamine, diluted in water, was added to OP-50 seeded NGM plates.

Neuronal activation

Gravid adults were allowed to lay eggs for 2 hours on an OP-50-seeded plate with freshly added ATR. The resultant synchronized population of L1 larvae was maintained at room temperature (23-25C). At T_{27} (L2 larvae), we used WormLab (MBF Bioscience) for exposure to repetitive cycles of 1 second ON + 4 seconds OFF for 6 hours of a 617nm precision LED (Mightex PLS-0617-030-10-S). Images were collected on an LSM880 AiryScan microscope with 60X/1.4 Plan-Apochromat oil objective lens. Control worms were not exposed to light but grown on ATR plates. 100mM ATR (Sigma, #A7410) was prepared in ethanol and stored at -20C. 300uM of ATR was added to OP-50 bacteria and seeded on NGM plates. Plates were dried in darkness overnight and used the next day for experiments.

Feeding RNAi

Clones from the RNAi feeding library (Source BioScience) were used in this study. RNAi plates were produced as described (Petersen et al., 2011). Briefly, RNAi bacteria were grown in the presence of ampicillin (50 µg/mL) and induced with IPTG (1 mM). 250µL of the RNAi bacterial culture was seeded on NGM plates. RNAi plates were kept at 4°C for up to one week until used. RNAi experiments were set-up as follows: 3 to 5 L4 worms (NC3458) were placed on RNAi plates and maintained at 20°C. Four days later, F1 progeny was imaged as young adults.

Ablation of DD neurons

Twenty gravid adults (NC3480) were allowed to lay eggs for 2 hours with the middle time point considered T_0. At T_{16}, (hours) DD neurons were ablated by miniSOG (Qi et al., 2012) activation by exposing worms for 45 min to a 470nm LED light (#M470L2, Thor Labs). Animals were then maintained at 20°C until imaging at ~T_{60} as young adults.

Statistical Analysis

For comparison between 2 groups, Student's T-test was used and $p<0.05$ was considered significant. ANOVA was used to compare between 3 or more groups followed by Dunnett's multiple-comparison test. Standard Deviations between two samples were compared using an F-test and considered $p<0.05$ as significant.

Table 3.1. List of plasmids used in this study

PLASMID NAME	DESCRIPTION
pACC4	p*unc-25*::LifeAct::GFP
pACC6	p*flp-13*::LifeAct::GFP
pACC12	p*flp-13*::LifeAct::mCherry
pACC83	p*flp-13*::GCaMP6s::SL2::mCherry
pACC86	p*unc-4*::ceChrimson::SL2::mCherry
pACC92	p*unc-4*::ceChrimson::SL2::3xNLS::GFP
pMLH09	p*unc-25*::gateway::GFP
pSH4	p*myo-2*::RFP
pSH21	P*str-1*::GFP
pSH40	p*unc-4*::HisCl::SL2::mCherry
pSH83	p*flp-13*::miniSOG::SL2::BFP

Table 3.2. List of strains used in this study

STRAIN NAME	DESCRIPTION
XMN46	bgIs6 [p*flp-13*::mCherry; Pttx-3::RFP] II?
NC3315	wdEx1016 [*pflp-13*::LifeAct::GFP; *pmyo-2*::RFP]
NC3376	ufIs63 (p*acr-2*::RAB3::mCherry) ; wdEx1016[p*flp-13*::LifeAct::GFP; pmyo-2::RFP]

NC3458	*eri-1(mg366)*; wdEx1016 [p*flp-13*::LifeAct::GFP; *pmyo-2*::RFP]
NC3355	*toca-1(tm2056)* X; wdEx1016 [p*flp13*::LifeAct::GFP; p*myo-2*::RFP]
NC3357	wdEx1029 [p*flp13*::LifeAct::GFP; p*unc4*::HisCl::SL2::mCherry; *pmyo-2*::RFP]
NC3455	*ace-2(g72)* I; *ace-1*(p100) X; wdEx1016 [p*flp-13*::LifeAct::GFP; p*myo-2*::RFP]
NC3462	*unc-17(e113)* IV; wdEx1016 [p*flp-13:*:LifeAct::GFP; p*myo-2*::RFP]
NC3469	wdEx1069 [p*flp13*::LifeAct::mCherry; p*str-1*::GFP]
NC3480	wdEx1074 [p*flp-13*::miniSOG::SL2::BFP; p*unc-25*::LifeActGFP; pmyo-2::RFP]
NC3482	*acr-12(ok367)* ufIs126 [*pflp-13*::ACR12::GFP] X, wdEx1069 [*pflp-13*::LifeActmCherry; pstr-1::GFP]
NC3484	wdEx1078 [*pflp-13*::GCaMP6s::SL2::mCherry; pmyo-2::RFP]
NC3486	*unc-31(e169)* IV; wdEx1016 [*pflp-13*::LifeAct::GFP; pmyo-2::RFP]
NC3489	wdEx1083 [*punc-4*::ceChrimson::SL2::mCherry; pflp-13::LifeAct::GFP; pmyo-2::RFP]
NC3569	*lin-15(n765);* wdIs117 [punc-4::Chrimson::SL2::3xNLSGFP; lin-15+] ; wdEx1112 [*pflp13*::GCaMP6s::SL2::mCherry]

RESULTS

Dendritic spines in *C. elegans* GABAergic neurons

In the adult, Dorsal D (DD) class GABAergic motor neurons extend axons to innervate dorsal muscles and receive cholinergic input at ventral dendrites (Figure 5.1A). We used AiryScan imaging, a type of super-resolution microscopy (Korobchevskaya, Lagerholm, Colin-york, & Fritzsche, 2017), to detect spine-like projections on the ventral processes of adult DD neurons labeled with a cytosolic mCherry marker (Figure 5.1B). Because the actin cytoskeleton is a structural hallmark of vertebrate dendritic spines (Cingolani & Goda, 2008), we also labeled DD neurons with the actin marker, LifeAct::GFP (Riedl et al., 2008). Super-resolution images detected apparent enrichment of LifeAct::GFP in DD spines versus the dendritic shaft. For a quantitative assessment, we calculated the ratio of the spine to shaft fluorescence (Figure 5.1D) and plotted the cumulative distribution for each marker (Figure 5.1E). This representation shows a clear separation between measurements of cytosolic mCherry that is evenly distributed

throughout dendrites (median spine/shaft ratio < 1) versus that of the LifeAct::GFP signal (median spine/shaft ratio > 1) (KS test, p<0.0001, Figure 5.1E). Thus, actin is enriched in DD spines.

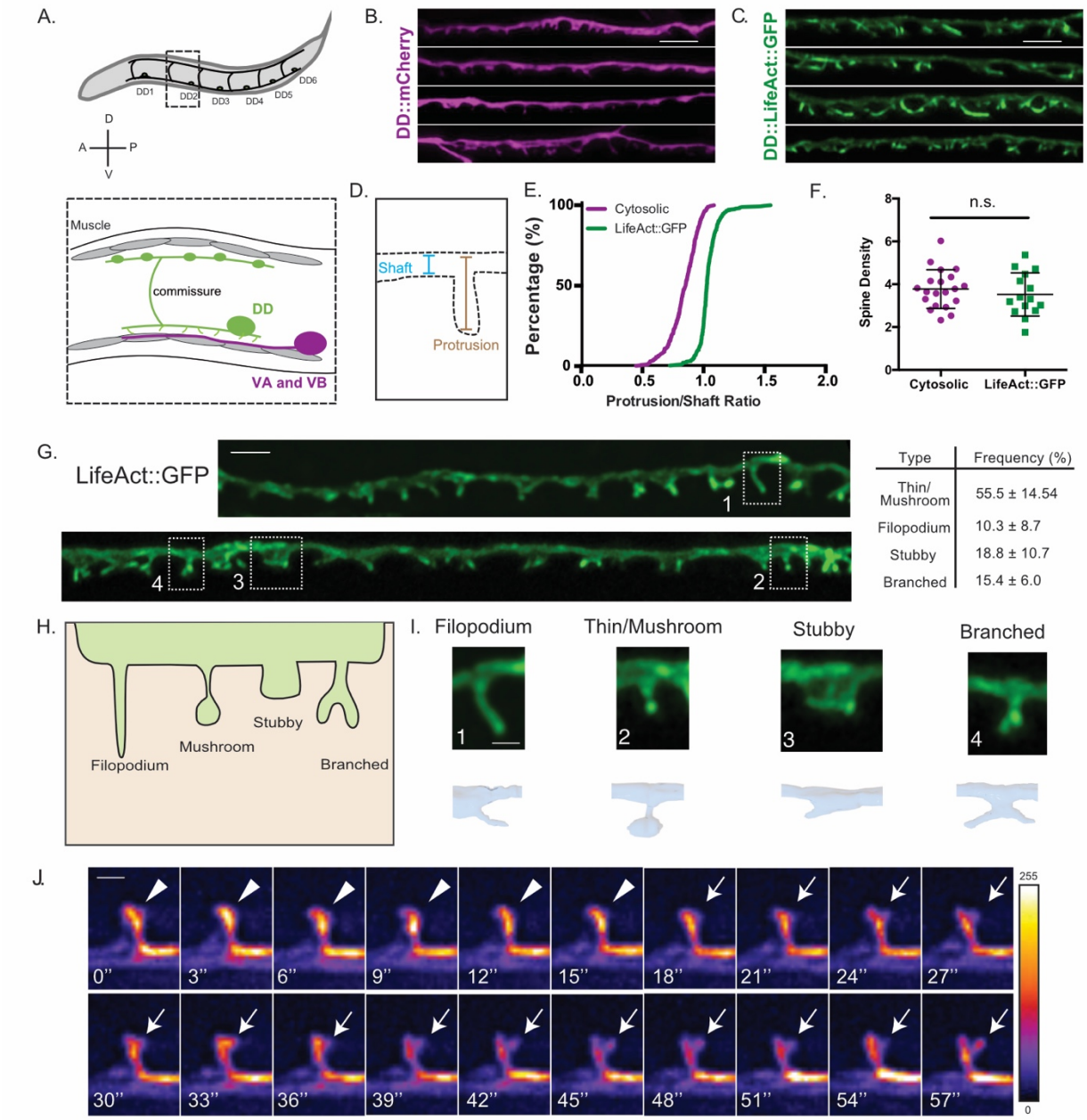

Figure 5. 1. DD GABAergic neurons display dendritic spines

A. Six DD motor neurons are located in the *C. elegans* ventral nerve cord. In the adult, DD presynaptic boutons (oblong ovals) innervate dorsal muscles (grey cells) and DD postsynaptic termini (spines) receive cholinergic input from VA and VB motor neurons on the ventral side (magenta). **B-F.** Airyscan imaging resolves ventrally projecting spines from DD neurons labeled with **(B)** cytosolic mCherry or **(C)** LifeAct::GFP. **D.** Intensity of spine over shaft ratio reveals that **(E)** LifeAct::GFP preferentially accumulates at the spine whereas cytosolic mCherry is evenly

distributed between the spine and shaft (KS test, $p<0.0001$, $n > 286$ spines). **F.** Spine density of young adults revealed by mCherry (3.68 ± 0.8 spines/10μm) or LifeAct::GFP (3.43 ± 1.2 spines/10μm) is not significantly different (t test, $p=0.0855$, $n > 16$ worms). Measurements are mean ± SD. Scale bars = 2 μm. **G-I.** LifeAct::GFP reveals 1. Thin/Mushroom (55.5 ± 14.5%), 2. Filopodial (10.3 ± 8.70%), 3. Stubby (18.8 ± 10.4%), 4. Branched spines (15.4 ± 6.0%) in adult DD motor neurons. Measurements are mean ± SD, n = 16 worms and 357 spines. For scatterplot, see Figure 5.2. (Scale bar = 1 μm). **H.** Schematic of spine shapes. **I.** Images of each type of spine identified by (top) Airyscan imaging (Scale bar = 500nm) of LifeAct::GFP or (bottom) 3D-reconstruction of DD1 from serial electron micrographs of a high-pressure frozen L4. See also Figure 5.2. **J.** Dendritic spines are dynamic. Snapshots of *in vivo* spine remodeling from a thin/mushroom (arrowhead) to branched morphology (arrow). Images (LifeAct::GFP) are shown with rainbow LUT. Higher intensity is represented by warm colors and dimmer intensity by cold colors. L4 stage worm. Scale bar = 500 nm.

This interpretation is strengthened by our finding that independent measurements of the spine density (mean spine numbers/10 μm) with either cytoplasmic mCherry, LifeAct::GFP or the membrane bound marker, myristolated-mRuby (myr::mRuby) are not significantly different (Figures 5.1F and 5.2A). Similar results were obtained by EM reconstruction (see below) (Figure 5.2A).

A close inspection of LifeAct::GFP-labeled protrusions revealed a variety of spine shapes which we grouped into morphological classes resembling those previously reported for mammalian dendritic spines (Bourne & Harris, 2008; Rochefort & Konnerth, 2012): thin/mushroom, filopodial, stubby and branched (Figure 5.1G-I) (see Methods). We merged "thin" and "mushroom" shapes into a single category because both are defined by an enlarged head region vs a narrower neck. By these criteria, adult DD neurons have predominantly thin/mushroom spines, with lesser fractions of filopodial, stubby and branched shapes (Figure 5.1G and 5.2C-D). A comparison of the morphological classes identified with the LifeAct::GFP vs myr::mRuby markers revealed some differences, notably the frequency of stubby spines, which is significantly elevated with the myr::mRuby label (Figure 5.2D). These differences could reflect the relative ease of scoring different spine morphologies with markers for either the cell membrane (myr::mRuby) or actin cytoskeleton (LifeAct::GFP). Alternatively, over-expression of these markers could alter spine morphology but, in this case, does not appear to perturb overall the spine density (Figure 5.2A).

As an independent method for assessing the presence of dendritic spines, we used EM to reconstruct the anterior-most 25 μm of the dendrite for DD1, the most anterior member of the DD class of motor neurons (White et al., 1986). For this experiment, young adult animals were prepared using High Pressure Freezing (HPF) to avoid potential artifacts arising from chemical fixation (Weimer et al., 2006; White et al., 1986). Reconstruction of 50 nm serial ultrathin sections

from the anterior DD1 dendrite detected twelve DD1 spines, with multiple morphological shapes that resemble classes revealed by fluorescent markers (Figure 5.1I and Figure 5.2C-D). Our

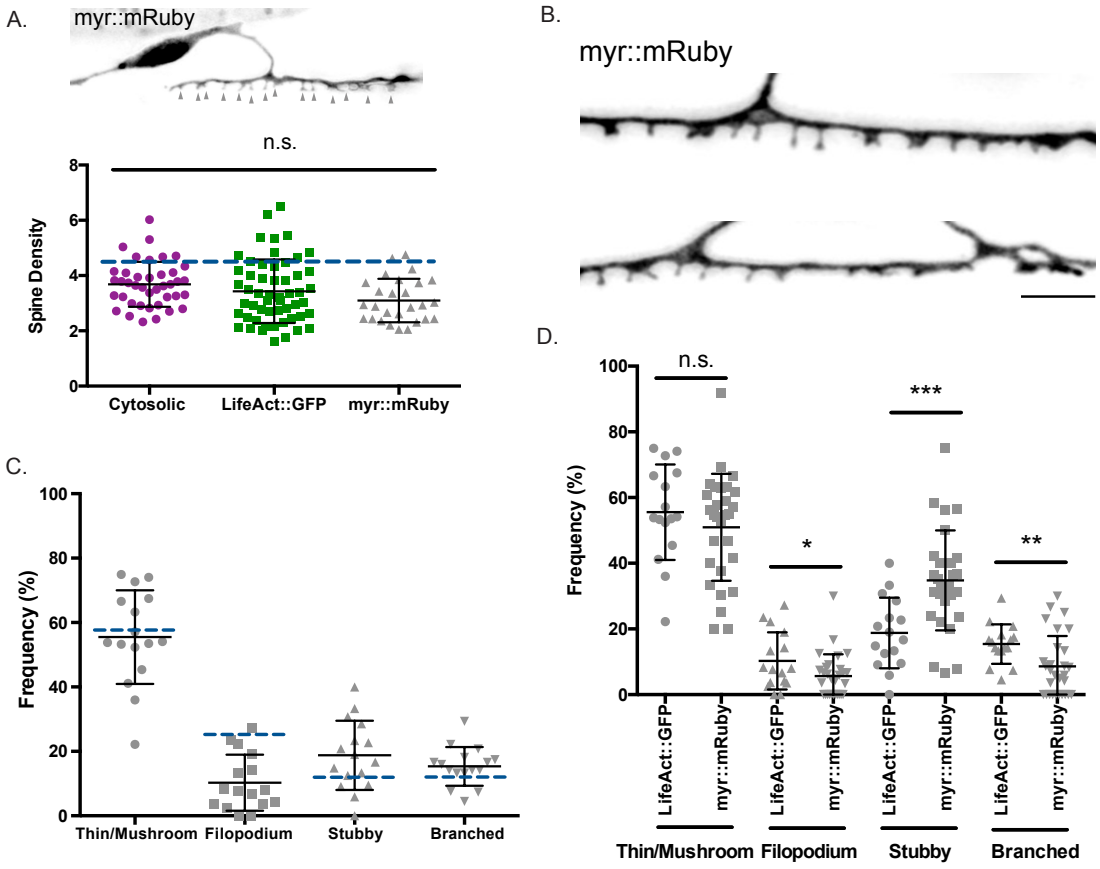

Figure 5. 2. Dendritic spines adopt distinct morphologies

A. Spine densities determined from young adult DD neurons labeled with mCherry (3.68 ± 0.8 spines/10µm), LifeAct::GFP (3.43 ± 1.2spines/10µm) and MYR::mRuby (3.09 ± 0.8 spines/10µm) are not significantly different and are comparable to spine density determined by 3D EM reconstruction of DD1 (4.2 spines/10µm) (dashed blue line). One-way ANOVA between mCherry, LifeAct::GFP and MYR::mRuby ($p>0.05$), $n>16$.
B. Example of DD spines labeled with membrane bound marker, myristolated mRuby (MYR::mRuby).
C. Frequency of spines by type labeled with LifeAct::GFP: Thin/Mushroom (55.5 ± 14.5%), Filopodial (10.3 ± 8.70%), Stubby (18.8 ± 10.7%), Branched (15.4 ± 6.01%). Dashed blue lines denote frequency for each spine type from EM reconstruction of DD1: Thin/Mushroom (58.3%), Filopodial (25%), Branched (8.3%) and Stubby (8.3%).
D. Frequency of spines by type, labeled with MYR::mRuby: Thin/Mushroom (52.2 ± 16.5%), Filopodial (5.68 ± 7.0%), Stubby (33.1 ± 14.8%), Branched (9.02 ± 9.6%). Unpaired T-test shows that frequency of Filopodial ($p=0.0339$); Stubby ($p=0.0009$) and Branched ($p=0.011$) classes labeled with MYR::mRuby is differs from frequency of spine types detected with with LifeAct::GFP labeling.

findings are consistent with observations from EM reconstructions of mammalian dendritic spines in the hippocampus where thin and mushroom shapes predominate (K M Harris & Stevens, 1989; Kristen M. Harris, Jensen, & Tsao, 1992) and filopodial and stubby spines are less abundant (Fiala, Feinberg, Popov, & Harris, 1998; Zuo, Lin, Chang, & Gan, 2005).

DD spines are shaped by a dynamic actin cytoskeleton

Although we have assigned DD motor neuron spines to four discrete classifications, both fluorescence imaging and EM reconstruction point to a broader array of spine types that includes potential intermediate forms (Figure 5.1G-I). A similarly heterogeneous array of spine shapes among mammalian neurons has been attributed to active remodeling of spine architecture (Sala & Segal, 2014; Zuo et al., 2005). To test for this possibility in *C. elegans*, we used live imaging to produce time-lapse recordings of DD spines. Our live-imaging revealed that some DD spines can remodel *in vivo*. For example, Figure 5.1J depicts the emergence of a nascent lateral branch near the tip of a thin/mushroom spine. During imaging sessions of $\geq$ 30 minutes, we observed several cases (11 out of 25 movies) of transient filopodial-like extensions from the dendritic shaft that destabilize in the course of minutes. In contrast, mature DD spines at the L4 stage were stable throughout a given imaging session. In the mature mammalian cortex, extended imaging has revealed transient filopodial extensions with a lifetime shorter than a day, and potential plasticity over longer intervals, where approximately half of spines are stable for months (Trachtenberg et al., 2002; Zuo et al., 2005). To our knowledge, our time lapse images are the first to directly visualize dynamic dendritic spines in a motor neuron of a living organism (Kanjhan, Noakes, & Bellingham, 2016).

Live-imaging of DD motor neurons also detected a dynamic actin cytoskeleton (Figure 5.3A-E), consistent with previous reports for mammalian dendritic spines (Honkura, Matsuzaki, Noguchi, Ellis-Davies, & Kasai, 2008; Mikhaylova et al., 2018). To ask if actin assembly is required for DD spine morphogenesis (Cingolani & Goda, 2008), we applied genetic methods to knock

down key regulators of actin polymerization and assessed their effect on DD spines (Figure 5.3F). We found that the Arp2/3 complex, and two of its activators, the F-BAR protein TOCA-1 (Ho et al., 2004) and the Wave Regulatory Complex (Chen et al., 2010a), are required to maintain DD spine density (Figure 5.3F). Expression of TOCA-1 in DD neurons rescued the spine density defect (Figure 5.3G) demonstrating that actin polymerization is required cell-autonomously to promote spine formation. Disruption of the Arp2/3 complex or its activators has been previously shown to reduce dendritic spine density in the mammalian brain and to impair function (Kim et al., 2013; Lippi et al., 2011; Soderling et al., 2003; Spence, Kanak, Carlson, & Soderling, 2016; Westphal et al., 2000).

Dendritic spines of DD neurons directly appose presynaptic terminals

Because functional dendritic spines are sites of presynaptic input (Alvarez & Sabatini, 2007; Hering et al., 2001; Petralia et al., 2016), we investigated the disposition of DD spines vis-a-vis their main presynaptic partners, the cholinergic VA and VB class motor neurons (Figure 5.4A). For super-resolution imaging, we used the synaptic vesicle-associated marker, mCherry::RAB-3, to label the presynaptic termini of VA and VB class cholinergic motor neurons in the ventral cord and LifeAct::GFP to label DD neurites and spines (Figure 5.4B). Clusters of mCherry::RAB-3-labeled puncta are located adjacent to DD spines (Figure 5.4B) (Philbrook et al., 2018). Among the 128 spines identified by LifeAct::GFP, most (~84 %) reside near at least one presynaptic cluster (denoted “contacted” in Figure 5.4D). Approximately ~40% (51/128) of DD spines are associated with multiple presynaptic clusters of RAB-3 puncta which suggests that individual spines receive input from > 1 presynaptic terminal (arrowheads, Figure 5.4B).

Our EM reconstruction revealed direct apposition of all DD spines (n = 12/12) with the presynaptic termini of cholinergic motor neurons (Figure 5.4C). Further analysis of the DD1 dendrite and cholinergic motor neuron (VA1, VA2 and VB2) axons in this region showed that most

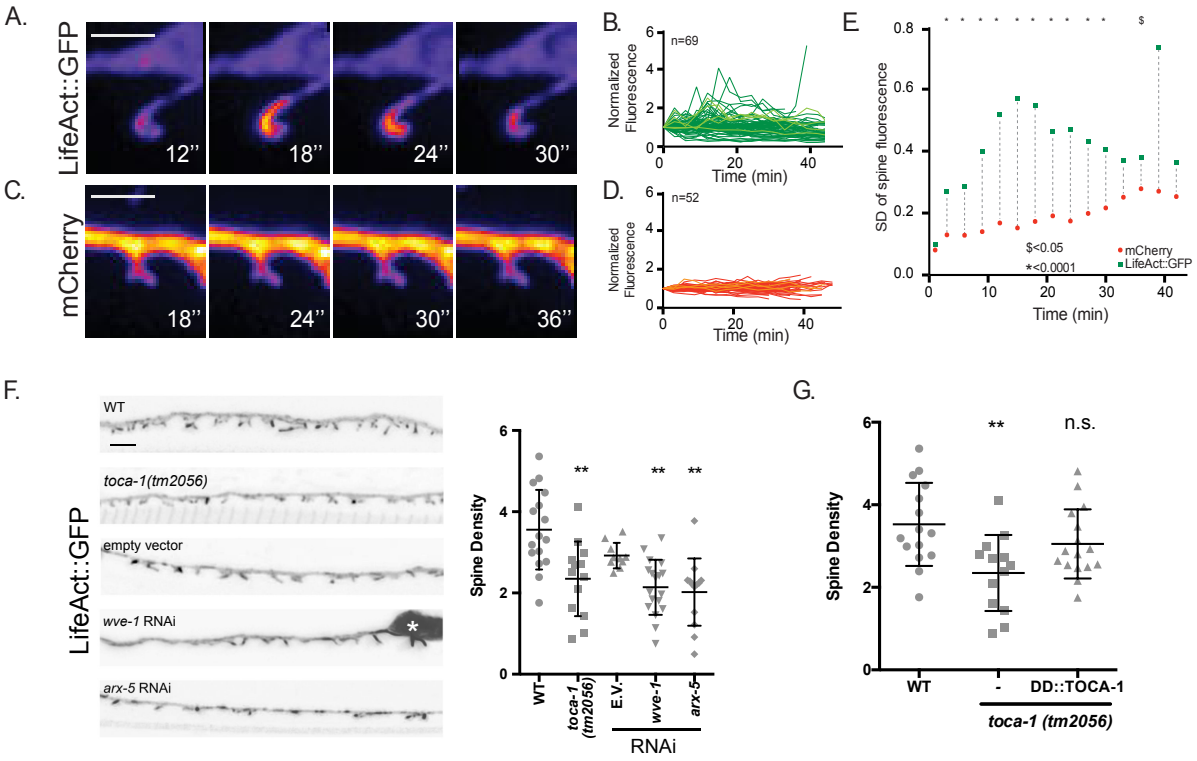

Figure 5. 3. Dendritic spines display a dynamic actin cytoskeleton.

A-E. Live-imaging of **(A,B)** LifeAct::GFP and **(C,D)** mCherry-labeled DD spines of L4 stage larvae reveals dynamic LifeAct::GFP vs stable cytosolic mCherry signals**.**
B,D. Normalized traces of LifeAct::GFP and mCherry fluorescence from live imaging. Different shades of green and red lines are used to allow visualization of individual traces. **E.** Comparison of standard deviations of all traces for each timepoint reveals significantly different variance between LifeAct::GFP vs cytosolic mCherry markers (F-test, * is $p < 0.0001$ from T_3 to T_{30} and $ is $p < 0.05$ at T_{39}, $n > 51$ traces). Scale bar = 500 nm.
F. Regulators of actin polymerization define spine density. (Left) Representative images (young adults) of DD spines for WT (wild type), *toca-1 (tm2056)*, empty vector (RNAi control), *wave/wve-1*(component of WRC) RNAi and *p21/arx-5* (component of Arp2/3 complex) RNAi**.** (Right) WT young adults show 3.53 ± 1.0 spines/10µm vs *toca-1 (tm2056*) with 2.77 ± 1.1 spines/10 µm (t test, *** is $p<0.001$). Spine density is reduced with RNAi of *wave/wve-1* (2.24 ± 0.7 spines/10 µm) or *p21/arx-5* RNAi (2.20 ± 0.7 spines/10 µm) versus Empty Vector (E.V.) control (2.9 ± 0.4 spines/10µm). One-way ANOVA with Dunnett's multiple comparison test, ** is $p<0.01$, $n > 9$ worms. Measurements are Mean ± SD. Scale bar is 1 µm.
G. TOCA-1 functions cell-autonomously in DD neurons. wild-type young adults show 3.53 ± 1.0 spines/10 µm vs 2.35 ± 0.9 spines/10 µm in *toca-1(tm2056)*, which is rescued with TOCA-1a expression in DD neurons (*Pflp-13::*TOCA-1a::mCherry) = 3.05 ± 0.8 spines/10 µm. One-way ANOVA with Dunnett's multiple comparison test. n.s.= not significant. ** is $p < 0.01$.

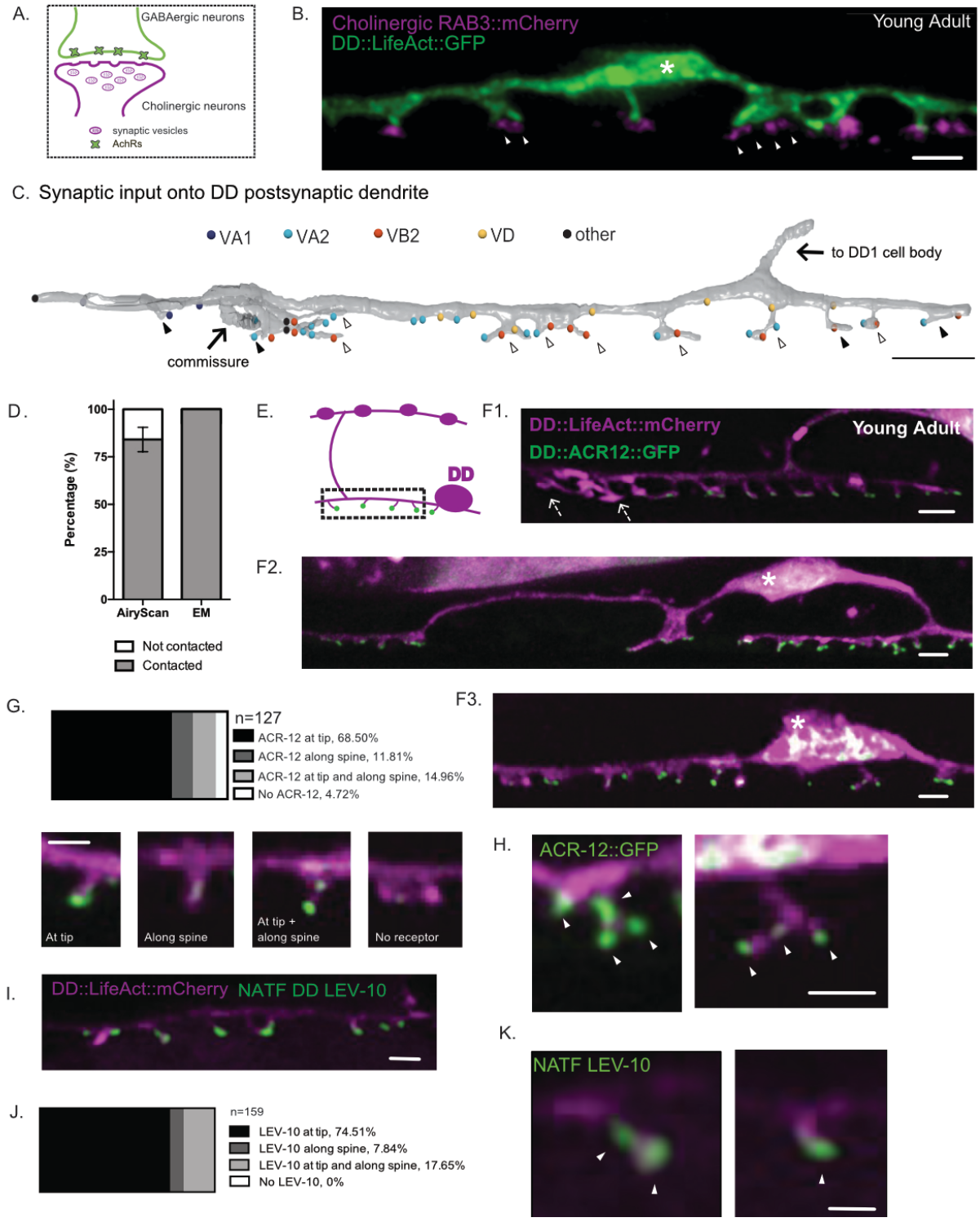

Figure 5. 4. DD spines appose presynaptic cholinergic vesicles

A. Postsynaptic ionotropic acetylcholine receptors (iAChRs) are localized in GABAergic motor neurons in apposition to input from cholinergic motor neurons.

B. Cholinergic RAB-3 presynaptic vesicles labeled with mCherry localize in close proximity to DD postsynaptic spines labeled with *flp-13::*LifeAct::GFP. Young adult stage worms. Scale bar = 1µm. Asterisk denotes the DD cell body. Arrowheads mark multiple RAB-3::mCherry clusters apposing dendritic spines.
C. Volumetric EM reconstruction of a portion of the DD1 dendrite (25 µm) in the ventral nerve cord (gray) detects contacts with 43 presynaptic termini from axons of the cholinergic (VA1, VA2, VB2) and GABAergic (VD) motor neurons, and other neurons (other). 84.8% (n=28/33) of VA and VB inputs are adjacent to DD spines. 33.3% (4/12) of spines directly oppose a single presynaptic partner (black arrowhead); the majority of spines (66.7%) appose more than one terminal (clear arrowhead). Scale bar = 2 µm.
D. Frequency of spines contacted by cholinergic presynaptic sites detected by Airyscan imaging (contacted, 84.1 ± 6.4% vs not contacted, 15.8 ± 6.4%, n = 128 spines from 7 worms) or by EM (contacted, 100% vs not contacted, 0%, n = 12 spines from 1 worm).
E. Schematic of DD presynaptic boutons (top) and postsynaptic spines (dashed box) with distal iAChR puncta (green dots) on the ventral side.
F1-3. iACh receptor subunit ACR-12::GFP (green) localizes to LifeAct::mCherry-labeled DD spines (magenta). Asterisk marks DD cell body. Arrows in F1denote spines without visible ACR-12::GFP clusters. Scale bars = 1 µm.
G-H. Locations of ACR-12::GFP puncta on DD spines. > 95% of spines have at least one ACR-12::GFP cluster (n = 127 spines from 8 young adult worms). Examples of spines from each category. Scale bars = 1 µm. (**H)** Examples of spines with more than one ACR-12::GFP cluster. White arrowheads point to ACR-12::GFP clusters at DD spines. Scale bar = 200 nm.
I-K. NATF labeling of endogenous iAChR auxiliary protein LEV-10 in DD neurons (I) detects LEV-10 localization to spines with **(J)** all spines showing NATF LEV-10::GFP puncta (n = 159 spines from 7 worms). Scale bars = 500 nm. **(K)** Example of spines with endogenous LEV-10 clusters. Scale bar = 200 nm.

(84.8%, n = 28/33) cholinergic presynaptic inputs appose DD1 spines, whereas a smaller number (15.2%, n = 5/33) are positioned along the dendritic shaft. This finding parallels the observation that only 10% of excitatory synapses in the mature mammalian cortex are positioned on dendritic processes (Cingolani & Goda, 2008). Two thirds of DD1 spines (n = 8/12) receive input from more than one neuron. That is, a single DD1 spine head is contacted by presynaptic termini of both VA and VB class cholinergic motor neurons (Figure 5.4C). This finding could explain the observation above from Airyscan imaging that multiple clusters of RAB-3 puncta are adjacent to ~40% of DD spines (Figure 5.4B). We note that individual spines on GABAergic neurons in the mammalian hippocampus can also have inputs from multiple presynaptic termini (Acsady, Kamondi, Sık, Freund, & Buzsaki, 1998; Gulyás, Miettinen, Jacobowitz, & Freund, 1992; Petralia et al., 2016). DD1 spines receive some inhibitory synapses from the other class of GABAergic motor neurons (VDs). Most of these VD inputs are restricted to the DD1 dendritic shaft (n = 5/6) (Figure 5.4C).

The acetylcholine receptor (AChR) subunit ACR-12 is postsynaptic to cholinergic inputs at GABAergic motor neurons, and has been previously shown to localize to DD1 dendritic protrusions (Figure 5.4E) (He et al., 2015; Petrash et al., 2013; Philbrook et al., 2018). We used Airyscan imaging to quantify the subcellular distribution of the ACR-12::GFP signal on DD spines. We detected ACR-12::GFP clusters on ~95% of DD spines (n = 121/127) (Figure 5.4E), with 68.5% (n = 87/127) localized at spine tips and the remainder either positioned along the lateral side of the spine (~12%, n = 15/127) or at both the side and tip (~15 %, n = 19/127) (Figure 5.4G). 43.3% of spines (n = 55/127) had more than one ACR-12::GFP cluster (Figure 5.4H), a finding that mirrors the recent observation that the spines of mammalian cortical neurons can display multiple postsynaptic assemblages of the postsynaptic protein PSD-95 (Hruska, Henderson, Le Marchand, Jafri, & Dalva, 2018).

To obviate the possibility that the localization of ACR-12::GFP clusters to DD spines results from over-expression, we used a new live-cell labeling scheme to detect an endogenous

component of the acetylcholine receptor complex, the co-factor protein LEV-10 (Gally, Eimer, Ung, Richmond, & Bessereau, 2004). NATF (Native and Tissue-Specific Fluorescence) relies on the reconstitution of superfolder GFP (sfGFP) from the split-sfGFP fragments, GFP1-10 and GFP11 (He et al., 2019). We used genome editing to fuse seven tandem copies of GFP11 to the C-terminus of the native LEV-10 coding sequence. GFP1-10 was then selectively expressed in DD neurons from a transgenic array (i.e., *flp-13::GFP1-10*). In this case, we detected LEV-10 NATF-GFP signal at 100% (n = 159/159) of DD spines (Figure 5.4I-J), further substantiating the hypothesis that DD spines are sites of presynaptic input.

Our EM analysis confirmed that DD spines do not display electron dense postsynaptic densities (PSDs), a feature that is also not detected in electron micrographs of other *C. elegans* postsynaptic terminals (White et al., 1976, 1986; Mei Zhen, Huang, Bamber, & Jin, 2000). Although robustly stained PSDs are observed at vertebrate glutamatergic synapses, PSDs are either absent or much less prominent in electron micrographs of vertebrate synapses at spines for other neurotransmitters (glycine, GABA, acetylcholine) (Knott, Quairiaux, Genoud, & Welker, 2002; Kubota, Hatada, Kondo, Karube, & Kawaguchi, 2007; Umbriaco, Watkins, Descarries, Cozzari, & Hartman, 1994). Thus, postsynaptic assemblages which are bound to occur at all of these synapses (Figure 5.4), are likely comprised of distinct sets of scaffolding proteins some of which are readily stained by heavy atom markers used for EM imaging (Petralia, Sans, Wang, & Wenthold, 2005; Petralia et al., 2016).

ER and ribosomes localize to DD neuron dendritic spines

Key cytoplasmic organelles such as Smooth Endoplasmic Reticulum (SER), have been reported in both the dendritic shaft and spines of mammalian neurons (K M Harris & Stevens, 1989). In addition to its role of processing membrane proteins, the SER in spines is known to

regulate activity-dependent Ca^{++} release through the ryanodine receptor (Fill & Copello, 2002). Other structures such as polysomes and rough ER have also been reported in spines, raising the

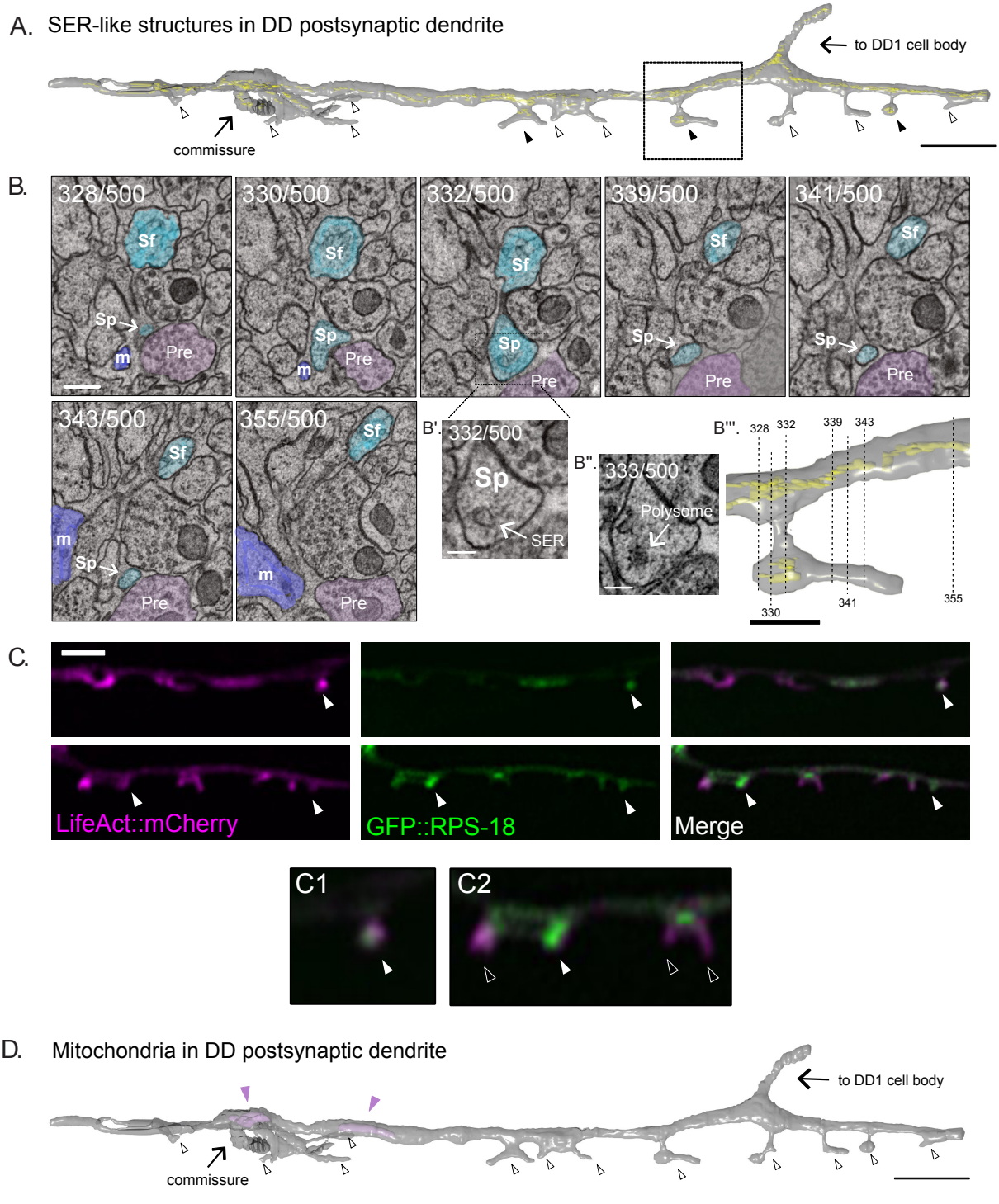

Figure 5. 5. SER-like structures and ribosomes in spines and dendritic shaft.

A. 3D EM reconstruction of DD1 dendrite reveals Smooth Endoplasmic Reticulum (SER)-like cisternae (yellow) in the dendritic shaft and some spines (black arrowheads). Most spines lack SER-like structures (clear arrowheads). Scale bar = 2 μm.
B. Serial cross-sections (328-355) of the ventral nerve cord show spines (Sp) budding from DD1 (blue) dendritic shaft (Sf). 'Pre' labels presynaptic terminals from a cholinergic VA neuron (pink); m, muscle arm (purple). (Scale bar = 200 nm) **B'.** Magnified region of section 332. Arrow points to SER-like structure in DD dendritic spine (Scale bar = 100 nm). **B''.** Section 333. Arrow points to polysome-like structure in DD dendritic spine (Scale bar = 100 nm). **B'''.** Volumetric reconstruction of DD1 dendrite (gray) and SER-like structures (yellow). Dashed lines denote location of each section shown in B. Scale bar = 500 nm.
C. Airyscan imaging shows GFP-labeled ribosomal protein, RPS-18 (Noma et al., 2017), localized to DD spines (arrowheads) labeled with LifeAct::mCherry. Scale bar = 2 μm.
D. Volumetric EM reconstruction of a portion of the DD1 (25 μm) dendrite shows mitochondria (purple) in the shaft (arrowheads) but not in spines (clear arrowheads).

possibility of local translation (Bourne & Harris, 2008; Nimchinsky, Sabatini, & Svoboda, 2002; Steward, Reeves, & Reeves, 1988).

Our EM reconstruction of DD1 revealed cisternae SER-like structures in both the dendritic shaft and spines (Figure 5.5A-B). Ribosome-like structures were detected in some DD1 spines (Figure 5.5B''). This observation is consistent with our independent finding that the ribosomal protein, RPS-18::GFP (Noma et al., 2017) is also detected in about half of (44.5 ± 12.0%) DD spines (Figure 5.5C). Mitochondria and microtubules are reported to be rare in the dendritic spines of mature mammalian neurons (Bourne & Harris, 2008; Nimchinsky et al., 2002). Our EM reconstruction did not mitochondria or microtubules in all twelve DD spines (Figure 5.5D). Both organelles were detected in DD1 dendritic shaft. These observations however should be interpreted cautiously given the small number of spines reconstructed.

Activation of presynaptic cholinergic motor neurons drives Ca^{++} transients in DD spines

Ca^{++} is one of the main signaling molecules to mediate activity-dependent synaptic plasticity (K. F. H. Lee, Soares, Thivierge, & Béïque, 2016; Rochefort & Konnerth, 2012). We reasoned that if DD spines are functional, we should detect dynamic Ca^{++} transients. To test this hypothesis, we expressed the Ca^{++} sensor GCaMP6s in DD neurons. Live-imaging (at 2 second intervals) revealed spontaneous Ca^{++} transients in both DD spines and shafts that lasted for several seconds (Figure 5.6A-C). Muscle cells that share cholinergic input with DD spines also display prolonged elevation of Ca^{++} over a period of seconds (Liu, Chen, & Wang, 2013), suggesting that cholinergic neurons regulate the long lasting bursts of Ca^{++} observed in spines and muscle cells. Interestingly, Ca^{++} transients were observed simultaneously in adjacent spines about 50% of the time (Figure 5.6D). To estimate the likelihood of simultaneous Ca^{++} peaks in adjacent spines occurring by chance, we compared the distribution of the observed time differences between neighboring spine Ca^{++} peaks ($\triangle T$) to a uniform distribution of time

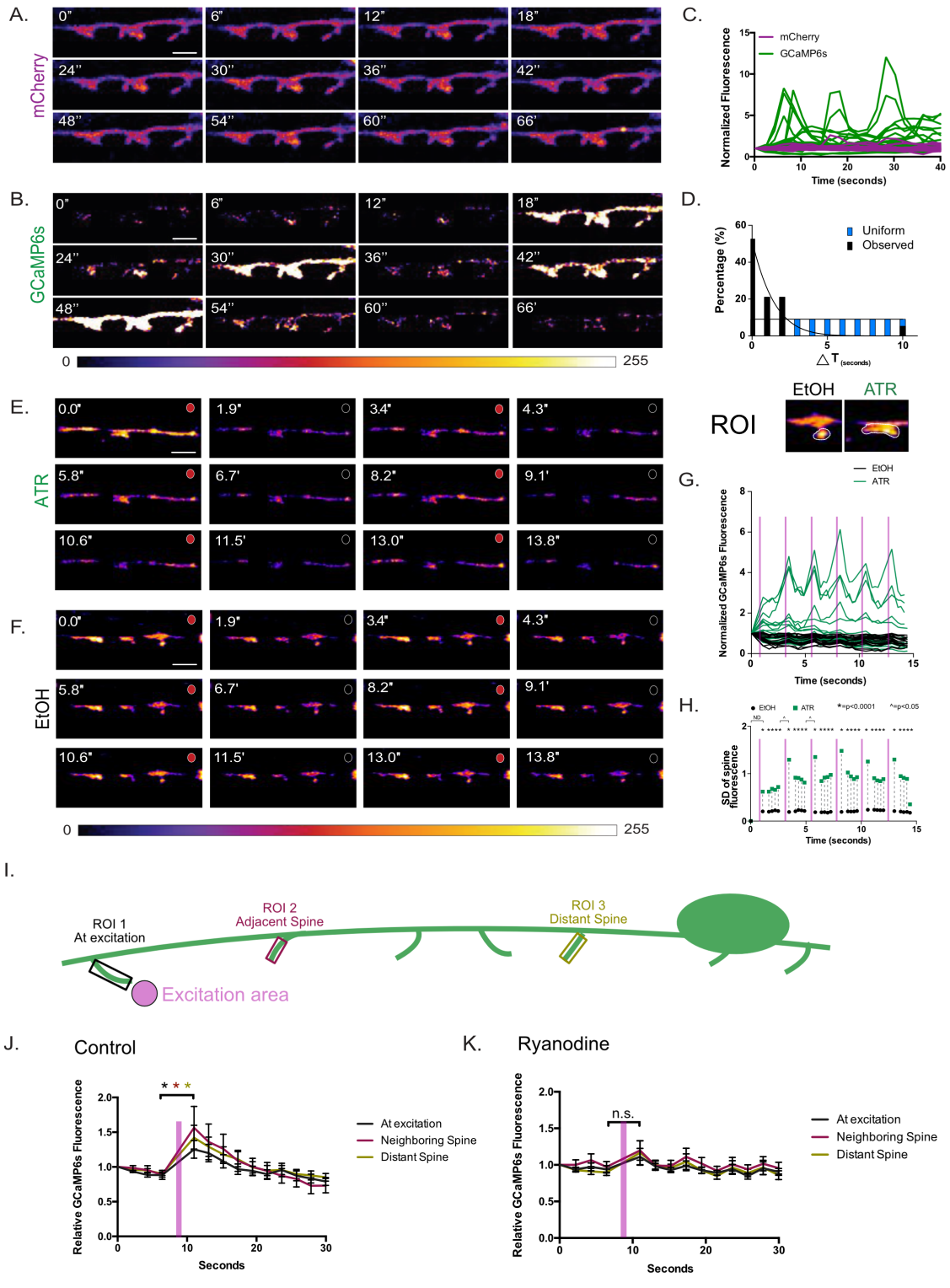

Figure 5. 6. Coordinated Ca^{++} transients in dendritic spines.

Series (time in seconds) of live-cell images of cytosolic **(A)** mCherry and **(B)** GCaMP6s in DD postsynaptic spines reveals (**C**) dynamic GCaMP6s vs stable mCherry signals, n = 11 movies, 31 spines. **D.** GCaMP6s transients occur in neighboring spines more frequently (> 50%) than predicted by a random distribution (KS test, $p<0.0001$). Scale bars = 500 nm.
E-H. VA motor neuron activation is correlated with Ca^{++} transients in DD1 spines. GCaMP6s fluorescence imaged (at 0.5 sec intervals) with periodic optogenetic activation (at 2.5 sec intervals) of ceChrimson, detects Ca^{++} transients with (**E**) ATR (n = 14) but not with carrier (**F**) (EtOH) (n = 12). Circles at the top right corner of each panel correspond to red light on (red) for ceChrimson activation vs off (black). Scale bars = 500 nm. (**G**) GCaMP6s fluorescence throughout the 15 sec recording period plotted for ATR (green) (n = 14) vs carrier (EtOH) (black) (n = 12). (**H**) Plot of the standard deviation (SD) of GCaMP6s signal at each time-point shows that fluctuations in the ATR-treated samples (green boxes) are significantly greater than in EtOH controls (black circles), F-test, *= $p < 0.0001$. Additionally, SDs are significantly different between timepoints before and after light activation (T_6 vs T_7 and T_{11} vs. T_{12}). F-test, ^ = $p < 0.05$. ND = not determined. Purple bars denote interval with red-light illumination (e.g., ceChrimson activation).
I-K. Ca^{++} propagation to neighboring spines depends on intracellular Ca^{++} stores. **(I)** Graphical representation of the experimental paradigm: 561nm laser excitation at a single spine (excitation area, pink) with subsequent GCaMP6s changes recorded from three different regions of interest at: (1) the excited spine, (2) an adjacent spine and (3) a distant spine. **(J)** In the wild type, significant Ca^{++} changes are detected at the excited spine ($p = 0.0182$), adjacent spine ($p = 0.0319$) and distant spine ($p = 0.0402$), n = 15 videos. **(K)** In ryanodine-treated worms, significant Ca^{++} changes are not detected at the excited spine ($p > 0.999$), at an adjacent spine ($p = 0.924$) or at a distant spine ($p = 0.552$), n = 16 videos.

differences (at 2 second intervals) over the period of observation (10 seconds). These distributions are statistically different (KS test, $p<0.0001$), which suggests that the observation of correlated Ca^{++} dynamics may reflect mechanisms for linking postsynaptic activity in adjacent DD spines (Figure 5.6D). Alternatively, coordinated Ca^{++} transients in adjacent spines could arise from input from a shared presynaptic neuron. For example, our EM reconstruction revealed that the majority of DD1 spines (9/12) are postsynaptic to the VA2 cholinergic motor neuron (Figure 5.4C). A similar explanation of convergent input was proposed for the coordinated firing of adjacent dendritic spines in rat hippocampal neurons (Takahashi et al., 2012).

We did not observe Ca^{++} signals in DD spines when cholinergic receptors were desensitized by administration of a cholinergic agonist levamisole (data not shown). This finding is consistent with the hypothesis that Ca^{++} transients in DD spines depend on presynaptic cholinergic signaling. To test this idea, we engineered a transgenic animal for optogenetic activation of VA neurons with red-light illumination (*Punc-4:*:ceChrimson::SL2::3xNLS::GFP) (Schild & Glauser, 2015) and detection of Ca^{++} changes in DD spines with blue-light excitation (*Pflp-13*::GCaMP6s::SL2::mCherry). VA motor neurons are presynaptic to DDs and therefore are predicted to evoke DD neuronal activity (White et al., 1986). ceChrimson was activated by a brief flash of red light (80ms) at 2.5 second intervals and the GCaMP6s signal in DD neurons was recorded at 2 Hz. This experiment detected a striking correlation of GCaMP6s fluorescence with ceChrimson activation (Figure 5.6E-G). Although GCaMP6s fluorescence also varied in DD spines in the absence of red-light illumination, fluctuations were strongly correlated with ceChrimson activation as shown by a plot of the standard deviation of GCaMP6s fluorescence for all traces across the 15-second sampling period (Figure 5.6H). These results are consistent with the interpretation that DD spines are responding to cholinergic input from presynaptic VA motor neurons.

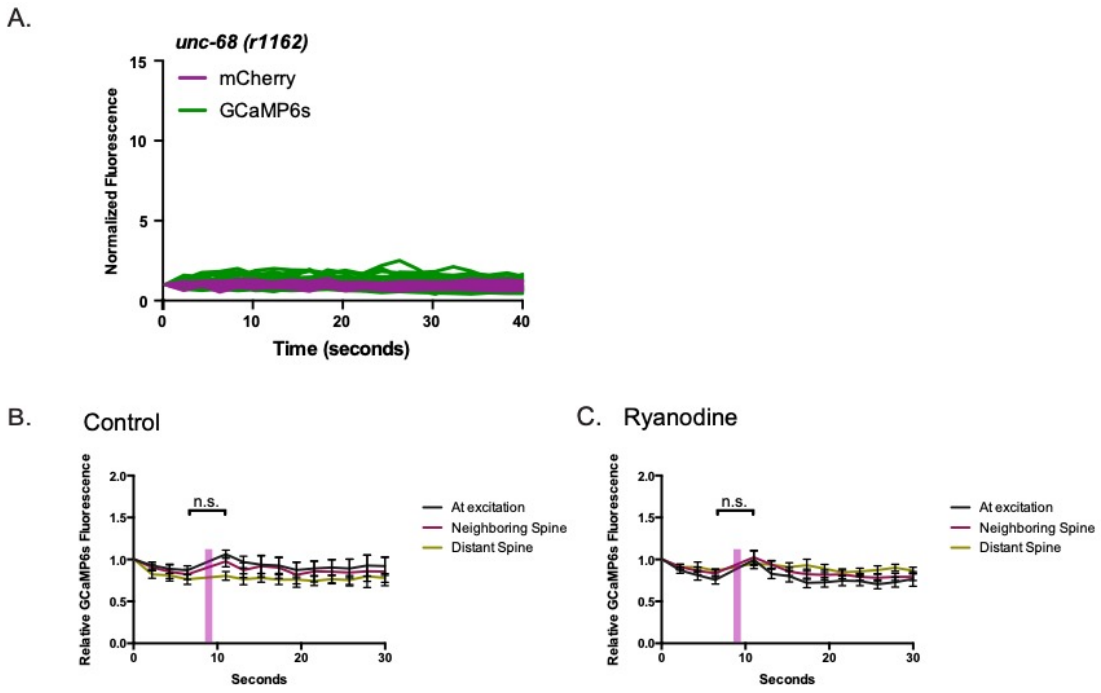

Figure 5. 7. Dendritic Ca^{++} transients depend on intracellular Ca^{++} stores.

A. Intrinsic GCaMP6s transients are dramatically reduced in *unc-68(r1142)* mutants. Neither **(B)** Control (EtOH only) or **(C)** ryanodine-treated (ryanodine + EtOH) worms show significant Ca^{++} changes after 561nm local excitation (n > 6 videos).

Activation of ceChrimson triggered Ca^{++} changes at neighboring spines and in the DD shaft (Figure 5.6F). As noted above, this effect could arise from shared input to adjacent spines from a single presynaptic motor neuron (Figure 5.4C). In addition, Ca^{++} waves might also spread along the DD dendrite from each activated spine. To test for this possibility, we selectively activated presynaptic domains adjacent to single DD spines and recorded Ca^{++} changes at (1) the excited spine; (2) an adjacent spine and (3) a distant spine (See Methods) (Figure 5.6I). Live imaging at two seconds after ceChrimson activation, detected elevated GCaMP signals in spines in all three regions that then waned with time (Figure 5.6J). This observation suggests that cholinergic release near a single spine can trigger Ca^{++} changes in neighboring and distant spines. In developing hippocampal neurons, Ca^{++} signal is propagated to neighboring spines via Ca^{++} release from intracellular stores (Lee et al., 2016). Because activation of intracellular Ca^{++} stores depend on ryanodine-sensitive channels, we repeated the local spine activation experiment (Figure 5.6I) in the presence of 1mM ryanodine to block Ca^{++} release from the ER. Treatment with ryanodine substantially attenuated Ca^{++} transients in all spines (Figure 5.6K) thus, suggesting that coordinated firing of adjacent spines may require the activation intracellular Ca^{++} stores. This possibility is consistent with our finding noted above of SER-like structures throughout the DD shaft and spines (Figure 5.5A-B). Additional support for the role of intracellular Ca^{++} in spine Ca^{++} dynamics is provided by our finding that a mutation that disrupts the UNC-68/Ryanodine receptor results in substantially reduced intrinsic Ca^{++} dynamics in DD spines (Figure 5.7). Overall, these observations show that Ca^{++} signals can propagate after local activation and that spreading depends on intracellular Ca^{++} stores.

Cholinergic signaling enhances DD spine density during development

In mammalian neurons, dendritic spine shape and density are modulated throughout development (Fiala et al., 1998; Kristen M. Harris et al., 1992; Kanjhan, Fogarty, Noakes, & Bellingham, 2016). To determine if DD spine morphogenesis is also developmentally-regulated,

we used the LifeAct::GFP marker to quantify spine density in four successive larval stages: L3, early L4, mid-L4 and young adult. This experiment revealed that spine density increases as DD neurons elongate during development (Figures 5.8 and 5.9).

Dendritic spines, as sites of synaptic input, can be modulated by changes in synaptic strength (Bourne & Harris, 2008; Nimchinsky et al., 2002; Rochefort & Konnerth, 2012). Long-term potentiation, for example, is correlated with increased numbers of spines in the mammalian brain (Engert & Bonhoeffer, 1999; Trachtenberg et al., 2002, 2005). Similarly, hyperactivity is associated with increased dendritic spine density in hypoglossal motor neurons (Kanjhan, Noakes, et al., 2016). Conversely, long-term depression has been shown to induce spine shrinkage (Q. Zhou, Homma, & Poo, 2004) that may lead to their elimination. To test the idea that DD spines may also respond to changes in the strength of cholinergic signaling, we altered acetylcholine levels and assessed possible effects on spine density.

To reduce acetylcholine signaling, we used *unc-17/vAChT (e113)* mutants, in which expression of the vesicular acetylcholine transporter (UNC-17/vAChT) is selectively eliminated in ventral cord cholinergic motor neurons (J. Rand, personal communication). For the converse condition of elevated acetylcholine signaling, we used mutants that disrupt acetylcholinesterase activity, *ace-1(p100)* and *ace-2(g720)* (Figure 5.8A). Reduced synaptic acetylcholine release (i.e., in the *unc-17/vAChT* mutant) results in lower DD spine density in the adult (Figure 5.8C and 5.8E). In contrast, increased synaptic acetylcholine (i.e., in *ace-1;ace-2* double mutants) results in precocious elevation of spine density during development (Figure 5.8D and 5.8E). Importantly, either chronic reduction (i.e., in the *unc-17*/vAChT mutant) or elevation (i.e., in *ace-1;ace-2* double mutants) of acetylcholine levels (Figure 5.8A-E and Figure 5.9A-C) impaired the developmentally regulated enhancement of spine density that is normally observed in wild-type animals. These findings are consistent with the idea that cholinergic signaling positively regulates the formation of DD spines. The developmental elevation of spine density is also blocked in

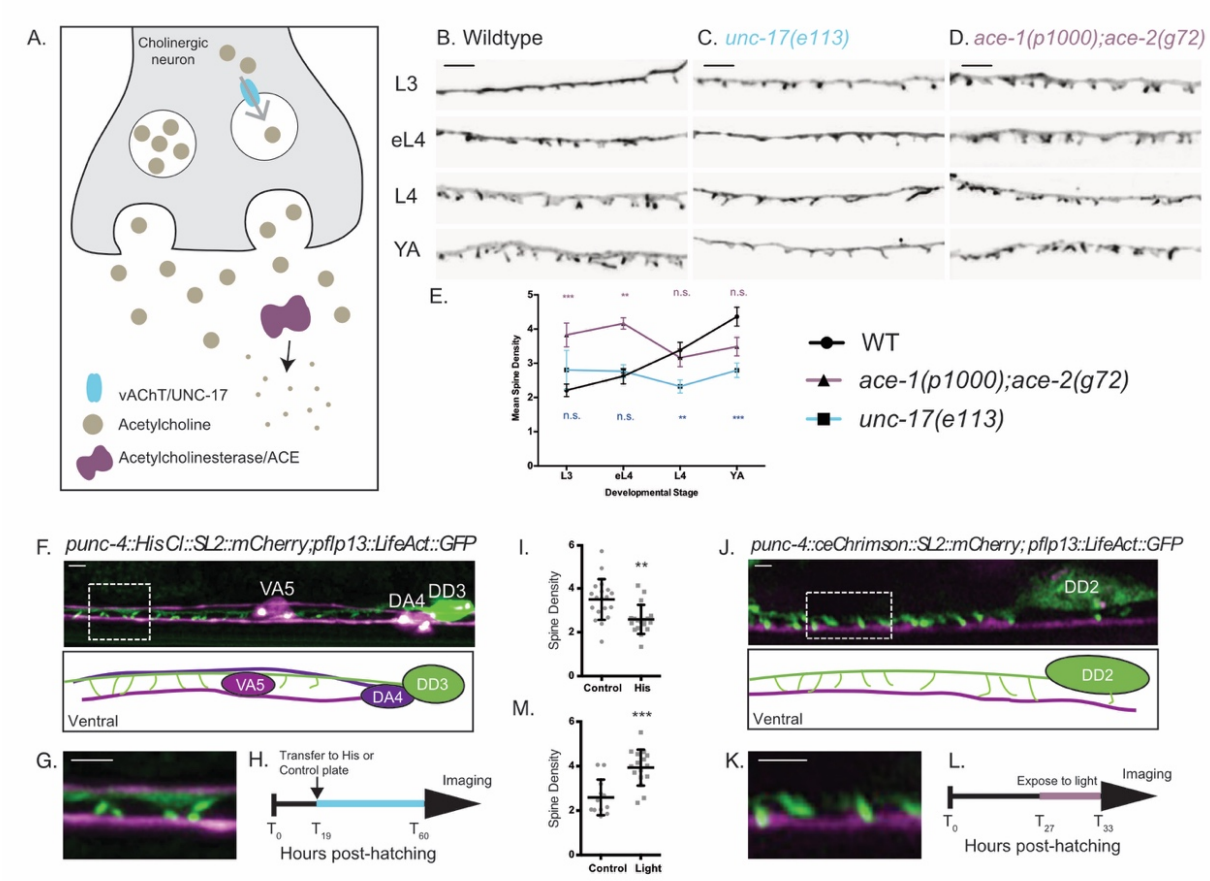

Figure 5. 8. Cholinergic activity regulates spine density during development.

A. Synaptic vesicles are loaded with acetylcholine (ACh) by the vesicular acetylcholine transporter (vAChT/UNC-17). Acetylcholinesterase enzymes (ACE) degrade synaptic ACh.
B-E. Spine density increases throughout development in the wild type (WT) but not in *unc-17(e113)* mutants whereas spine density is precociously elevated in *ace-1(p1000);ace-2(g72)* mutants. Representative images of **(B)** WT, **(C)** *unc-17 (e113)* and **(D)** *ace-1(p100); ace-2(g72)*. Scale bars = 2 µm.
F-I. Reduced ACh signaling in cholinergic motor neurons decreases postsynaptic spine density. (**F)** Expression of Histamine-gated Chloride channels and mCherry in cholinergic (VA and DA) motor neurons (*punc4::HisCl::SL2::mCherry*) (Pokala et al., 2014) vs DD motor neurons labeled with LifeAct::GFP shows (**G)** DD spines (green) extending to the ventral process of the VA5 motor neuron (magenta). Note dorsal placement of DA4 axon. (**H)** Synchronized L2 larvae were transferred to either histamine or control plates at T_{29} (hours post-laying) for growth up to the L4 stage (~T_{50}), see Methods. **(I)** DD spine density at the L4 stage is reduced by growth on histamine (2.58 ± 0.6) vs control (3.49 ± 0.9). T-test, ** = p<0.01, n > 17. Scale bars = 1 µm.
J-M. Temporal activation of A-class cholinergic motor neurons increases spine density. **(J)** Cholinergic motor neurons (e.g., VA4) express ceChrimson (Schild & Glauser, 2015) and mCherry (*punc4::ceChrimson::SL2::mCherry).* LifeAct::GFP marks DD2. **(K)** DD spines (green) extend ventrally toward VA process (magenta). **(L)** Synchronized L2 stage larvae (T_{27}, hours post-laying) were transferred to ATR or control plates (see Methods) for 6 hours (until T_{33}, ~L3 stage) and exposed to red-light pulses vs control group grown in the dark. **(M**) Exposure to red-light for

6 hours elevates spine density at the L3 stage (3.9 ± 0.8) vs control (2.59 ± 0.8). T-test, *** is p<0.001, n>10. Scale bars = 1 µm.

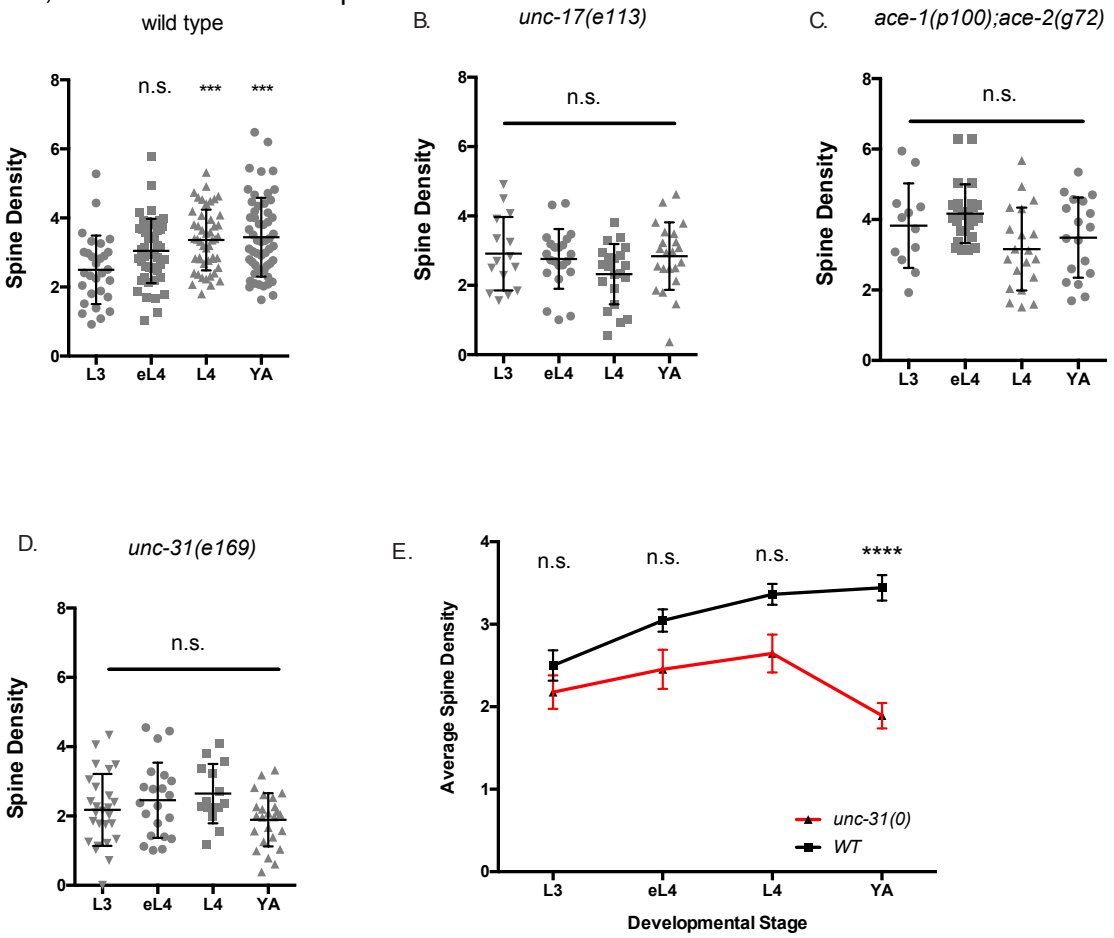

Figure 5. 9. Synaptic activity regulates postsynaptic DD spine density.

A. Spine density (spines/10 µm) increases throughout development in the wild type (WT). L3 (2.5 ± 0.9), (early L4) eL4 (3.1 ± 0.9), L4 (3.4 ± 0.9) and (Young Adult) YA (3.4 ± 1.1). One-way ANOVA of all groups vs L3 shows that spine densities at L4 and YA stages are different from L3. *** is p<0.001.
B. Spine density (spines/10 um) does not increase during development with reduced cholinergic signaling in *unc-17(e113)*. L3 (2.91 ± 1.0), eL4 (2.76 ± 0.9), L4 (2.32 ± 0.87) and YA (2.84 ± 0.9). One-way ANOVA of all groups against L3 stage shows no statistically significant difference during development.
C. Spine density (spines/10µm) is elevated throughout development in acetylcholinesterase deficient *ace-1(p100);ace-2(g72)* mutant animals. L3 (3.83 ± 1.2), eL4 (4.17 ± 0.8), L4 (3.16 ± 1.2) and YA (3.49 ± 1.1). One-way ANOVA of all groups against L3 stage shows no statistically significant difference during development.
D. Spine density (spines/10µm) does not increase during development in *unc-31(e169)* mutants with impaired dense core vesicle release L3 (2.18 ± 1.0), eL4 (2.45 ± 1.1), L4 (2.65 ± 0.9) and YA (1.89 ± 0.8). One-way ANOVA of all groups against L3 stage shows no statistically significant difference during development.

E. Spine density (spines/10μm) does not increase during development in *unc-31(e169)* and shows lower spine density than wild type (WT) at the Young Adult (YA) stage. T-test at each timepoint between genotypes, **** is $p<0.0001$. Measurements are mean ± SD.

unc-31/CAPS mutants (Speese et al., 2007), in which release of neuropeptide and catecholamine neurotransmitters is selectively prevented (Figure 5.9D-E).

For an additional test of activity-dependent regulation of DD spine density, we modulated presynaptic cholinergic function for specific periods during larval development. To reduce cholinergic activity, we expressed the histamine-gated chloride channel (Pokala et al., 2014) in A-class (DA, VA) cholinergic motor neurons, which are direct presynaptic partners of DD neurons (White et al., 1976). Animals grown in the presence of histamine showed reduced spine density at the L4 stage compared to animals grown on plates without histamine (Figure 5.8F-I). To elevate cholinergic activity, we expressed the red-light activated opsin, ceChrimson (Schild and Glauser 2015), in A-class motor neurons and measured spine density at the L3 stage when wild-type animals show fewer DD spines than in adults (Figure 5.8B and 5.8E). Animals were exposed to red light to activate ceChrimson for a brief period (1 second every 4 seconds) during the L2-L3 stage larval development (See Methods). This treatment led to increased spine density (scored in L3 larvae) in comparison to animals grown in the absence of red light or ATR (Figure 5.8J-M). These results demonstrate that DD spine density depends on presynaptic cholinergic signaling, thus confirming that DD spines share the fundamental property of mammalian dendritic spines of positive regulation by neuronal activity (Kanjhan, Fogarty, et al., 2016; Trachtenberg et al., 2005).

VD-class GABAergic neurons also display dendritic spines

In the *C. elegans* motor circuit, dendrites of the DD-class GABAergic motor neurons receive cholinergic input in the ventral nerve cord, whereas the VD class dendrites are located in the dorsal nerve cord (Figure 5.10A). Because the original EM reconstruction of the *C. elegans* nervous system detected spine-like structures on VD neurons (White et al., 1976), we sought to verify this finding by using the LifeAct::GFP marker for Airyscan imaging. We used miniSOG (Qi

et al., 2012) for selective ablation of DDs (See Methods) since LifeAct::GFP was expressed in both DD and VD neurons in this case and would otherwise obscure VD morphology.

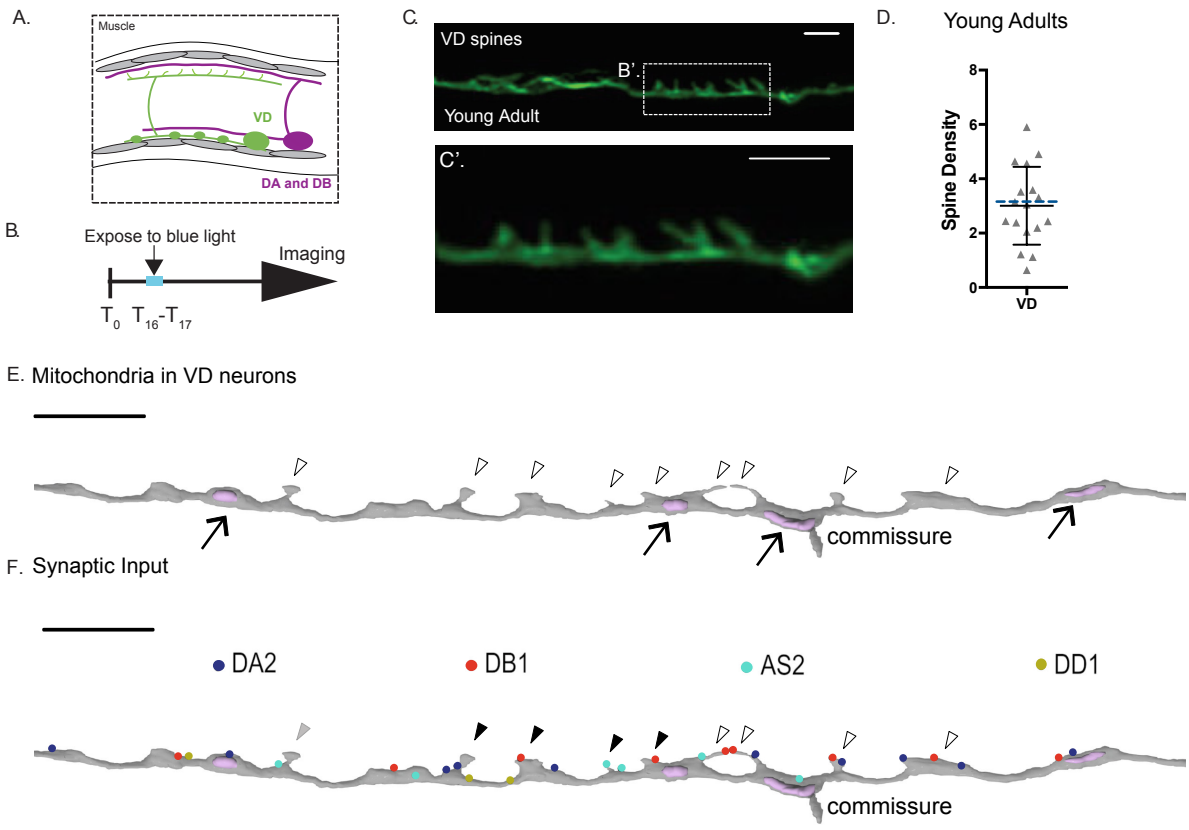

Figure 5. 10. Ventral D-GABAergic motor neurons have dendritic spines

A. VD motor neurons (green) are located in the ventral nerve cord. In the adult, VD presynaptic boutons (oblong ovals) innervate ventral muscles (gray cells) and VD postsynaptic termini (spines) receive cholinergic input from DA and DB motor neurons (magenta) on the dorsal side.
B-D. GABAergic VD neurons show dendritic spines. GABA neurons were labeled with LifeAct::GFP (*Punc-25::LifeAct::GFP*) and DD neurons expressed miniSOG (*Pflp-13::miniSOG::SL2::BFP*). **(B)** Synchronized L1 larvae were exposed to blue light for 45 minutes during T_{16}-T_{17} (hours after egg laying) to ablate DD neurons and maintained at 20°C until the adult stage. **(C)** Airyscan imaging of the dorsal cord in young adults (T_{60}) (hours after egg laying) shows spine-like protrusions on VD neurons. **(C')** Inset from **C**. Scale bars = 1 µm. **(D)** VD spine density (3.01 ± 1.43 spines/10µm), n = 17. Dashed blue line represents spine density detected in VD2 with 3D EM (3.33 spines/10µm).
E. 3D EM reconstruction shows mitochondria in the shaft of VD dendrites (arrows) but not in VD spines (clear arrowheads).
F. Volumetric EM reconstruction of a portion of the VD2 dendrite (27 µm) in the dorsal nerve cord (gray) detects contacts with 36 presynaptic termini from axons of the cholinergic (DA, DB or AS) and GABAergic (DD) motor neurons. 50.0% (n=11/22) of DA and DB inputs are adjacent to VD spines. 44.4% (4/9) of spines directly oppose a single presynaptic partner (black arrowhead) or

more than one terminal (clear arrowhead). One VD spines does not appose any presynaptic density (gray arrowhead). Scale bar = 2 μm.

This experiment confirmed the presence of dendritic spines in VD neurons throughout the dorsal nerve cord (Figure 5.10A-D).

Our EM reconstruction of 27 μm of the anterior VD2 dendrite detected 9 dendritic spines (Figure 5.10E). Similar to DD1, most VD spines are closely apposed to presynaptic termini of cholinergic motor neurons (DA2, DB1, AS2). Additional presynaptic inputs from other cholinergic and GABAergic motor neurons (DD) are distributed along the dendritic shaft (Figure 5.10F) and several mitochondria are also observed in VD2 dendritic shaft (Figure 5.10E). Thus, our results confirm that both the DD and VD classes of ventral cord GABAergic motor neurons display dendritic spines (White et al., 1976, 1986).

DISCUSSION

The prevalence of postsynaptic protrusions in vertebrate and invertebrate nervous systems suggests that spines are ancient structures and thus could be effectively investigated in a variety of model organisms (Leiss et al., 2008; Petralia et al., 2016). Our analyses revealed salient, conserved features of *C. elegans* dendritic spines: (1) A key role for the actin cytoskeleton in spine morphogenesis; (2) Postsynaptic receptor complexes at the tips of spines in close proximity to presynaptic active zones; (3) Postsynaptic calcium transients evoked by presynaptic activity and propagated from intracellular Ca^{++} stores; (4) The presence of endoplasmic reticulum and ribosomes; (5) Regulation of spine density by presynaptic activity.

C. elegans offers several advantages for studies of spine morphogenesis and function. Because *C. elegans* is transparent, live imaging does not require surgery or other invasive methods that are typically necessary for *in vivo* imaging of spines in an intact mammalian nervous system. Well-developed *C. elegans* genetic tools for targeted genomic manipulation (Nance & Frøkjær-Jensen, 2019) and unbiased forward genetic screens can be used to reveal new

determinants of spine assembly. A recent study, for example, reported that neurexin, a conserved membrane protein and established regulator of synaptic assembly, is necessary for spine morphogenesis in DDs. Interestingly, in this case, neuroligin, the canonical neurexin ligand, is not required, suggesting a potentially new neurexin-dependent mechanism of synaptogenesis (Oliver et al., 2018; Philbrook et al., 2018).

Our study confirmed that both DD and VD motor neurons display dendritic spines. Thus, other neurons reported to have “short branches” in the original EM reconstruction of the adult *C. elegans* (White et al., 1986), the cholinergic (RMD, SMD) and GABAergic (RME) motor neurons and the interneuron (RIP), are likely to display *bona fide* dendritic spines. An ongoing effort to produce a gene expression fingerprint of each type of *C. elegans* neuron (Hammarlund, Hobert, Miller, & Sestan, 2018; S. Taylor et al., 2019) may be useful for identifying genetic programs that uniquely correlate with spine morphogenesis since only a small number (White et al., 1976) of neurons have been reported to have spine-like structures. Finally, a developmentally regulated remodeling program (Kurup and Jin 2016; Petersen et al. 2011; John G. White, Albertson, and Anness 1978) transforms presynaptic boutons into postsynaptic spines in larval DD neurons and thus could be especially useful for live imaging studies of synaptic plasticity and spine morphogenesis.

ACKNOWLEDGEMENTS

I thank Douglas Holmyard (Nanoscale Biomedical Imaging Facility) for preparing serial EM sections; Dylan Burnette, Aidan Fenix and Nilay Taneja for insightful imaging discussions; and Erin Miller for help with aligning serial electron micrographs. Some C. elegans strains used in this work were provided by the Caenorhabditis Genetics Center, which is funded by the NIH Office of

Research Infrastructure Programs (P40 OD010440). Super-resolution imaging was acquired at the Vanderbilt Cell Imaging Shared Resource (1S10OD201630-01).

AUTHOR CONTRIBUTIONS

Douglas Holmyard prepared the *C. elegans* sample for high-pressure freezing electron microscopy (Figure 5.4C and 5.5A-B). Ben Mulcahy assisted in the acquisition, alignment and analysis of the serial EM reconstruction by providing expertise advice. Ben Mulcahy produced animations of the serial EM reconstruction (Figure 5.4C and 5.5A-B). Siwei He performed CRISPR/Cas9 to tag $GFP11_{x7}$ into the *lev-10* locus (Figure 5.4 I). Sierra Palumbos assisted with the integration of wdIs117 line which expresses Chrimson in VA and DA neurons (Figure 5.6). The remaining experiments were performed by Andrea Cuentas-Condori.

Chapter VI

Section “Insights from synaptic remodeling in *C. elegans*” has been published in the Journal of Neurogenetics, 2020.

Cuentas-Condori, A., & Miller, D. M. (2020). Synaptic remodeling, lessons from *C . elegans*. *Journal of Neurogenetics*, *34*(3–4), 307–322. https://doi.org/10.1080/01677063.2020.1802725

CONCLUSIONS AND FUTURE DIRECTIONS

Insights from synaptic remodeling in *C. elegans*

As described above, DD motor neurons effectively reverse functional polarity with presynaptic (axonal) and postsynaptic (dendritic) compartments exchanging locations at opposite ends of each DD neuron (Figure 1.4). Similar examples of polarity reversal are currently unknown in other organisms. Remarkably, however, the asymmetric features that distinguish dendritic vs axonal compartments can be reallocated in response to injury. Axotomy, for example, can result in the transformation of an existing dendrite into an axon both in cultured neurons (Dotti & Banker, 1987) and in a living organism (Whitington & Sink, 2004). In addition, synapses are extensively relocated in the developing and mature mammalian nervous system (See Chapter I). Thus, the transcriptional and cellular pathways that drive synaptic remodeling DD neurons may also control refinement of mammalian circuits.

Activity-dependent removal of presynaptic domains in the mammalian visual circuit

In the developing mammalian visual circuit, retinal ganglion cells (RGCs) project to the thalamus to innervate geniculate neurons. Initially, presynaptic boutons are dispersed throughout each RGC axon to synapse with multiple geniculate targets. This arrangement in the connectivity is then refined in a mechanism that eliminates distal RGC boutons while clustering others at proximal locations (Figure 1.3) (Hong et al., 2014). Importantly, RGC axonal projections remain intact as boutons are relocated and are not retracted until a later, separate pruning step (Hong & Chen, 2011). Inputs to RGCs from rod Bipolar Cells (BCs) in the retina are also eliminated from stable axonal-dendritic contacts during development (Morgan et al., 2011). Thus, synaptic remodeling within existing RGC and BC axons parallels refinement of the DD circuit in which presynaptic domains are repositioned to new locations within the DD neurite. As discussed above, at least one presynaptic protein, RAB-3, is recycled from old to new boutons in DD neurons (See Chapter III) (Park et al., 2011). It will be interesting to determine whether RGCs similarly recycle existing synaptic material from distal regions to the newly formed bouton clusters. This possibility seems plausible because a related phenomenon occurs in the mature mammalian nervous system in which presynaptic components can be actively exchanged between *en-passant* synapses (Darcy et al., 2006; Herzog et al., 2011; Staras et al., 2010; Tsuriel et al., 2006).

Synaptic remodeling in RGC axons is also activity-dependent as deprivation of sensory neuron input diminishes bouton clustering (Hong et al., 2014). Similarly, reduced synaptic activity impairs DD remodeling by delaying both the formation of new synapses in the dorsal DD neurite (Thompson-Peer et al., 2012) as well as the elimination of old presynaptic domains on the ventral side (Miller-Fleming et al., 2016). The activity-dependent effect on DD presynaptic disassembly depends on the cell-autonomous roles of the UNC-8/DEG/ENaC cation channel and the serine-threonine phosphatase TAX-6/Calcineurin which function together to elevate intracellular Ca^{++}

(See Chapter II) (Miller-Fleming et al., 2016). It will be interesting to determine if similar components direct synaptic remodeling in RGCs.

Altered behavior in the barn owl involves the reallocation of the presynaptic apparatus

Anatomical and functional studies of the barn owl auditory localization pathway provide additional examples of activity-dependent remodeling that involves the coincident assembly of synapses in new locations as others are removed. Juvenile owls, fitted with prisms that distort the visual field, learn to associate auditory cues with the imposed new optical location (Knudsen & Knudsen, 1989). This phenomenon is correlated with the expansion of axonal arbors into receptive fields associated with the learned behavior (Debello, Feldman, & Knudsen, 2001). Clustering of presynaptic boutons in these new adaptive zones is also enhanced in comparison to the normal receptive field but the overall number of synapses in each region is not significantly different. Thus, this mechanism appears to have effectively reduced the separation between adjacent presynaptic domains by balancing nascent assembly with synaptic elimination in nearby regions (Debello et al., 2001; Mcbride et al., 2008). Notably, synaptic remodeling in the *C. elegans* GABAergic circuit also involves the elimination of established synapses paired with assembly of presynaptic boutons in new locations (Figure 1.4). Interestingly, prism-trained owls retain the capacity to associate auditory cues with the normal visual field after the prisms are removed. This finding suggests that the adaptive synaptic clusters, which are maintained in trained animals, are functionally silenced with the restoration of normal visual cues (Mcbride & Debello, 2015). We speculate that this example of synaptic silencing in the barn owl auditory circuit could be potentially accomplished as in the *C. elegans* GABAergic neurons by the selective disassembly of key components such as ELKS or Munc13 that are required for neurotransmitter release but are not needed for the maintenance of synaptic structure (Chapter IV) (Miller-Fleming et al.,

2020). In the case of the barn owl, this surgically precise mechanism could facilitate an adaptive response to temporal cues while also maintaining the long-term capacity to restore normal visual input (Mcbride & Debello, 2015).

Open questions regarding the UNC-8-dependent upregulation of Ca^{++} in remodeling boutons

In Chapter II, we determined that Ca^{++} is maintained in remodeling boutons due to the presynaptic activity of ENaC/UNC-8 and CaN/TAX-6. However, ENaC/UNC-8 is a conserved Na^{+} channel that does not gate Ca^{++} ions (Ying Wang et al., 2013). In remodeling DD boutons, the VGCC/UNC-2 is predicted to gate Ca^{++} to increase synaptic Ca^{++} levels. We have proposed that VGCC/UNC-2 activity is stimulated by the depolarization of presynaptic membrane by UNC-8-dependent Na+ influx (Figure 2.1). Thus, a key prediction of this model is that mutations in the VGCC/UNC-2 should prevent Ca^{++} transients in remodeling boutons. Now that we have established a paradigm to monitor Ca^{++} transients in remodeling boutons, we can test this idea by repeating the experiment in *unc-2* mutants. It would also be interesting to determine the localization of UNC-2 during DD remodeling. The key role of UNC-2 in elevating presynaptic Ca^{++}, suggests that the UNC-2 channel is maintained in DD neurons until the final stages of Ca^{++}-dependent elimination of ventral DD boutons. CRISPR/Cas9 technology could be used for endogenous labeling of UNC-2 in DD neurons. To this end, a recent knock-in strategy has labeled UNC-2 in *C. elegans* without apparent alteration of UNC-2 function (Oh, Krout, Richmond, & Kim, 2021). The addition of a flippase dependent cassette in that knock-in strategy should allow the generation of a cell-specific labeling of endogenous UNC-2 in intact animals (Schwartz & Jorgensen, 2016).

Identification of a Ca^{++}-dependent step during DD remodeling also predicts that direct stimulation of DD neurons or activation of presynaptic DA and DB neurons (Figure 1.4) should

accelerate DD remodeling. Consistent with this idea, optogenetic activation of GABAergic neurons accelerates the elimination of ventral synapses as well as the assembly of new dorsal synapses in DD neurons (Miller-Fleming, 2016; Miller-Fleming et al., 2016). However, chronic activation of presynaptic DA neurons failed to promote DD remodeling (Figure 6.1). This result is surprising because we have previously shown that activation of presynaptic cholinergic motor neurons is sufficient to induce Ca^{++} transients in postsynaptic GABAergic motor neurons (See Chapter V) (Cuentas-Condori et al., 2019). Thus, the fact that this indirect strategy did not accelerate DD remodeling could mean that presynaptic neurons in this circuit may release additional signals that oppose DD synaptic remodeling. This observation is intriguing because previous studies in the developing visual circuit, the auditory system and the somatosensory cortex (Pan & Monje, 2020) have shown that spontaneous synaptic activity increases in the neuron subject to remodeling but may not require neighboring presynaptic signaling or sensory activity. Additionally, the existance of developmentally defined critical periods for synaptic remodeling across species suggests that neuronal refinement is governed by intrinsic genetic programs.

Another interesting follow-up study is to investigate the cytosolic vs presynaptic enrichment of CaN/ TAX-6 in GABAergic motor neurons. CaN has been proposed to function as a free, cytosolic phosphatase (Emma L. Clayton & Cousin, 2009; Klee et al., 1979). Recent findings in yeast and mammalian cardiomyocytes, however, suggest that CaN might be locally anchored through F-BAR protein-containing scaffolds (Li et al., 2020; Martín-García et al., 2018; Snider et al., 2020). Intriguingly, recent studies have also revealed that neuronal Dynamin is distributed over cytosolic vs synaptic pools. Perisynaptic localization of Dynamin depends on the F-BAR protein Syndapin, which is proposed to prime clusters of Dynamin for ultrafast endocytosis (Imoto et al., 2021). Intriguingly, my studies have determined that CaN and the F-BAR protein TOCA-1 are co-

localized at adult GABAergic presynaptic boutons. Intriguingly, the presynaptic level of endogenous CaN is altered in *toca-1* mutants (Figure 6.2) with higher ventral TAX-6::GFP

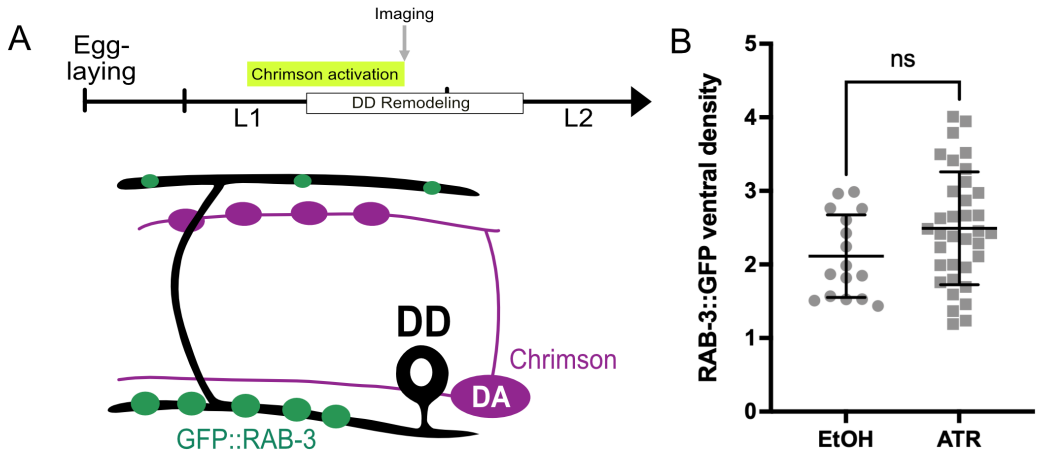

Figure 6. 1. Activation of presynaptic DA neurons does not promote DD remodeling.

A. (Top) Synchronized animals were exposed to light to activate Chrimson for 7 hours before and at the beginning of DD remodeling (yellow bar). Animals were then imaged at T_{26}. (Bottom) Endogenous GFP::RAB-3 was used to monitor RAB-3 remodeling and Chrimson was expressed in presynaptic DA neurons.
B. Animals grown with either Control EtOH or ATR have a similar number of GFP::RAB-3 puncta on the ventral side, suggesting that DA stimulation does not accelerate synapse elimination.

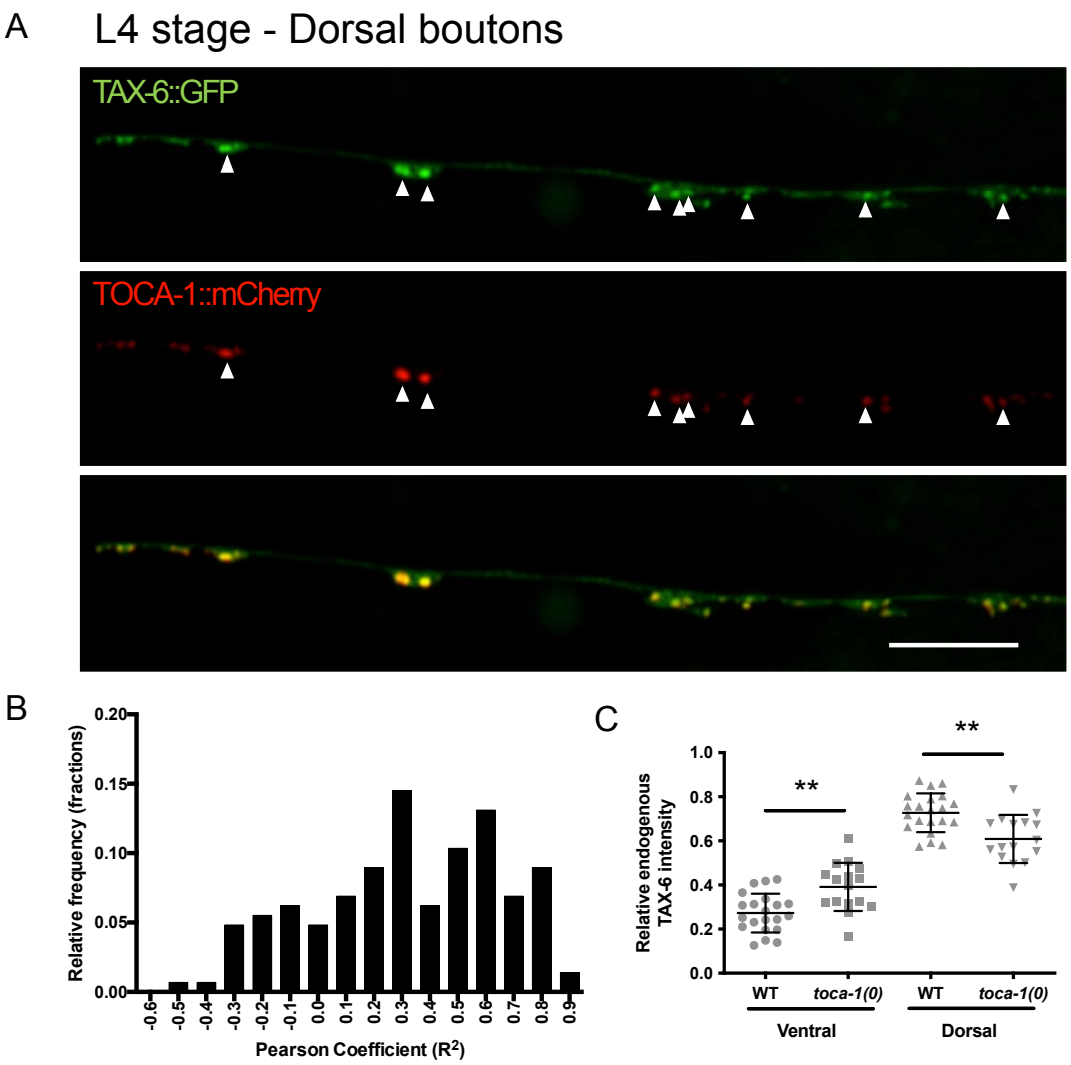

Figure 6. 2. Calcineurin and TOCA-1 transiently associate within GABAergic boutons

A. Ayriscan imaging of TAX-6::GFP (green) and TOCA-1::mCherry (red) labeling the dorsal cord of wild-type animals. Arrowheads show coincidental enrichment of TAX-6 and TOCA-1 in mature dorsal boutons. Scale bar = 10µm.
B. TAX-6 and TOCA-1 co-localization. Distribution of Pearson Coefficients obtained from individual bouton analysis. More than 40% of the boutons have a Person Coefficient higher than 0.5.
C. Endogenous NATF TAX-6::GFP intensity at dorsal and ventral cords of DD neurons in wild type and *toca-1* mutant L4 larvae.

intensity and lower on dorsal side. These preliminary observations point to potential functional interactions between CaN/TAX-6 and TOCA-1 in DD remodeling that should be interesting to investigate given the strong evolutionary conservation of these proteins.

Open question on the actin-dependent endocytic mechanism remodeling the presynaptic membrane of DD synapses

Chapter III describes an actin-dependent endocytic pathway that recycles synaptic material from old to new boutons. We propose that a bulk endocytic pathway similar to ADBE is repurposed during DD development for recycling synaptic vesicles to distal rather than local synapses as in ADBE. However, there are still several open questions regarding this cellular mechanism.

For example, experiments in Chapter III demonstrated that the native synaptic vesicle protein RAB-3 can recycle from old to new boutons. This result could mean that additional presynaptic proteins are also recycled in remodeling DD neurons. For example, it would be particularly intriguing to determine if the active zone components, Piccolo/Bassoon/CLA-1 and VGCC/UNC-2, are recycled from ventral to dorsal DD synapses. This question could be addressed by repeating our photoconversion experiment (Chapter III) with Dendra-labeled endogenous CLA-1 or UNC-2.

Live imaging experiments in Chapter III also determined that actin dynamics is elevated at the onset of DD remodeling along with the appearance of transient RAB-3 particles (Figure 3.10). Consistent with the idea that RAB-3 dynamics increases due to actin polymerization, mutations in *toca-1* or *unc-8* result in decreased actin polymerization as well as fewer transient RAB-3 particles. I propose to challenge the idea that actin polymerization promotes recycling and separation of RAB-3 clusters by asking if increased actin polymerization is sufficient to elevate the number of transient RAB-3 events. Over expression of the VCA domain of the WRC is

sufficient to accelerate the rate of DD remodeling (Figure 3.8). Because the VCA domain can activate the Arp2/3 complex, VCA overexpression should be sufficient to increase branched actin polymerization. We predict that overexpression of VCA will not only increase branched-actin polymerization but will also increase the formation of transient RAB-3 clusters that appear between synapses (Figure 3.10) thus offering a rigorous test of our model of actin-dependent remodeling and elimination of RAB-3 clusters.

Although the photoconversion experiments described in Chapter III firmly established that RAB-3 is recycled from old to new synapses in remodeling DD neurons, the roles of known remodeling proteins in this mechanism need additional clarification. For example, levels of GFP::RAB-3 at mature dorsal DD synapses in *unc-8* and *toca-1* mutants are indistinguishable from the wild type (Figure 3.12). However, levels of recycled (i.e., photoconverted) Dendra2::GFP at mature dorsal DD synapses are substantially reduced in *unc-8* and *toca-1* mutants in comparison to wild type (Figure 3.17). This finding could mean that nascent RAB-3, derived from de novo translation during remodeling, may be incorporated into dorsal DD synapses and that this contribution could compensate for deficient levels of recycled RAB-3 in *unc-8* and *toca-1* mutants. We also note that removal of ventral RAB-3 is strongly impaired in *rab-11(csRNAi)*-treated DD neurons but not in either *unc-8* or *toca-1* mutants. This disparity could result from the partially redundant roles of UNC-8 and TOCA-1 in remodeling (Figure 3.12) and could be potentially resolved by the finding of impaired removal of photoconverted Dendra2::RAB-3 in *unc-8; toca-1* double mutants.

It has been shown that the SNARE protein, VAMP4, is enriched on bulk endosomes at mammalian synapses (Nicholson-Fish et al., 2015). Thus, VAMP4 can serve as a genetically-encoded marker for monitoring bulk endosomes in vivo. Unfortunately, VAMP4 is not conserved in *C. elegans* (Zeng et al., 2003). However, the original screen that identified remodeling genes in the Miller Lab (Petersen et al., 2011), reported that the SNARE protein Synaptobrevin/SNB-2

is necessary for removal of presynaptic terminals (Figure 6A), highlighting the possibility that it may be enriched in remodeling endosomes. Therefore, I confirmed the the previously published result by showing that global RNAi knockdown of *snb-2* impairs the removal of the presynaptic SNARE protein, SNB-1::GFP from ventral synapses in remodeling GABAergic neurons. For this experiment, I exploited the ectopic synaptic remodeling phenotype of *unc-55* mutants. In *unc-55* mutants, both DD and VD neurons remodel resulting in the relocation of all GABAergic boutons to the dorsal nerve cord (H. Zhou & Walthall, 1998). Thus, RNAi knockdown of a necessary remodeling gene results in the appearance of SNB-1::GFP puncta at residual ventral GABAergic synapses. Accordingly, RNAi knockdown on *snb-2* retards elimination of ventral GABAergic synapses in *unc-55* mutants (Figure 6.3A) (Petersen et al., 2011). To determine if SNB-2 is also required for the native synaptic remodeling program in DD neurons, I used cell specific RNAi to target SNB-2 specifically in DD neurons (Figure 6.3B). This experiment demonstrated that *snb-2(csRNAi)*-treated DD neurons retain more ventral Synaptobrevin/SNB-1::GFP than control cells (Figure 6.3C), thus, confirming that SNB-2 functions in remodeling neurons to promote presynaptic disassembly. Consistent with a possible role as a molecular marker for synaptic endosomes, GFP-tagged SNB-2 localizes in a punctated-fashion along the dorsal cord of adult animals (Figure 6.3D). However, overexpression of GFP::SNB-2 seems to localize to both dorsal and ventral cords throughout development (data not shown). To understand the cellular role of SNB-2 during DD remodeling, I propose to use genome engineering to GFP-tag the endogenous SNB-2 protein and thus circumvent potential over expression artifacts. It is important to note that the *snb-2* transcript is detected at low levels in the CeNGEN atlas of gene expression in the C. elegans nervous system at the L4 larval stage (S. R. Taylor et al., 2020). Thus, to ensure visualization of native SNB-2, I propose using the NATF strategy to enhance the fluorescent signal of the labeled endogenous SNB-2 protein (He et al., 2019).

Highlighting the possibility that specific molecular codes localize to the membrane of remodeling endosomes, Micah Foster, a high school student from the Vanderbilt School for Science and Math discovered that the Synaptotagmin4/SNT-4 protein is required for the removal of Synaptobrevin/SNB-1::GFP from ventral synapses in remodeling DD neurons (Figure 6.3E).

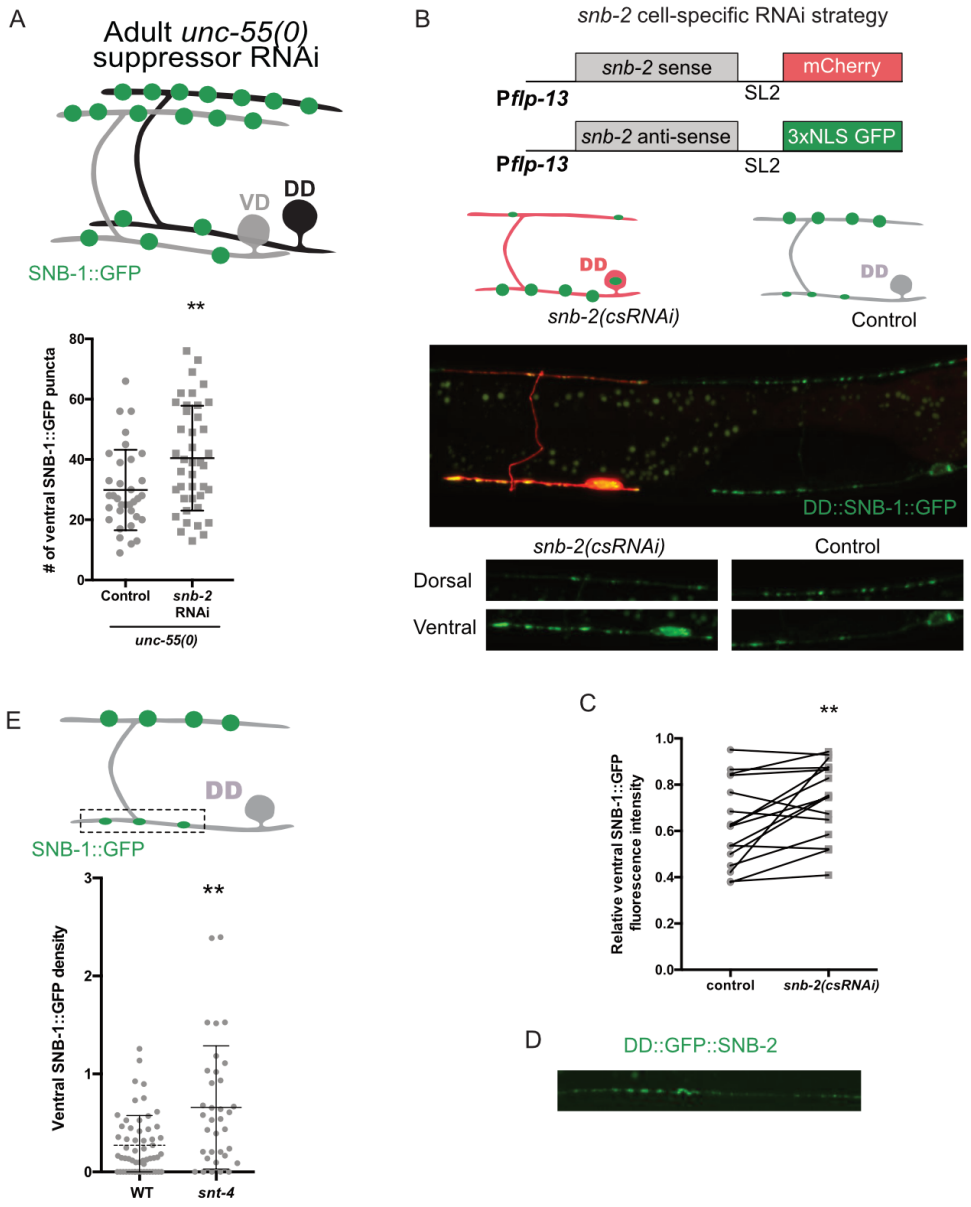

Figure 6. 3. SNB-2 and SNT-4 are potential molecular markers of remodeling endosomes

A. (Top) Suppressors of the Unc-55 phenotype retain GABAergic motor neuron synapses on the ventral side of *unc-55* mutants. (Bottom) Quantification of the number of residual ventral SNB-1::GFP in Control and *snb-2* RNAi knockdown of L4 larvae.

B. (Top) Cell-specific RNAi strategy to knockdown *snb-2* in DD neurons. *snb-2(csRNAi)* treated DD neurons are co-labeled with cytosolic mCherry and nuclear GFP vs neighboring unlabeled control DD neurons. (Bottom) SNB-1::GFP puncta is retained on the ventral side of *snb-2(csRNAi)* cells but not controls.
C. Quantification of Control and *snb-2(csRNAi)*-treated DD neurons.
D. Dorsal cord of adult animals shows punctate expression of SNB-2::GFP
E. *snt-4* mutants maintain ventral SNB-1::GFP in contrast to wild type at the L4 larval stage.

Because synaptotagmin4 is postsynaptic in Drosophila neurons (K. P. Harris, Zhang, Piccioli, Perrimon, & Troy Littleton, 2016), it will be important to use a cell-specific RNAi approach to determine if SNT-4 functions in remodeling DD neurons or in postsynaptic muscle. Additionally, genetic epistasis analysis could determine if SNT-4 functions in a common pathway with UNC-8/SDPN-1 or TOCA-1 as an important step in dissecting its specific role in DD remodeling.

Open questions on the parallel mechanisms that disassemble specific subsets of presynaptic components during remodeling.

In Chapter IV, we reported that at least two key regulators of neurotransmitter release, UNC-13/Munc13 and ELKS, are disassembled by a separate pathway regulated by the homeodomain transcription factor, IRX-1/Iroquois, but are not removed by UNC-8 activity (Figure 4.11) (Fleming-Miller et al., 2021). Additionally, in Chapter II we observed the differential effects of the parallel pathways regulated by UNC-8/SDPN-1 or TOCA-1 on the active zone protein Bassoon/Piccolo/CLA-1. Our results indicate that UNC-8/SDPN-1 has a more active role in eliminating synaptic vesicle proteins, whereas the TOCA-1 pathway seemed to play a dominant role in the elimination of the active zone protein Piccolo/Bassoon/CLA-1. The existence of distinct disassembly pathways is indicative of specific molecular interactions that selectively eliminate presynaptic components. This observation is quite notable since synapse elimination is not a gross mass destruction of the synaptic terminal, but a rather organized process that may be conserved across evolution during circuit refinement or in response to injury.

One first important follow-up question would be to determine if TOCA-1, which regulates the elimination of the active zone protein CLA-1, is also required to disassemble UNC-13 or ELKS-1, both members of the active zone and eliminated by an IRX-1/Iroquois-dependent pathway. Because toca-1 is broadly expressed across *C. elegans* neurons (S. R. Taylor et al., 2020) (See also CeNGENapp), it seems likely that an additional transcriptionally-regulated gene is may be

required to activate TOCA-1 for active zone elimination. RNA-Seq profiling experiments to identify additional IRX-1/Iroquois targets (Spencer et al., 2014; S. R. Taylor et al., 2020) could be useful for delineating the mechanism of these effects. This approach could also be useful for delineating the mechanism of postsynaptic remodeling, which is also regulated by IRX-1/Iroquois (He et al., 2015) but has not been extensively investigated.

With participation from Siqi Chen (Undergraduate student) John Tipps (Research Assistant) and Seth Taylor (Assistant Research Professor), I implemented a strategy to identify additional transcriptionally-regulated remodeling genes in DD neurons. In this approach, we labeled the nuclei of GABAergic neurons with TagRFP (P*ttr-39*::nuclearTagRFP) to mark DD and VD neurons for FACS sorting, and labeled the endogenous presynaptic protein RAB-3 with GFP (GFP::RAB-3) to track the native program of DD remodeling (Figure 6.4A). The usual strategy for synchronizing *C. elegans* is to arrest newly hatched embryos at the L1 stage by restricting food availability (Spencer et al., 2014). Because DD remodeling occurs during this period and could thus be disrupted by environmental stress, we developed an alternative method for synchronizing larvae that did not depend on starving L1 larvae. For our method, we collected newly hatched L1 larvae that crawled through the pores of a nylon mesh over a fixed period of time to obtain a synchronized population (Figure 6.5A-B). In initial experiments, we correlated the appearance of DD and VD neurons in the ventral cord with the progression of DD synaptic remodeling. Six DD neurons develop embryonically and 13 VD neurons originate during the L1 to L2 stage transition which corresponds to the period of DD remodeling (Sulston, 1976). By counting the number of TagRFP nuclei in synchronized populations of L1 larvae, we determined that VD nuclei first appear at 26 hours after collection (T_{26}) with 13 VD neurons emerging by T_{30} hours (Figure 6.4C). Next, we tracked DD synaptic remodeling from T_{21}-T_{28} by following the position of the GFP::RAB-3 signal in ventral and dorsal DD neurites (Figure 6.4B-C). These experiments determined that 80% of DD neurons had initiated remodeling by T_{21} and that later, at T_{28}, 70% of the DD neurons

are either largely or fully remodeled (Figure 6.4D). By relying on this detailed description of the stages of DD remodeling we then designed a strategy to use FACS to isolate TagRFP-positive cells (i.e., DD and/or VD neurons) from three different stages of DD remodeling: Before (T_{13}-T_{18}), during (T_{20}-T_{25}) and after DD remodeling (T_{33}-T_{38}) (Figure 6.5C-D). FACS-isolated tagRFP-labeled neurons from these three stages of DD remodeling were then submitted for single cell RNA-Sequencing (scRNA-seq) using the 10X Genomics Chromium system available in VANTAGE. scRNA reads were processed by Seth Taylor, PhD, (S. R. Taylor et al., 2020) to produce the UMAP plots depicted in Figure 6.5E. Notably, cells isolated from each of the three developmental windows separate into partially overlapping clusters. For interpreting this result, it is important to note that DD neurons should be represented at in all three timepoints whereas VD neurons are limited to the final timepoint (T_{33}-T_{38}). It follows that genes with known roles in DD remodeling should be expressed at predictable times and within specific cells in the UMAP. For example, we expect to detect pro-remodeling genes in cells collected during the remodeling (T_{22}) period (green). Consistently, two known pro-remodeling genes, *irx-1* and *unc-8* (See Chapter IV) (Fleming-Miller et al., 2021; Miller-Fleming et al., 2016; Petersen et al., 2011), are enriched in cells obtained at T_{22} (Figure 6.6A-B). Conversely, *unc-55*, a gene that is known to antagonize remodeling in VD neurons (Zhou & Walthall, 1998), is selectively expressed in the cell population obtained after the remodeling period (T_{35}) which should be enriched for VD neurons (Figure 6.6C). Interestingly, other cells that cluster with VD neurons but do not express unc-55, are likely to correspond to DD neurons after remodeling. Another anti-remodeling gene, the Ig-domain protein OIG-1, is known to be expressed in DD neurons in newly hatched larvae where it is downregulated as remodeling ensues and also, later, in VD neurons which normally do not remodel. Remarkably, this pattern of expression is reflected in the UMAP in which *oig-1* transcripts are enriched in cells isolated before remodeling (T_{15}), relatively depleted in cells isolated during remodeling (T_{22}) and robustly expressed in cells collected after remodeling (T_{35}) which, as noted above, includes VD

neurons (Figure 6.6A and C). Thus, this dataset contains transcripts that are specifically upregulated during the beginning of DD remodeling and might be key to identifying parallel

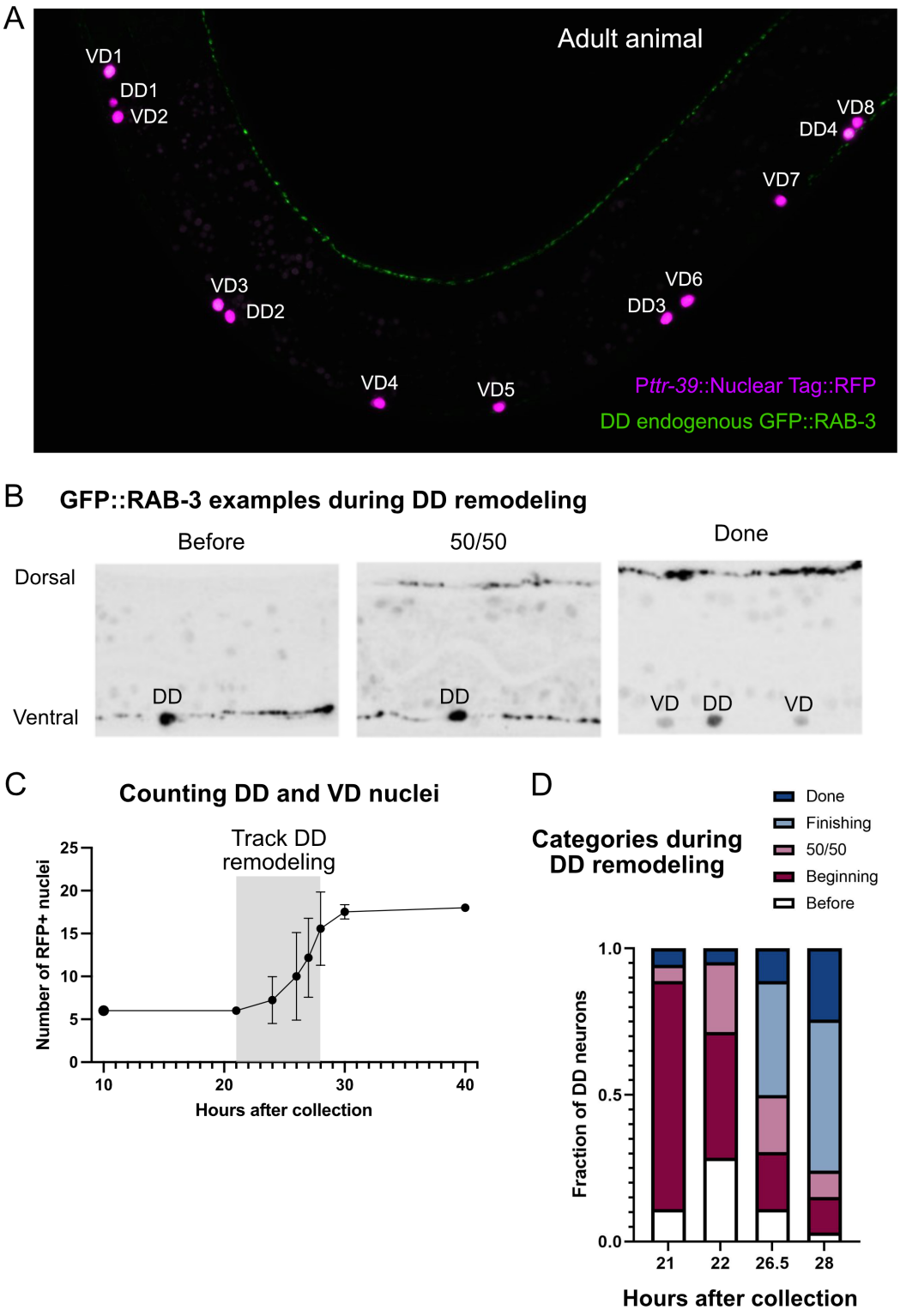

Figure 6. 4. Tracking the progression of DD remodeling

A. Fluorescent image of animal used to sort DD neurons. Here, DD and VD nuclei are labeled with TagRFP (magenta) and endogenous GFP::RAB-3 (green) localizes to dorsal DD neurites of adult animals.
B. Examples of DD remodeling stages: Before, ongoing (50/50) and when it is Done.
C. Quantification of the number of TagRFP-positive cells observed at different time-points. The endogenous GFP::RAB-3 marker was used to evaluate the progress of DD remodeling (Gray Bar).
D. Distribution of selected stages of DD remodeling assessed in individual neurons.

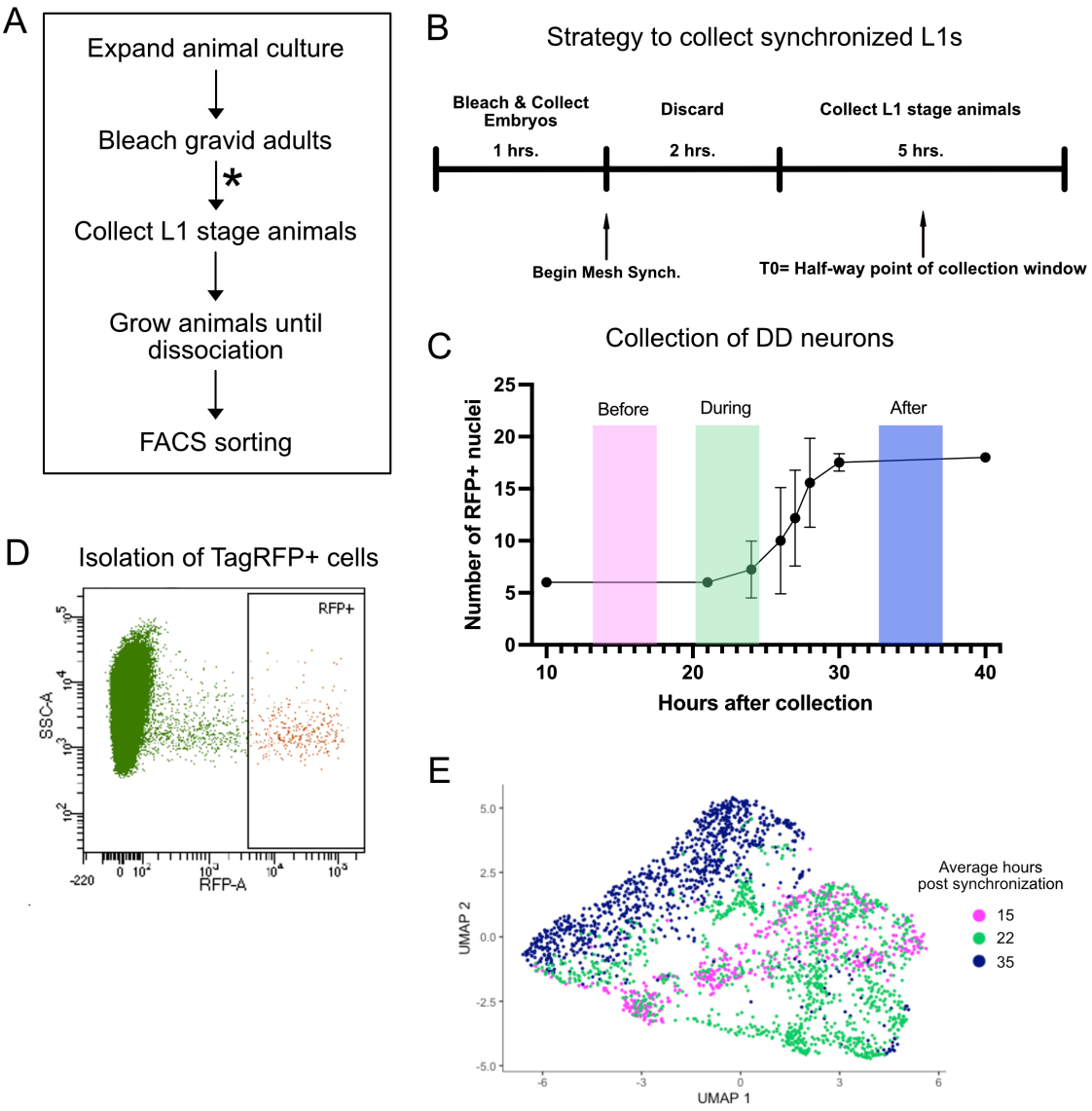

Figure 6. 5. Strategy to isolate remodeling DD neurons at different developmental windows

A-B. Series of steps leading to the isolation of GABAergic neurons from larvae. The asterisk refers to panel B which outlines the strategy for collecting synchronized populations of L1 larvae from embryos derived by treating gravid adults with an alkaline bleach solution.
C. Counts of tagRFP-positive motor neuron nuclei (DD and VD) in the ventral cord during larval development. Vertical bars label developmental periods in which larval animals were collected for isolating tagRFP+ neurons for FACS.
D. Representative scatter plot of RFP-positive cells (RFP-A) vs size (SSCA). Window to the right denotes gate for collecting bright RFP+ cells.

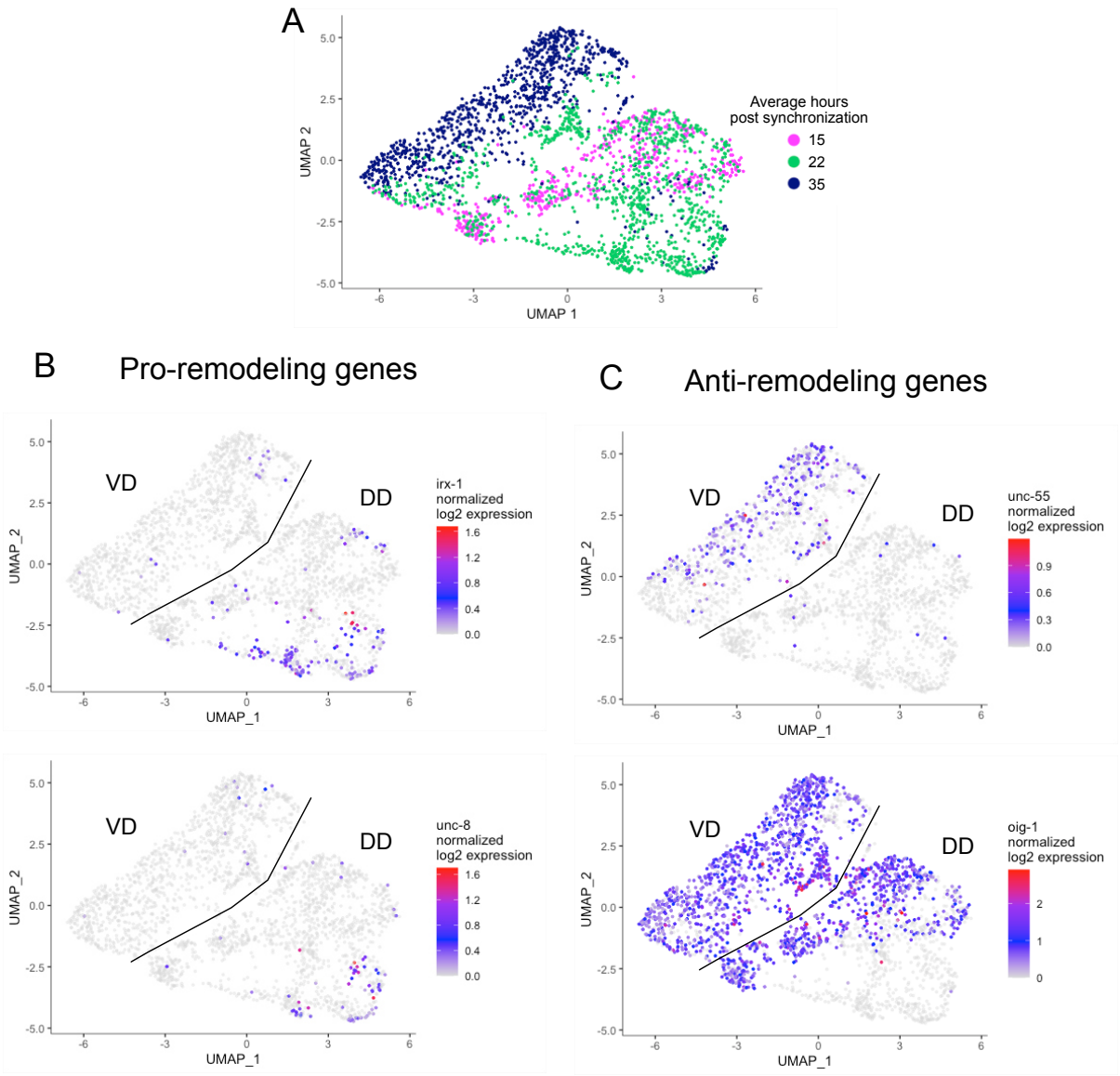

Figure 6. 6. Expression of pro and anti-remodeling genes in remodeling neurons

A. UMAP plots of DD and VD scRNA profiles from the three different developmental windows. T_{13}-T_{18} (T_{15}, pink), T_{20}-T_{25} (T_{22}, green) and T_{33}-T_{38} (T_{35}, blue).
B. UMAP showing expression of pro-remodeling genes *irx-1* and *unc-8*.
C. UMAP showing expression of anti-remodeling genes *unc-55* and *oig-1*.
Heat-map denotes relative expression of each gene.

pathways downstream of IRX-1 for ELKS-1 or UNC-13 remodeling as well a potential transcriptionally-regulated activator for TOCA-1. In addition, this data set could highlight genes with specific roles in remodeling the postsynaptic apparatus in DD neurons (He et al., 2015).

Open questions regarding DD dendritic spines

Chapter V describes a detailed characterization of dendritic spines in the *C. elegans* motor circuit. Although these dendritic protrusions were initially noted by John White in 1976 and also by others in more recent reports (Philbrook et al., 2018; White et al., 1976, 1986), our work provides a rigorous demonstration that key characteristics of mammalian dendritic spines are also observed in C. elegans GABAergic neurons (Byrd & Jin, 2021; Cuentas-Condori et al., 2019). This characterization of DD spines establishes a new model for investigating the development and function of dendritic spines that exploit the power of *C. elegans* genetics and ease of live cell imaging. For example, a recent study used live-imaging and genetic analysis of developing DD spines to demonstrate that the transsynaptic organizer, Neurexin/NRX-1, functions at presynaptic cholinergic terminals to maintain postsynaptic acetylcholine receptor clustering and DD dendritic spine morphology (Oliver et al., 2021). Importantly, the temporal resolution of this approach established that Neurexin promotes synapse stabilization and maturation rather than initiating synaptogenesis, thus resolving a long-standing debate about the in vivo role of neurexin in developing circuits.

An additional intriguing question remains unanswered: What is the postsynaptic trans-synaptic partner of Neurexin in DD spines? A previous study reported that the well-characterized trans-synaptic protein Neuroligin/NLG-1 is dispensable for the Neurexin-dependent formation of DD dendritic spines (Philbrook et al., 2018). This result demonstrates that an alternative trans-synaptic protein expressed in DD GABAergic neurons could interact with Neurexin to stabilize dendritic spines. To this end, I explored the literature and discovered that Neurexin can also

interact with transmembrane proteins containing Leucine Rich Repeats (LRR) (T. C. Südhof, 2017). Scanning the expression patterns of known LRR proteins in the *C. elegans* genome, I determined that *iglr-1* is highly expressed in GABAergic neurons at the L2 stage (Figure 6.7A). This finding was notable because establishment of DD spines takes place specifically in L2 larvae (Oliver et al., 2021). To ask if IGLR-1 is required for DD spine formation, I used feeding RNAi to knock down *iglr-1* and LifeAct::GFP to monitor DD spines. Imaging of DD spines in adult animals demonstrated a mild but significant depletion of spine density with *iglr-1* knock down (Figure 6.7B), suggesting that IGRL-1 normally promotes either spine formation or maintenance. Because feeding RNAi can result in varying levels of reduction of *iglr-1* levels across animals, it can lead to variable phenotypes possibly explaining the wide dispersion of observed effects of *iglr-1* RNAi on spine density (Figure 6.7B). To obviate this problem, I used CRISPR/Cas9 to target the third exon of *iglr-1* (Figure 6.7C), and generated two deletion alleles that result in premature stop codons (Figure 6.7D). These new alleles could now be used to determine if IGLR-1 stabilizes DD dendritic spines and if it does so by working with NRX-1. Overall, this experiment will help identify the trans-synaptic interactions that maintain dendritic spines and follow-up live-imaging studies could reveal the temporal nature of these interaction in an intact nervous system and the possible interplay between adhesion molecules and synaptic activity.

Another intriguing question: What is the role of UNC-8 after DD remodeling? UNC-8 remains in the ventral dendrites of remodeled DD neurons (Figure 6.8A). Live-imaging reveals that UNC-8::GFP puncta are anchored as well as mobile at postsynaptic regions (Figure 6.8B). The mobile UNC-8 vesicles are particularly intriguing as their motion does not seem to be directed or processive, but rather bounces back and forth. This observation suggests that postsynaptic ENaC/UNC-8 trafficking might be independent of molecular motors. In contrast, UNC-8 localization depends on the Kinesin3/UNC-104 in presynaptic DD neurites before remodeling (Figure 2.3). Consistent with the idea that UNC-8 vesicles might traffic independently of UNC-104

in postsynaptic dendrites, live-imaging of adult *unc-104* mutant animals reveals mobile UNC-8 particles (Figure 6.8C). Live-imaging has also shown that UNC-8 particles can enter dendritic spines (data not shown), thus suggesting that UNC-8 could function in spines. Interestingly, the ASIC subfamily of ENaC channels are proposed to function at postsynaptic terminals potentially in LTP for learning and memory (Hill & Ben-Shahar, 2018; Wemmie et al., 2002). Thus, our observations support a model in which ENaC/UNC-8 promotes presynaptic Ca^{++} levels of remodeling boutons (See Chapter II) but later could also function actively at postsynaptic dendrites. These versatile roles for the ENaC/UNC-8 subunit offers a unique developmental paradigm to understand the context-specific roles of synaptic ENaC channels and their adaptable trafficking strategies across development and neurites.

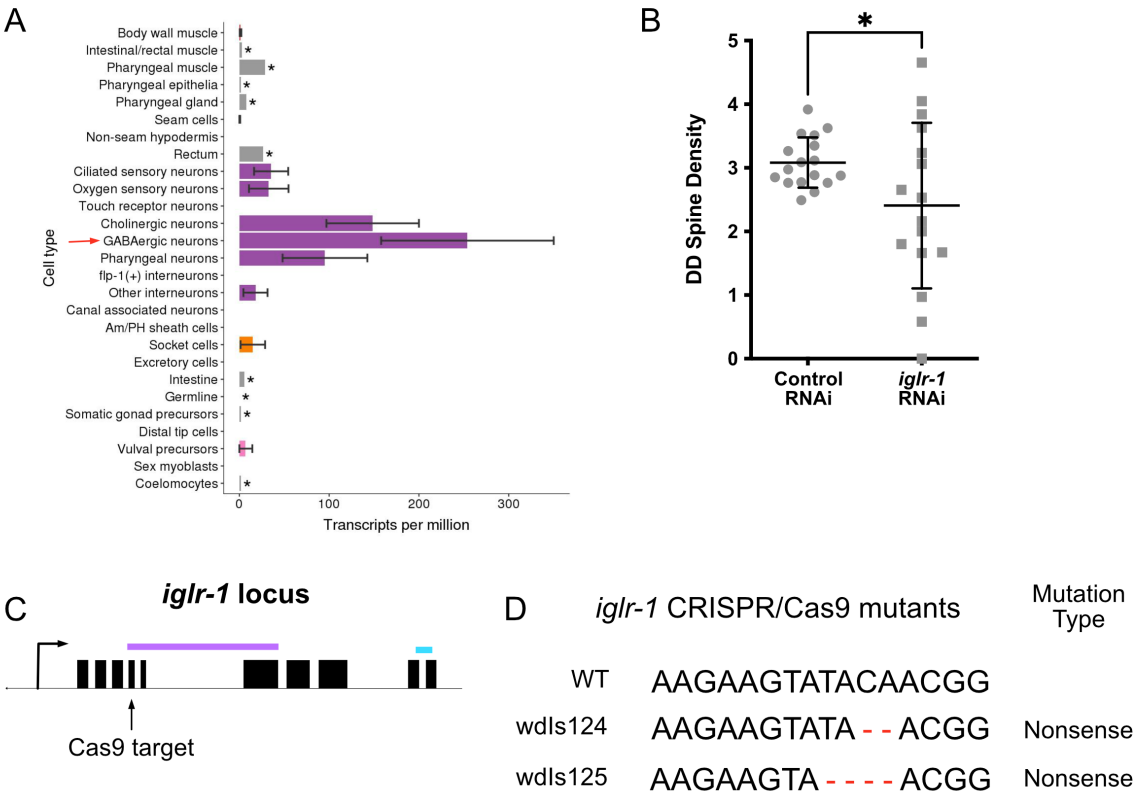

Figure 6. 7. The LRR protein IGLR-1 may function in DD neurons to maintain dendritic spines

A. Expression of *iglr-1* across different tissues. Red arrow point to expression in GABAergic neurons like DD and VDs. Data extracted from GExplorer: http://genome.sfu.ca/gexplore/
B. DD spine density is reduced with *iglr-1* RNAi in comparison to control RNAi-treated animals.
C. *iglr-1* locus highlighting exons (black boxes) and introns. Arrow denotes location of Cas9 target sequence. Purple bar denotes location of LRR domains and blue point to transmembrane domain.
D. Novel CRISPR/Cas9 mutant alleles for the *iglr-1* gene are small deletions that shift the reading frame and result in premature nonsense (stop) codons.

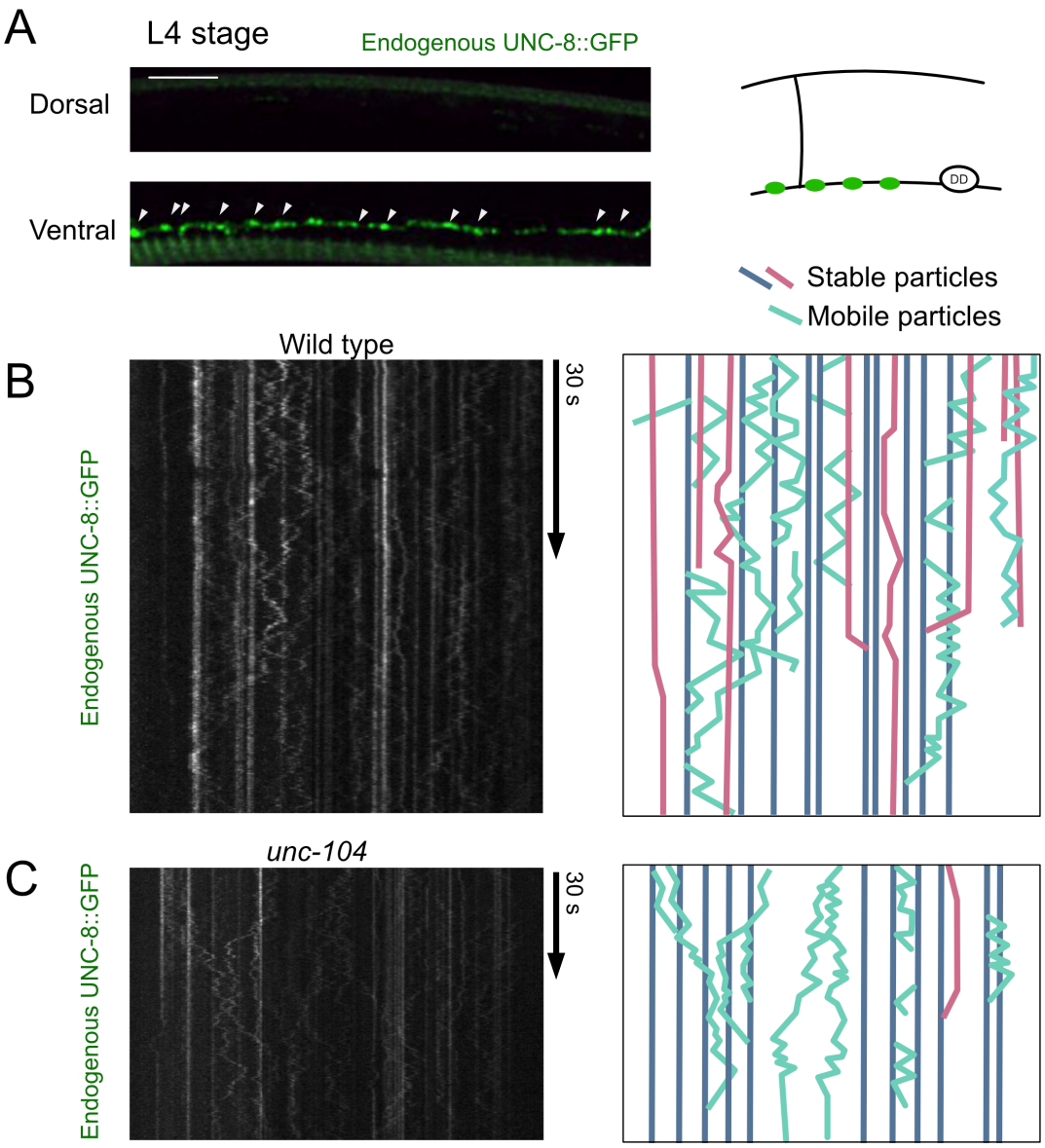

Figure 6. 8. UNC-8 is retained in ventral postsynaptic DD dendrites after remodeling.

A. Endogenous labeling of UNC-8 with NATF (See Figure 2.2) reveals UNC-8::GFP puncta on the ventral dendrite of DD neurons at the L4 stage.
B-C. Time-lapse imaging at 5fps (frames per second) detects both stable (blue and pink and mobile (green) UNC-8::GFP particles in DD dendrites of **(B)** wild-type and **(C)** *unc-104* mutant L4 larvae.

REFERENCES

Ackermann, F., Waites, C. L., & Garner, C. C. (2015). Presynaptic active zones in invertebrates and vertebrates. *EMBO Reports*, *16*(8), 1–16. https://doi.org/10.15252/embr.201540434

Ackley, B. D. (2005). The Two Isoforms of the Caenorhabditis elegans Leukocyte-Common Antigen Related Receptor Tyrosine Phosphatase PTP-3 Function Independently in Axon Guidance and Synapse Formation. *Journal of Neuroscience*, *25*(33), 7517–7528. https://doi.org/10.1523/JNEUROSCI.2010-05.2005

Acsady, L., Kamondi, A., Sık, A., Freund, T., & Buzsaki, G. (1998). GABAergic Cells Are the Major Postsynaptic Targets of Mossy Fibers in the Rat Hippocampus. *The Journal of Neuroscience*, *18*(9), 3386–3403.

Alvarez, V. A., & Sabatini, B. L. (2007). Anatomical and Physiological Plasticity of Dendritic Spines. *Annual Review of Neuroscience*, *30*(1), 79–97. https://doi.org/10.1146/annurev.neuro.30.051606.094222

Anggono, V., Smillie, K. J., Graham, M. E., Valova, V. A., Cousin, M. A., & Robinson, P. J. (2006). Syndapin I is the phosphorylation-regulated dynamin I partner in synaptic vesicle endocytosis. *Nature Neuroscience*, *9*(6), 752–760. https://doi.org/10.1038/nn1695

Angstadt, J. D., Donmoyer, J. E., & Stretton, A. O. W. (1989). Retrovesicular ganglion of the nematode Ascaris. *Journal of Comparative Neurology*, *284*(3), 374–388. https://doi.org/10.1002/cne.902840305

Augustin, I., Rosenmund, C., Su, T. C., & Brose, N. (1999). Munc13-1 is essential for fusion competence of glutamatergic synaptic vesicles. *Letters to Nature*, *263*, 457–461.

Baas, P. W., & Lin, S. (2010). Hooks and Comets : The Story of Microtubule Polarity Orientation in the Neuron. *Developmental Neurobiology*. https://doi.org/10.1002/dneu.20818

Bai, Z., & Grant, B. D. (2015). A TOCA/CDC-42/PAR/WAVE functional module required for

retrograde endocytic recycling. *Proceedings of the National Academy of Sciences of the United States of America*, *112*(12), E1443-52. https://doi.org/10.1073/pnas.1418651112

Berry, K. P., & Nedivi, E. (2016). Experience-Dependent Structural Plasticity in the Visual System. *Annual Review of Vision Science*, *2*, 17–35. https://doi.org/10.1146/annurev-vision-111815-114638

Bloom, O., Evergren, E., Tomilin, N., Kjaerulff, O., Löw, P., Brodin, L., … Shupliakov, O. (2003). Colocalization of synapsin and actin during synaptic vesicle recycling. *Journal of Cell Biology*, *161*(4), 737–747. https://doi.org/10.1083/jcb.200212140

Böhme, M. A., Beis, C., Reddy-Alla, S., Reynolds, E., Mampell, M. M., Grasskamp, A. T., … Sigrist, S. J. (2016). Active zone scaffolds differentially accumulate Unc13 isoforms to tune Ca2+ channel-vesicle coupling. *Nature Neuroscience*, *19*(10), 1311–1320. https://doi.org/10.1038/nn.4364

Böhme, M. A., Mccarthy, A. W., Grasskamp, A. T., Beuschel, C. B., Goel, P., Jusyte, M., … Walter, A. M. (2019). Rapid active zone remodeling consolidates presynaptic potentiation. *Nature Communications*, 1–16. https://doi.org/10.1038/s41467-019-08977-6

Bourne, J. N., & Harris, K. M. (2008). Balancing Structure and Function at Hippocampal Dendritic Spines. *Annual Review of Neuroscience*, *31*(1), 47–67. https://doi.org/10.1146/annurev.neuro.31.060407.125646

Brenner, S. (1973). The genetics of behaviour. *British Medical Bulletin*, *29*(3), 269–271.

Brenner, S. (1974). The genetics of Caenorhabditis elegans. *Genetics*, *77*, 71–94.

Brose, N., Hofmann, K., Hata, Y., & Sudhof, T. C. (1995). Mammalian homologues of Caenorhabditis elegans unc-13 gene define novel family of C2-domain proteins. *Journal of Biological Chemistry*, *270*(42), 25273–25280. https://doi.org/10.1074/jbc.270.42.25273

Bu, W., Chou, A. M., Lim, K. B., Sudhaharan, T., & Ahmed, S. (2009). The Toca-1-N-WASP complex links filopodial formation to endocytosis. *Journal of Biological Chemistry*, *284*(17),

11622–11636. https://doi.org/10.1074/jbc.M805940200

Bujalka, H., Koenning, M., Jackson, S., Perreau, V. M., Pope, B., Hay, C. M., … Emery, B. (2013). MYRF Is a Membrane-Associated Transcription Factor That Autoproteolytically Cleaves to Directly Activate Myelin Genes. *PLoS Biology*, *11*(8). https://doi.org/10.1371/journal.pbio.1001625

Bushey, D., Tononi, G., & Cirelli, C. (2011). Sleep and Synaptic Homeostasis: Strucutral evidence in Drosophila. *Science*, *332*(June), 1576–1582.

Byrd, D. T., & Jin, Y. (2021). Wired for insight—recent advances in Caenorhabditis elegans neural circuits. *Current Opinion in Neurobiology*, *69*, 159–169. https://doi.org/10.1016/j.conb.2021.02.009

Cardona, A., Saalfeld, S., Schindelin, J., Arganda-Carreras, I., Preibisch, S., Longair, M., … Douglas, R. J. (2012). TrakEM2 software for neural circuit reconstruction. *PLoS ONE*, *7*(6). https://doi.org/10.1371/journal.pone.0038011

Carrillo, J., Cheng, S., Ko, K. W., Jones, T. A., & Nishiyama, H. (2013). The Long-term Structural Plasticity of Cerebellar Parallel Fiber Axons and Its Modulation by Motor Learning, *33*(19), 8301–8307. https://doi.org/10.1523/JNEUROSCI.3792-12.2013

Cavodeassi, F., Modolell, J., & Gómez-skarmeta, J. L. (2001). The Iroquois family of genes: from body building to neural patterning. *Development*, *128*, 2847–2855.

Chanaday, N. L., Cousin, M. A., Milosevic, I., Watanabe, S., & Morgan, J. R. (2019). The synaptic vesicle cycle revisited: New insights into the modes and mechanisms. *Journal of Neuroscience*, *39*(42), 8209–8216. https://doi.org/10.1523/JNEUROSCI.1158-19.2019

Chen, Z., Borek, D., Padrick, S. B., Gomez, T. S., Metlagel, Z., Ismail, A. M., … Rosen, M. K. (2010a). Structure and control of the actin regulatory WAVE complex. *Nature*, *468*. https://doi.org/10.1038/nature09623

Chen, Z., Borek, D., Padrick, S. B., Gomez, T. S., Metlagel, Z., Ismail, A. M., … Rosen, M. K.

(2010b). Structure and control of the actin regulatory WAVE complex. *Nature*, *468*(7323), 533–538. https://doi.org/10.1038/nature09623

Chenouard, N., Xuan, F., & Tsien, R. W. (2020). Synaptic vesicle traffic is supported by transient actin filaments and regulated by PKA and NO. *Nature Communications*, *11*(1). https://doi.org/10.1038/s41467-020-19120-1

Cherra, S. J., & Jin, Y. (2016). A Two-Immunoglobulin-Domain Transmembrane Protein Mediates an Epidermal-Neuronal Interaction to Maintain Synapse Density. *Neuron*, *89*(2), 325–336. https://doi.org/10.1016/j.neuron.2015.12.024

Cheung, G., Jupp, O. J., & Cousin, M. A. (2010). Activity-dependent bulk endocytosis and clathrin-dependent endocytosis replenish specific synaptic vesicle pools in central nerve terminals. *Journal of Neuroscience*, *30*(24), 8151–8161. https://doi.org/10.1523/JNEUROSCI.0293-10.2010

Cho, J. H., & Askwith, C. C. (2008). Presynaptic release probability is increased in hippocampal neurons from ASIC1 knockout mice. *Journal of Neurophysiology*, *99*(2), 426–441. https://doi.org/10.1152/jn.00940.2007

Cinar, H., Keles, S., & Jin, Y. (2005). Expression Profiling of GABAergic Motor Neurons in Caenorhabditis elegans. *Current Biology*, *15*, 340–346. https://doi.org/10.1016/j

Cingolani, L. a, & Goda, Y. (2008). Actin in action: the interplay between the actin cytoskeleton and synaptic efficacy. *Nature Reviews Neuroscience*, *9*(5), 344–356. https://doi.org/10.1038/nrn2373

Clark, S. G., Shurland, D. L., Meyerowitz, E. M., Bargmann, C. I., & Van Der Bliek, A. M. (1997). A dynamin GTPase mutation causes a rapid and reversible temperature-inducible locomotion defect in C. elegans. *Proceedings of the National Academy of Sciences of the United States of America*, *94*(19), 10438–10443. https://doi.org/10.1073/pnas.94.19.10438

Clayton, E. L., Anggono, V., Smillie, K. J., Chau, N., Robinson, P. J., & Cousin, M. A. (2009).

The Phospho-Dependent Dynamin-Syndapin Interaction Triggers Activity-Dependent Bulk Endocytosis of Synaptic Vesicles. *Journal of Neuroscience*, *29*(24), 7706–7717. https://doi.org/10.1523/JNEUROSCI.1976-09.2009

Clayton, Emma L., & Cousin, M. A. (2009). The molecular physiology of activity-dependent bulk endocytosis of synaptic vesicles. *Journal of Neurochemistry*, *111*(4), 901–914. https://doi.org/10.1111/j.1471-4159.2009.06384.x

Clayton, Emma L, Evans, G. J. O., & Cousin, M. a. (2007). Activity-dependent control of bulk endocytosis by protein dephosphorylation in central nerve terminals. *The Journal of Physiology*, *585*(Pt 3), 687–691. https://doi.org/10.1113/jphysiol.2007.137539

Cousin, M. A., Robinson, P. J., & Robinson, P. J. (2001). The dephosphins : dephosphorylation by calcineurin triggers synaptic vesicle endocytosis, *24*(11), 659–665.

Cuentas-Condori, A., & Miller, D. M. (2020). Synaptic remodeling, lessons from C . elegans. *Journal of Neurogenetics*, *34*(3–4), 307–322. https://doi.org/10.1080/01677063.2020.1802725

Cuentas-Condori, A., Mulcahy, B., He, S., Palumbos, S., Zhen, M., & Miller, D. M. (2019). C. elegans neurons have functional dendritic spines. *ELife*, *8*, 1–23. https://doi.org/10.7554/elife.47918

Cullen, P. J., & Steinberg, F. (2018). To degrade or not to degrade: mechanisms and significance of endocytic recycling. *Nature Reviews Molecular Cell Biology*, *19*(11), 679–696. https://doi.org/10.1038/s41580-018-0053-7

Darcy, K. J., Staras, K., Collinson, L. M., & Goda, Y. (2006). Constitutive sharing of recycling synaptic vesicles between presynaptic boutons. *Nature Neuroscience*, *9*(3), 315–321. https://doi.org/10.1038/nn1640

De Paola, V., Holtmaat, A., Knott, G., Song, S., Wilbrecht, L., Caroni, P., & Svoboda, K. (2006). Cell Type-Specific Structural Plasticity of Axonal Branches and Boutons in the Adult

Neocortex. *Neuron*, *49*, 861–875. https://doi.org/10.1016/j.neuron.2006.02.017

Debello, W. M., Feldman, D. E., & Knudsen, E. I. (2001). Adaptive Axonal Remodeling in the Midbrain Auditory Space Map. *The Journal of Neuroscience*, *21*(9), 3161–3174.

Deken, S. L. (2005). Redundant Localization Mechanisms of RIM and ELKS in Caenorhabditis elegans. *Journal of Neuroscience*, *25*(25), 5975–5983. https://doi.org/10.1523/JNEUROSCI.0804-05.2005

Dillon, C., & Goda, Y. (2005). The actin cytoskeleton: integrating form and function at the synapse. *Annual Review of Neuroscience*, *28*, 25–55. https://doi.org/10.1146/annurev.neuro.28.061604.135757

Dotti, C., & Banker, G. (1987). Experimentally induced alteration in the polarity of developin neurons. *Nature*, *330*.

Doussau, F., & Augustine, G. J. (2000). The actin cytoskeleton and neurotransmitter release: An overview. *Biochimie*, *82*(4), 353–363. https://doi.org/10.1016/S0300-9084(00)00217-0

Duan, B., Liu, D. S., Huang, Y., Zeng, W. Z., Wang, X., Yu, H., … Xu, T. Le. (2012). PI3-kinase/Akt pathway-regulated membrane insertion of acid-sensing ion channel 1a underlies BDNF-induced pain hypersensitivity. *Journal of Neuroscience*, *32*(18), 6351–6363. https://doi.org/10.1523/JNEUROSCI.4479-11.2012

Dube, S., Rácz, B., Brown, W. E., Gao, Y., Soderblom, E. J., Yasuda, R., & Soderling, S. H. (2020). Action potential-coupled Rho GTPase signaling drives presynaptic plasticity. *BioRxiv*, 1–69.

Earls, L. R., Hacker, M. L., Watson, J. D., & Miller, D. M. (2010). Coenzyme Q protects Caenorhabditis elegans GABA neurons from calcium-dependent degeneration. *Proceedings of the National Academy of Sciences of the United States of America*, *107*(32), 14460–14465. https://doi.org/10.1073/pnas.0910630107

Eastman, C., Horvitz, H. R., & Jin, Y. (1999). Coordinated transcriptional regulation of the unc-

25 glutamic acid decarboxylase and the unc-47 GABA vesicular transporter by the Caenorhabditis elegans UNC-30 homeodomain protein. *Journal of Neuroscience*, *19*(15), 6225–6234. https://doi.org/10.1523/jneurosci.19-15-06225.1999

Eden, S., Rohatgi, R., Podtelejnikov, A. V, Mann, M., & Kirschner, M. W. (2002). Mechanism of regulation of WAVE1-induced actin nucleation by Rac1 and Nck. *Nature*, *418*(6899), 790–793. https://doi.org/10.1038/nature00859

Edwards, S. L., Yorks, R. M., Morrison, L. M., Hoover, C. M., & Miller, K. G. (2015). Synapse-assembly proteins maintain synaptic vesicle cluster stability and regulate synaptic vesicle transport in Caenorhabditis elegans. *Genetics*, *201*(1), 91–116. https://doi.org/10.1534/genetics.115.177337

Engert, F., & Bonhoeffer, T. (1999). Dendritic spine changes associated with hippocampal long-term synaptic plasticity. *Nature*, *399*(May). https://doi.org/10.1038/19978

Falet, H., Hoffmeister, K. M., Neujahr, R., Italiano, J. E., Stossel, T. P., Southwick, F. S., & Hartwig, J. H. (2002). Importance of free actin filament barbed ends for Arp2/3 complex function in platelets and fibroblasts. *Proceedings of the National Academy of Sciences of the United States of America*, *99*(26), 16782–16787. https://doi.org/10.1073/pnas.222652499

Ferguson, S. M., & Camilli, P. De. (2012). Dynamin, a membrane-remodelling GTPase. *Nature Publishing Group*, *13*(2), 75–88. https://doi.org/10.1038/nrm3266

Fiala, J., Feinberg, M., Popov, V., & Harris, K. M. (1998). Synaptogenesis via dendritic filopodia in developing hippocampal area CA1. *The Journal of Neuroscience*, *18*(21), 8900–8911. https://doi.org/1998/10/24 00:01

Fill, M., & Copello, J. A. (2002). Ryanodine Receptor Calcium Release Channels. *Physiological Reviews*, *82*(4), 893–922. https://doi.org/10.1152/physrev.00013.2002

Fleming-Miller, T., Cuentas-Condori, A., Manning, L., Palumbos, S., Richmond, J., & Miller III,

D. M. (2021). Transcriptional control of parallel-acting pathways that remove discrete presynaptic proteins in remodeling neurons. *Journal of Neuroscience*, *10*. https://doi.org/10.1101/2020.02.21.959700

Fricke, R., Gohl, C., & Bogdan, S. (2010). The F-BAR protein family Actin' on the membrane. *Communicative & Integrative Biology*, *3*(2), 89–94. https://doi.org/10.4161/cib.3.2.10521

Fricke, R., Gohl, C., Dharmalingam, E., Grevelhörster, A., Zahedi, B., Harden, N., … Bogdan, S. (2009). Drosophila Cip4/Toca-1 Integrates Membrane Trafficking and Actin Dynamics through WASP and SCAR/WAVE. *Current Biology*, *19*(17), 1429–1437. https://doi.org/10.1016/j.cub.2009.07.058

Gallop, J. L., Walrant, A., Cantley, L. C., & Kirschner, M. W. (2013). Phosphoinositides and membrane curvature switch the mode of actin polymerization via selective recruitment of toca-1 and Snx9. *Proceedings of the National Academy of Sciences of the United States of America*, *110*(18), 7193–7198. https://doi.org/10.1073/pnas.1305286110

Gally, C., Eimer, S., Ung, H., Richmond, J., & Bessereau, J. (2004). A Transmembrane Protein Required for Acetylcholine Receptor Clustering in C. elegans. *Nature*, *431*(September). https://doi.org/10.1038/nature02907.1.

Gan, Q., & Watanabe, S. (2018). Synaptic vesicle endocytosis in different model systems. *Frontiers in Cellular Neuroscience*, *12*(June), 1–27. https://doi.org/10.3389/fncel.2018.00171

Gardner, M. K., Zanic, M., & Howard, J. (2013). Microtubule catastrophe and rescue. *Current Opinion in Cell Biology*, *25*(1), 1–9. https://doi.org/10.1016/j.ceb.2012.09.006

Ghosh-Roy, A., Goncharov, A., Jin, Y., & Chisholm, A. D. (2012). Kinesin-13 and Tubulin Posttranslational Modifications Regulate Microtubule Growth in Axon Regeneration. *Developmental Cell*, *23*(4), 716–728. https://doi.org/10.1016/j.devcel.2012.08.010

Ghosh-Roy, A., Wu, Z., Goncharov, A., Jin, Y., & Chisholm, A. D. (2010). Calcium and cyclic

AMP promote axonal regeneration in Caenorhabditis elegans and require DLK-1 kinase. *Journal of Neuroscience*, *30*(9), 3175–3183. https://doi.org/10.1523/JNEUROSCI.5464-09.2010

Girao, H., Geli, M. I., & Idrissi, F. Z. (2008). Actin in the endocytic pathway: From yeast to mammals. *FEBS Letters*, *582*(14), 2112–2119. https://doi.org/10.1016/j.febslet.2008.04.011

Giuliani, C., Troglio, F., Bai, Z., Patel, F. B., Zucconi, A., Malabarba, M. G., … Scita, G. (2009). Requirements for F-BAR proteins TOCA-1 and TOCA-2 in actin dynamics and membrane trafficking during Caenorhabditis elegans oocyte growth and embryonic epidermal morphogenesis. *PLoS Genetics*, *5*(10). https://doi.org/10.1371/journal.pgen.1000675

Gleason, A. M., Nguyen, K. C. Q., Hall, D. H., & Grant, B. D. (2016). Syndapin/SDPN-1 is required for endocytic recycling and endosomal actin association in the Caenorhabditis elegans intestine. *Molecular Biology of the Cell*, *27*(23), 3746–3756. https://doi.org/10.1091/mbc.E16-02-0116

Goda, Y., & Davis, G. W. (2003). Mechanisms of synapse assembly and disassembly. *Neuron*, *40*(2), 243–264. https://doi.org/10.1016/S0896-6273(03)00608-1

Gormal, R. S., Nguyen, T. H., Martin, X. S., Papadopulos, A., & Meunier, F. A. (2015). An Acto-Myosin II Constricting Ring Initiates the Fission of Activity-Dependent Bulk Endosomes in Neurosecretory Cells, *35*(4), 1380–1389. https://doi.org/10.1523/JNEUROSCI.3228-14.2015

Gottlieb, T. a, Ivanov, I. E., Adesnik, M., & Sabatini, D. D. (1993). Actin filaments play a critical role in endocytosis at the apical but not the basolateral surface of polarized epithelial cells. *J. Cell Biol.*, *120*(3), 695–710. https://doi.org/10.1083/jcb.120.3.695

Gracheva, E. O., Hadwiger, G., Nonet, M. L., & Richmond, J. E. (2008). Direct interactions between C. elegans RAB-3 and Rim provide a mechanism to target vesicles to the

presynaptic density. *Neuroscience Letters*, *444*(2), 137–142. https://doi.org/10.1016/j.neulet.2008.08.026

Gramlich, M. W., & Klyachko, V. A. (2017). Actin/Myosin-V- and Activity-Dependent Inter-synaptic Vesicle Exchange in Central Neurons. *Cell Reports*, *18*(9), 2096–2104. https://doi.org/10.1016/j.celrep.2017.02.010

Gratz, S. J., Goel, P., Bruckner, J. J., Hernandez, R. X., Khateeb, K., Macleod, G. T., … O'Connor-Giles, K. M. (2019). Endogenous tagging reveals differential regulation of Ca2+ channels at single active zones during presynaptic homeostatic potentiation and depression. *Journal of Neuroscience*, *39*(13), 2416–2429. https://doi.org/10.1523/JNEUROSCI.3068-18.2019

Grillo, F. W., Song, S., Ruivo, L. M. T., Huang, L., Gao, G., & Knott, G. W. (2013). Increased axonal bouton dynamics in the aging mouse cortex. https://doi.org/10.1073/pnas.1218731110/-/DCSupplemental.www.pnas.org/cgi/doi/10.1073/pnas.1218731110

Gu, M., Liu, Q., Watanabe, S., Sun, L., Hollopeter, G., Grant, B. D., & Jorgensen, E. M. (2013). AP2 hemicomplexes contribute independently to synaptic vesicle endocytosis. *ELife*, *2013*(2), 1–21. https://doi.org/10.7554/eLife.00190

Gu, M., Schuske, K., Watanabe, S., Liu, Q., Baum, P., Garriga, G., & Jorgensen, E. M. (2008). µ2 adaptin facilitates but is not essential for synaptic vesicle recycling in Caenorhabditis elegans. *Journal of Cell Biology*, *183*(5), 881–892. https://doi.org/10.1083/jcb.200806088

Guiney, E. L., Goldman, A. R., Elias, J. E., & Cyert, M. S. (2015). Calcineurin regulates the yeast synaptojanin Inp53/Sjl3 during membrane stress. *Molecular Biology of the Cell*, *26*(4), 769–785. https://doi.org/10.1091/mbc.E14-05-1019

Gulyás, A. I., Miettinen, R., Jacobowitz, D. M., & Freund, T. F. (1992). Calretinin is present in non-pyramidal cells of the rat hippocampus-I. A new type of neuron specifically associated

with the mossy fibre system. *Neuroscience*, *48*(1), 1–27. https://doi.org/10.1016/0306-4522(92)90334-X

Hall, D. H., & Hedgecock, E. M. (1991). Kinesin-related gene unc-104 is required for axonal transport of synaptic vesicles in C. elegans. *Cell*, *65*(5), 837–847. https://doi.org/10.1016/0092-8674(91)90391-B

Hallam, S. J., & Jin, Y. (1998). lin-14 regulates the timing of synaptic remodelling in Caenorhabditis elegans. *Nature*, *395*(6697), 78–82. https://doi.org/10.1038/25757

Halls, M. L., & Cooper, D. M. F. (2011). Regulation by Ca2+-Signaling Pathways of Adenylyl Cyclases. *Cold Spring Harbor Perspectives in Biology*, *3*.

Hamm, L. L., Feng, Z., & Hering-Smith, K. S. (2010). Regulation of sodium transport by ENaC in the kidney. *Current Opinion in Nephrology and Hypertension*, *19*(1), 98–105. https://doi.org/10.1097/MNH.0b013e328332bda4

Hammarlund, M., Hobert, O., Miller, D. M., & Sestan, N. (2018). The CeNGEN Project: The Complete Gene Expression Map of an Entire Nervous System. *Neuron*, *99*(3), 430–433. https://doi.org/10.1016/j.neuron.2018.07.042

Han, B., Bellemer, A., & Koelle, M. R. (2015). An Evolutionarily Conserved Switch in Response to GABA Affects Development and Behavior of the Locomotor Circuit of Caenorhabditis elegans. *Genetics*, *199*, 1159–1172. https://doi.org/10.1534/genetics.114.173963

Hardy, P. A. (1990). Genetic aspects of nervous system development. *Journal of Neurogenetics*, *6*(3), 115–131. https://doi.org/10.3109/01677069009107105

Harris, K. P., Zhang, Y. V., Piccioli, Z. D., Perrimon, N., & Troy Littleton, J. (2016). The postsynaptic t-SNARE syntaxin 4 controls traffic of neuroligin 1 and synaptotagmin 4 to regulate retrograde signaling. *ELife*, *5*(MAY2016), 1–26. https://doi.org/10.7554/eLife.13881

Harris, K M, & Stevens, J. K. (1989). Dendritic spines of CA 1 pyramidal cells in the rat

hippocampus: serial electron microscopy with reference to their biophysical characteristics. *The Journal of Neuroscience : The Official Journal of the Society for Neuroscience*, *9*(8), 2982–2997. https://doi.org/10.1021/la0512603

Harris, Kristen M., Jensen, F., & Tsao, B. (1992). Three-dimensional structure of dendritic spines and synapses in rat hippocampus (CA1) at postnatal day 15 and adult ages: Implications for the maturation of synaptic physiology and long-term potentiation. *The Journal of Neuroscience*, *12*(July), 2685–2705. https://doi.org/10.1523/JNEUROSCI.12-07-02685.1992

Havrylenko, S., Noguera, P., Abou-ghali, M., Manzi, J., & Pollard, T. D. (2015). WAVE binds Ena / VASP for enhanced Arp2 / 3 complex – based actin assembly, *26*. https://doi.org/10.1091/mbc.E14-07-1200

He, S., Cuentas-Condori, A., & Miller, D. M. (2019). NATF (Native and Tissue-Specific Fluorescence): A strategy for brigth, tissue-specific GFP labeling of native proteins in Caenorhabditis elegans. *Genetics*, *212*(June), 387–395.

He, S., Philbrook, A., McWhirter, R., Gabel, C. V., Taub, D. G., Carter, M. H., … Miller, D. M. (2015). Transcriptional control of synaptic remodeling through regulated expression of an immunoglobulin superfamily protein. *Current Biology*, *25*(19), 2541–2548. https://doi.org/10.1016/j.cub.2015.08.022

Held, R. G., Liu, C., & Kaeser, P. S. (2016). ELKS controls the pool of readily releasable vesicles at excitatory synapses through its N-terminal coiled-coil domains, 1–20. https://doi.org/10.7554/eLife.14862

Hensch, T. K. (2004). Critical Period Regulation. *Annual Review of Neuroscience*, *27*(1), 549–579. https://doi.org/10.1146/annurev.neuro.27.070203.144327

Hering, H., Sheng, M., & Medical, H. H. (2001). Dendritic Spines : Structure, dynamics and regulaion. *Nature Reviews Neuroscience*, *2*(December), 880–888.

Herzog, E., Nadrigny, F., Silm, K., Biesemann, C., Helling, I., Bersot, T., … Brose, N. (2011). In vivo imaging of intersynaptic vesicle exchange using VGLUT1 Venus knock-in mice. *Journal of Neuroscience*, *31*(43), 15544–15559. https://doi.org/10.1523/JNEUROSCI.2073-11.2011

Heuser, J. E., & Reese, T. S. (1973). Evidence for recycling of synaptic vesicle membrane during transmitter release at the frog neuromuscular junction. *Journal of Cell Biology*, *57*(2), 315–344. https://doi.org/10.1083/jcb.57.2.315

Higashi, T., Tanaka, S., Iida, T., & Okabe, S. (2018). Synapse Elimination Triggered by BMP4 Exocytosis and Presynaptic BMP Receptor Activation. *Cell Reports*, *22*(4), 919–929. https://doi.org/10.1016/j.celrep.2017.12.101

Higgs, H. N., & Pollard, T. D. (2000). Activation by Cdc42 and PIP 2 of Wiskott-Aldrich syndrome protein (WASp) stimulates actin nucleation by Arp2 / 3 complex WASp alone is inactive in the presence or absence of. *The Journal of Cell Biology*, *150*(6), 1311–1320. https://doi.org/10.1083/jcb.150.6.1311

Hill, A. S., & Ben-Shahar, Y. (2018). The synaptic action of degenerin/epithelial sodium channels. *Channels*, *12*(1), 262–275. https://doi.org/10.1080/19336950.2018.1495006

Ho, H. Y. H., Rohatgi, R., Lebensohn, A. M., Le Ma, Li, J., Gygi, S. P., & Kirschner, M. W. (2004). Toca-1 mediates Cdc42-dependent actin nucleation by activating the N-WASP-WIP complex. *Cell*, *118*(2), 203–216. https://doi.org/10.1016/j.cell.2004.06.027

Hogenaar, J. T. T., & van Bokhoven, H. (2021). Schizophrenia: Complement cleaning or killing. *Genes*, *12*(2), 1–15. https://doi.org/10.3390/genes12020259

Holtmaat, A., & Svoboda, K. (2009). Experience-dependent structural synaptic plasticity in the mammalian brain, (August). https://doi.org/10.1038/nrn2699

Hong, Y. K., & Chen, C. (2011). Wiring and rewiring of the retinogeniculate synapse. *Current Opinion in Neurobiology*, *21*(2), 228–237. https://doi.org/10.1016/j.conb.2011.02.007

Hong, Y. K., Park, S. H., Litvina, E. Y., Morales, J., Sanes, J. R., & Chen, C. (2014). Refinement of the Retinogeniculate Synapse by Bouton Clustering. *Neuron*, *84*(2), 332–339. https://doi.org/10.1016/j.neuron.2014.08.059

Honkura, N., Matsuzaki, M., Noguchi, J., Ellis-Davies, G. C. R., & Kasai, H. (2008). The Subspine Organization of Actin Fibers Regulates the Structure and Plasticity of Dendritic Spines. *Neuron*, *57*(5), 719–729. https://doi.org/10.1016/j.neuron.2008.01.013

Houweling, A. C., Dildrop, R., Peters, T., Mummenhoff, J., Christoffels, V. M., Moorman, A. F. M., & Ru, U. (2001). Gene and cluster-specific expression of the Iroquois family members during mouse development. *Mechanisms of Development*, *107*, 169–174.

Howell, K., White, J. G., & Hobert, O. (2015). Spatiotemporal control of a novel synaptic organizer molecule. *Nature*, *523*(7558), 83–87. https://doi.org/10.1038/nature14545

Hristova, M., Birse, D., Hong, Y., & Ambros, V. (2005). The Caenorhabditis elegans Heterochronic Regulator LIN-14 Is a Novel Transcription Factor That Controls the Developmental Timing of Transcription from the Insulin/Insulin-Like Growth Factor Gene ins-33 by Direct DNA Binding. *Molecular and Cellular Biology*, *25*(24), 11059–11072. https://doi.org/10.1128/mcb.25.24.11059-11072.2005

Hruska, M., Henderson, N., Le Marchand, S. J., Jafri, H., & Dalva, M. B. (2018). Synaptic nanomodules underlie the organization and plasticity of spine synapses. *Nature Neuroscience*, *21*(5), 671–682. https://doi.org/10.1038/s41593-018-0138-9

Hu, Z., Tong, X. J., & Kaplan, J. M. (2013). UNC-13L, UNC-13S, and Tomosyn form a protein code for fast and slow neurotransmitter release in Caenorhabditis elegans. *ELife*, *2013*(2), 1–20. https://doi.org/10.7554/eLife.00967

Huang, X., Cheng, H. J., Tessier-Lavigne, M., & Jin, Y. (2002). MAX-1, a novel PH/MyTH4/FERM domain cytoplasmic protein implicated in netrin-mediated axon repulsion. *Neuron*, *34*(4), 563–576. https://doi.org/10.1016/S0896-6273(02)00672-4

Huttenlocher, P. R. (1979). Synaptic density in human frontal cortex - Developmental changes and effects of aging. *Brain Research*, *163*(2), 195–205. Retrieved from http://linkinghub.elsevier.com/retrieve/pii/0006899379903494

Ievglevskyi, O., Isaev, D., Netsyk, O., Romanov, A., Fedoriuk, M., Maximyuk, O., … Krishtal, O. (2016). Acid-sensing ion channels regulate spontaneous inhibitory activity in the hippocampus: Possible implications for epilepsy. *Philosophical Transactions of the Royal Society B: Biological Sciences*, *371*(1700). https://doi.org/10.1098/rstb.2015.0431

Imoto, Y., Raychaudhuri, S., Fenske, P., Sandoval, E., Itoh, K., Blumrich, M., … Cousin, M. A. (2021). Dynamin is primed at endocytic sites for ultrafast endocytosis. *BioRxiv*.

Ismail, A. M., Padrick, S. B., Chen, B., Umetani, J., & Rosen, M. K. (2009). The WAVE regulatory complex is inhibited. *Nature Structural & Molecular Biology*, *16*(5), 561–563. https://doi.org/10.1038/nsmb.1587

Jakobs, M. A., Dimitracopoulos, A., & Franze, K. (2019). Kymobutler, a deep learning software for automated kymograph analysis. *ELife*, *8*, 1–19. https://doi.org/10.7554/eLife.42288

Kaeser, P. S., Deng, L., Wang, Y., Dulubova, I., Liu, X., Rizo, J., & Südhof, T. C. (2011). RIM proteins tether Ca2+ channels to presynaptic active zones via a direct PDZ-domain interaction. *Cell*, *144*(2), 282–295. https://doi.org/10.1016/j.cell.2010.12.029

Kaeser, P. S., & Regehr, W. G. (2017). The readily releasable pool of synaptic vesicles. *Current Opinion in Neurobiology*, *43*, 63–70. https://doi.org/10.1016/j.conb.2016.12.012

Kakimoto, T., Katoh, H., & Negishi, M. (2006). Regulation of neuronal morphology by Toca-1, an F-BAR/EFC protein that induces plasma membrane invagination. *Journal of Biological Chemistry*, *281*(39), 29042–29053. https://doi.org/10.1074/jbc.M604025200

Kanjhan, R., Fogarty, M. J., Noakes, P. G., & Bellingham, M. C. (2016). *Developmental changes in the morphology of mouse hypoglossal motor neurons*. *Brain Structure and Function* (Vol. 221). Springer Berlin Heidelberg. https://doi.org/10.1007/s00429-015-1130-8

Kanjhan, R., Noakes, P. G., & Bellingham, M. C. (2016). Emerging roles of filopodia and dendritic spines in motoneuron plasticity during development and disease. *Neural Plasticity*, *2016*. https://doi.org/10.1155/2016/3423267

Kano, M., & Watanabe, T. (2019). Developmental synapse remodeling in the cerebellum and visual thalamus. *F1000Research*, *8*, 1–14. https://doi.org/10.12688/f1000research.18903.1

Kawabe, H., Mitkovski, M., Kaeser, P. S., Hirrlinger, J., Opazo, F., Nestvogel, D., … Brose, N. (2017). ELKS1 localizes the synaptic vesicle priming protein bMunc13-2 to a specific subset of active zones. *Journal of Cell Biology*, *216*(4), 1143–1162.

Kessels, M. M., & Qualmann, B. (2002). Syndapins integrate N-WASP in receptor-mediated endocytosis. *EMBO Journal*, *21*(22), 6083–6094. https://doi.org/10.1093/emboj/cdf604

Kessels, M. M., & Qualmann, B. (2004). The syndapin protein family : linking membrane trafficking with the cytoskeleton. https://doi.org/10.1242/jcs.01290

Kim, I. H., Racz, B., Wang, H., Burianek, L., Weinberg, R., Yasuda, R., … Soderling, S. H. (2013). Disruption of Arp2/3 results in asymmetric structural plasticity of dendritic spines and progressive synaptic and behavioral abnormalities. *J Neurosci*, *33*(14), 6081–6092. https://doi.org/10.1523/JNEUROSCI.0035-13.2013

Kinosian, H. J., Newman, J., Lincoln, B., Selden, L. A., Gershman, L. C., & Estes, J. E. (1998). Ca2+ regulation of gelsolin activity: Binding and severing of F-actin. *Biophysical Journal*, *75*(6), 3101–3109. https://doi.org/10.1016/S0006-3495(98)77751-3

Kittelmann, M., Hegermann, J., Goncharov, A., Taru, H., Ellisman, M. H., Richmond, J. E., … Eimer, S. (2013). Liprin-α/SYD-2 determines the size of dense projections in presynaptic active zones in C. elegans. *Journal of Cell Biology*, *203*(5), 849–863. https://doi.org/10.1083/jcb.201302022

Kittelmann, M., Liewald, J. F., Hegermann, J., Schultheis, C., & Brauner, M. (2013). In vivo synaptic recovery following optogenetic hyperstimulation. *Proceedings of the National*

Academy of Sciences, E3007–E3016. https://doi.org/10.1073/pnas.1305679110

Klee, C. B., Crouch, T. H., & Krinks, M. H. (1979). Calcineurin: A calcium- and calmodulin-binding protein of the nervous system. *Proceedings of the National Academy of Sciences of the United States of America*, *76*(12), 6270–6273. https://doi.org/10.1073/pnas.76.12.6270

Knott, G. W., Quairiaux, C., Genoud, C., & Welker, E. (2002). Formation of dendritic spines with GABAergic synapses induced by whisker stimulation in adult mice. *Neuron*, *34*(2), 265–273. https://doi.org/10.1016/S0896-6273(02)00663-3

Knudsen, E. I. (2002). Instructed learning in the auditory localization pathway of the barn owl. *Nature*, *417*(6886), 322–328. https://doi.org/10.1038/417322a

Knudsen, E. I., & Knudsen, F. (1989). Vision Calibrates Sound Localization in Developing Barn Owls. *The Journal of Neuroscience*, (September).

Koch, S. M., Dela Cruz, C. G., Hnasko, T. S., Edwards, R. H., Huberman, A. D., & Ullian, E. M. (2011). Pathway-Specific Genetic Attenuation of Glutamate Release Alters Select Features of Competition-Based Visual Circuit Refinement. *Neuron*, *71*(2), 235–242. https://doi.org/10.1016/j.neuron.2011.05.045

Kohn, R. E., Duerr, J. S., McManus, J. R., Duke, A., Rakow, T. L., Maruyama, H., … Rand, J. B. (2000). Expression of multiple UNC-13 proteins in the Caenorhabditis elegans nervous system. *Molecular Biology of the Cell*, *11*(10), 3441–3452. https://doi.org/10.1091/mbc.11.10.3441

Kokotos, A. C., Peltier, J., Davenport, E. C., Trost, M., & Cousin, M. A. (2018). Activity-dependent bulk endocytosis proteome reveals a key presynaptic role for the monomeric GTPase Rab11. *Proceedings of the National Academy of Sciences of the United States of America*, *115*(43), E10177–E10186. https://doi.org/10.1073/pnas.1809189115

Kokotos, Alexandros C., & Low, D. W. (2015). Myosin II and Dynamin Control Actin Rings to

Mediate Fission during Activity-Dependent Bulk Endocytosis. *Journal of Neuroscience*, *35*(23), 8687–8688. https://doi.org/10.1523/JNEUROSCI.1172-15.2015

Körber, C., Horstmann, H., Sätzler, K., & Kuner, T. (2012). Endocytic structures and synaptic vesicle recycling at a central synapse in awake rats. *Traffic*, *13*(12), 1601–1611. https://doi.org/10.1111/tra.12007

Korobchevskaya, K., Lagerholm, B. C., Colin-york, H., & Fritzsche, M. (2017). Exploring the Potential of Airyscan Microscopy for Live Cell Imaging. https://doi.org/10.3390/photonics4030041

Kozorovitskiy, Y., Gross, C. G., Kopil, C., Battaglia, L., McBreen, M., Stranahan, A. M., & Gould, E. (2005). Experience induces structural and biochemical changes in the adult primate brain. *Proceedings of the National Academy of Sciences*, *102*(48), 17478–17482. https://doi.org/10.1073/pnas.0508817102

Krueger, S. R., Kolar, A., & Fitzsimonds, R. M. (2003). The Presynaptic Release Apparatus Is Functional in the Absence of Dendritic Contact and Highly Mobile within Isolated Axons. *Neuron*, *40*(5), 945–957. https://doi.org/10.1016/S0896-6273(03)00729-3

Kubota, Y., Hatada, S., Kondo, S., Karube, F., & Kawaguchi, Y. (2007). Neocortical Inhibitory Terminals Innervate Dendritic Spines Targeted by Thalamocortical Afferents. *Journal of Neuroscience*, *27*(5), 1139–1150. https://doi.org/10.1523/jneurosci.3846-06.2007

Kuromi, H., & Kidokoro, Y. (1998). Two distinct pools of synaptic vesicles in single presynaptic boutons in a temperature-sensitive Drosophila mutant, shibire. *Neuron*, *20*(5), 917–925. https://doi.org/10.1016/S0896-6273(00)80473-0

Kurup, N., & Jin, Y. (2016). Neural circuit rewiring: insights from DD synapse remodeling. *Worm*, *5*(1), e1129486. https://doi.org/10.1080/21624054.2015.1129486

Kurup, N., Li, Y., Goncharov, A., & Jin, Y. (2018). Intermediate filament accumulation can stabilize microtubules inCaenorhabditis elegansmotor neurons. *Proceedings of the*

National Academy of Sciences, *115*(12), 3114–3119.

Kurup, N., Yan, D., Goncharov, A., & Jin, Y. (2015). Dynamic Microtubules Drive Circuit Rewiring in the Absence of Neurite Remodeling. *Current Biology*, *25*(12), 1594–1605. https://doi.org/10.1016/j.cub.2015.04.061

Kushibiki, Y., Suzuki, T., Jin, Y., & Taru, H. (2019). RIMB-1/RIM-Binding Protein and UNC-10/RIM redundantly regulate presynaptic localization of the voltage-gated calcium channel in caenorhabditis elegans. *Journal of Neuroscience*, *39*(44), 8617–8631. https://doi.org/10.1523/JNEUROSCI.0506-19.2019

Lee, K. F. H., Soares, C., Thivierge, J. P., & Béïque, J. C. (2016). Correlated Synaptic Inputs Drive Dendritic Calcium Amplification and Cooperative Plasticity during Clustered Synapse Development. *Neuron*, *89*(4), 784–799. https://doi.org/10.1016/j.neuron.2016.01.012

Lee, S., Kim, K., & Zhou, Z. J. (2010). Role of ACh-GABA Cotransmission in Detecting Image Motion and Motion Direction. *Neuron*, *68*(6), 1159–1172. https://doi.org/10.1016/j.neuron.2010.11.031

Leiss, F., Koper, E., Hein, I., Fouquet, W., Lindner, J., Sigrist, S., & Tavosanis, G. (2008). Characterization of Dendritic Spines in the Drosophila Central Nervous System, *1*. https://doi.org/10.1002/dneu.20699

Li, X., Li, J., Martinez, E. C., Froese, A., Passariello, C. L., Henshaw, K., … Kapiloff, M. S. (2020). Calcineurin Aβ-Specific Anchoring Confers Isoform-Specific Compartmentation and Function in Pathological Cardiac Myocyte Hypertrophy. *Circulation*, 948–962. https://doi.org/10.1161/CIRCULATIONAHA.119.044893

Linkenhoker, B. A., Ohe, C. G. Von Der, & Knudsen, E. I. (2005). Anatomical traces of juvenile learning in the auditory system of adult barn owls, *8*(1), 93–98. https://doi.org/10.1038/nn1367

Lippi, G., Steinert, J. R., Marczylo, E. L., D'Oro, S., Fiore, R., Forsythe, I. D., … Young, K. W.

(2011). Targeting of the Arpc3 actin nucleation factor by miR-29a/b regulates dendritic spine morphology. *Journal of Cell Biology*, *194*(6), 889–904. https://doi.org/10.1083/jcb.201103006

Lisa Timmons, & Andrew Fire. (1998). Specific interference by ingested dsRNA. *Nature*, *395*(October), 854. Retrieved from http://www.dnai.org/media/rnai/resources/rnai_by_feeding.pdf

Liu, P., Chen, B., & Wang, Z. W. (2013). Postsynaptic current bursts instruct action potential firing at a graded synapse. *Nature Communications*, *4*(May), 1911. https://doi.org/10.1038/ncomms2925

Machesky, L. M., Mullins, R. D., Higgs, H. N., Kaiser, D. a, Blanchoin, L., May, R. C., … Pollard, T. D. (1999). Scar, a WASp-related protein, activates nucleation of actin filaments by the Arp2/3 complex. *Proceedings of the National Academy of Sciences of the United States of America*, *96*(7), 3739–3744. https://doi.org/10.1073/pnas.96.7.3739

Marik, S. A., Yamahachi, H., Mcmanus, J. N. J., Szabo, G., & Gilbert, C. D. (2010). Axonal Dynamics of Excitatory and Inhibitory Neurons in Somatosensory Cortex, *8*(6). https://doi.org/10.1371/journal.pbio.1000395

Marik, S. A., Yamahachi, H., Meyer, S., & Gilbert, C. D. (2014). Large-Scale Axonal Reorganization of Inhibitory Neurons following Retinal Lesions, *34*(5), 1625–1632. https://doi.org/10.1523/JNEUROSCI.4345-13.2014

Martín-García, R., Arribas, V., Coll, P. M., Pinar, M., Viana, R. A., Rincón, S. A., … Pérez, P. (2018). Paxillin-Mediated Recruitment of Calcineurin to the Contractile Ring Is Required for the Correct Progression of Cytokinesis in Fission Yeast. *Cell Reports*, *25*(3), 772-783.e4. https://doi.org/10.1016/j.celrep.2018.09.062

Matthewman, C., Miller-Fleming, T. W., Miller, D. M., & Bianchi, L. (2016). The role of Ca2+ permeability and Na+ conductance in cellular toxicity caused by hyperactive DEG/ENaC

channels. *American Journal of Physiology - Cell Physiology*, *311*, 920–930. https://doi.org/10.1152/ajpcell.00247.2016

May-Britt, M., Mari, T., Thore, E., & Per, A. (1998). Spatial training in a complex environment and isolation alter the spine distribution differently in rat CA1 pyramidal cells. *Journal of Comparative Neurology*, *380*(3), 373–381. https://doi.org/10.1002/(SICI)1096-9861(19970414)380:3<373::AID-CNE6>3.0.CO;2-#

Mcbride, T. J., & Debello, W. M. (2015). Input clustering in the normal and learned circuits of adult barn owls. *Neurobiology of Learning and Memory*, *121*, 39–51. https://doi.org/10.1016/j.nlm.2015.01.011

Mcbride, T. J., Rodriguez-Contreras, A., Trinh, A., Bailey, R., & Debello, W. M. (2008). Learning Drives Differential Clustering of Axodendritic Contacts in the Barn Owl Auditory System. *The Journal of Neuroscience*, *28*(27), 6960–6973. https://doi.org/10.1523/JNEUROSCI.1352-08.2008

Mcintire, S. L., Jorgensen, E. M., Kaplan, J. M., & Horvitz, H. R. (1993). The GABAergic Nervous System of C. elegans. *Nature*, *27*(7), 407–414.

Meng, J., Ma, X., Tao, H., Translocation, C. N., Meng, J., Ma, X., … Dong, M. (2017). Myrf ER-Bound Transcription Factors Drive C . elegans Synaptic Plasticity via Cleavage-Dependent Nuclear Translocation. *Developmental Cell*, *41*(2), 180-194.e7. https://doi.org/10.1016/j.devcel.2017.03.022

Meng, L., Mulcahy, B., Cook, S. J., Neubauer, M., Wan, A., Jin, Y., & Yan, D. (2015). The Cell Death Pathway Regulates Synapse Elimination through Cleavage of Gelsolin in Caenorhabditis elegans Neurons. *Cell Reports*, *11*(11), 1737–1748. https://doi.org/10.1016/j.celrep.2015.05.031

Mikhaylova, M., Bär, J., van Bommel, B., Schätzle, P., YuanXiang, P. A., Raman, R., … Kreutz, M. R. (2018). Caldendrin Directly Couples Postsynaptic Calcium Signals to Actin

Remodeling in Dendritic Spines. *Neuron*, *97*(5), 1110-1125.e14. https://doi.org/10.1016/j.neuron.2018.01.046

Miller-Fleming, T. W. (2016). *Molecular Dissection of Synaptic Remodeling in GABAergic Neurons*.

Miller-Fleming, T. W., Cuentas-Condori, A., Palumbos, S., Manning, L., Richmond, J. R., & Miller, D. M. (2020). Transcriptional control of parallel-acting pathways that remove discrete presynaptic proteins in remodeling neurons. *BioRxiv*.

Miller-Fleming, T. W., Petersen, S. C., Manning, L., Matthewman, C., Gornet, M., Beers, A., … Iii, D. M. M. (2016). The DEG / ENaC cation channel protein UNC-8 drives activity-dependent synapse removal in remodeling GABAergic neurons. *ELife*, 1–28. https://doi.org/10.7554/eLife.14599

Miller, T. M., & Heuser, J. E. (1984). Endocytosis of synaptic vesicle membrane at the frog neuromuscular junction. *Journal of Cell Biology*, *98*(2), 685–698. https://doi.org/10.1083/jcb.98.2.685

Misgeld, T., Burgess, R. W., Lewis, R. M., Cunningham, J. M., Lichtman, J. W., & Sanes, J. R. (2002). Roles of neurotransmitter in synapse formation: Development of neuromuscular junctions lacking choline acetyltransferase. *Neuron*, *36*(4), 635–648. https://doi.org/10.1016/S0896-6273(02)01020-6

Mok, D. Z. L., Sternberg, P. W., & Inoue, T. (2015). Morphologically defined sub-stages of C. Elegans vulval development in the fourth larval stage. *BMC Developmental Biology*, *15*(1), 1–8. https://doi.org/10.1186/s12861-015-0076-7

Mollard, G. F. V, Mignerytt, G. A., Baumert, M., Perin, M. S., Hansont, T. J., Burger, P. M., … Sudhof, T. C. (1992). Rab3 is a small GTP-binding protein exclusively localized to synaptic vesicles. *Proceedings of the National Academy of Sciences*, *87*(March 1990), 1988–1992.

Monday, H. R., & Castillo, P. E. (2017). Closing the gap : long-term presynaptic plasticity in

brain function and disease. *Current Opinion in Neurobiology*, *45*, 106–112. https://doi.org/10.1016/j.conb.2017.05.011

Mooren, O. L., Galletta, B. J., & Cooper, J. A. (2012). Roles for Actin Assembly in Endocytosis. *Annu. Rev. Biochem*, *81*, 661–686. https://doi.org/10.1146/annurev-biochem-060910-094416

Morgan, J. L., Soto, F., Wong, R. O. L., & Kerschensteiner, D. (2011). Development of Cell Type-Specific Connectivity Patterns of Converging Excitatory Axons in the Retina. *Neuron*, *71*(6), 1014–1021. https://doi.org/10.1016/j.neuron.2011.08.025

Mulcahy, B., Witvliet, D., Holmyard, D., Mitchell, J., Chisholm, A. D., Samuel, A. D. T., & Zhen, M. (2018). A Pipeline for Volume Electron Microscopy of the Caenorhabditis elegans Nervous System. *Frontiers in Neural Circuits*, *12*(November). https://doi.org/10.3389/fncir.2018.00094

Mullins, R. D., Heuser, J. a, & Pollard, T. D. (1998). The interaction of Arp2/3 complex with actin: nucleation, high affinity pointed end capping, and formation of branching networks of filaments. *Proceedings of the National Academy of Sciences of the United States of America*, *95*(11), 6181–6186. https://doi.org/10.1073/pnas.95.11.6181

Murthy, V. N., & De Camilli, P. (2003). Cell biology of the presynaptic terminal. *Annual Review of Neuroscience*, *26*, 701–728. https://doi.org/10.1146/annurev.neuro.26.041002.131445

Nance, J., & Frøkjær-Jensen, C. (2019). *The* Caenorhabditis elegans *Transgenic Toolbox*. *Genetics* (Vol. 212). https://doi.org/10.1534/genetics.119.301506

Ng, R., Salem, S. S., Wu, S. T., Wu, M., Lin, H. H., Shepherd, A. K., … Su, C. Y. (2019). Amplification of Drosophila Olfactory Responses by a DEG/ENaC Channel. *Neuron*, *104*(5), 947-959.e5. https://doi.org/10.1016/j.neuron.2019.08.041

Nguyen, T. H., Maucort, G., Sullivan, R. K. P., Schenning, M., Lavidis, N. A., McCluskey, A., … Meunier, F. A. (2012). Actin- and dynamin-dependent maturation of bulk endocytosis

restores neurotransmission following synaptic depletion. *PLoS ONE*, *7*(5). https://doi.org/10.1371/journal.pone.0036913

Nicholson-Fish, J. C., Kokotos, A. C., Gillingwater, T. H., Smillie, K. J., & Cousin, M. A. (2015). VAMP4 Is an Essential Cargo Molecule for Activity-Dependent Bulk Endocytosis. *Neuron*, *88*(5), 973–984. https://doi.org/10.1016/j.neuron.2015.10.043

Nimchinsky, E., Sabatini, B. L., & Svoboda, K. (2002). Structure and funciton of Dendritic Spines. *Annu. Rev. Physiology.*, *64*, 313–353. https://doi.org/10.1146/annurev.physiol.64.081501.160008

Noda, T., Kim, J., Huang, W. P., Baba, M., Tokunaga, C., Ohsumi, Y., & Klionsky, D. J. (2000). Apg9p/Cvt7p is an integral membrane protein required for transport vesicle formation in the Cvt and autophagy pathways. *Journal of Cell Biology*, *148*(3), 465–479. https://doi.org/10.1083/jcb.148.3.465

Noma, K., Goncharov, A., Ellisman, M. H., & Jin, Y. (2017). Microtubule-dependent ribosome localization in C . elegans neurons, (Dcc), 1–23.

Nonet, M. L., Saifee, O., Zhao, H., Rand, J. B., & Wei, L. (1998). Synaptic transmission deficits in Caenorhabditis elegans synaptobrevin mutants. *Journal of Neuroscience*, *18*(1), 70–80. https://doi.org/10.1523/jneurosci.18-01-00070.1998

Nonet, M. L., Staunton, J. E., Kilgard, M. P., Fergestad, T., Hartwieg, E., Horvitz, H. R., … Meyer, B. J. (1997). Caenorhabditis elegans rab-3 Mutant Synapses Exhibit Impaired Function and Are Partially Depleted of Vesicles. *Journal of Neuroscience*, *17*(21), 8061–8073.

Oh, K. H., Krout, M., Richmond, J. E., & Kim, H. (2021). UNC-2 CaV2 channel localization at presynaptic active zones depends on UNC-10/RIM and SYD-2/Liprin-α in Caenorhabditis elegans . *The Journal of Neuroscience*, (April), JN-RM-0076-21. https://doi.org/10.1523/jneurosci.0076-21.2021

Oliver, D., Alexander, K., & Francis, M. M. (2018). Molecular Mechanisms Directing Spine Outgrowth and Synaptic Partner Selection in Caenorhabditis elegans. *Journal of Experimental Neuroscience*, *12*, 10–13. https://doi.org/10.1177/1179069518816088

Oliver, D., Ramachandran, S., Philbrook, A., Lambert, C. M., Nguyen, K. C. Q., Hall, D. H., & Francis, M. M. (2021). Kinesin-3 mediated delivery of presynaptic neurexin stabilizes growing dendritic spines and postsynaptic components. *BioRxiv*.

Orr, B. O., Gorczyca, D., Younger, M. A., Jan, L. Y., Jan, Y. N., & Davis, G. W. (2017). Composition and Control of a Deg/ENaC Channel during Presynaptic Homeostatic Plasticity. *Cell Reports*, *20*(8), 1855–1866. https://doi.org/10.1016/j.celrep.2017.07.074

Otsuka, A. J., Jeyaprakash, A., García-Añoveros, J., Tang, L. Z., Fisk, G., Hartshorne, T., … Bornt, T. (1991). The C. elegans unc-104 4 gene encodes a putative kinesin heavy chain-like protein. *Neuron*, *6*(1), 113–122. https://doi.org/10.1016/0896-6273(91)90126-K

Pan, Y., & Monje, M. (2020). Activity shapes neural circuit form and function: A historical perspective. *Journal of Neuroscience*, *40*(5), 944–954. https://doi.org/10.1523/JNEUROSCI.0740-19.2019

Park, M., Watanabe, S., Poon, V. Y. N., Ou, C. Y., Jorgensen, E. M., & Shen, K. (2011). CYY-1/Cyclin Y and CDK-5 Differentially Regulate Synapse Elimination and Formation for Rewiring Neural Circuits. *Neuron*, *70*(4), 742–757. https://doi.org/10.1016/j.neuron.2011.04.002

Patel, F. B., & Soto, M. C. (2013). WAVE/SCAR promotes endocytosis and early endosome morphology in polarized C. elegans epithelia. *Developmental Biology*, *377*(2), 319–332. https://doi.org/10.1016/j.ydbio.2013.03.012

Patel, M. R. (2010). Molecular mechanisms of presynaptic assembly at defined synapses in Caenorhabditis Elegans. *Dissertation Abstracts International: Section B: The Sciences and Engineering*, *70*(10-B), 6024. Retrieved from

http://search.ebscohost.com/login.aspx?direct=true&db=psyh&AN=2010-99080-068&site=ehost-live&scope=site

Petersen, S. C., Watson, J. D., Richmond, J. E., Sarov, M., Walthall, W. W., & Miller, D. M. (2011). A Transcriptional Program Promotes Remodeling of GABAergic Synapses in Caenorhabditis elegans. *Journal of Neuroscience*, *31*(43), 15362–15375. https://doi.org/10.1523/JNEUROSCI.3181-11.2011

Petralia, R. S., Sans, N., Wang, Y. X., & Wenthold, R. J. (2005). Ontogeny of postsynaptic density proteins at glutamatergic synapses. *Molecular and Cellular Neuroscience*, *29*(3), 436–452. https://doi.org/10.1016/j.mcn.2005.03.013

Petralia, R. S., Wang, Y.-X., Mattson, M., & Yao, P. (2016). The Diversity of Spine Synapses in Animals. *NeuroMolecular Medicine*, *18*(4), 497–539. https://doi.org/10.1007/s12017-016-8405-y

Petrash, H. A., Philbrook, A., Haburcak, M., Barbagallo, B., & Francis, M. M. (2013). ACR-12 Ionotropic Acetylcholine Receptor Complexes Regulate Inhibitory Motor Neuron Activity in Caenorhabditis elegans. *The Journal of Neuroscience*, *33*(13), 5524–5532. https://doi.org/10.1523/JNEUROSCI.4384-12.2013

Philbrook, A., Ramachandran, S., Lambert, C. M., Oliver, D., Florman, J., Alkema, M. J., … Francis, M. M. (2018). Neurexin directs partner-specific synaptic connectivity in C. Elegans. *ELife*, *7*, 1–30. https://doi.org/10.7554/eLife.35692

Piochon, C., Kano, M., & Hansel, C. (2016). LTD-like molecular pathways in developmental synaptic pruning. *Nature Neuroscience*, *19*(10), 1299–1310. https://doi.org/10.1038/nn.4389

Pokala, N., Liu, Q., Gordus, A., & Bargmann, C. I. (2014). Inducible and titratable silencing of Caenorhabditis elegans neurons in vivo with histamine-gated chloride channels. *Proceedings of the National Academy of Sciences*, *111*(7), 2770–2775.

https://doi.org/10.1073/pnas.1400615111

Pollard, T. D., & Borisy, G. G. (2003). Cellular motility drive by assembly and disassembly of actin filaments. *Cell*, *112*, 453–465. https://doi.org/10.1007/BF02073506

Qi, Y. B., Garren, E. J., Shu, X., Tsien, R. Y., & Jin, Y. (2012). Photo-inducible cell ablation in Caenorhabditis elegans using the genetically encoded singlet oxygen generating protein miniSOG. *Proceedings of the National Academy of Sciences*, *109*(19), 7499–7504. https://doi.org/10.1073/pnas.1204096109

Raingo, J., Khvotchev, M., Liu, P., Darios, F., Li, Y. C., Ramirez, D. M. O., … Kavalali, E. T. (2012). VAMP4 directs synaptic vesicles to a pool that selectively maintains asynchronous neurotransmission. *Nature Neuroscience*, *15*(5), 738–745. https://doi.org/10.1038/nn.3067

Rao, Y., Ma, Q., Vahedi-Faridi, A., Sundborger, A., Pechstein, A., Puchkov, D., … Haucke, V. (2010). Molecular basis for SH3 domain regulation of F-BAR-mediated membrane deformation. *Proceedings of the National Academy of Sciences of the United States of America*, *107*(18), 8213–8218. https://doi.org/10.1073/pnas.1003478107

Ratnayaka, A., Marra, V., Branco, T., & Staras, K. (2011). Extrasynaptic vesicle recycling in mature hippocampal neurons. *Nature Communications*, *2*(1). https://doi.org/10.1038/ncomms1534

Richards, D. a, Rizzoli, S. O., & Betz, W. J. (2004). Effects of wortmannin and latrunculin A on slow endocytosis at the frog neuromuscular junction. *The Journal of Physiology*, *557*(Pt 1), 77–91. https://doi.org/10.1113/jphysiol.2004.062158

Richmond, J. E., Davis, W. S., & Jorgensen, E. M. (1999). Unc-13 is required for synaptic vesicle fusion in C. elegans. *Nature Neuroscience*, *2*(11), 959–964. https://doi.org/10.1038/14755

Richmond, J. E., & Jorgensen, E. M. (1999). One GABA and two acetylcholine receptors function at the C. elegans neuromuscular junction. *Nature Neuroscience*, *2*(9), 791–798.

https://doi.org/10.1038/12160

Riedl, J., Crevenna, A. H., Kessenbrock, K., Yu, J. H., Neukirchen, D., Bista, M., … Wedlich-Soldner, R. (2008). Lifeact: a versatile marker to visualize F-actin. *Nature Methods*, *5*(7), 605–607. https://doi.org/10.1038/nmeth.1220

Rochefort, N. L., & Konnerth, A. (2012). Dendritic spines: From structure to in vivo function. *EMBO Reports*, *13*(8), 699–708. https://doi.org/10.1038/embor.2012.102

Rohatgi, R., Ma, L., Miki, H., Lopez, M., Kirchhausen, T., Takenawa, T., & Kirschner, M. W. (1999). The interaction between N-WASP and the Arp2/3 complex links Cdc42-dependent signals to actin assembly. *Cell*, *97*(2), 221–231. https://doi.org/10.1016/S0092-8674(00)80732-1

Rostaing, P., Weimer, R. M., Jorgensen, E. M., & Triller, A. (2004). Preservation of Immunoreactivity and Fine Structure of Adult C . elegans Tissues Using High-pressure Freezing The Journal of Histochemistry & Cytochemistry. *Journal of Histochemistry & Cytochemistry*, *52*(1), 1–12.

Rotty, J. D., Wu, C., & Bear, J. E. (2013). New insights into the regulation and cellular functions of the ARP2/3 complex. *Nature Reviews. Molecular Cell Biology*, *14*(1), 7–12. https://doi.org/10.1038/nrm3492

Sala, C., & Segal, M. (2014). Dendritic spines: the locus of structural and functional plasticity, 141–188. https://doi.org/10.1152/physrev.00012.2013

Salcini, A. E., Hilliard, M. A., Croce, A., Arbucci, S., Luzzi, P., Tacchetti, C., … Bazzicalupo, P. (2001). The Eps15 C. elegans homologue EHS-1 is implicated in synaptic vesicle recycling. *Nature Cell Biology*, *3*(8), 755–760. https://doi.org/10.1038/35087075

Sanes, J. R., & Lichtman, J. W. (2009). Development of the vertebrate neuromuscular junction. *Annual Review of Neuroscience*, 39–84. https://doi.org/10.1007/978-0-387-92708-4_3

Schild, L. C., & Glauser, D. A. (2015). Dual color neural activation and behavior control with

chrimson and CoChR in Caenorhabditis elegans. *Genetics*, *200*(4), 1029–1034. https://doi.org/10.1534/genetics.115.177956

Schindelin, J., Arganda-Carreras, I., Frise, E., Kaynig, V., Longair, M., Pietzsch, T., … Cardona, A. (2012). Fiji: An open-source platform for biological-image analysis. *Nature Methods*, *9*(7), 676–682. https://doi.org/10.1038/nmeth.2019

Schindler, A. J., & Sherwood, D. R. (2013). Morphogenesis of the Caenorhabditis elegans vulva. *Wiley Interdisciplinary Reviews: Developmental Biology*, *2*(1), 75–95. https://doi.org/10.1002/wdev.87

Schoch, S., Castillo, P. E., Jo, T., Mukherjee, K., Geppert, M., Wang, Y., … Sudhof, T. C. (2002). RIM1 a forms a protein scaffold for regulating neurotransmitter release at the active zone. *Nature*, *415*(January), 1–6.

Schottler, F., Fabiato, H., Leland, J. M., Chang, L. Y., Lotfi, P., Getachew, F., & Lee, K. S. (2001). Inhibition of the Arp2/3 complex-nucleated actin polymerization and branch formation by tropomyosin. *Current Biology*, *11*(16), 1300–1304. https://doi.org/10.1016/S0960-9822(01)00395-5

Schuske, K. R., Richmond, J. E., Matthies, D. S., Davis, W. S., Runz, S., Rube, D. A., … Jorgensen, E. M. (2003). Endophilin is required for synaptic vesicle endocytosis by localizing synaptojanin. *Neuron*, *40*(4), 749–762. https://doi.org/10.1016/S0896-6273(03)00667-6

Schwartz, M. L., & Jorgensen, E. M. (2016). SapTrap, a Toolkit for High-Throughput CRISPR/Cas9. *Genetics*, *202*(April), 1277–1288. https://doi.org/10.1534/genetics.115.184275

Scott, E. K., Reuter, J. E., & Luo, L. (2003). Dendritic development of Drosophila high order visual system neurons is independent of sensory experience. *BMC Neuroscience*, *6*, 1–6.

Shan, G., Kim, K., Li, C., & Walthall, W. W. (2005). Convergent genetic programs regulate

similarities and differences between related motor neuron classes in Caenorhabditis elegans. *Developmental Biology*, *280*(2), 494–503. https://doi.org/10.1016/j.ydbio.2005.01.032

Shepherd, G. M. G., & Harris, K. M. (1998). Three-dimensional structure and composition of CA3→CA1 axons in rat hippocampal slices: Implications for presynaptic connectivity and compartmentalization. *Journal of Neuroscience*, *18*(20), 8300–8310. https://doi.org/10.1523/jneurosci.18-20-08300.1998

Shupliakov, O., Bloom, O., Gustafsson, J. S., Kjaerulff, O., Low, P., Tomilin, N., … Brodin, L. (2002). Impaired recycling of synaptic vesicles after acute perturbation of the presynaptic actin cytoskeleton. *Proceedings of the National Academy of Sciences of the United States of America*, *99*(22), 14476–14481. https://doi.org/10.1073/pnas.212381799

Siksou, L., Rostaing, P., Lechaire, J.-P., Boudier, T., Ohtsuka, T., Fejtova, A., … Marty, S. (2007). Three-Dimensional Architecture of Presynaptic Terminal Cytomatrix. *Journal of Neuroscience*, *27*(26), 6868–6877. https://doi.org/10.1523/JNEUROSCI.1773-07.2007

Smith, C. J., Watson, J. D., Spencer, W. C., Brien, T. O., Cha, B., Albeg, A., … Miller, D. M. (2010). Time-lapse imaging and cell-speci fi c expression pro fi ling reveal dynamic branching and molecular determinants of a multi-dendritic nociceptor in C . elegans. *Developmental Biology*, *345*(1), 18–33. https://doi.org/10.1016/j.ydbio.2010.05.502

Snider, C. E., Chandra, M., McDonald, N. A., Willet, A. H., Collier, S. E., Ohi, M. D., … Gould, K. L. (2020). Opposite Surfaces of the Cdc15 F-BAR Domain Create a Membrane Platform That Coordinates Cytoskeletal and Signaling Components for Cytokinesis. *Cell Reports*, *33*(12), 108526. https://doi.org/10.1016/j.celrep.2020.108526

Soderling, S. H., Langeberg, L. K., Soderling, J. a, Davee, S. M., Simerly, R., Raber, J., & Scott, J. D. (2003). Loss of WAVE-1 causes sensorimotor retardation and reduced learning and memory in mice. *Proceedings of the National Academy of Sciences of the United States of*

America, *100*(4), 1723–1728. https://doi.org/10.1073/pnas.0438033100

Sonntag, M., Englitz, B., Kopp-Scheinpflug, C., & Rübsamen, R. (2009). Early postnatal development of spontaneous and acoustically evoked discharge activity of principal cells of the medial nucleus of the trapezoid body: An in vivo study in mice. *Journal of Neuroscience*, *29*(30), 9510–9520. https://doi.org/10.1523/JNEUROSCI.1377-09.2009

Speese, S., Petrie, M., Schuske, K., Ailion, M., Ann, K., Iwasaki, K., … Martin, T. F. J. (2007). UNC-31 (CAPS) Is Required for Dense-Core Vesicle But Not Synaptic Vesicle Exocytosis in Caenorhabditis elegans, *27*(23), 6150–6162. https://doi.org/10.1523/JNEUROSCI.1466-07.2007

Spence, X. E. F., Kanak, X. D. J., Carlson, B. R., & Soderling, S. H. (2016). The Arp2 / 3 Complex Is Essential for Distinct Stages of Spine Synapse Maturation , Including Synapse Unsilencing, *36*(37), 9696–9709. https://doi.org/10.1523/JNEUROSCI.0876-16.2016

Spencer, W. C., McWhirter, R., Miller, T., Strasbourger, P., Thompson, O., Hillier, L. W., … Miller III, D. M. (2014). Isolation of specific neurons from C. elegans larvae for gene expression profiling. *PLoS ONE*, *9*(11).

Staras, K., Branco, T., Burden, J. J., Pozo, K., Darcy, K., Marra, V., … Goda, Y. (2010). A Vesicle Superpool Spans Multiple Presynaptic Terminals in Hippocampal Neurons. *Neuron*, *66*(1), 37–44. https://doi.org/10.1016/j.neuron.2010.03.020

Stavoe, A. K. H., Hill, S. E., Hall, D. H., & Colón-Ramos, D. A. (2016). KIF1A/UNC-104 Transports ATG-9 to Regulate Neurodevelopment and Autophagy at Synapses. *Developmental Cell*, *38*(2), 171–185. https://doi.org/10.1016/j.devcel.2016.06.012

Stettler, D. D., Yamahachi, H., Li, W., Denk, W., & Gilbert, C. D. (2006). Axons and Synaptic Boutons Are Highly Dynamic in Adult Visual Cortex. *Neuron*, (49), 877–887. https://doi.org/10.1016/j.neuron.2006.02.018

Steward, O., Reeves, T. M., & Reeves, M. (1988). Protein-synthetic machinery beneath

postsynaptic sites on CNS neurons: association between polyribosomes and other organelles at the synaptic site. *The Journal of Neuroscience : The Official Journal of the Society for Neuroscience*, *8*(1), 176–184. https://doi.org/10.1523/JNEUROSCI.08-01-00176.1988

Stigloher, C., Zhan, H., Zhen, M., Richmond, J., Bessereau, J., & Supe, N. (2011). The Presynaptic Dense Projection of the Caenorhabiditis elegans Cholinergic Neuromuscular Junction Localizes Synaptic Vesicles at the Active Zone through SYD-2 / Liprin and UNC-10 / RIM-Dependent Interactions. *Journal of Neuroscience*, *31*(12), 4388–4396. https://doi.org/10.1523/JNEUROSCI.6164-10.2011

Stretton, A. O. W., Fishpool, R. M., Southgate, E., Donmoyer, J. E., Walrond, J. P., & Kass, I. S. (1978). Structure and physiological activity of the motorneurons of the nematode Ascaris. *Proceedings of the National Academy of Sciences, USA*, *75*(7), 3493–3497. https://doi.org/10.1073/pnas.75.7.3493

Südhof, T. (2018). Towards an Understanding of Synapse Formation. *Neuron*, *100*(2), 276–293. https://doi.org/10.1016/j.neuron.2018.09.040

Sudhof, T. C. (2018). Towards an Understanding of Synapse Formation. *Neuron*, *100*(2), 276–293.

Südhof, T. C. (2012). The presynaptic active zone. *Neuron*, *75*(1), 11–25. https://doi.org/10.1016/j.neuron.2012.06.012

Südhof, T. C. (2013). A molecular machine for neurotransmitter release: synaptotagmin and beyond. *Nature Medicine*, *19*(10), 1227–1231. https://doi.org/10.1038/nm.3338

Südhof, T. C. (2017). Synaptic Neurexin Complexes: A Molecular Code for the Logic of Neural Circuits. *Cell*, *171*(4), 745–769. https://doi.org/10.1016/j.cell.2017.10.024

Sugei, A., Hakeda-Suzuki, S., Suzuki, E., Silies, M., Shimozono, M., Mohl, C., … Tavosanis, G. (2015). Molecular Remodeling of the Presynaptic Active Article Molecular Remodeling of

the Presynaptic Active Zone of Drosophila Photoreceptors via Activity-Dependent Feedback. *Neuron*, (86), 711–725. https://doi.org/10.1016/j.neuron.2015.03.046

Sulston, J. E. (1976). Post-Embryonic Development in the Ventral Cord of Caenorhabditis elegans J . E . Sulston Philosophical Transactions of the Royal Society of London . Series B , Biological Sciences , Vol . *Philosophical Transactions of the Royal Society of London*, *275*(938), 287–297.

Sulston, J. E., & Horvitz, H. R. (1977). Post-embryonic Cell Lineages of the Nematode, Caenorhabditis elegans. *Developmental Biology*, *156*, 110–156.

Takahashi, N., Kitamura, K., Matsuo, N., Mayford, M., Kano, M., Matsuki, N., & Ikegaya, Y. (2012). Locally synchronized synaptic inputs. *Science*, *335*(January), 353–357.

Takano, K., Takano, K., Toyooka, K., & Suetsugu, S. (2008). EFC/F-BAR proteins and the N-WASP-WIP complex induce membrane curvature-dependent actin polymerization. *The EMBO Journal*, *27*(21), 2817–2828. https://doi.org/10.1038/emboj.2008.216

Takenawa, T., & Suetsugu, S. (2007). The WASP–WAVE protein network: connecting the membrane to the cytoskeleton. *Nature Reviews Molecular Cell Biology*, *8*(1), 37–48. https://doi.org/10.1038/nrm2069

Taylor, S. R., Santpere, G., Weinreb, A., Barrett, A., Reilly, M., Xu, C., … Miller III, D. M. (2020). Molecular topography of an entire nervous system. *BioRxiv*.

Taylor, S., Santpere, G., Reilly, M., Glenwinkel, L., Poff, A., McWhirther, R., … Miller III, D. M. (2019). Expression profiling of the mature C. elegans nervous system by single-cell RNA-Sequencing. *BioRxiv*.

Tennant, K. A., Taylor, S. L., White, E. R., & Brown, C. E. (2017). Optogenetic rewiring of thalamocortical circuits to restore function in the stroke injured brain. *Nature Communications*, *8*(May), 1–14. https://doi.org/10.1038/ncomms15879

Thompson-Peer, K. L., Bai, J., Hu, Z., & Kaplan, J. (2012). HBL-1 patterns synaptic remodeling

in C.elegans. *Neuron*, *73*(3), 453–465. https://doi.org/10.1016/j.neuron.2011.11.025

Tom Dieck, S., Sanmartí-Vila, L., Langnaese, K., Richter, K., Kindler, S., Soyke, A., … Gundelfinger, E. D. (1998). Bassoon, a novel zinc-finger CAG/glutamine-repeat protein selectively localized at the active zone of presynaptic nerve terminals. *Journal of Cell Biology*, *142*(2), 499–509. https://doi.org/10.1083/jcb.142.2.499

Trachtenberg, J. T., Chen, B., Knott, G. W., Feng, G., Sanes, J. R., Welker, E., & Svoboda, K. (2002). Long-term in vivo imaging of experience-dependent synaptic plasticity in adult cortex. *Nature*, *420*(19/26), 788–794. https://doi.org/10.1111/j.1528-1157.1986.tb03495.x

Trachtenberg, J. T., Wilbrecht, L., Shepherd, G. M., Zhang, X., Knott, G. W., & Svoboda, K. (2005). Transient and Persistent Dendritic Spines in the Neocortex In Vivo. *Neuron*, *45*, 279–291. https://doi.org/10.1016/j.neuron.2005.01.003

Tsuriel, S., Geva, R., Zamorano, P., Dresbach, T., Boeckers, T., & Gundelfinger, E. D. (2006). Local Sharing as a Predominant Determinant of Synaptic Matrix Molecular Dynamics. *PLOS Biology*, *4*(9). https://doi.org/10.1371/journal.pbio.0040271

Ullrich, O., Reinsch, S., Urbé, S., Zerial, M., & Parton, R. G. (1996). Rab11 regulates recycling through the pericentriolar recycling endosome. *Journal of Cell Biology*, *135*(4), 913–924. https://doi.org/10.1083/jcb.135.4.913

Umbriaco, D., Watkins, K. C., Descarries, L., Cozzari, C., & Hartman, B. K. (1994). Ultrastructural and morphometric features of the acetylcholine innervation in adult rat parietal cortex: An electron microscopic study in serial sections. *Journal of Comparative Neurology*, *348*(3), 351–373. https://doi.org/10.1002/cne.903480304

Urbano, F. J., Lino, N. G., González-Inchauspe, C. M. F., González, L. E., Colettis, N., Vattino, L. G., … Uchitel, O. D. (2014). Acid-sensing ion channels 1a (ASIC1a) inhibit neuromuscular transmission in female mice. *American Journal of Physiology - Cell Physiology*, *306*(4), 396–406. https://doi.org/10.1152/ajpcell.00301.2013

Voglis, G., & Tavernarakis, N. (2008). A synaptic DEG/ENaC ion channel mediates learning in C. elegans by facilitating dopamine signalling. *EMBO Journal*, *27*(24), 3288–3299. https://doi.org/10.1038/emboj.2008.252

Walthall, W. W., & Plunkett, J. A. (1995). Genetic transformation of the synaptic pattern of a motoneuron class in Caenorhabditis elegans. *Journal of Neuroscience*, *15*(2), 1035–1043. https://doi.org/10.1523/jneurosci.15-02-01035.1995

Wang, X., Kibschull, M., Laue, M. M., Lichte, B., Petrasch-Parwez, E., & Kilimann, M. W. (1999). Aczonin, a 550-kD putative scaffolding protein of presynaptic active zones, shares homology regions with Rim and Bassoon and binds profilin. *Journal of Cell Biology*, *147*(1), 151–162. https://doi.org/10.1083/jcb.147.1.151

Wang, Ying, Matthewman, C., Han, L., Miller, D. M., & Bianchi, L. (2013). Neurotoxic unc-8 mutants encode constitutively active DEG/ENaC channels that are blocked by divalent cations. *Journal of General Physiology*, *142*(2), 157–169. https://doi.org/10.1085/jgp.201310974

Wang, Yun, Okamoto, M., Schmitz, F., Hofmann, K., & Sudhof, T. C. (1997). Rim is a putative Rab3 effector in regulating synaptic-vesicle fusion. *Nature*, *388*(August), 1878–1882.

Wang, Yun, Sugita, S., & Südhof, T. C. (2000). The RIM/NIM family of neuronal C2 domain proteins: Interactions with Rab3 and a new class of Src homology 3 domain proteins. *Journal of Biological Chemistry*, *275*(26), 20033–20044. https://doi.org/10.1074/jbc.M909008199

Watanabe, S., Liu, Q., Davis, M. W., Hollopeter, G., Thomas, N., Jorgensen, N. B., & Jorgensen, E. M. (2013). Ultrafast endocytosis at Caenorhabditis elegans neuromuscular junctions, 1–24. https://doi.org/10.7554/eLife.00723

Watanabe, S., Trimbuch, T., Camacho-Pérez, M., Rost, B. R., Brokowski, B., Söhl-Kielczynski, B., … Jorgensen, E. M. (2014). Clathrin regenerates synaptic vesicles from endosomes.

Nature, *515*(7526), 228–233. https://doi.org/10.1038/nature13846

Weimer, R. M., Gracheva, E. O., Meyrignac, O., Miller, K. G., Richmond, J. E., & Bessereau, J. (2006). UNC-13 and UNC-10 Rim Localize Synaptic Vesicles to Specific Membrane Domains. *The Journal of Neuroscience*, *26*(31), 8040–8047. https://doi.org/10.1523/JNEUROSCI.2350-06.2006

Wemmie, J. A., Chen, J., Askwith, C. C., Hruska-Hageman, A. M., Price, M. P., Nolan, B. C., … Welsh, M. J. (2002). The acid-activated ion channel ASIC contributes to synaptic plasticity, learning, and memory. *Neuron*, *34*(3), 463–477. https://doi.org/10.1016/S0896-6273(02)00661-X

Westphal, R. S., Soderling, S. H., Alto, N. M., Langeberg, L. K., & Scott, J. D. (2000). Scar/WAVE-1 , a Wiskott-Aldrich syndrome protein , assembles an actin-associated multi-kinase scaffold. *The EMBO Journal*, *19*(17), 4589–4600.

White, John G., Albertson D. G., A. M. A. R. (n.d.). Connectivity changes in a class of motorneuron during development of a nematode.

White, J. G., Albertson, D. G., & Anness, M. (1978). Connectivity changes in a class of motoneurone during the development of a nematode. *Nature*, *271*, 764–766. https://doi.org/10.1038/271764a0

White, J. G., Southgate, E., Thomson, J. N., & Brenner, S. (1976). The Structure of the Ventral Nerve Cord of Caenorhadbitis elegans. *Philosophical Transactions of the Royal Society of London*, *275*.

White, J. G., Southgate, E., Thomson, J. N., & Brenner, S. (1986). The Structure of the Nervous System of the Nematode Caenorhabditis elegans. *Philosophical Transactions of the Royal Society of London*, *314*(1165), 1–340. https://doi.org/10.1098/rstb.1986.0056

Whitington, P. M., & Sink, H. (2004). Development of a polar morphology by identified embryonic motoneurons. *International Journal of Developmental Neuroscience*, *22*, 39–45.

https://doi.org/10.1016/j.ijdevneu.2003.10.004

Wu, W., & Wu, L. G. (2007). Rapid bulk endocytosis and its kinetics of fission pore closure at a central synapse. *Proceedings of the National Academy of Sciences of the United States of America*, *104*(24), 10234–10239. https://doi.org/10.1073/pnas.0611512104

Wu, X., Lee, S. H., Sheng, J., Charnay, P., Ervasti, J. M., Wu, L., … Wang, D. (2016). Actin Is Crucial for All Kinetically Distinguishable Forms of Endocytosis at Synapses. *Neuron*, *92*(5), 1020–1035. https://doi.org/10.1016/j.neuron.2016.10.014

Xuan, Z., Manning, L., Nelson, J., Richmond, J. E., Colón-Ramos, D. A., Shen, K., & Kurshan, P. T. (2017). Clarinet (CLA-1), a novel active zone protein required for synaptic vesicle clustering and release. *ELife*, *6*. https://doi.org/10.7554/eLife.29276

Yamada, H., Padilla-Parra, S., Park, S. J., Itoh, T., Chaineau, M., Monaldi, I., … Takei, K. (2009). Dynamic interaction of amphiphysin with N-WASP regulates actin assembly. *Journal of Biological Chemistry*, *284*(49), 34244–34256. https://doi.org/10.1074/jbc.M109.064204

Yamahachi, H., Marik, S. A., Mcmanus, J. N. J., Denk, W., & Gilbert, C. D. (2009). Article Rapid Axonal Sprouting and Pruning Accompany Functional Reorganization in Primary Visual Cortex. *Neuron*, *64*(5), 719–729. https://doi.org/10.1016/j.neuron.2009.11.026

Yang, S., Park, D., Manning, L., Hill, S. E., Cao, M., Xuan, Z., … Colón-Ramos, D. A. (2020). Presynaptic autophagy is coupled to the synaptic vesicle cycle via ATG-9. *BioRxiv*. https://doi.org/10.1101/2020.12.28.424508

Yao, C., Liu, Y., Lee, I., Wang, Y., & Wu, P. (2017). A Ca 2 + channel differentially regulates Clathrin-mediated and activity-dependent bulk endocytosis. *PLoS Biology*, *15*(4), 1–33. https://doi.org/10.1371/journal.pbio.2000931

Yasuda, M., Johnson-Venkatesh, E. M., Zhang, H., Parent, J. M., Sutton, M. A., & Umemori, H. (2011). Multiple Forms of Activity-Dependent Competition Refine Hippocampal Circuits In

Vivo. *Neuron*, *70*(6), 1128–1142. https://doi.org/10.1016/j.neuron.2011.04.027

Yeh, E. (2005). Identification of Genes Involved in Synaptogenesis Using a Fluorescent Active Zone Marker in Caenorhabditis elegans. *Journal of Neuroscience*, *25*(15), 3833–3841. https://doi.org/10.1523/JNEUROSCI.4978-04.2005

Younger, M. A., Mu, M., Tong, A., Pym, E. C., & Davis, G. W. (2013). A Presynaptic ENaC Channel Drives Homeostatic Plasticity. *Neuron*, *79*, 1183–1196. https://doi.org/10.1016/j.neuron.2013.06.048

Yu, B., Wang, X., Wei, S., Fu, T., Dzakah, E. E., Waqas, A., … Shan, G. (2017). Convergent Transcriptional Programs Regulate cAMP Levels in C . elegans GABAergic Motor Neurons. *Developmental Cell*, 1–15. https://doi.org/10.1016/j.devcel.2017.09.013

Yu, S., Jánosi, B., Liewald, J. F., Wabnig, S., & Gottschalk, A. (2018). Endophilin A and B Join Forces With Clathrin to Mediate Synaptic Vesicle Recycling in Caenorhabditis elegans. *Frontiers in Molecular Neuroscience*, *11*(June), 1–17. https://doi.org/10.3389/fnmol.2018.00196

Yuste, R. (2015). The discovery of dendritic spines by Cajal, *9*(April), 1–6. https://doi.org/10.3389/fnana.2015.00018

Zeng, Q., Tran, T. T. H., Tan, H. X., & Hong, W. (2003). The cytoplasmic domain of Vamp4 and Vamp5 is responsible for their correct subcellular targeting: The N-terminal extension of Vamp4 contains a dominant autonomous targeting signal for the trans-Golgi network. *Journal of Biological Chemistry*, *278*(25), 23046–23054. https://doi.org/10.1074/jbc.M303214200

Zhang, X. M., François, U., Silm, K., Angelo, M. F., Busch, M. V. F., Maged, M., … Herzog, E. (2019). A proline-rich motif on VGLUT1 reduces synaptic vesicle super-pool and spontaneous release frequency. *ELife*, *8*, 1–24. https://doi.org/10.7554/eLife.50401

Zhen, Mei, Huang, X., Bamber, B., & Jin, Y. (2000). Regulation of presynaptic terminal

organization by C. elegans RMP-1, a putative guanine nucleotide exchanger with a RING-H2 finger domain. *Neuron*, *26*, 331–343.

Zhen, Mel, & Jin, Y. (1999). The liprin protein SYD-2 regulates the differentiation of presynaptic termini in C. elegans. *Nature*, *401*(6751), 371–375. https://doi.org/10.1038/43886

Zhou, H., & Walthall, W. (1998). UNC-55 , an Orphan Nuclear Hormone Receptor , Orchestrates Synaptic Specificity among Two Classes of Motor Neurons in Caenorhabditis elegans. *The Journal of Neuroscience*, *18*(24), 10438–10444.

Zhou, Q., Homma, K. J., & Poo, M. M. (2004). Shrinkage of dendritic spines associated with long-term depression of hippocampal synapses. *Neuron*, *44*(5), 749–757. https://doi.org/10.1016/j.neuron.2004.11.011

Zielinska, D. F., Gnad, F., Jedrusik-bode, M., Wis, J. R., & Mann, M. (2009). Caenorhabditis elegans Has a Phosphoproteome Atypical for Metazoans That Is Enriched in Developmental and Sex Determination Proteins research articles. *Journal of Proteome Research*, *8*, 4039–4049.

Zucker, R. S., Kullmann, D. M., & Kaeser, P. S. (2014). *Release of Neurotransmitters*. *From Molecules to Networks: An Introduction to Cellular and Molecular Neuroscience: Third Edition* (Third Edit). Elsevier Inc. https://doi.org/10.1016/B978-0-12-397179-1.00015-4

Zuo, Y., Lin, A., Chang, P., & Gan, W. B. (2005). Development of long-term dendritic spine stability in diverse regions of cerebral cortex. *Neuron*, *46*(2), 181–189. https://doi.org/10.1016/j.neuron.2005.04.001